FUNDAMENTAL STUDY OF HOT TEARING MECHANISMS OF ALUMINUM-SILICON ALLOYS

Joseph Langlais

Department of Mining, Metals and Materials Engineering

McGill University, Montreal

November, 2006

A thesis submitted to McGill University in partial fulfillment of the requirements of the degree of Doctor of Philosophy

Your file Votre référence
ISBN: 978-0-494-32205-5
Our file Notre référence
ISBN: 978-0-494-32205-5

Sommaire

La déchirure à chaud est un défaut commun pendant la coulée DC de lingot de laminage de quelques alliages d'aluminium commerciaux et peut entraîner une perte de productivité considérable. Afin d'améliorer la compréhension sur la déchirure à chaud, une technique originale, le DCSS pour « Direct Chill Surface Simulator » ou le simulateur de surface de coulée DC, a été développée pour reproduire les conditions de refroidissement à l'interface du métal liquide et du moule et reproduire la surface unique ainsi que la microstructure de sous-surface du lingot DC. L'appareil a été aussi conçu pour appliquer et mesurer une force en tension et la déformation de la surface. Ces quantités mécaniques ont été alors utilisées pour dériver les courbes de contrainte et déformation qui représentent mieux le comportement du matériau pendant la solidification et sa capacité pour résister à la déchirure à chaud.

Le travail présent décrit l'approche a utilisé pour déterminer la résistance mécanique de trois alliages binaire d'aluminium et de silicium (Al-0.5wt%Si, Al-1.5wt%Si, et Al-2.5wt%Si). En plus, ce travail couvre le modélisation du transfert de chaleur à l'aide d'un logiciel commercial (ProCAST™) pour comprendre les champs de température durant la solidification et traquer l'évolution de la fraction solide. Des analyses de la microstructure ont été réalisées afin de déterminer la morphologie des grains et leur taille, les mesures physiques et l'investigation minutieuse des surfaces déchirées. L'information a été utilisée comme entre autres dans divers modèles développés et utilisés dans le présent travail.

Un modèle théorique a été amélioré en incorporant des quantités métallurgiques plus réalistes. Cette recherche a mené aussi au développement d'un modèle de probabilité (automate cellulaire) pour simuler la microstructure des alliages étudiés et déterminer un coefficient de propagation de la déchirure à chaud (CPC).

Les phénomènes complexes et couplés tels que le fluage et la microségrégation ne sont pas couverts dans de ce travail. Plutôt, des hypothèses sont proposées selon les observations expérimentales et leurs plus probables contributions.

Ces études ont avancé à un certain degré la compréhension scientifique de la déchirure à chaud et le comportement mécanique pendant la solidification. En plus, le DCSS a été utilisé avec succès pour l'ordonnancement des alliages commerciaux selon la susceptibilité à la déchirure à chaud.

Abstract

Hot tearing is a common defect during DC casting of some commercial aluminum alloys and can result in considerable productivity loss in the cast-house. In order to better understand the hot tearing, a novel technique, dubbed DCSS for Direct Chill Surface Simulator, has been developed to reproduce the cooling conditions at the mould/liquid metal interface and to generate the unique surface and sub-surface microstructure of the DC ingot. The apparatus has been designed also to apply and measure a tensile load and the surface strain. These mechanical quantities were then used to derive the stress-strain curves that best represent the material behaviour during solidification and its capacity to resist hot tearing.

The present work describes the approach used to determine the mechanical resistance of three different aluminum-silicon binary alloys (Al-0.5wt%Si, Al-1.5wt%Si, and Al-2.5wt%Si). In addition, the present work covers the modeling of the heat transfer encountered during the test using commercial software (ProCAST™) to better understand the temperature field upon solidification and tracking the solid fraction. Microstructure analyses were made to obtain various metallurgical quantities (e.g., grain morphology, size), physical measurements and thorough investigation of the torn surfaces. Information was used as inputs to the various models developed and used in the present work.

A theoretical model was updated from previous work using more realistic metallurgical quantities. This research led also to the development of a probalistic model (cellular automata) to simulate the microstructure of the cast sample. The model has been used to determine a crack propagation coefficient (CPC) that was used in the theoretical model to better represent the hot tear propagation.

Work to include even more complex coupled phenomena such as creep phenomena and microsegregation are not covered in the present scope of this work. Hypotheses are raised according to experimental work and observations made that suggest their most probable contributions. These studies have advanced to a certain degree the scientific understanding of hot tearing such as the inherent mechanical behaviour during solidification. In addition, the DCSS was used successfully to rank DC cast commercial wrought alloys in terms of hot tearing susceptibility.

Preface

This thesis is a description of work that I performed for the Department of Mining, Metals and Materials Engineering at McGill University. The work described on the method to quantify the hot tearing propensity is original to that of others as it involved the development of a novel apparatus to reproduce more realistically the conditions encountered during DC-casting of ingot. No part of this work has been or is being submitted for any other qualification at this or other academic institution. The work described is original except where due reference is given to that of others.

Related Publications

Some parts of the work have already been published as author or co-author. The first publication [102,103] described the original approach (DCSS) to characterize the mechanical behaviour of Al-Si alloys during solidification. The hot tearing propensity was presented as the inverse of the maximum tensile force. This work allowed ranking different commercial alloys in terms of tendency to hot tear during casting. One publication [104] described the impact of the chill plate surface roughness on the microstructure development at the interface mould/metal. The last paper on the DCSS has been co-authored and presents a constitutive model for the tensile deformation of a binary aluminum alloy at high fractions of solid [114].

Contribution to Research

This work has advanced the scientific understanding of hot tearing mechanisms using a unique method to apply a displacement and measure a tensile load during solidification. In addition, a theoretical model has been adapted which allows understanding the impact of tensile loading, loading rate and metallurgical values on the overall material response. In so doing, the degree to which the behaviour of aluminum alloys can be explained has progressed. The DCSS technique has been used industrially to rank different alloys and to study the impact of alloying addition and grain refinement. This approach has contributed to improve the DC casting of specific alloys. The hot tearing study using the DCSS technique is part of the continuing research program at Laval University.

Acknowledgements

I am extremely grateful to my supervisor, Professor John Gruzleski from McGill University, and co-supervisor, Professor Daniel Larouche from Laval University, for their guidance and help throughout my Ph.D. works. I am not only grateful for the scientific guidance, but also to have given me the wisdom and displaying great patience. It is undeniable that both are responsible for creating an enjoyable, challenging and mostly stimulating work. I would like to express my sincere gratitude to Professor Mihriban Pekguleryuz (McGill University) who first convinced me to embark on this amazing journey. I would like to express my sincere thanks to Messrs. Ghyslain Dubé (Alcan-ARDC) and Jean-Pierre Martin (NRC-ATC) who immediately endorsed my goal. I am also grateful to Alcan to have provided me with financial support. I am indebted to many people, especially at the Arvida Research & Development Centre, who believed in me and supported me until the end, despite their already overloaded agendas. Special thanks go to the technical staff, Mr. Gilles Lemire of the Alcan Chaire at the Université du Québec à Chicoutimi (UQAC) and Mr. Luc Belley (STAS) who helped me on the experimental aspects. Special thanks also go to Mrs. Lise Castonguay who kindly supported me and found the good words to motivate me in completing the final stretch. I also wish to thank my colleagues who provided many useful ideas and fruitful discussions. Last but not least is an utmost thank you to my wife Johanne and my son Thomas who gave me their unconditional support and love to continue and reach the sometimes unattainable goal.

...all those memories will be lost in time as a tear in rain

Table of Contents

Nomenclature

A list of symbols is given with a brief description and units used.

Symbol Definition and Units

a	side dimension of the hexagon in the idealized microstructure (m)
a_c	new side dimension of the hexagon in the idealized microstructure (m)
$C_{o\dagger}$	bulk solute content (wt.%; at.%)
$C_{E\dagger}$	eutectic concentration
C_L	$C_{S\dagger}$ interfacial solute content in liquid and solid (wt.%; at.%)
D_L	diffusivity of solute in the melt ($m^2\ s^{-1}$)
dt	time interval (s)
f_S	solid fraction
f_L	liquid fraction
g_S	solid volume fraction
g_L	solid volume fraction
G	temperature gradient ($K\ m^{-1}$)
h	heat-transfer coefficients ($W\ m^{-2}\ K^{-1}$)
h	liquid film thickness (special case in the idealized microstructure (m)
h_i	liquid film thickness in the inclined channel of the idealized microstructure (m)
h_h	liquid film thickness in the horizontal channel of the idealized microstructure (m)
k	solute partition coefficient (C_S / C_L)
L	length of a sample in reference to $\varepsilon=\alpha\Delta TL\ l^{-1}$ (m)
l	length of a hot spot in reference to $\varepsilon=\alpha\Delta TL\ l^{-1}$ (m)
l	CA model network step value representing a numerical cell size (m)
m_L	liquidus slope with respect to solute content ($K\ wt.\%^{-1}$; $K\ at.\%^{-1}$)
$\dot{n}$	nucleation rate with respect to temperature
n_o	initial nucleation site density (m^{-3})
n_{max}	maximum nucleation sites (m^{-3})
n	a special case representing a material constant (Equation 49)
p	distribution coefficient (Equation 55)
p	pressure distribution (idealized microstructure, Appendix I)
p_c	pressure distribution at corner (idealized microstructure, Appendix I)
P_{oh}	maximum tensile pressure in the horizontal channel (MPa)
P_{oi}	maximum tensile pressure in the inclined channel (MPa)
P_c	pressure distribution at corner (idealized microstructure, Appendix I)
Q_a	activation energy ($kJ\ mole^{-1}$)
r	radius of grain (m)
SΔTn	maximum rate for the surface nucleation law
SΔTS	standard deviation (solutal undercooling) for the surface nucleation law
BΔTn	maximum rate for the bulk nucleation law
BΔTS	standard deviation (solutal undercooling) for the bulk nucleation law
#	number of numerical cells between surface asperities
T	temperature (K)
T_L	liquidus temperature (K)
T_s	solidus temperature (K)
T_L	a special case (Equation 18) of temperature at the dendrite tips (K)

T_s a special case (Equation 18) of temperature at the root of the dendrites (K)
T_L a special case (Equation 18) of temperature at the tip of the dendrites (K)
T_m a special case (Equation 35) of temperature of fusion of the alloy (K)
T a special case (Equation 35) of temperature given by T_m-ΔT (K)
ΔT a special case (Equation 35) of temperature gradient (K)
$\dot{T}$ cooling rate (K s−1)
t time (s)
V velocity (m s^{-1})
v velocity (m s^{-1})
v velocity (m s^{-1})
w_a average velocity of the flow in the channel of the idealized microstructure (m s^{-1})
ΔT total undercooling (Tliq -T) (K)
ΔT_L temperature difference between liquidus and solidus (K)
ΔT_{max} maximum undercooling experienced during recalescence (K)
ΔT_n constitutional undercooling available for nucleation events (K)
ΔT_σ solutal undercooling termed standard deviation in the CA (K)
α thermal diffusivity (m^2 s^{-1})
α a special case representing the material thermal expansion (m K^{-1})
α†† a special case representing a material constant (Equation 49)
β solidification contraction
β†† a special case representing a material constant (Equation 49)
ε deformation or strain
$\dot{\varepsilon}$ deformation or strain rate (s^{-1})
ε_f strain to fracture
ε_b strain in material related to $\varepsilon_b = \alpha\Delta T L\phi/l^2$
ϕ microstructure grain size related to $\varepsilon_b = \alpha\Delta T L\phi/l^2$ (m)
γ_{GS} interfacial energy between gas and solid (J m^{-2})
γ_{SL} interfacial energy between solid and liquid (J m^{-2})
γ_{LG} interfacial energy between liquid and gas (J m^{-2})
k thermal conductivity (W m^{-1} K^{-1})
λ_1 primary dendrite arm spacing (m)
λ_2 secondary dendrite arm spacing (m)
Λ the Greek letter describing the Lambda-curve (hot tearing sensitivity)
μ coefficient of viscosity (Pa s)
Ω dimensionless supersaturation parameter
τ shear stress
θ wetting angle (a special case of the *contact* or *dihedral* angle)
σ_f stress to fracture (MPa)
σ_{max} maximum tensile stress (MPa)
σ_{avg} average tensile stress (MPa)

† Solute contents are generally designated by either *x* or *C* depending on whether they are quantified by fractions or percentages respectively.

†† This is used in the power law proposed by Sellars and Tegart [95]

Constant

Symbol Name Value

R perfect gas constant 8.314 J K^{-1} $mole^{-1}$

Abbreviations

CA Cellular-Automaton
CPC Crack Propagation Coefficient
DC Direct Chill
DCSS Direct Chill Surface Simulator
HTC Heat Transfer Coefficient
HTS Hot Tearing Sensitivity
SEM Scanning Electron Microscopy
2D two dimensions
3D three dimensions
DICTRA Diffusion Controlled Transformation
DGM DICTRA™ variable representing the diffusion driving force

List of Figures

List of Tables

List of Equations

Chapter 1: Introduction

Hot tearing is recognized as one of the most common and serious defects encountered during casting and ingot making and closely related defects occur during fusion welding, soldering and brazing. This phenomenon (hot tearing) is also referred to as solidification cracking, hot shortness, super-solidus cracking, and shrinkage brittleness and has been the subject of numerous studies [1-6].

Hot tearing is associated with both ferrous and non-ferrous systems. In general, the phenomenon of hot tearing is defined by the formation of a macroscopic fissure in a casting as a result of stresses (and the consequential strains) generated during cooling, at a temperature above the non-equilibrium solidus. The hot tear nucleates and grows interdendritically within the solidifying material.

During the liquid-to-solid transition most metals undergo a certain amount of volume contraction, β, which generates strain (usually $\beta \sim 5$ to 6 percent). The latter can be reinforced by thermal contractions in the solid. If this contraction is hindered or cannot be freely accommodated by mechanisms such as plastic deformation and movement of solid or liquid, then regions of the solidifying mass may be subjected to strains being imposed upon a material having very poor mechanical properties in the solidification interval.

1.1 The Direct Chill (DC) Casting Process

DC casting process is used for the production of aluminum sheet ingots and extrusion billets. A diagram of the DC casting process and the cooling zones is shown in Figure 1. The process [7] is essentially an open mould used to confine the molten metal and distribute the cooling water around its periphery via a water chamber. The mould opening is closed during the start-up with a bottom block mounted on a vertical lowering table. The molten metal is transferred (trough/tube arrangement) into the cavity on the bottom block (starting block) where solidification begins. The metal level in the mould is kept constant as the bottom block is lowered at a specific rate.

The liquid metal is subjected to primary cooling by conduction of heat through the water cooled mould wall. The secondary cooling is obtained through direct impingement of water onto the solidified shell exiting the mould cavity.

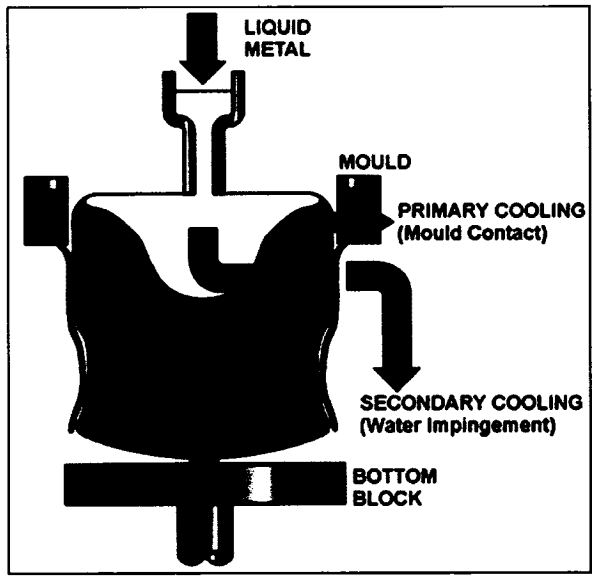

Figure 1: DC casting process

The secondary cooling achieved by the cooling water is approximately 95 to 98% while the primary cooling represents 2 to 5% of the total heat extraction. The DC casting process is divided into three distinct phases: the start-up phase, the transition phase, and the steady-state phase. During these phases, the ingot is subjected to many distortions [8,9] which are the result of coupled thermal and mechanical effects.

The most critical phases (start-up and transition phase) typically represent a small percent of the overall ingot casting length. The direct contact between melt and mould (primary cooling) results in a rapidly growing shell zone while the secondary heat extraction (cooling water) produces an advanced solidification front. Figure 2 shows a diagram of the typical heat extraction paths and solidification fronts observed during DC casting of a sheet ingot.

During solidification, the shell starts to shrink and pull away from the mould wall to form an air gap. The heat extraction is greatly reduced in the air gap causing reheating and sometimes local remelting. This results in a cyclical movement of the solidified shell.

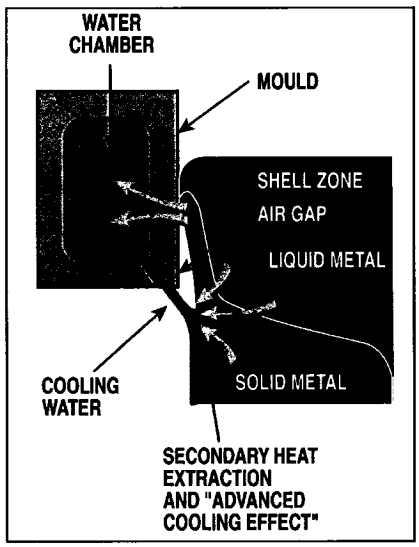

Figure 2: Diagram of the Solidification Fronts during DC Casting

The action of both primary and secondary cooling generates stresses in the thin solidified shell which could induce surface hot tearing. The presence of such a defect causes, in most cases, the rejection of the entire cast ingot. In fact, hot tears will propagate over the full ingot length if they reach the steady-state phase of the cast.

1.2 Hot Tearing of DC Cast Ingot

Hot tearing is a recurrent defect during DC casting of commercial aluminum alloys such as 3XXX and 6XXX series. The phenomenon occurs as a result of distortions due to differential contractions of the ingot during solidification and results in considerable defect levels and metal loss in the cast-house. Grain refining or trace elements that alter growth kinetics and prevent early grain coherency may be effective in reducing susceptibility to hot tearing.

Hot tearing that occurs during the DC casting of certain alloys has been the subject of studies for some years [10,18]. Information exists on the theories of hot tearing and on the importance of various process parameters related to it. Most of these studies have been conducted on hot-tearing problems that occur in the bulk of the cast. What needs more study is the hot tearing problem that occurs at the surface of a solidifying DC ingot, i.e. in the shell region. Figure 3 shows a hot tear generated at the surface (shell region) of a DC cast ingot. The morphology of the surface hot tear shows a typical interdendritic separation.

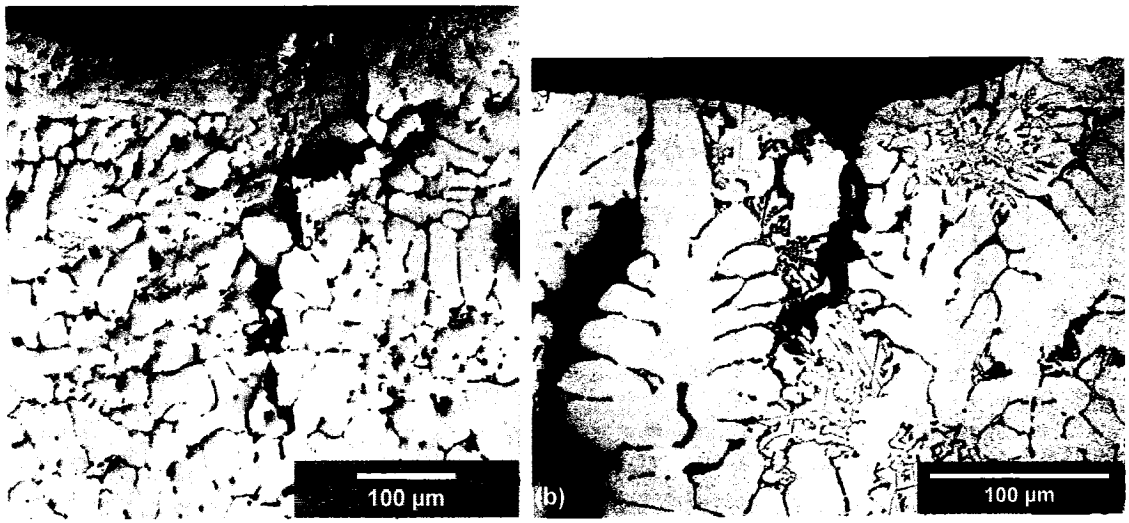

Figure 3: Surface Hot Tearing on DC Cast Ingot (a) and interdentritic details (b)

The hot tearing phenomenon in the shell region of a DC-cast ingot is a complex interaction (Figure 4) between, inverse segregation, properties of the interdendritic liquid, second phases and intermetallics that precipitate in the interdendritic liquid and surface strains and stresses.

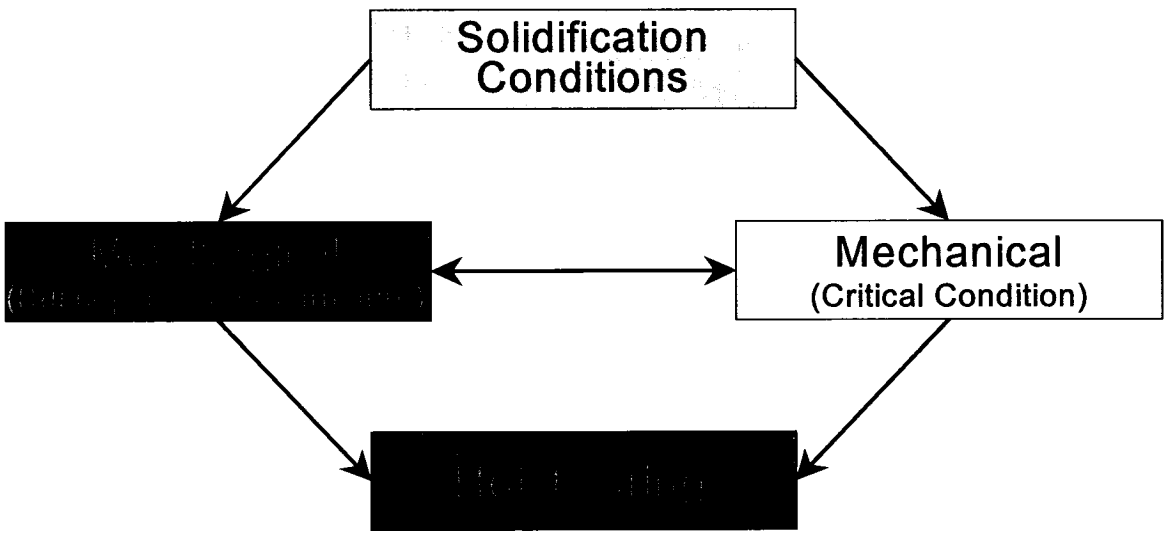

Figure 4: Diagram of the complex interactions related to the hot tearing phenomenon

Chapter 2: Hot Tearing Theory and Literature Review

2.1 Introduction

Hot tearing is recognized as one of the most common and serious defects encountered during casting and ingot making and closely related defects occur during fusion welding, soldering and brazing.

This phenomenon (hot tearing) is also variously referred to as solidification cracking, hot shortness, super-solidus cracking, and shrinkage brittleness and has been the subject of numerous studies [1-6]. This phenomenon is associated with both ferrous and non-ferrous systems.

In general, the phenomenon of hot tearing is essentially defined by the formation of a macroscopic fissure in a casting as a result of strains (and the consequential stresses) generated during cooling, at a temperature above the non-equilibrium solidus. The fissure nucleates and grows interdendritically within the solidifying material.

During the liquid-to-solid transition most metals undergo a certain amount of volume contraction,β which generates strain (usually $\beta \sim 5$ percent). The latter can be reinforced by thermal contractions in the solid. If this contraction is hindered or cannot be freely accommodated by mechanisms such as plastic deformation and movement of solid or liquid, then regions of the solidifying mass may be subjected to strains being imposed upon a material having very poor mechanical properties in the solidification interval.

It should be noted that most of the figures presented in this chapter were adapted from the original for better clarity.

2.2 Basic Theories of Hot Tearing Mechanisms

Based upon experimental investigations, many theories have been proposed to explain the occurrence of hot tears in casting. However, it is unanimously agreed that the mechanisms involved in the intercrystalline separation of the material are a combination

of metallurgical and mechanical effects. In fact, hot tearing requires both a sufficient amount of mechanical restraint (strain) and a susceptible microstructure [48].

2.2.1 Shrinkage-brittleness theory

The shrinkage-brittleness theory [1,7-9,14] results from numerous studies of hot tearing susceptibility of aluminum alloys. A theory accounting for the hot tearing observed in specific aluminum alloy systems (i.e., Al-Si) was first advanced by Verö [7]. During the liquid-solid stage, the primary crystals growing at the expense of the decreasing volume of liquid come into contact (coherency temperature) and form a coherent network. The theory postulated was that tearing was caused by the contraction strains of the primary dendrites during subsequent cooling between the liquidus and solidus. It also mentioned that in the presence of more than a certain critical proportion of liquid any incipient fissures between the primaries were healed by liquid feeding as they were formed. Figure 5 summarizes Vero's results according to the Al-Si phase diagram.

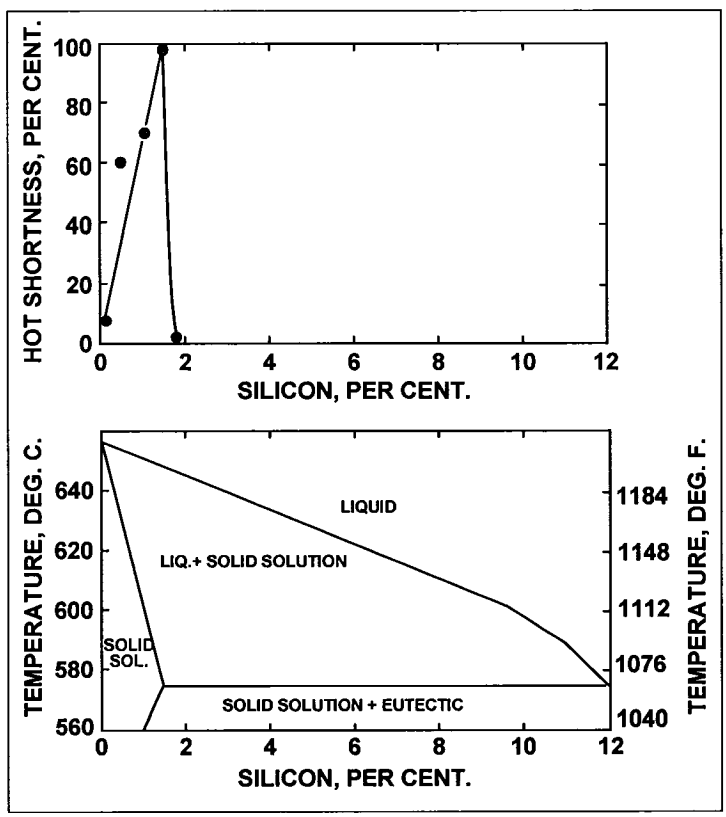

Figure 5: Relationship between hot tearing and alloy constitution for the Al-Si binary system [7]

However, Verö [7] stipulated that the healing process was prevented by the narrowness of the interdendritic channels when the remaining liquid was less than the critical proportion. In addition, he assumed that the formation of a fissure could occur only during contraction of the dendrites and that no tearing was possible when the amount of liquid freezing at constant temperature (eutectic temperature) was greater than the critical value.

The experimental results indicated that in aluminum-silicon alloys, the hot tearing increased from zero at low silicon content to a maximum at approximately 1.6 percent silicon and then decreased abruptly to zero at 1.88 percent silicon. Alloys with higher silicon content were not prone to hot tearing. The critical amount of liquid (necessary to heal cracks) was calculated to be between 12 and 13 percent for the Al-Si binary system using the effective solid solubility at the eutectic temperature of approximately 0.4 percent.

However, it was indicated [1,14] that the sudden decrease in hot tearing cannot be explained by Verö's theory as it stands. In fact, based on a simple binary system, the modified theory, which included, in a modified form, the concept of freezing range [8] and the volume proportion of eutectic (eutectic index [9]), specified that the severity of tearing will depend on the amount of contraction while the hottest zone of the casting passes through the critical hot tearing range. It appeared that tearing was possible even though the residual liquid solidifies at constant temperature. Consequently, the hot tearing of castings was accounted for theoretically by a single factor, the extent of the hot tearing temperature range. The tears are unlikely to be formed when the alloy has passed below the solidus. Hot tearing is only likely to occur in the "brittle range" or the so-called effective interval of solidification which is the range of temperature between the coherency temperature and the solidus (Figure 6).

Hot tearing is prevented during the "brittle range" by "accommodation [31]". The latter designates the degree to which an alloy is able to withstand shrinkage strains by movement of the grains within the semi-solid mass. It has been mentioned [31] also that the hot tearing tendency is proportional to the extent of the "brittle range". Other factors affecting the incidence of hot tearing were given by Lees [9,13]. These factors included the effect of mould variables (i.e., moulding materials, cores in hindering contraction),

constitution of the alloy (especially the proportion of eutectic), grain size, and gas content.

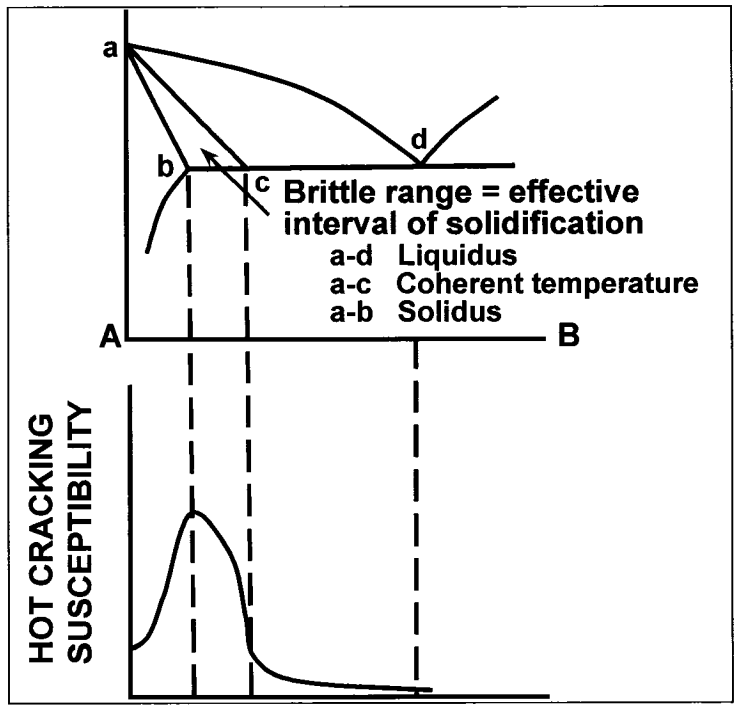

Figure 6: Hot Tearing Susceptibility of Eutectiferous Alloy (Shrinkage-Brittleness Theory) [7]

The basic relationship between these factors is related to the extent of mechanical restraint, the promotion of grain boundary film, coherent temperature modification, and their impact on the mobility of the grains and the liquid feeding behaviour.

2.2.2 Strain theory

The first new theory to explain the mechanisms of hot tearing is undoubtedly that attributed to Pellini [2] and his co-workers [3]. They published a new idea about the strain theory based on the film stage concept. This theory suggests that hot tearing is caused by the localized strains, generated by thermal gradients that tend to pull apart solid masses of material separated by essentially continuous films of liquid. This liquid film results from the segregated residual melt. Because of its fundamental nature, the strength and ductility of a mass of solid grains separated by liquid films is of an extremely low order. The strain theory provides a generalized explanation of the mechanism of hot

tearing in terms of the strain rate imposed on the liquid film regions. Figure 7 illustrates the theory schematically.

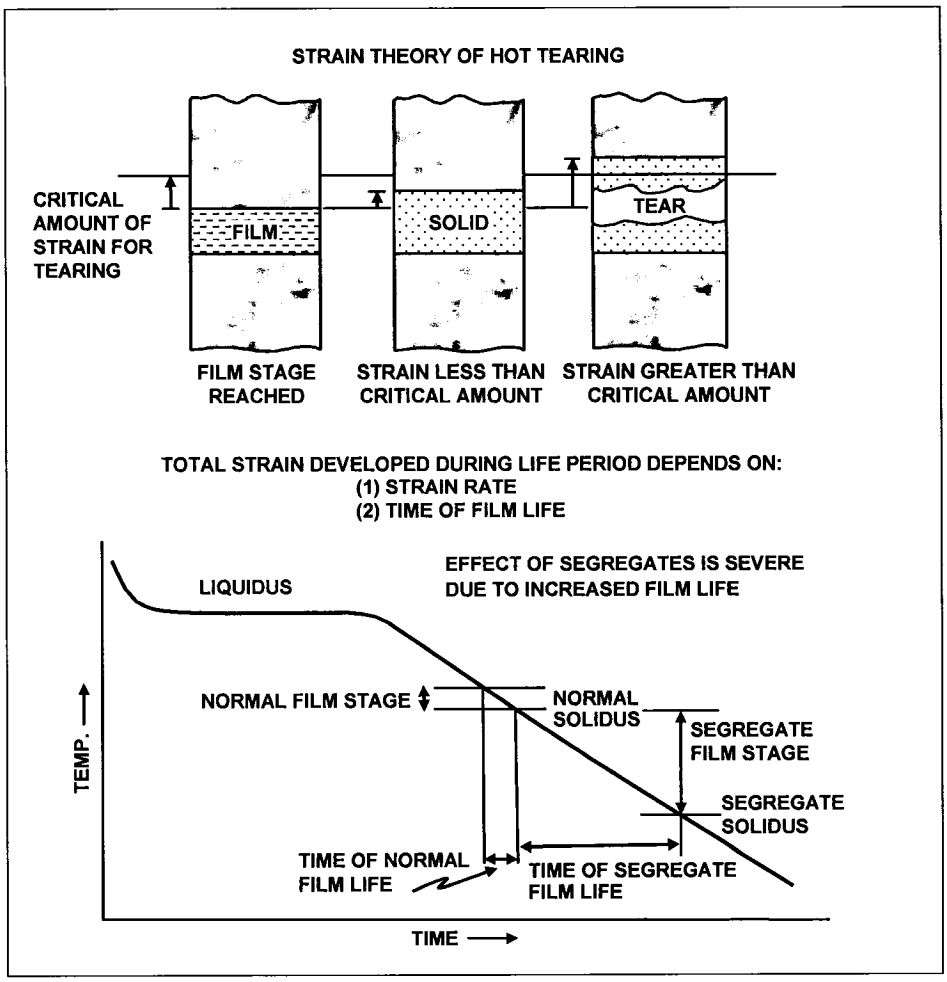

Figure 7: Diagram illustrating basic concepts of the theory [2]

The strain rate of the film regions may vary widely due to various factors that contribute to the development of hot tearing. These factors include; a) large regions undergoing contraction, b) fast cooling of regions undergoing contraction, and c) small regions undergoing extension.

In slight contrast to the previous theory (Shrinkage-Brittleness), it has been suggested that hot tearing cannot take place during the mushy-stage of solidification since the shrinkage strains are uniformly distributed. In fact, the interdendritic liquid zones are relatively large and general feeding of the mushy mass could result. Hot tearing occurs only when the film stage is reached and the strain within the hot spot is concentrated into narrow liquid films of low strength. Low melting point segregates which exist, in the

molten state, below the equilibrium solidus of the material are the most detrimental in this respect.

Figure 8 shows schematically the strain distributions within a hot spot (extension and contraction) during various stages of solidification.

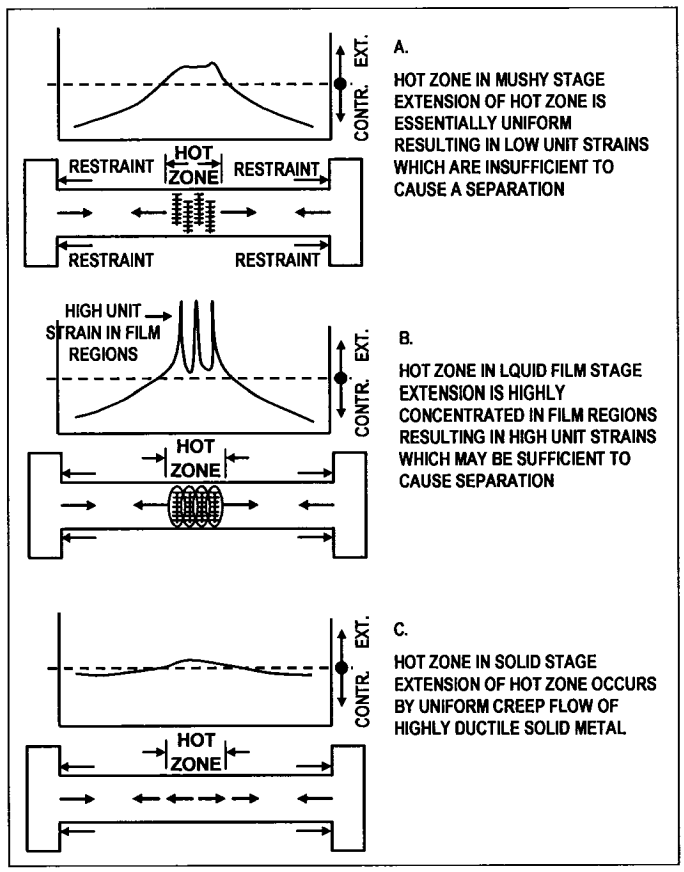

Figure 8: Diagram showing the strain distribution within a hot spot [2]

The length of the hot spot must be considered as an important factor determining the occurrence of hot tears. A small hot spot that contains few liquid films must accommodate a great amount of strain on each film. Conversely, a longer hot spot will contain many liquid films and the strain per film will be less important.

If separation (fissure) does not occur during the film stage of solidification, then, hot tearing is no longer possible below the true solidus temperature. Actually, the strains in the hot spot are distributed relatively uniformly across the coherent and ductile solid metal. Further cooling of the casting will cause the stresses to continue to build-up. Creep flow will occur after the low yield point of the hot metal is exceeded.

The dependence of the hot tearing mechanism on the microstructure was mentioned by Dodd [13]. The latter considered that during the solidification of solid solution alloys, deep channels of liquid metal are formed between the growing dendrites. These deep channels could act as "stress-raisers" in the final stage of solidification if they are isolated from the liquid feeding metal. However, this approach implies that tearing occurs through solid metal which is a fundamentally different assumption from that of Pellini [2]. Apblett and Pellini [10] showed clearly (Figure 9) the relationship between the force absorption capacity and the elongation-to-fracture during the various stages of the solidification.

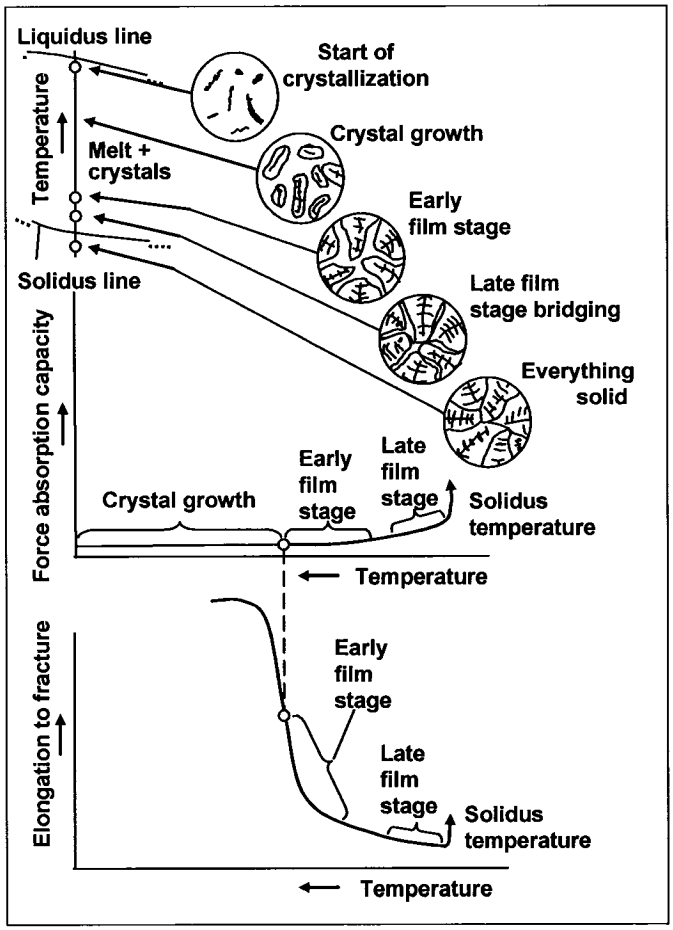

Figure 9: Diagram showing the tensile strength and elongation versus the microstructure [10]

Figure 9 shows the decrease in the elongation during the transition from the early liquid film stage to the late film stage. It has been shown schematically that the development of the microstructure decreases the overall mobility of the grains. It has been mentioned [11,12] that during the solidification interval of almost every casting material, the tensile strength and elongation-to-fracture were very low compared with the values in the solid

state. The eventual occurrence of hot tearing during the critical temperature range depends mainly on the strain rate, the increase of the liquid film stage as a function of time and the amount of segregated material, and grain size.

2.2.3 Generalized Theory

Various attempts to explain hot tearing formation lead to various theories that are supported by experimental evidence. Among them is the generalized theory by Borland [5,16,17] (supported by others [9,14,26]). It is intended to explain the mechanisms of hot tearing as a combination of the *"Shrinkage-Brittleness Theory"* (brittle temperature range), and the *"Strain Theory"* (liquid film stage). The main objective was to modify and extend both theories and explain how the liquid quantity and distribution during solidification affects the hot tearing tendency.

The theory on the liquid film stage is limited to the temperature range around the solidus. On the other hand, the shrinkage-brittleness theory commences at the so-called coherency temperature. The coherency temperature is defined [18,19,20] as the temperature at which the fraction of solid (f_s) at which the growing equiaxed dendrites begin to interact mechanically and grow to form a coherent network. Figure 10 also shows the subdivision of the solidification process into four different stages and the associated risk for hot tearing.

The generalized theory suggested, in particular, that the distribution of liquid is largely influenced by the ratio of the interphase (solid-liquid) and intercrystalline boundary energies. The development of a liquid film covering the entire surface of a grain (faces and edges) is associated with a low ratio while a high ratio will restrict the remaining liquid to edges and corners. The latter arrangement appears to be beneficial because a relatively larger area of the grain can interconnect and create a more coherent network to accommodate the thermal stresses created during cooling. In general, fissures are less likely to be formed with this liquid film distribution.

The hot tearing tendency will be affected by various considerations during the cooling between the liquidus and solidus. These include; a) the effect of solidification mode, b) effect of interphase and grain boundary energies (dihedral angle), and c) effect of solute elements.

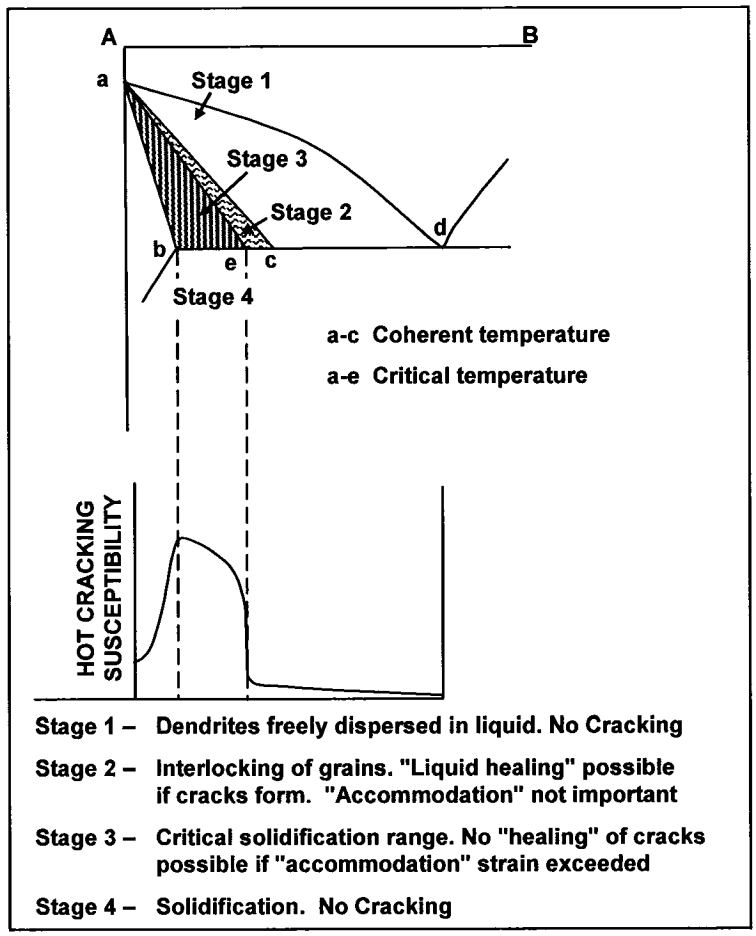

Figure 10: Effect of constitutional features on tearing susceptibility in binary systems [16]

2.2.3.1 Effect of the Solidification Process

The solidification process may be described in four stages [16].

Stage 1: (Primary dendrite formation) - The solid phase is dispersed while the liquid is continuous; both liquid and solid phases are capable of relative movement.

Stage 2: (Dendrite interlocking) - Both liquid and solid phases are continuous, but only the liquid is capable of relative movement and is able to circulate freely between the interlocking dendrites.

Stage 3: (Grain boundary development) - The solid crystals are in an advanced stage of development and the semi-continuous network restricts the free passage of liquid. Relative movement of the two phases is impossible.

Stage 4: (Solidification) - The remaining liquid has solidified

It has been postulated that materials are susceptible to hot tearing once the coherency temperature is reached; this is Stage 2 in the solidification process. During this stage the healing process by liquid feeding of tears is possible whereas further development of the microstructure prevents the free movement of liquid. The accommodation of strains by movement of the grains within the mushy mass becomes important in Stage 3 where tears that have been initiated cannot be healed by the remaining liquid.

Stage 3 is termed [16] the "Critical Solidification Range" (CSR) and the temperature at the beginning of this stage is the critical temperature (T_c). However, the liquid melt does not solidify according to equilibrium conditions and, consequently it is possible that the liquidus and solidus are depressed by undercooling. In addition, the solidus may be further depressed by the lack of diffusion and will increase the CSR (hot tearing).

2.2.3.2 Effect of Interphase and Grain Boundary Energies (Dihedral Angle)

The occurrence of hot tearing is not related only to the condition where a large freezing range exists. The condition requires that the liquid should also be present over a relatively wide temperature interval (liquid film life [2,27]) in a form that will permit high stresses to build up between grains. High stresses will be developed, during solidification, on the narrow bridges joining adjacent grains in the case where the liquid is covering almost all of the grain face. On the other hand, even higher stresses will be required to cause hot tearing when the liquid is restricted to the grain edges and corners.

The distribution of liquid during the solidification process is related to the liquid/solid interfacial energies. However, it has been mentioned [16] that the process of adjustment to equilibrium conditions is not instantaneous and depends strongly on the cooling rate.

The shape of the liquid phase at the grain boundaries is determined to a large extent by the ratio between the solid/liquid interfacial energies (γ_{LS}) and grain boundary energies

(γ_{SS}). The distribution and quantity of liquid is influenced by the grain size and shape, and the effect of temperature (and cooling rate) on the slope of liquidus and solidus lines. The slopes determine the composition of the liquid (largely determines the value of the ratio γ_{SL}/γ_{SS}) in contact with the growing crystals. Smith [21] was the first to establish the concept of the wettability of grain boundaries by the presence of a liquid phase. He determined the ratio γ_{SL}/γ_{SS} (the relative interface energy) in terms of the dihedral angle (θ) of the solid/liquid interface as given by Equation 1,

$$\frac{\gamma_{SL}}{\gamma_{SS}} = \frac{1}{2 \cdot cos(\theta)} \qquad \textbf{Equation 1}$$

where: γ_{SL}: solid/liquid interfacial energy,

γ_{SS}: grain boundary energy,

θ: dihedral angle.

The dihedral angle can be determined by quantitative measurements of the shapes of the liquid films from metallographic sections [5,16,22,43]. Rogerson and Borland [5] determined the dihedral angles of the solid/liquid interfaces of some binary systems. They concluded that the shape (type and distribution) of intergranular liquid regions is one of the metallurgical factors determining the tendency to hot tearing during solidification. In fact, liquid in the form of globules should be less harmful than liquid having continuous films because of the possibility of having more intergranular cohesion. Figure 11 shows the effect of dihedral angle on shapes of liquid regions [5].

The most suitable shape of the interdendritic regions in the solidifying metal may be obtained by compositional changes in the liquid phases in order to reduce the hot tearing propensity.

The ratio γ_{SL}/γ_{SS} is designated τ for convenience and the dihedral angle is zero for τ = 0.5. Figure 12 shows the effect of the ratio between the solid/liquid interfacial energies (τ) as a function of the dihedral angle for $\tau \geq 0.5$. It has been suggested [21] that almost complete wetting of the grain faces and edges will take place when the liquid and the previously solidified material is of similar chemical composition. The value for τ must be slightly greater than 0.5 to have this nearly complete wetting state. Hot tearing could develop under adverse strain conditions if this situation exists over a relatively wide

temperature interval during solidification because high stresses build up on adjacent grains joined by only small regions.

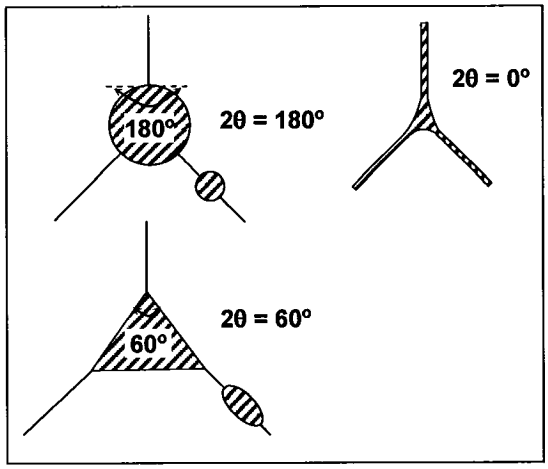

Figure 11: Effect of dihedral angles on shapes of liquid regions [5]

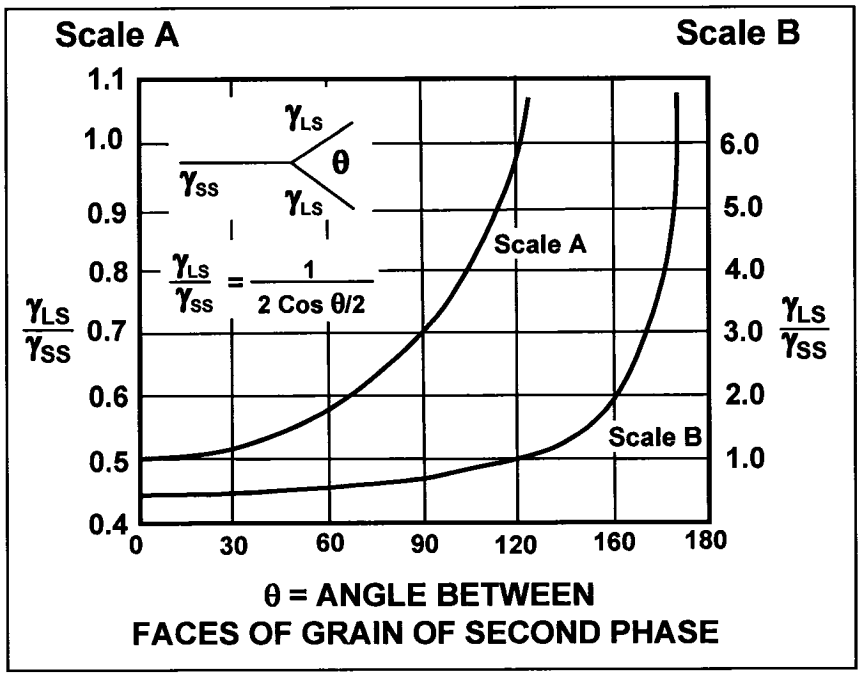

Figure 12: Ratio of the solid/liquid interfacial energies as a function of dihedral angle [5]

On the other hand, the hot tearing susceptibility will be lower in systems where the liquid is mainly restricted to grain edges and corners since higher stresses are required to separate the large interconnected areas of the grains. Figure 13 shows a diagram of the effect of dihedral angle on distribution of liquid phase (on grain corners, edges, and faces).

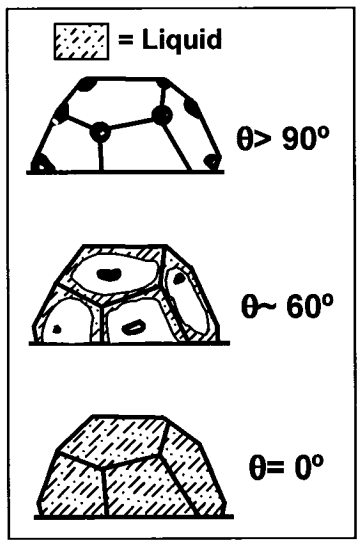

Figure 13: Diagram of the effect of dihedral angle on distribution of liquid phase [21]

The relationship between the area of the boundary which is occupied by the liquid, the dihedral angle, and the volume fraction of liquid involves complicated geometrical calculations which were addressed by subsequent researches [23,24,25].

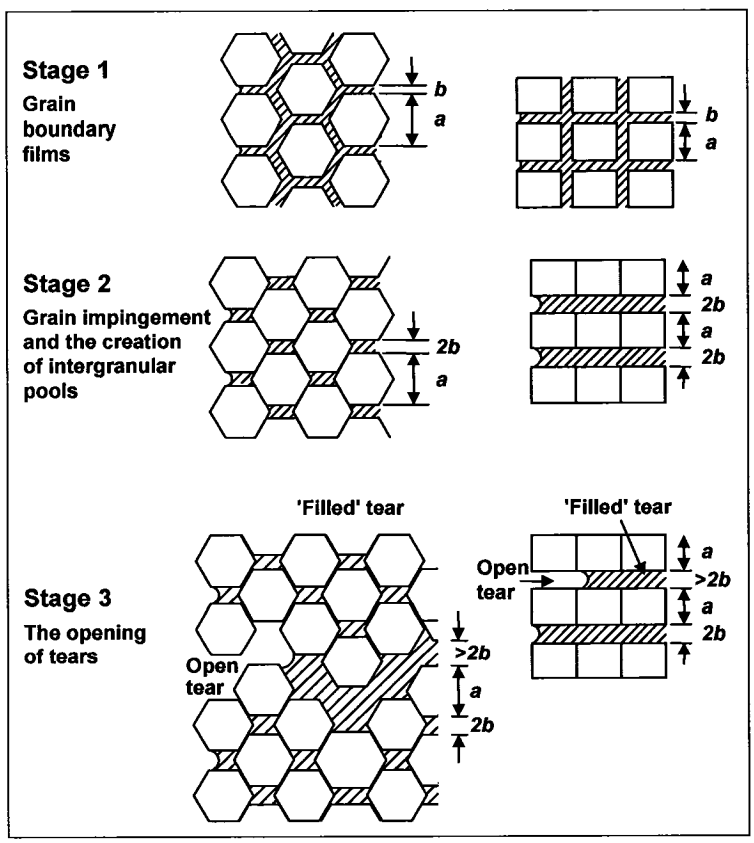

Figure 14: Models [15] showing the mechanisms of pre-tear extension

Figure 14 shows [15] hexagonal and square models of grains, size "a", surrounded by a liquid film having a thickness "b" to illustrate the mechanisms of pre-tear extension.

The geometrical models show that the pre-tear extension (ε), for a grain size of average diameter "a", and a liquid film thickness "b", is approximately equal to b/a. The relationship is given by $b/a = f_L/3$ and $b/a = f_L/2$ (f_L is the volume fraction of liquid) for a three and a two-dimensional model, respectively.

The model shows that the pre-tear extension is proportional to the amount of liquid present and the extension is inversely proportional to the grain size. Consequently, more strain can be accommodated without hot tearing by easy slipping along the lubricated boundaries in the case of more residual liquid and finer grain size. It has been mentioned also by other researchers [15] that even the smallest strain values (typically less than 1 to 2 percent strain) in the brittleness temperature interval are of significance in the reduction of stresses to avoid material separation (pre-tear extension).

Therefore the grain size, shape and distribution as well as the wettability of the residual liquid are important parameters for the reduction of stresses during the solidification of material.

Figure 15 shows [30] three possible strain curves as a function of the temperature. The curves are the difference between good wetting of the grain structure by residual liquid brittleness at the grain boundaries (1), good wetting without brittleness (2), and poor wetting (3), respectively.

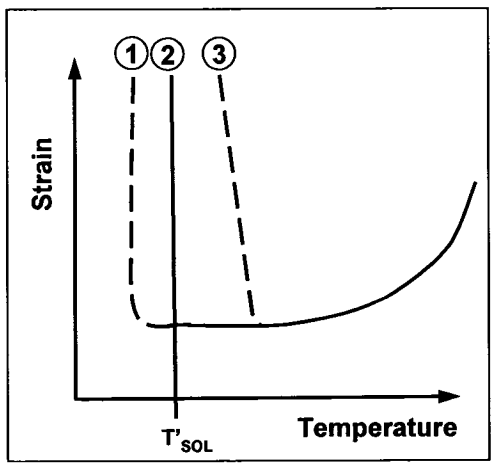

Figure 15: Elongation properties as a function of temperature [30]

Typical behaviour for industrial alloys is characterized by a drop in elongation with decreasing temperature followed by a steep increase immediately after the solidus temperature T_{sol} (Figure 15, curve 2). The film stage is generally present until the end of solidification due to the good wettability.

It has been mentioned [12,27] that only the interdendritic liquid films which are perpendicular to the stress axis will be decisive for the tensile strength. Figure 16 shows hot tearing mechanisms based on this assumption.

This theory could be used for both columnar and equiaxed grain structures. The measured elongations are attributed to the plastic deformation of the solid matrix.

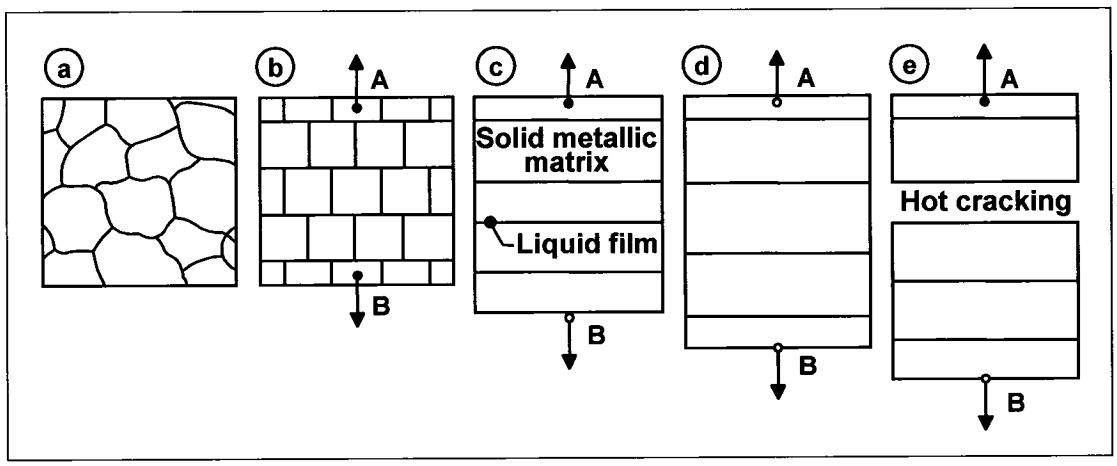

Figure 16: Hot tearing mechanisms based on liquid film perpendicular to the stress axis [30]

The tensile strength corresponds only to the stress required to separate two grains (assuming plane surfaces) between which exist a liquid film of thickness "b" with a known surface tension γ_{LG}. The required tensile stress "σ" can be determined by Equation 2.

$$\sigma = \frac{2 \cdot \gamma_{LG}}{b} \qquad \textbf{Equation 2}$$

A similar description was given by Pellini [2] but without mention of a specific orientation of the stress axis in relation to the liquid films. It should be noted here that the present approach will be used in the theoretical model to determine the Al-Si binary alloy fracture stress.

2.2.4 Effect of Solute Additions

The shape of the equilibrium diagram (Figure 10) showing the hot tearing propensity in a binary system [16] is accounted for by the increasing amounts of solute. The critical temperature (T_c) will be depressed because of the greater amount of liquid persisting to lower temperatures. Simultaneously, the solidus is lowered because of changes in solid solubility. Consequently, the critical solidification range (CSR) increases concurrently. Similarly the hot tearing tendency increases due to the greater amount of non-equilibrium solidification.

It has been mentioned [16] that one fundamental reason for hot tearing formation during the early stage of solidification can be the nearly similar chemical composition of the liquid (at the grain faces and edges) and the solid being frozen. Based on the latter statement, it has been stipulated [16,28,29] that hot tearing may be prevented by modifying the liquid phase composition in order to that this composition is very different from that of the solid.

2.3 Methods of Assessing Susceptibility to Hot Tearing

Various methods have been used to assess the relative susceptibility of different alloys to hot tearing. The important reasons for determining the alloy susceptibility to hot tearing are to allow theories to be assessed, and then to enable predictions to be made about the alloy behaviour in industrial casting and welding situations. Basically, the simplest methods were designed to mechanically restrain the casting or welding during freezing in order to produce contraction conditions varying from mild to severe.

The Al-Si and Al-Cu binary alloys are among the few which have been selected in order to study the mechanisms of hot tearing and its dependence on various parameters such as the alloy, trace elements, grain size, melt superheat, and gas content. These particular binary alloys were selected due to their relative simplicity but also because some experiments have already been carried out by other investigators.

Different hot tearing tendencies result from variations in mechanical factors (stress, strain). In general, the test methods are designed to induce stresses by external factors [35]. The factors which produce hot tearing are; a) restraint of metal contraction caused

by mould or cores, b) restraint of contraction caused by the casting itself or the gating system, c) temperature gradients or "hot spots" operating in conjunction with restraint of contraction.

2.3.1 Methods of Testing and Quantification of Hot Tearing Susceptibility

In order to produce stress conditions in a solidifying material, a sufficient level of mechanical constraints is required to prevent the shrinkage of the test piece in order to induce material separation eventually. An early attempt [34] to evaluate hot tear susceptibility was in conformity with the belief that low mechanical properties at elevated temperatures were conducive to hot tearing. The test involved a solidifying casting which raised a weight which was being increased gradually until a fracture occurred. However, one of the earliest investigations of hot tearing in aluminum alloys was by Archbutt [33] who prepared die castings in several alloys in common use. Two types of casting were used, a complicated branched tubular casting and a shouldered tensile test piece. The alloys were classified in terms of mechanical properties and their tendency to fissure. However, the choice of alloys was such as to be of little value in forming a theory of hot tearing.

Verö [7] made a more valuable contribution by casting U-shaped test pieces consisting of one horizontal and two vertical bars each 10 mm in diameter. Both vertical parts formed by the pouring and the rising gate resist the contraction of the horizontal bar in which a tear would arise in castings of alloys prone to hot tearing. The mould was made of mild steel and used without coatings. The degree of hot tearing was determined by the relative quantity of cracked castings (expressed as a percentage of all castings) in the horizontal section caused by the mechanical restraint imposed by the vertical arms. The evaluation of different alloys was made with 12 to 14 castings. Castings without tears were valued as 0, castings with a flaw as 0.5 and those showing deep tears as 1.

In addition, Verö [7] determined the strength of a number of aluminum alloys, including aluminum-silicon series, at temperatures both below and above the solidus. The castings from his U-shaped mould gave suitable test pieces for the later strength tests (bending and tensile tests). Figure 17 shows both pieces of apparatus [7] used to evaluate the mechanical properties of the castings. The results (Figure 18) show essentially that the bending strength of all alloys decreased (more or less) rapidly with increasing

temperature. However, the attempt to correlate mechanical properties with hot tearing was abandoned because of contradiction between the strength measurements and the casting experiments.

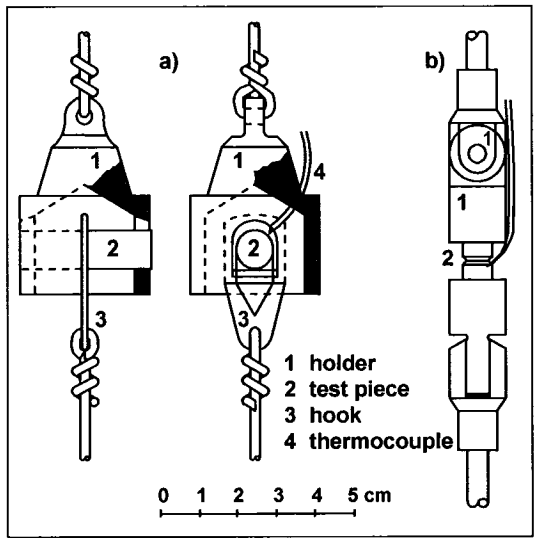

Figure 17: Holders used in bending and tensile tests [7]

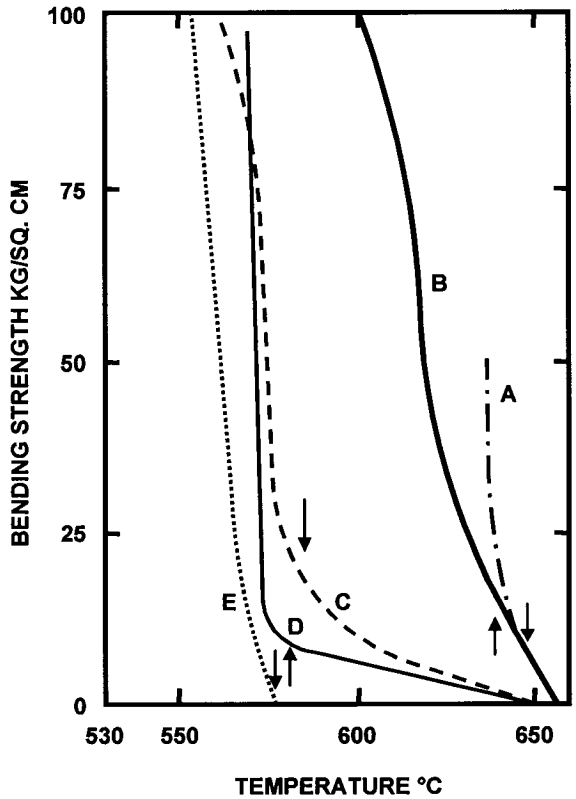

Figure 18: Bending strength of aluminium alloys in the melting range [7]

An investigation was carried out by Lees [9] to determine the hot tearing tendencies of aluminum alloys. Two tests were developed, one in sand moulds and the other in copper dies. Tests were made to determine the stage in freezing at which the alloys show substantial strength and to relate the results to hot tearing behaviour. The test casting in sand moulds (Figure 19) requires chill inserts connected to the steel moulding boxes to restrain contraction externally rather than by means of the sand (strength properties of sands and cores are difficult to standardize). The results of the hot tearing tests were expressed by a letter ranging from A to C for the sand moulds and from A' to E' for the copper dies. The "A" rating indicates a superior resistance to hot tear. Various modifications were made to improve this approach. However, experiments failed to produce a more discriminating test and subsequent work was oriented to tests in metal moulds. Tatur's [37] modifications of Lees' original tests in copper dies (Figure 20) is an attractive method and appears to work well but apparently it suffers from the disadvantage that it does not include a hot spot.

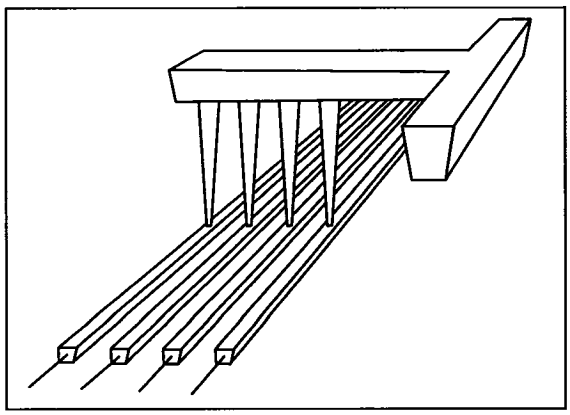

Figure 19: Test casting in sand moulds [9]

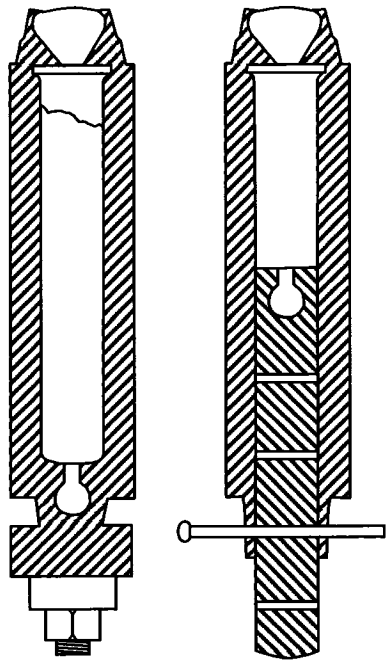

Figure 20: Test casting in copper dies [37]

Singer and Cottrell [14] carried a stage further the work done by Verö [7] on the hot tearing of aluminum-silicon alloys. The tensile properties were determined at temperatures in the region of the solidus to explain the mechanisms of hot tearing. Some

experiments on cast steel bars were carried out by Hall [36] where the tensile strengths and elongation were determined during and shortly after solidification. The results, however, were made difficult to interpret by the steep thermal gradient present in the castings at the time of testing. Hall concluded that it was necessary to go some distance below the solidus before a significant elongation was observed and hot tearing was no longer possible.

Singer and Cottrell [14] used a Hounsfield tensometer in combination with a tube furnace (Figure 21) for testing materials both below and above the solidus.

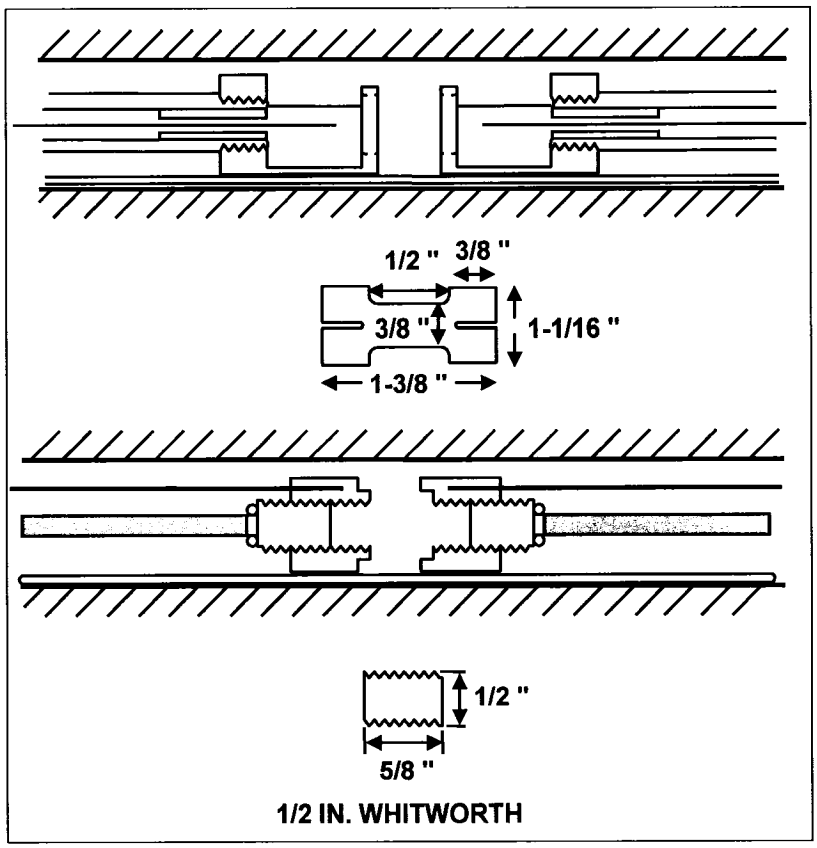

Figure 21: Apparatus used for testing the tensile properties in the region of the solidus [14]

Figure 22 and Figure 23 show the tensile strength of the alloys at temperatures in the region of and above the solidus, respectively. The main conclusion was that there exists a range of temperature above the solidus over which some alloys have a finite strength and coherence, and at the same time a negligible ductility. It was suggested from this work that the extent of the hot tearing temperature range is one of the most important factors in determining the hot tearing properties of the alloys.

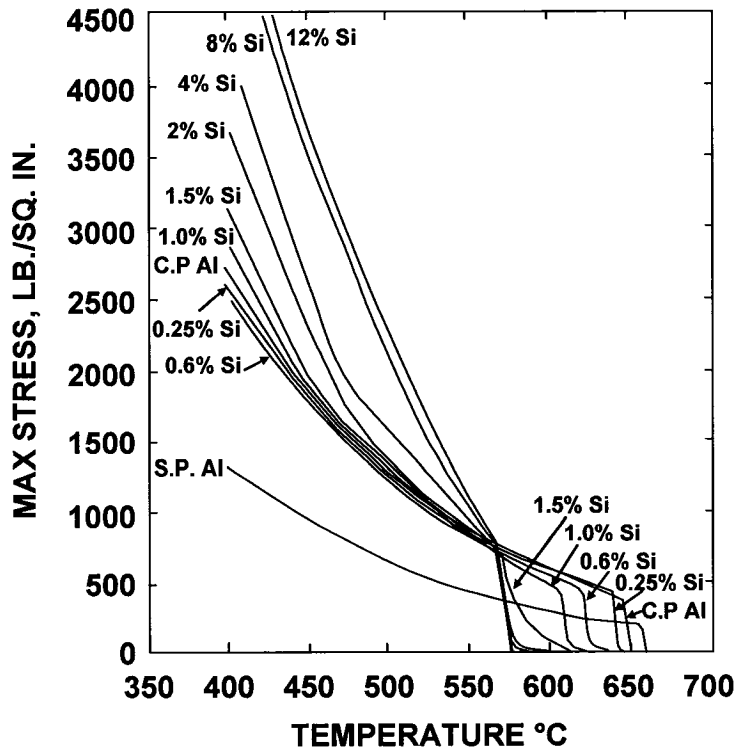

Figure 22: Tensile strength properties of Al-Si alloys at temperatures near the solidus [14]

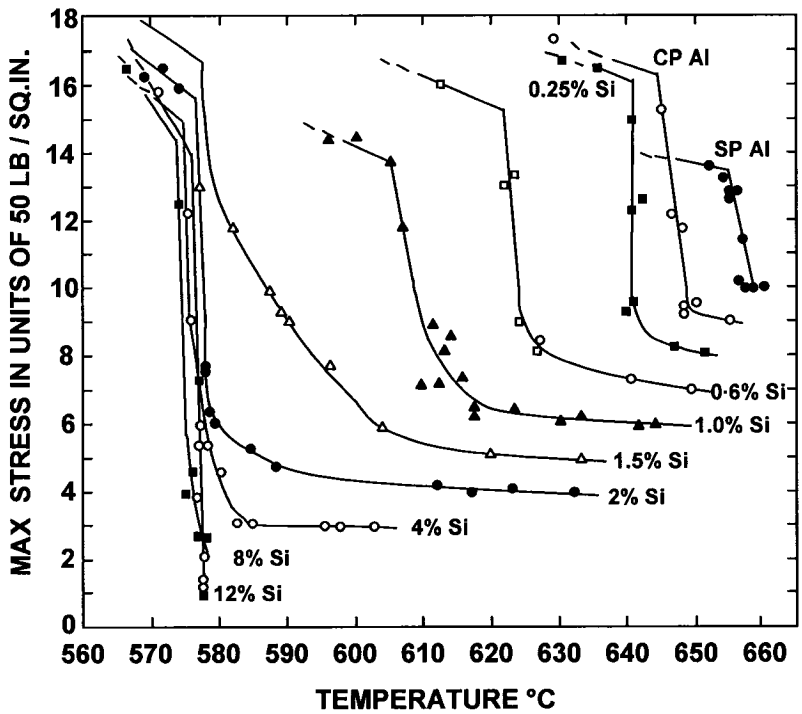

Figure 23: Tensile strength properties of Al-Si alloys at temperatures above the solidus [14]

The greater the range, the greater would be the bulk thermal contraction in portions at a more advanced stage of solidification, and, consequently, the greater would be the propensity to hot tearing. It was stipulated from the results that in simple binary alloy systems, the degree of hot tearing taking place above the solidus reaches a maximum in the alloy having the composition corresponding to the maximum solid solubility of the alloying elements. The more important results are incorporated in Figure 24 which reveals that the hot tearing range rises to a maximum at 1.8 percent silicon.

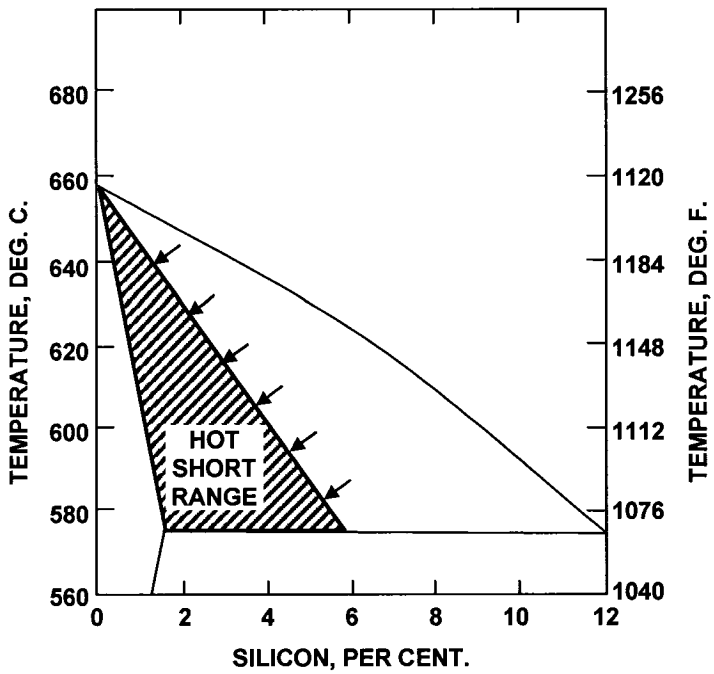

Figure 24: Relationship between hot short temperature range and composition of Al-Si alloys as determined by high temperature tensile tests [14]

Singer and Jennings [1] conducted work on the hot tearing of aluminum-silicon alloys of commercial purity by casting alloys into cylindrical metal ring moulds (Figure 25).

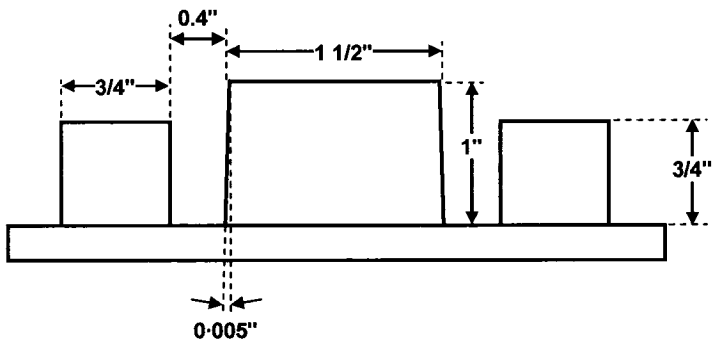

Figure 25: Mould for ring castings [1]

The test employed consisted of casting an annular ring in an open mould made up of a plate on which rested concentric ring and core.

The mould material was cast iron. One stipulated advantage is that the whole process of solidification of an alloy could be observed visually. The tensile stress was given by contraction around the core which caused fissuring on alloys prone to hot tearing. The results were influenced significantly by altering the pouring temperature which was maintained 100 °C above the liquidus. The mould was used uncoated to ensure uniform chilling effect and the mould temperature was kept at approximately 150 °C. The evaluation required between 4 and 14 ring castings followed by an examination to determine the extent and the nature of the hot tears. The severity of tearing is expressed numerically as the total length of the hot tears on all surfaces. It has been mentioned that the procedure has the disadvantage that it does not take into account the width or depth of the hot tears.

Figure 26 shows the results from the experiments using the ring casting method to evaluate the hot tearing propensity of aluminum-silicon alloys. The results [1] indicate that the severity of hot tearing increases to a maximum with increasing silicon content from 0 to 0.7% and then decreases to zero at 3% silicon. There was no hot tearing observed for alloys containing more than 3% percent silicon. The curve behaviour was described by Feurer [75] as the lambda curve (after the shape of the Greek capital letter, Λ).

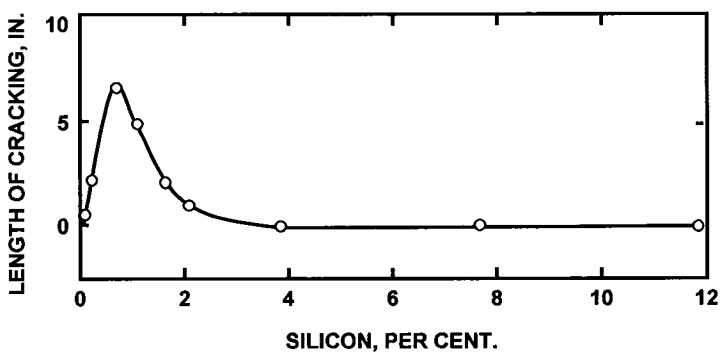

Figure 26: Average length of cracking of ring castings in Al-Si alloys [1]

The methods involving casting flat rings around sand or metal cores have been quite widely used [29,38-40]. According to Dodd [13], it is not easy to visualize a logical basis for this test, but the method has been used with particular success by Singer and

Jennings [1] and also in modified forms [37]. This test method is still used by some researchers, alone or sometimes in combination with other analytical methods, to evaluate the hot tearing susceptibility of aluminum alloys such as the Al-Cu binary [41,42] and the Al-Zn-Mg ternary [44] systems.

Other methods to evaluate the hot tearing susceptibility of an alloy involve the contraction of cylindrical bars of different diameters with flanged ends to restrain their free contraction (i.e., constrained rod casting). Dodd [13] mentioned that based on the strain theory [2], the most logical tests are those employing test castings in which the strain arising from the solid contraction is concentrated in a narrow hot spot. The hot spot may be at a junction of a runner [39] or riser but more commonly at the junction of different sections [3,7]. The majority of these tests do not, however, permit easy alteration of the strain applied to the hot spot. In addition, it is necessary to assess the severity of tearing by visual estimation of the length, width and extent of the cracks.

Hall [45] conducted the development of what is believed to be the first test method (before the description of the strain theory [1]) which employs flanged bars of different lengths containing hot spots of constant dimensions in the middle of the bar (Figure 27).

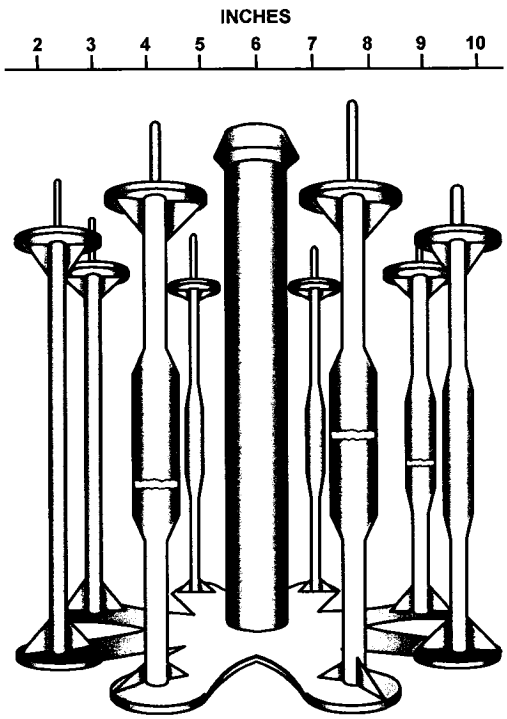

Figure 27: Hot tear test [45] employing flanged bars and containing a hot spot

Figure 27 shows the resulting castings (sand mould) with flanged bars and a bigger section at the middle of the bars to simulate hot spots.

Hall [45] stipulated that if there is a hot spot, the casting length determines the strain developed in the hot spot and, therefore, whether or not the casting will break. The reliability of this test, however, is upset if the ramming density or sand composition is not kept constant. Lees [9] comments adversely on this test for this reason and better consistency could be achieved by using metallic or ceramic moulds [8,37].

Rosenberg, Flemings and Taylor [4] developed and adapted a test for studying the relative hot tearing tendencies of non-ferrous alloys. The test pattern consists of a long, thin cylinder joined to a heavier cylindrical section (Figure 28). The ends of the test pattern are restrained by flanges. The lengths of the thin cylindrical bars can be altered to vary the severity of hot tearing. The severity of hot tearing for each alloy was rated as the maximum length test casting showing no tears. Castings were considered free of hot tears if no hot tear was visible using micrographic examination of a section (magnification 10X).

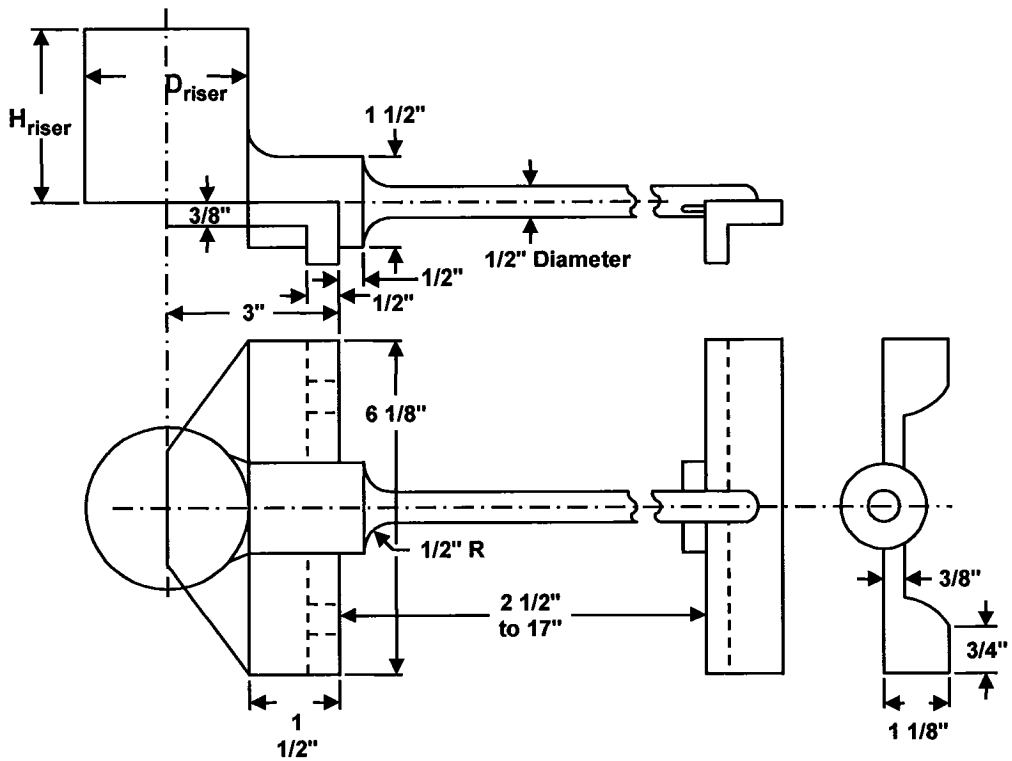

Figure 28: Plan view of the test pattern [4]

Tearing in the Al-Mg, Al-Sn, Al-Cu, Mg-Al, and Mg-Zn binary systems was studied [4]. An example of the results is shown in Figure 29 where hot tearing characteristics for grain refined and non-grain refined aluminum-copper alloys are compared. The curve relating hot tearing resistance is superimposed on the phase diagram.

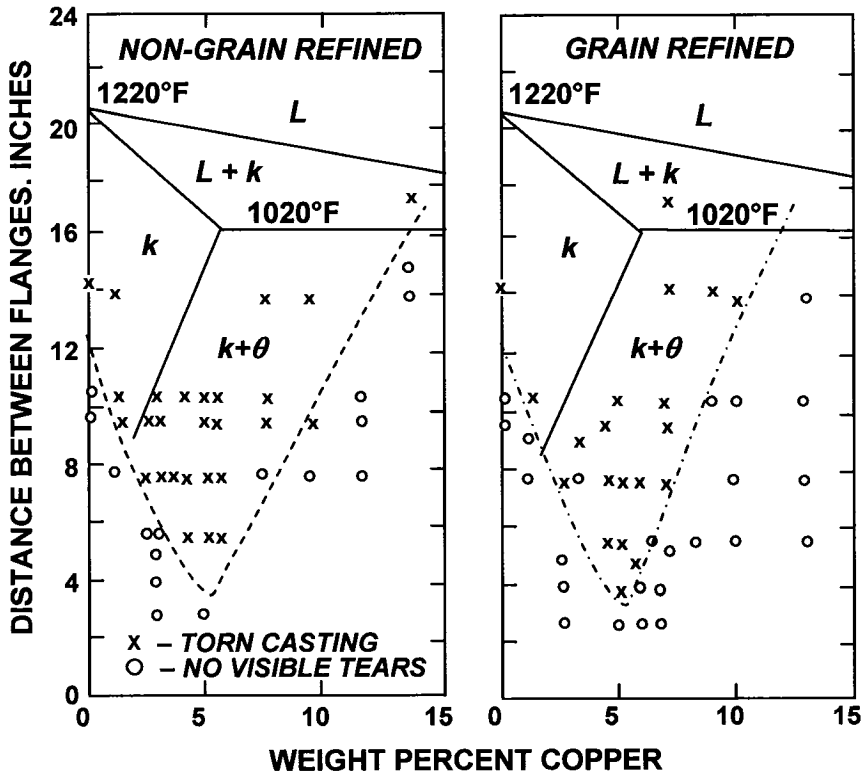

Figure 29: Hot tearing characteristics of the Al-Cu binary system [4]

Numerous designs of the constrained rod casting test can be found in the literature [37,46,47]. Gamber [46] developed a test method (C-shaped bar casting) to impose a stress to be concentrated at a fillet radius to evaluate the resistance to hot tearing of commercial alloys (Figure 30). The stress is maximum when the radius is zero and decreases as the ratio of the fillet radius over the bar thickness tends to one (r/t = 1).

The specific design is associated with a corresponding stress concentration factor (K_t). Figure 31 shows the relationship between fillet radius, stress concentration and castability at the hot spot location (L-junctions). Gamber's method offers several advantages such as: a direct and simple relative rating system, increased sensitivity (wider rating range), and a directional solidification, that forces the hot spot to be located at the fillet radius.

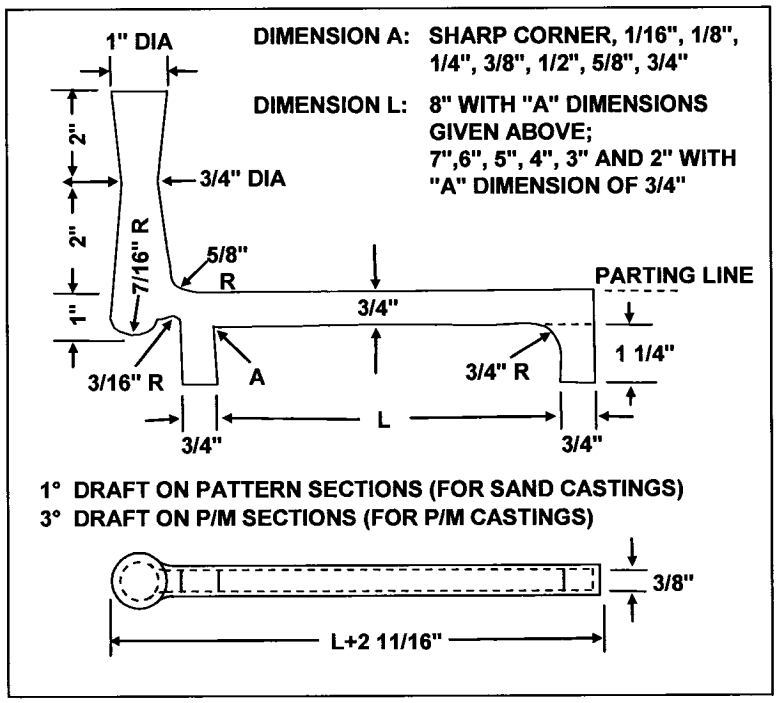

Figure 30: Diagram of the C-shaped testing method [46]

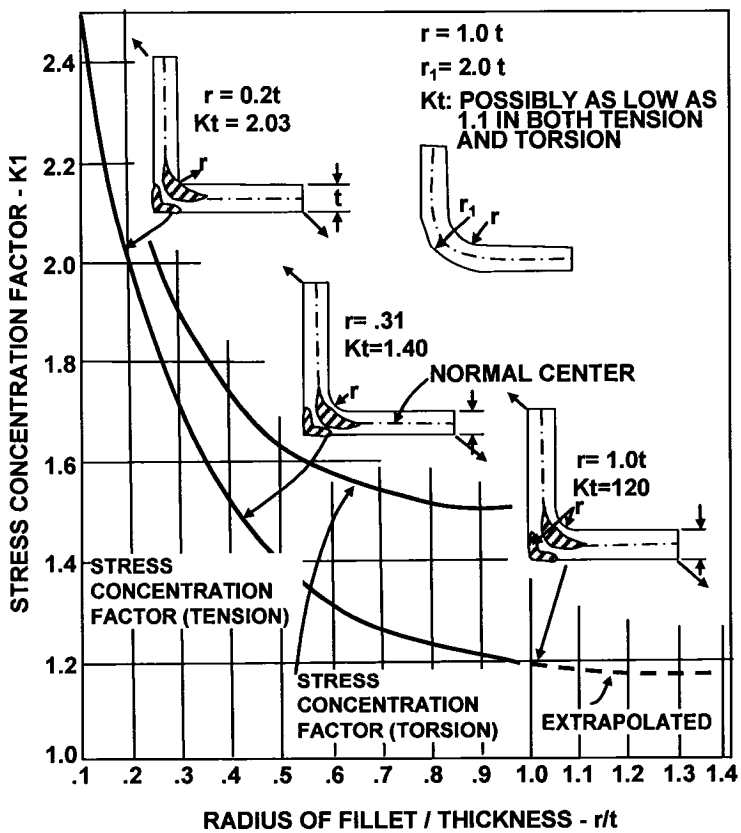

Figure 31: Relationship between fillet radius, stress concentration factor & L-junctions [46]

The rating consists of ascribing a severity factor of 1 for alloys that do not hot tear in the sharp-notched mould. The severity factor increases to 9 for the test bar showing a hot tear with the largest fillet radius and shortest length. A typical representation of the results is shown in Figure 32 for the hot tearing resistance of commercial aluminum-silicon alloy.

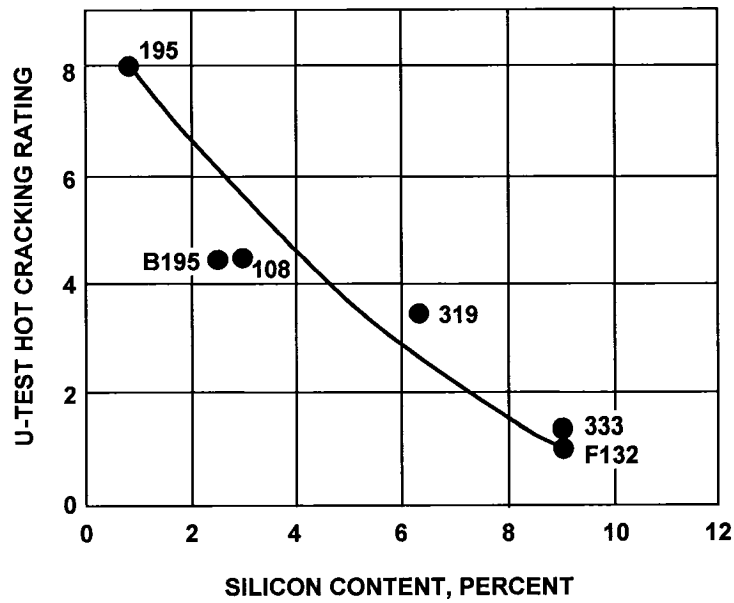

Figure 32: Representation of the hot tearing resistance of commercial Al-Si alloy [46]

Liu's [47] modification consisted basically in having horizontal rods of various lengths positioned randomly (Figure 33). The metal is fed to the flanged rods by a common sprue. The severity of hot tear was designated by a number from 0 (free of crack) to 5 (completely cracked bar) to each casting bar based on visual examination.

Warrington and McCartney [49,50] developed a hot cracking test for aluminum alloys. The main objective was to investigate hot tearing behaviour of aluminum alloys in a way which is relevant to the shell zone of DC cast ingot.

The test method consisted of an internally tapered steel crucible held in an open-ended tube furnace together with a separate water-cooled copper chill with a tapered conical portion. The chill section of the apparatus was inserted at a pre-determined depth into the molten alloy. Figure 34 shows a diagram of the test method used to assess the effects of grain structure and alloy composition on the hot tearing susceptibility of Al-Cu binary alloys.

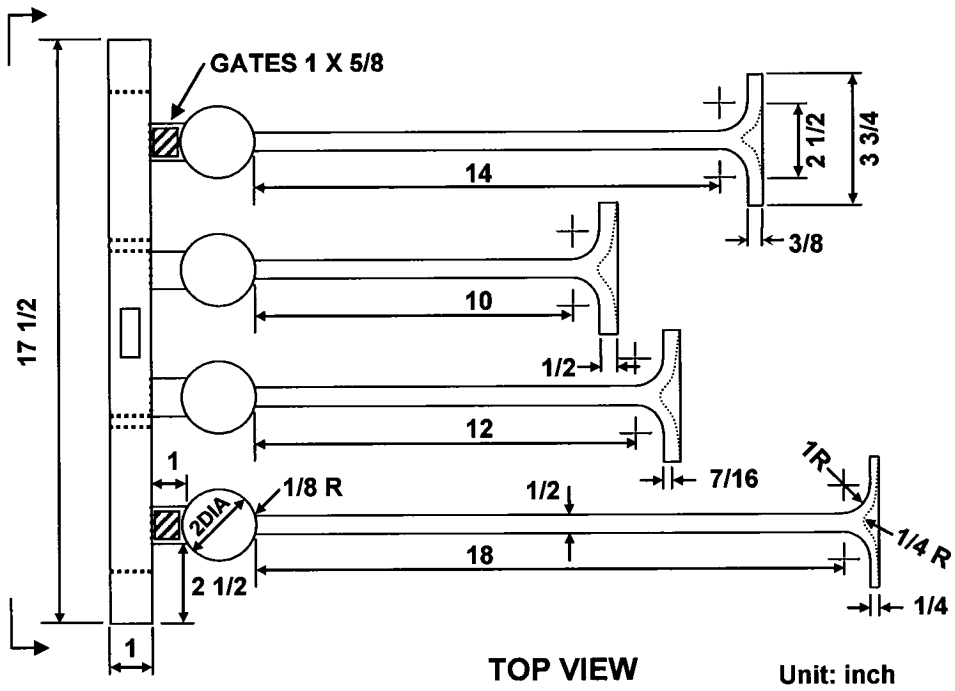

Figure 33: Diagram of the design showing randomly positioned flanged rods [47]

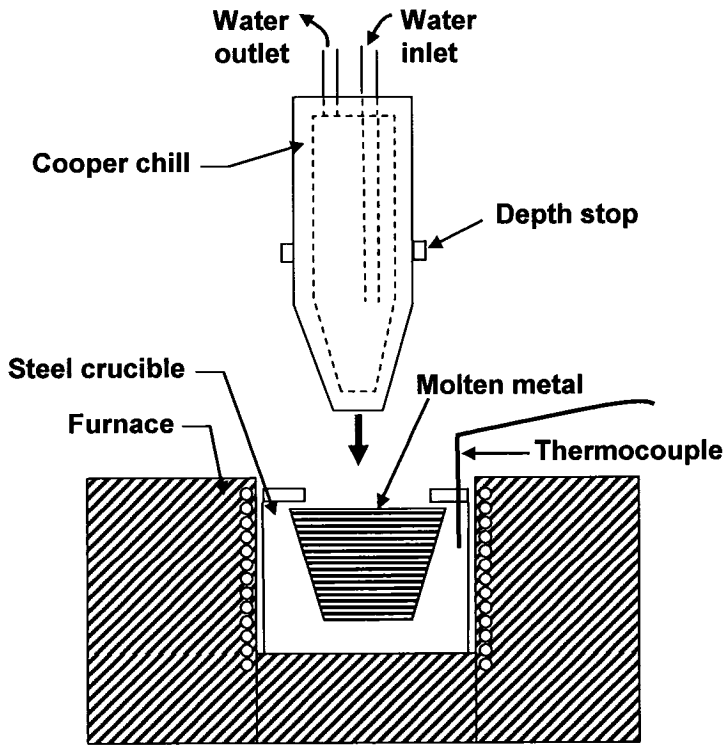

Figure 34: Diagram of the test method [49]

Several tests [49] were performed with temperature measurements which allowed thermal conditions to be characterized. Two conical chills with a 17.5° taper angle were used during the course of their work. The smaller chill had maximum and minimum diameters of 38 mm and 15 mm, respectively. The larger chill had maximum and minimum diameters of 60 mm and 20 mm, respectively. The taper arrangement of the chill and the crucible provided castings with 10mm wall thickness.

The melt temperature and the insertion depth were important parameters. However, the surface finish of the chill was a crucial element in reproducibility of the tests. Consequently, the surface was cleaned and polished prior to each test. An important feature about this test, is the ability to include a hot spot by simply painting a strip (8mm wide) of colloidal graphite on the chill surface to reduce the local heat transfer.

The crack length was used to express the hot tearing susceptibility [49,50] of each alloy. Figure 35 shows the crack length as a function of alloy composition.

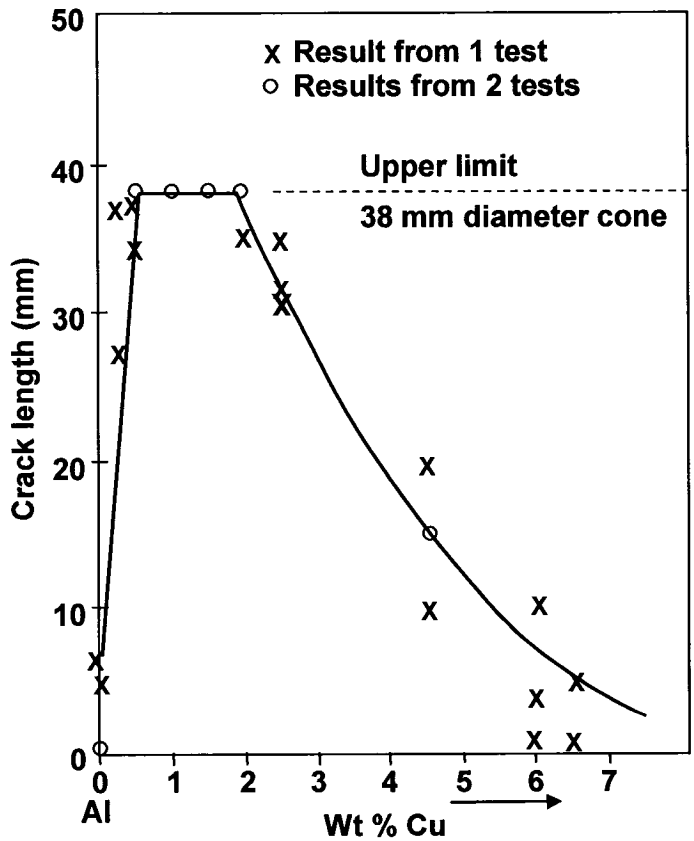

Figure 35: Diagram showing the crack length as a function of alloy composition [49]

In general, the compositional dependence of hot tearing was found to be broadly similar to that determined by others [1,7,9,14]. The hot tears produced with the apparatus were always intergranular in nature.

The methods described above were also used to determine the weldability of alloys. In fact, the weldability is often defined as the hot tearing susceptibility of alloys. Generally, the study of the weldability of alloys lead to the development of various techniques and approaches [51-55] dealing with both fixed and variable mechanical restraint [74] of the weld test.

The most popular technique to evaluate the relative hot cracking sensitivity of materials is attributed to Savage and Lundin [52] who developed the Varistraint. The augmented-strain concept for synthesizing full-scale restraint has proved useful in the studies of, 1) hot cracking sensitivity of filler metals, b) the effect of specific alloying elements, and 3) establishing the basic mechanisms of hot cracking. Briefly, the Varistraint technique utilizes a small specimen supported as a cantilever beam (Figure 36).

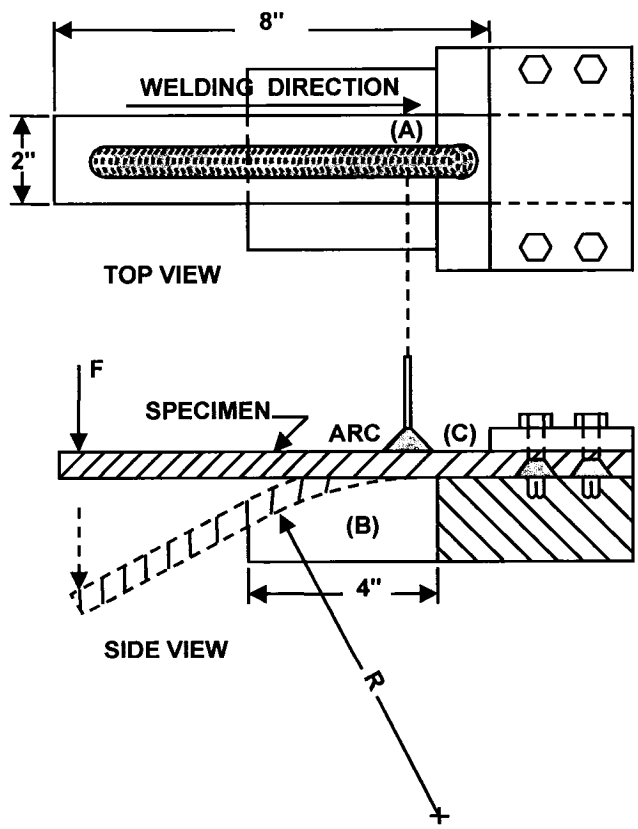

Figure 36: Diagram showing the Varistaint testing device [52]

A load is applied at a certain point to bend the specimen downward (augmented-strain) as the weld is deposited. Figure 37 shows the total crack length, measured directly from the as-welded surface, as a function of augmented-strain percentage.

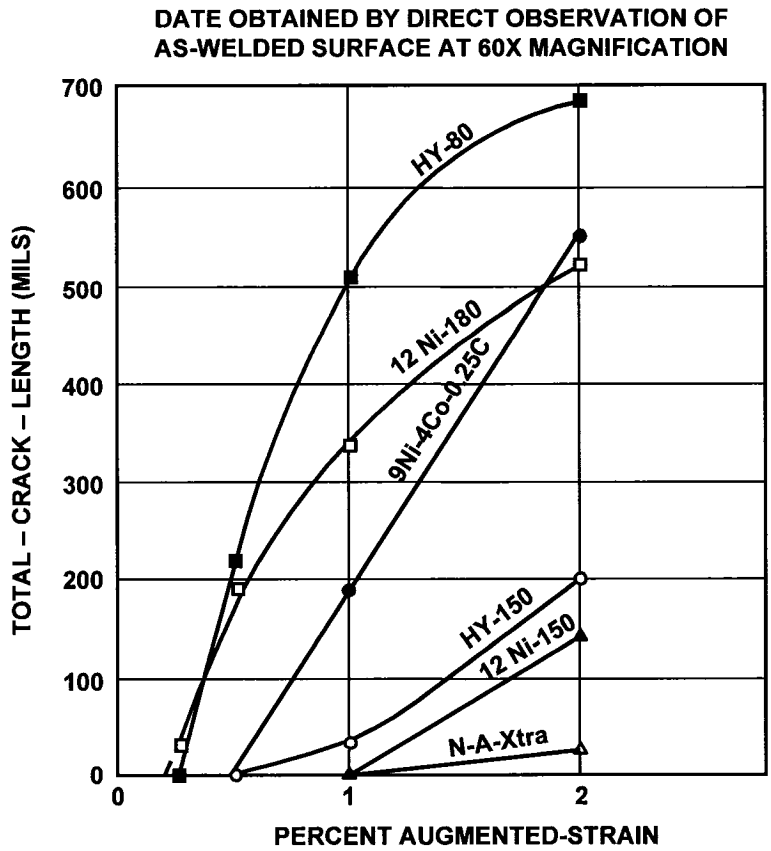

Figure 37: Total crack length as function of augmented-strain percentage [52]

Clyne and Davies [57,58] assessed the severity of cracking by monitoring the effect of the cracking on electric current flow. The method involves measuring resistance across different locations on the cast specimen. The experimental apparatus (Figure 38) consists of a dog-bone shaped mould (to create restraint) which is made of steel. Each end is water-cooled and the central portion of the mould is seated on a firebrick heater. The mould is positioned beneath a graphite crucible heated by an induction coil. The crucible has a hole, plugged temporarily with a graphite rod, at its bottom to allow quick filling of the mould at the appropriate time.

The experimental setup is such that the cracking is restricted to the 20mm wide central portion of the dog-shaped mould (Figure 39).

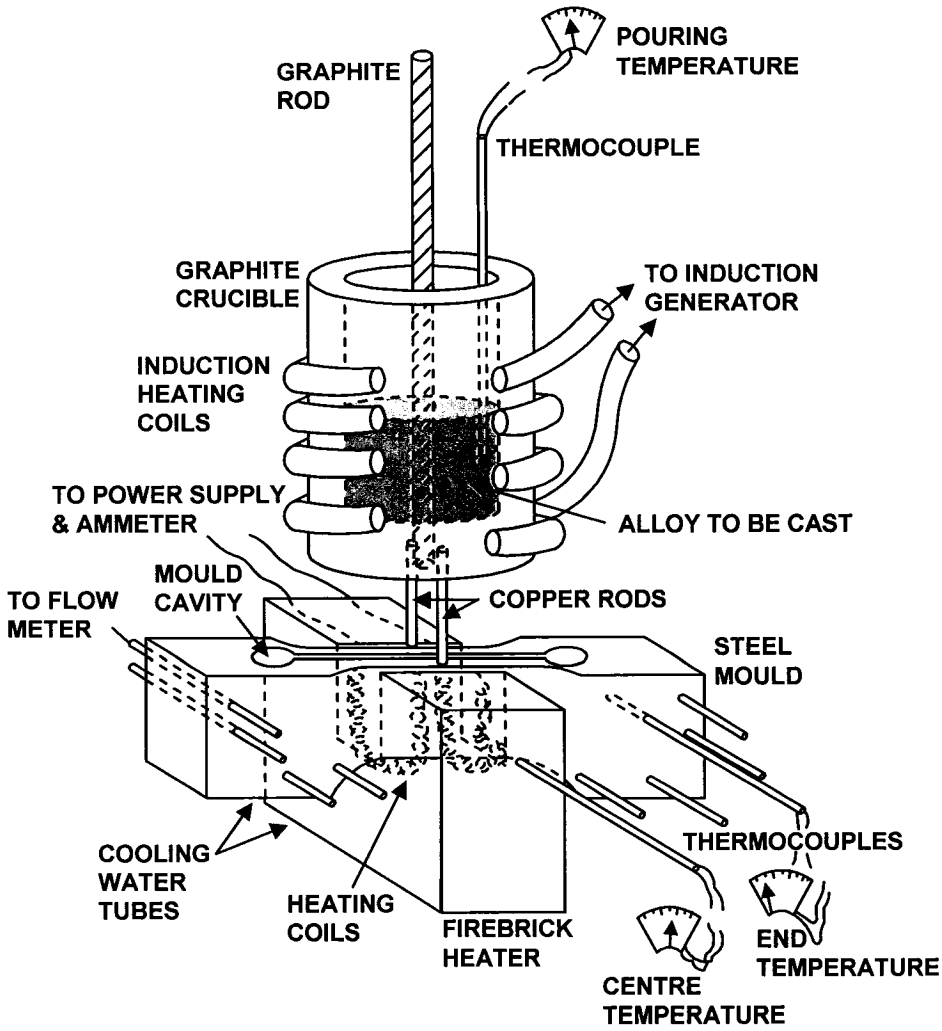

Figure 38: Diagram of the casting apparatus [58]

After pouring the melt and solidification is completed, the test specimen is removed and the central portion is machined to a uniform section for resistance measurements. The reduction in cross sectional area from the initial value to the obtained final value due to cracking of the test piece is related to the resistance measured and expressed as fractional area of cracking, X_{cr}.

Consequently, the parameter extracted X_{cr}= 0 represents a completely uncracked specimen and X_{cr}= 1 a fully cracked section. Figure 40 shows the variation of cracking fraction X_{cr} as a function of alloying element and melt superheat. It has been shown to represent in a meaningful way the severity of the cracking based on the two assumptions a) that the values of X_{cr} represent an actual reduction of the cross section area or the crack surface area, and b) that the changes in the resistance are a direct consequence

of the presence of cracks only and not the results of changes in composition produced by macrosegregation or microstructure.

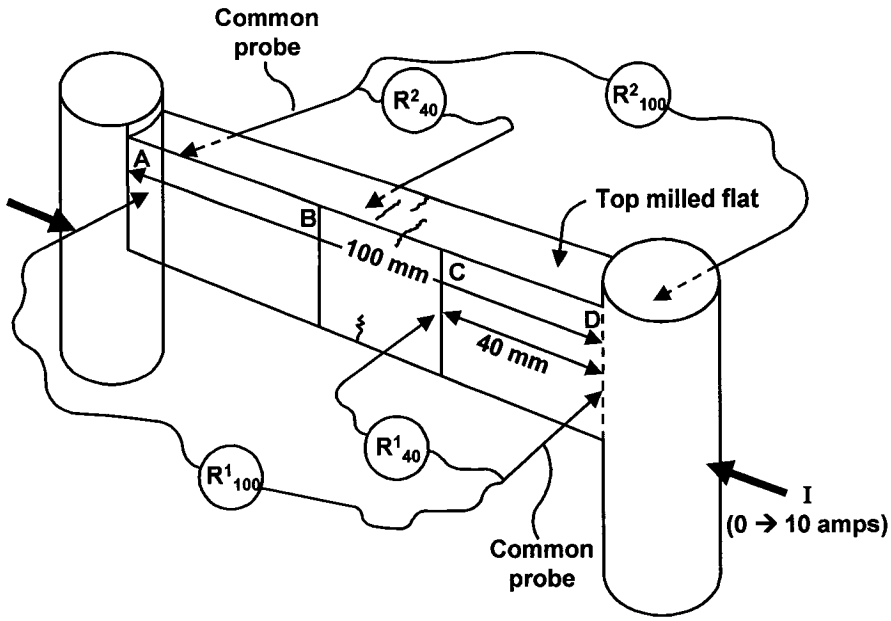

Figure 39: Machined section for resistance measurements [58]

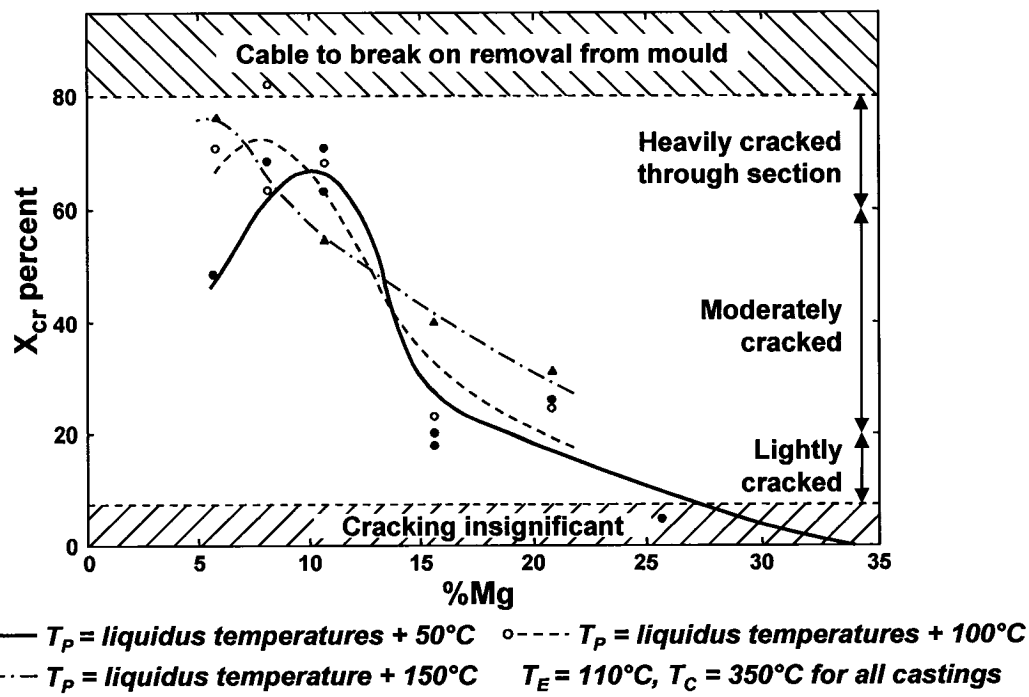

Figure 40: Variation of cracking fraction Xcr as a function of alloying element and melt superheat [58]

Figure 41 shows a typical comparison of theory and experiment for the Al-Si alloys; the hot cracking susceptibility of Al-Si alloys measured by Clyne and Davies (through electrical resistance [58] and by Feurer (through direct measurement of the crack length [75]). The experimental results are from the ring test and the dog-bone test.

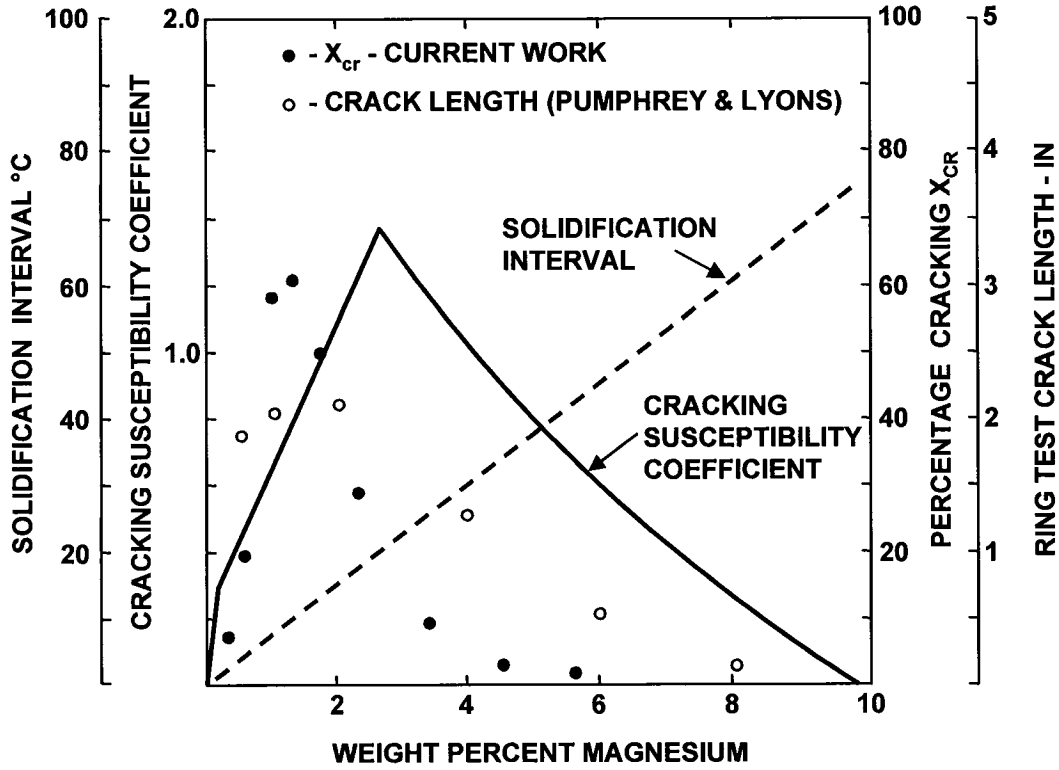

Figure 41: Comparison of theory and experiment for the Al-Mg system [58]

The observation of hot tears formation allowed a better understanding of this phenomenon. Fredriksson [59] observed initiation and propagation of hot tears during tensile testing under a scanning electron microscope (SEM). Two alloys were used (Al-4wt%Sn and Al-4wt%Cd). The samples were heated between the liquidus and the solidus temperature before tensile testing. These two alloys showed completely different behaviours. The alloy Al-4wt%Sn presented a fragile rupture while the alloy Al-4wt%Cd was ductile. In fact, the eutectic liquid located at the grain boundary wets the grain that favours hot tearing when a tensile load is applied. On the other hand, the eutectic liquid did not wet the grain boundaries of the Al-4wt%Cd. In fact, the eutectic liquid remained under the form of spherical drops. These results showed the important role of the wetting ability of the grain boundaries by the liquid metal and the formation of the hot tears.

Grasso [60] used an organic alloy of succinonitrile-acétone and a device (Figure 42) to perform unidirectional solidification in order to observe in situ the hot tear formation. The use of this organic alloy avoided the problems related to visual observation at high temperature with metallic alloys. The device was composed of a small cavity containing the alloy subjected to a thermal gradient. A lever allowed initiating hot tears while separating the dendrites of one another. The temperature of the solid liquid front was measured by thermocouples.

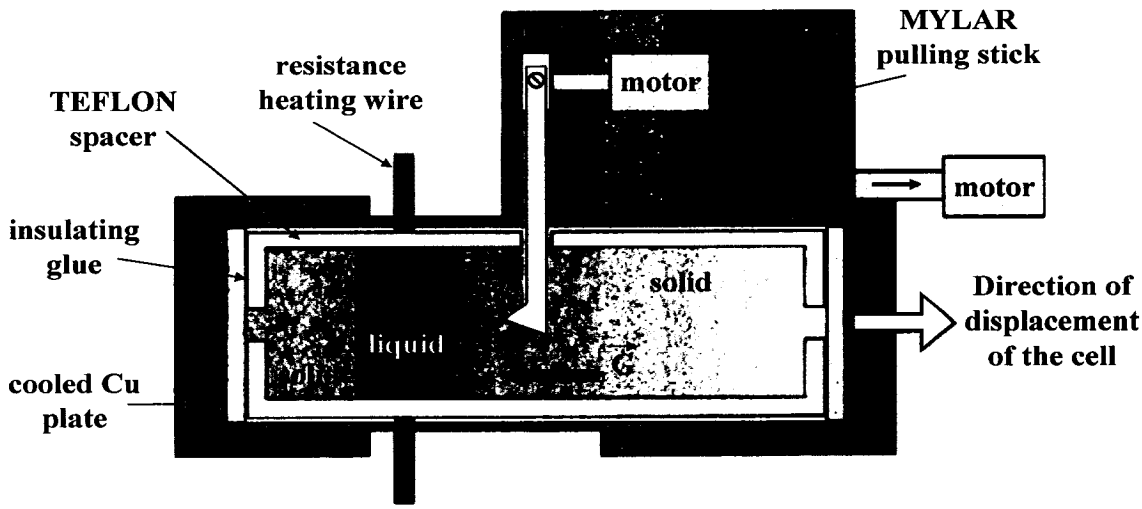

Figure 42: Device to observe in-situ hot tearing [60]

These two studies showed that the hot tear will be healed by the surrounding liquid if the dendrites are separated at lower solid fraction (i.e., no coherency between dendrites). Nevertheless when the permeability becomes too low (i.e., no inflow), pores will form at the extremity of the healed hot tear. The liquid will spread itself in the perpendicular direction until separation. These studies show that the phenomenon of hot tearing is not only interdendritic but also intergranular.

Tensile testing of aluminum alloys during solidification requires that the sample start at the liquid state. The tensile test concept by Ackerman [60] is certainly a completely different experimental approach. The experimental set-up (Figure 43) used two water-cooled movable copper cylinders that were immersed in the molten metal. The solidification began immediately and a shell zone surrounded the water-cooled device shortly after. When the formed shell attained a certain thickness, the lower portion of the

cylinder moved downward to apply a tensile load perpendicular to the direction of the solidifying shell.

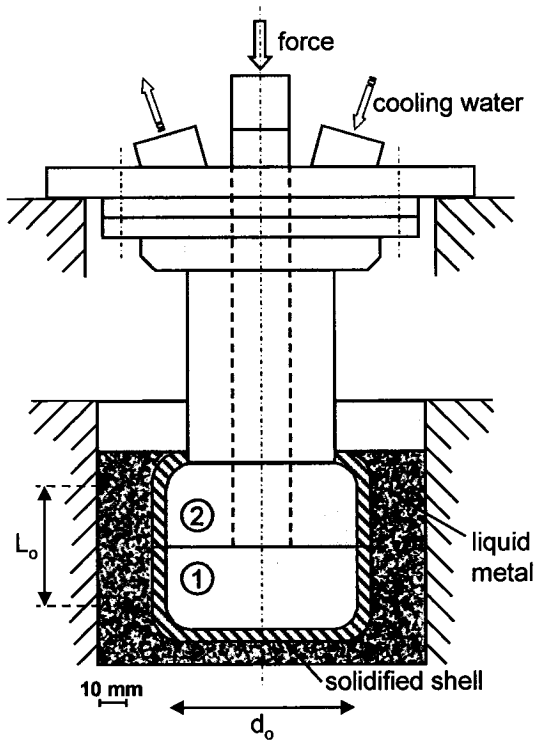

Figure 43: Experimental to apply tensile force during solidification [60]

This configuration does not allow a direct measurement of the strain in the molten metal. The strain rate was determined by assuming that the shell is strained over the total height, L_o. The latter can be affected by the friction between the shrinking shell and internal stresses can develop but are not considered in the tensile strength determination. In addition, molten metal will penetrate between the incipient hot tear. This makes the hot tear zone and the load bearing area difficult to evaluate. This approach gave results that were in agreement with previous studies. However, the approach does not cover the range of interest in the solidification interval and completely different failure mechanisms might probably take place.

Ohm and Engler [62-65] represents the first and only documented attempts to measure the stress and strain at the surface of a casting chilled by a metallic mould. The apparatus included an insulated U-shaped crucible on which a water-cooled copper

mould is positioned (Figure 44). The crucible is filled with the molten alloy which makes contact with the water-cooled copper mould almost simultaneously over the total contact area. The alloy is therefore solidified directionally from the top and a shell grows downwardly into the metal pool. The supplementary cooling of the mould ends ensures that the hot tearing will take place at the centre of the sample. After reaching the target temperature, the mould is removed and a constant displacement velocity is applied to the cast sample using the specially designed jaw or cast-in anchors. The force and the displacement velocity were recorded.

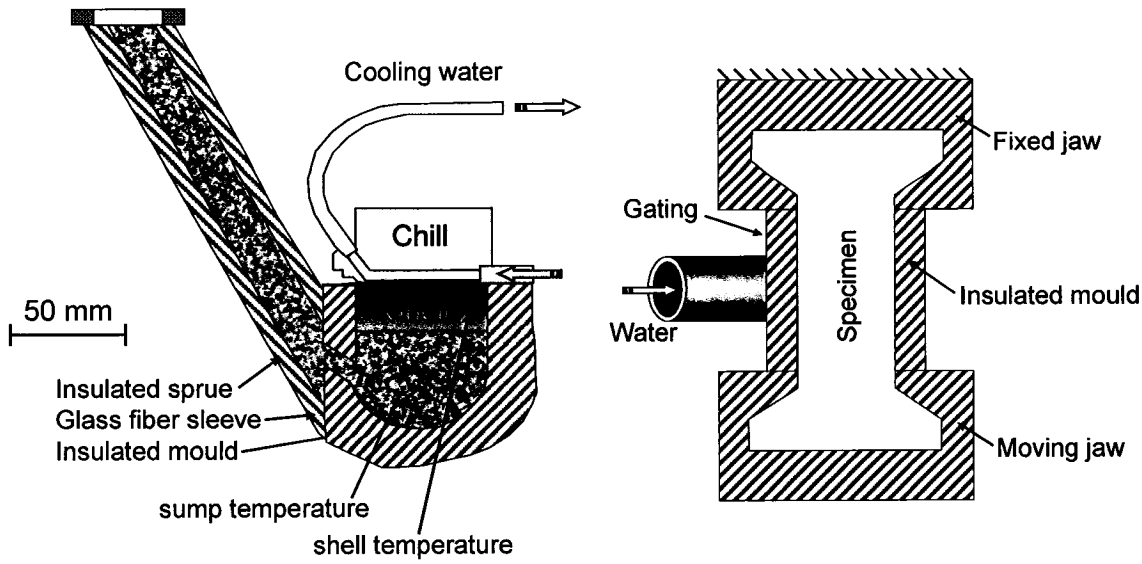

Figure 44: Diagram of the apparatus designed by Olm and Engler [62-65]

Magnin et al [63] used the apparatus developed by Ohm and Engler [64,65] for the tensile testing of a solidifying shell cooled by a chill plate. They presented stress-strain curves for aluminum alloys above their solidus temperature. The measured tensile strengths were in the range of 0.25 to 2 MPa and elongations at maximum stress were typically less than 0.5%. The alloys investigated were Al-0.9Mg-0.6Si (6063) [62], Al-4Cu (A295.2) [62] and Al-4.5Cu (2024) [63].

Colley et al [67] measured the tensile properties of as-cast aluminum alloy AA5182 in the 500-580 °C interval using the reheated bar technique equipped with a digital video camera to evaluate the instantaneous true strain from diameter measurements. They observed a sharp decrease in strength as the temperature raised above 570 °C giving

mass fraction liquid greater than 5% according to Arnberg et al [68]. The cause of such a decrease in strength was not associated to a visible change in the microstructure in the 570-575 °C interval, but an increase in the proportion of liquid was evident above 575°C. The maximum stress measured at 575 °C was around 2.5 MPa. The loading portion of the stress-strain curve was unfortunately too steep to evaluate the strain at maximum stress. Applied strain rates were between ~10^{-2} and ~10^{-4} s^{-1}.

2.3.2 Prediction of Hot Tearing Susceptibility

Over the years, there have been many attempts to define an effective working theory of hot tearing. The most useful work has been the attempt to predict the hot tearing susceptibility as a function of composition for binary alloys. This is considered [32] as a severe and discriminating test because the theory has to contend with a pure metal, having low solute content (only solid solution dendrites), and eutectic concentrations increasing with solute levels. Consequently, the ability to deal with all of these aspects in a single alloy system represents a test of the theory which covers the majority of solidification structures in real castings.

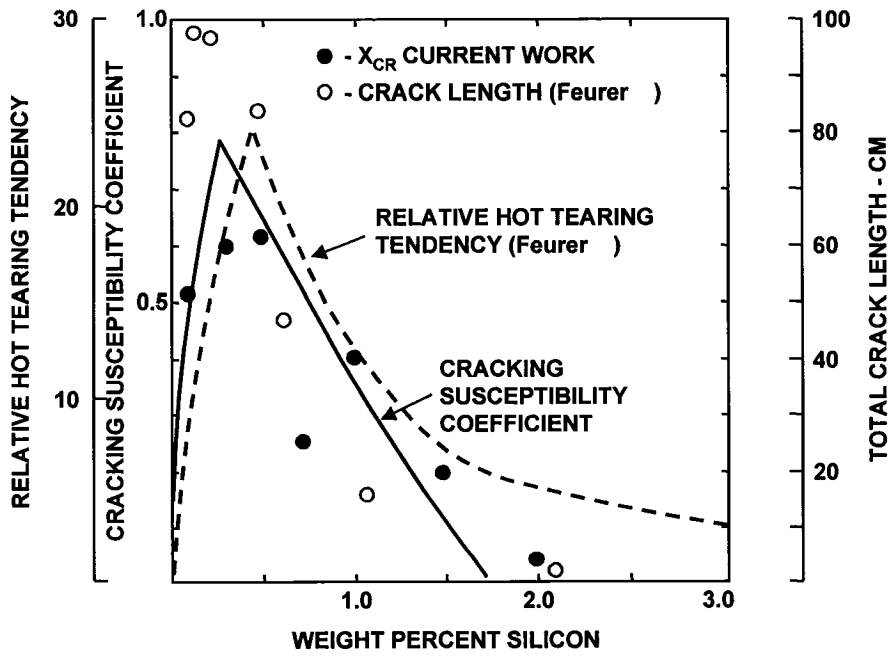

Figure 45: Diagram showing the relative hot tearing tendency (Λ-curve) for the Al-Si system [75]

However, there are relatively few usefully predictive models and it is difficult to derive a satisfactory theoretical description from decades of research on hot tearing. One particular example is the typical experimental result (Figure 45) which reveals a steeply peaked curve (relative hot tearing tendency) which Feurer [75] called a lambda curve (after the shape of the Greek capital letter,Λ). The problem is to find a theoretical description which will allow the lambda curves to be simulated for different alloy systems.

Generally, the tendency to hot tearing is based on balancing parameters having a positive or negative effect on one another. Quantitative characterization using computer simulation of solidification and the prediction of hot tearing cannot be built on experience or estimates of influencing variables. In this case, it is necessary to deal with parameters which can be described mathematically and be determined from measurable quantities. The theoretical approaches and the known concepts to explain the experimental results are presented in this section.

According to Fortina [66,70] the curve for the solid fraction curve as a function of temperature, f_s, deviates greatly from a hypothetical linear curve. The positive or negative deviation, ΔT, should describe the hot tearing tendency according to Equation 3,

$$FC=\frac{(\Delta T_{pos})_{\max}\cdot s^{+}-(\Delta T_{neg})_{\max}\cdot s^{-}}{R_{mc}} \qquad \textbf{Equation 3}$$

where: $(\Delta T_{pos})_{max}$: largest positive temperature deviation (°C),

s^{+}: f_s value of ΔT_{pos},

$(\Delta T_{neg})_{max}$: largest negative temperature deviation (°C),

s^{-}: f_s value of ΔT_{neg},

R_{mc}: hot tensile strength of the solidified alloy (MPa),

$(1-s^{-})$: liquid fraction ($1-f_s$).

The value of the hot tearing coefficient FC should be as low as possible. This coefficient was used by Fortina [66,70] to make a relative estimate of the hot tearing tendency of wrought aluminum alloys.

Flender and Hansen [71] sees the hot tear development as a competition between the solidification rate, v, and the contraction rate, u. The solidification front requires a certain time to pass through a critical zone of length a, at a rate, v. During this time, the considered zone contracts with the rate component ($u_k \cdot \cos \varphi$). The strain forced in this direction should be less than the critical strain ($\varepsilon^* \cdot \Delta L$) where ε^* represents a material property. The condition for the occurrence of a hot tear is, therefore, given by Equation 4,

$$K_w = \frac{\frac{v}{a}}{u_k \cdot \cos\varphi} < \frac{1}{\varepsilon^* \cdot \Delta L} = K_W^{crit} \qquad \textbf{Equation 4}$$

where:
- v: solidification rate (°C/s),
- a: length of the critical temperature range (m),
- u_k: free contraction rate,
- ε^*: critical strain,
- ΔL: length of the critical zone (m),
- φ: angle between u_k and the perpendicular to v.

Feurer [75,94] derived a mathematical model for the hot tearing tendency of hypoeutectic alloys based on solidification shrinkage and its feeding by the residual interdendritic liquid. The hot tearing criteria is given by Equation 5,

$$\left(\frac{d\ln V}{dt}\right)_{total} < 0 \qquad \textbf{Equation 5}$$

with; $$\left(\frac{d\ln V}{dt}\right)_{total} = \left(\frac{\delta \ln V}{\delta t}\right)_{feeding} + \left(\frac{\delta \ln V}{\delta t}\right)_{shrinkage}$$

where "V" represent the positively acting part (feeding) or the negatively acting part (shrinkage) of the volume deficiency. However, this description does not take into account any small elastic or plastic deformation [12].

Clyne and Davies [58] define a cracking susceptibility coefficient (CSC) assuming that the local liquid fraction, f_L, in any volume element decreases monotonically until the

solidification is complete. It is indicated that in the vicinity of the hot spot (the most vulnerable region) the following processes can occur:

i) Strain accommodation by solid movement (mass feeding)

ii) Strain accommodation by liquid movement (interdendritic feeding)

iii) Interdendritic separation (interdendritic film stage)

iv) Interdendritic bridging

The cracking susceptibility coefficient was defined according to Equation 6 where t_V is the vulnerable time period and t_R is the time available for stress relief processes.

$$CSC = \frac{t_V}{t_R} \qquad \textbf{Equation 6}$$

It is necessary, however, to obtain the f_L/time curves corresponding to a range of initial compositions to predict the variation of CSC with composition. In order to calculate these times, it is necessary to have a $f_L(t)$ or $f_s(t)$ relationship. This can be achieved using a microsegregation model (Scheil or with some back diffusion) and knowing the local thermal history. The first approximation to the f_L limits can be taken from previous work concerned with liquid-solid rheology and interdendritic mobility [72] which suggested the following:

i) mass and liquid feeding: $0.1 < f_L < 0.6$

ii) interdendritic separation: $0.01 < f_L < 0.1$

iii) interdendritic bridging: $f_L < 0.01$.

Figure 46 shows the model for the regimes during which either stress relaxation or vulnerability to hot tearing occur. The model is used to determine the t_R and t_v values. During the time t_R ($0.40 < f_s < 0.90$) liquid and mass feeding will prevent or heal any incipient hot tear. On the other hand, in the period t_v ($0.90 < f_s < 0.99$) structural separations are possible.

Consequently, to avoid the occurrence of hot tears, it is necessary to have the lowest values for the CSC coefficient. The agreement was improved later by Katgerman[62] for the Al-Mg system.

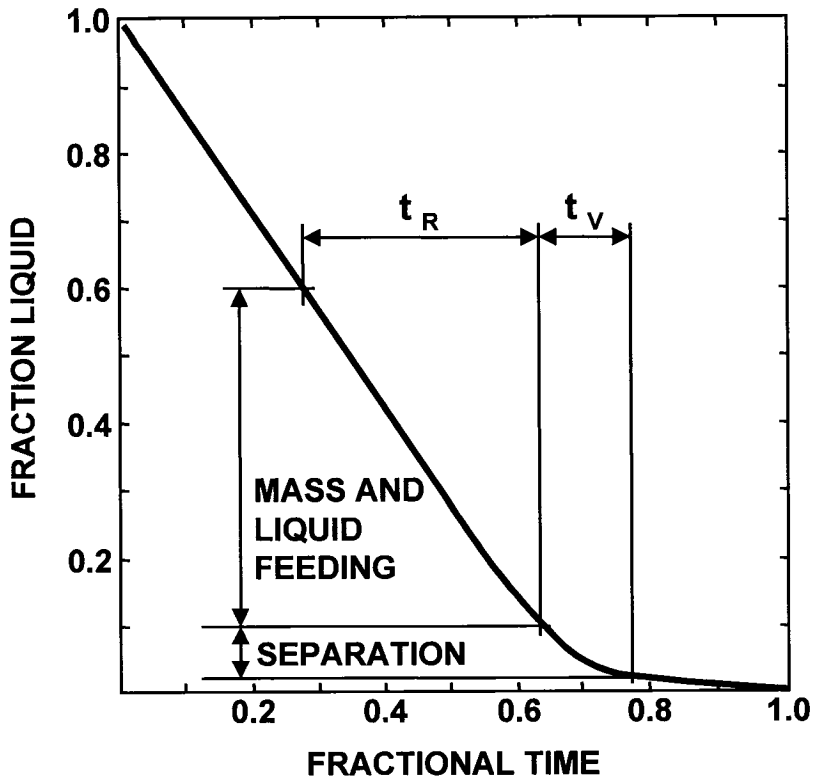

Figure 46: Model for the determination of t_R and t_v [58]

In addition, Campbell [15], has suggested a modified criterion for the susceptibility to hot tearing as shown by Equation 7.

$$CSC_b = \frac{\alpha \Delta T L a}{l^2} \cdot \frac{t_V}{t_R} \qquad \textbf{Equation 7}$$

where "ΔT" is the interval of solidification, "L" is the overall length of the casting, "a" the grain size, and "α" the coefficient of thermal expansion. The first term on the right hand side refers to the thermal strain accumulated in the hot spot with grains of size "a", and "l" the length of the hot spot measured in the direction of the strain.

Feurer [75] has proposed a theory to explain hot tearing tendency from a concept which is in fact more relevant to microporosity formation. First, he considered the suction of liquid that is needed to compensate for the shrinkage of the metal without formation of pores. On the other hand, he calculated the pressure drop associated with a given flow

of liquid through a mushy region (Darcy's law) and estimated that hot tears will form when the feeding cannot compensate for the shrinkage.

This approach [75] assumes a pressure drop in the mushy zone (i.e., which normally leads to microporosity formation) and not uniaxial tensile stresses. However, Guven and Hunt [93] have shown that hot tears form in the aluminum-copper system only if the casting is restrained from opposite solidifying zones; this situation generates a hot spot under tensile stress. Consequently, the approach by Feurer [75] to explain the form of the lambda curves can be discounted because it is based on the modeling of liquid flow and hence the development of hydrostatic stress, not uniaxial tension as presented by Campbell and Clyne [32]. Figure 47 shows the hot tearing response of Al-Cu alloys with a peak at approximately 0.7% Cu from the conical ring test by Warrington and McCartney [49] compared with various theoretical models.

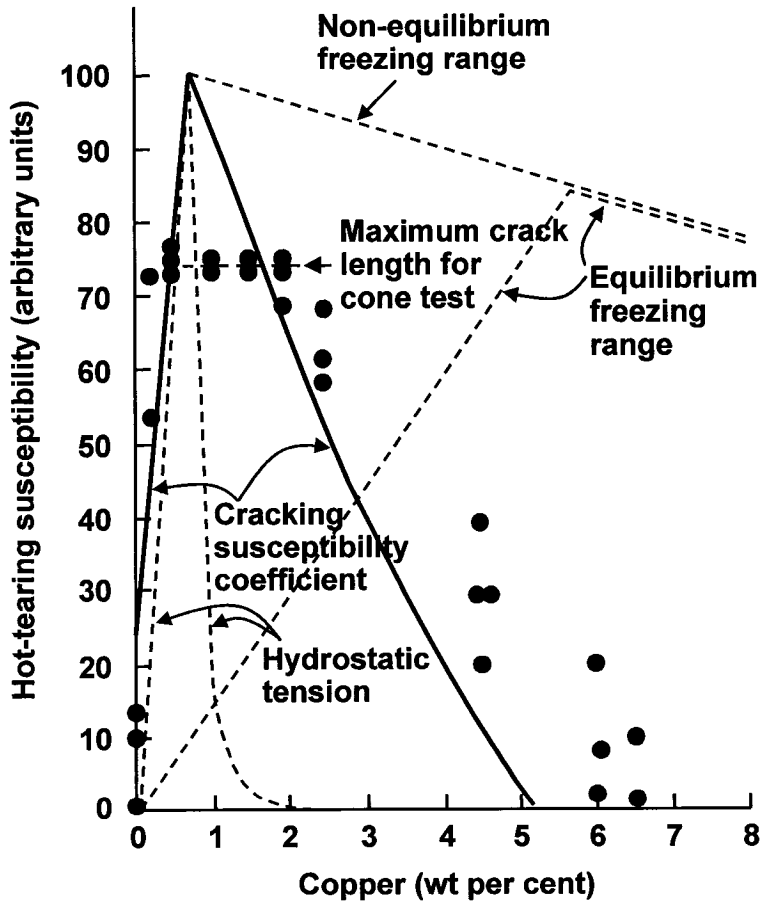

Figure 47: Hot tearing response of Al-Cu alloys compared with various theoretical models – Freezing ranges and hydrostatic tension [76] and CSC [58]

During their studies on the computer simulation and modeling of the hot tearing behaviour, Flender, Hensen, and Sahm [71] show the most advanced formulation of a hot tearing criterion as being given by Equation 8.

$$K_W = \frac{\left(v = \frac{\dot{T}}{G_S}\right)^n \cdot \left(\frac{G_S}{\sqrt{\dot{T}}}\right)^m \cdot L}{\left(u = \sum \alpha \cdot \Delta y \cdot \dot{T}\right)^l \cdot \left(C \cdot \dot{T}\right)^{-1/2}} \qquad \textbf{Equation 8}$$

where v: solidification rate,

u: contraction rate in y-direction,

$\dot{T}$: cooling rate,

G_s: temperature gradient at the solidification front,

L: length of the stress relief,

α: coefficient of thermal expansion,

Δy: shrinkage length of an element,

C: constant,

K_w: parameter for the hot tearing criterion,

n, m, l: weighting constants.

However, the use of the above calculation methods can be made significantly more difficult by taking into account factors such as, phase transformation, segregation of alloying and trace elements, grain size and distribution, wetting behaviour of the residual liquid as well as the mobility of the grain and melt system under stress.

2.3.3 Mathematical Model

Mathematical models that predict the evolution of temperature, stress, and strain fields in metals during industrial processing have become an important tool in obtaining a better understanding of the processes and in optimizing them.

An important problem in casting is the formation of thermally induced strains and stresses, which can lead to defects such as hot tearing, hot cracking, and cold cracking during or at the end of the process.

Approaches to modeling the magnitude of thermal stresses and strains during solidification for the prediction of hot tears have been covered by several researchers [77-83]. A specific objective is to establish a mathematical model to predict the hot tearing susceptibility of aluminum alloys.

Chandra [77,78] described the development and application of a new approach for the prediction of hot tears in castings. The proposed methodology is based upon Pellini's theory and is divided into two main parts: 1) prediction of grain size and thickness of liquid film around solid grains at various stages of solidification, and 2) development of a strain based hot tear or fracture criterion.

Hannard [84] used a specific finite element program (MARC) to model the butt curl and stress built up during DC casting of aluminum sheet ingot. The magnitude of the stress is used to predict the cold cracking tendency. Figure 48 shows the boundary conditions used to calculate temperature distribution and thermal stresses during both the start-up and the steady-state regime of the cast.

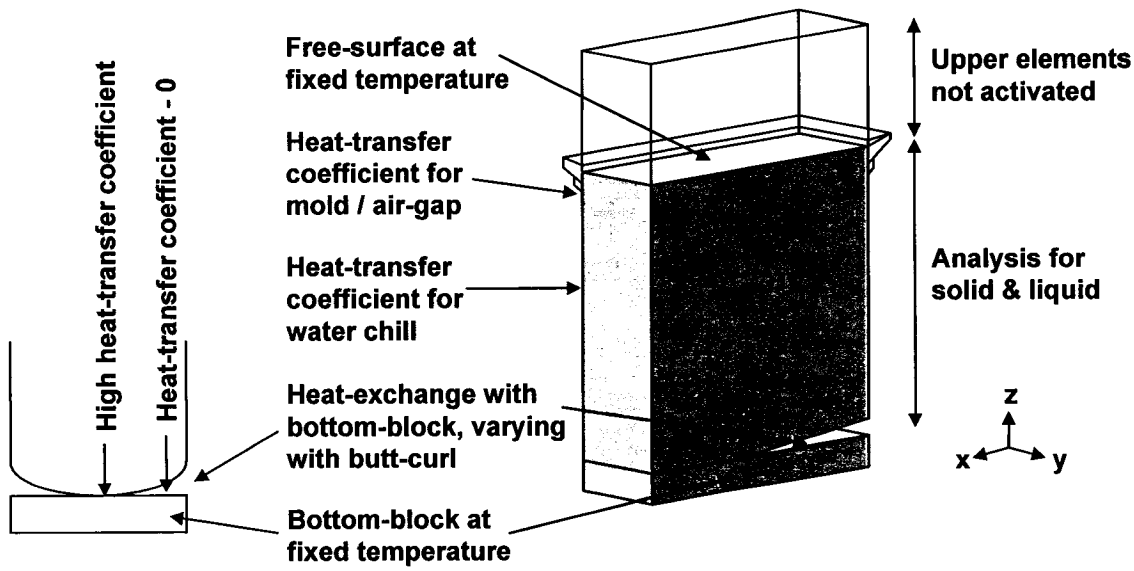

Figure 48: Boundary conditions for the DC casting model (MARC) using finite element [84]

Drezet [85,86] developed a thermo-mechanical model to describe the stress generation in the solidifying ingot. The main objectives of the work included the understanding of the basic mechanisms responsible for the non-uniform lateral face pull-in and to quantify the shape of the final cold ingot through numerical simulation.

Purvis [87,88] used acoustic emission (AE) to determine the precise moment for the occurrence of a hot tear during solidification. Larikov [89] used the same method to determine stress generation during liquid embrittlement of aluminum. The AE signal generated during solidification provided various pieces of information concerning the liquid-solid phase change such as primary and eutectic phase formation, and intermetallic phase precipitation. The approach was also able to detect certain casting defects such as hot tearing, hot cracking and porosity [88] formation. He conducted solidification experiments [87, 88] with cast restrained bars of variable length and used acoustic emission in combination with thermal analysis to investigate hot tearing mechanisms. It was found that the acoustic emission signal tended to increase abruptly during the generation of a hot tear. Figure 49 shows an example of the results obtained during solidification with acoustic emission and thermal analysis.

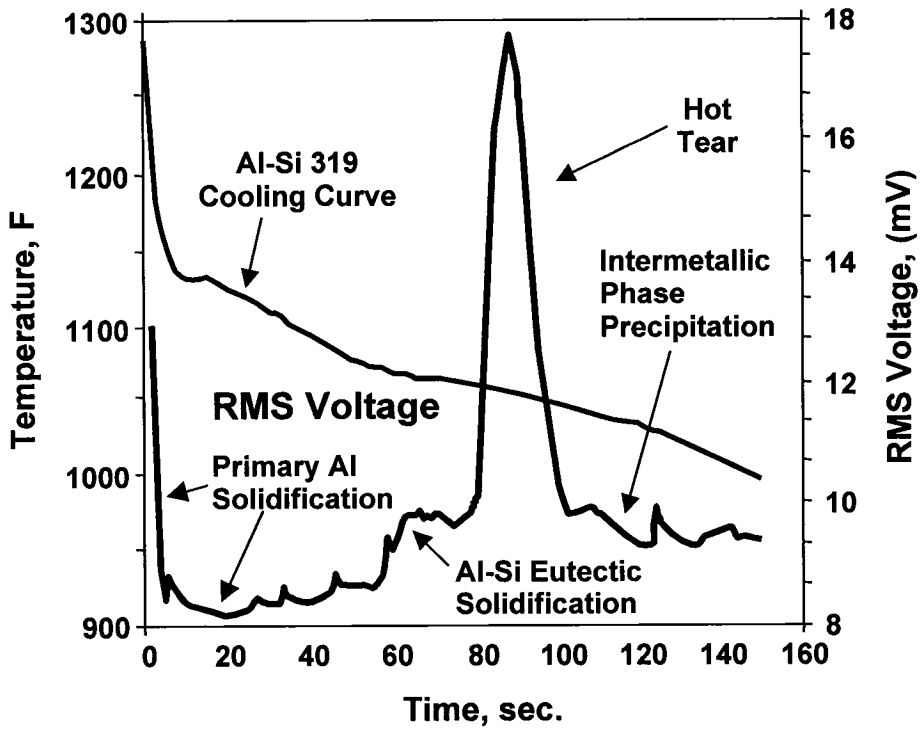

Figure 49: Acoustic emission signal during solidification of Al-Si alloy (A319) and the associated cooling curve [87]

2.4 Influencing Variables on Hot Tearing

Hot tearing is likely to be found in all material groups. The aluminum-silicon and aluminum-copper binary systems are prone to hot tear and were intensely investigated by, among the others, Verö [7], Singer and Jennings [1], and others like Warrington and McCartney [49] or Chadwick [42].

Numerous studies in the steel industry summarize the latest development in the research on hot tearing and consistent agreement can be found in the literature for most groups of influencing variables. The results concerning the impact of specific parameters and variables are compiled under the following descriptions.

2.4.1 Alloy - Solidification interval - Amount of residual eutectic liquid

The extent of the solidification interval depends on the principal components of the alloy. Beginning with pure metal (not susceptible to hot tearing), the solidification interval of a A-B binary alloy usually increases rapidly when the quantities of the B atoms of the alloying element increase. Further addition of the alloying element will result (in the case of binary systems with eutectic and a partition coefficient $k<1$) in a continuous drop in the solidification interval from the maximum solubility in the α phase to the eutectic composition. In general, an alloy having a wide solidification interval is considered to be more prone to hot tearing [9,10] and the susceptibility to hot tearing reaches its maximum at approximately the maximum solubility. Although the solidification interval usually decreases almost linearly between the maximum solubility and the eutectic composition, the hot tearing phenomenon has already started to diminish. Based on this fact, the increase of the content of residual eutectic liquid proved to be beneficial [6,9,29].

2.4.2 Trace Elements

The effects of trace elements or impurities are detrimental because during solidification the strong segregation will cause the remaining liquid to be much below the equilibrium temperature of the alloy. Indeed, sulfur and phosphorous are known [2] to promote hot tearing in the steel industry. In addition, below the true solidus temperature, undesired

trace elements could also form brittle, plate or needle-like phases at grain boundaries. This could prevent the usually strong increase in elongation immediately below the solidus temperature [13]. Trace elements could also reduce the surface tension of the interdendritic residual liquid. Consequently, the hot tearing susceptibility increases because of the improved wetting [21].

2.4.3 Casting design - Geometry of the hot spot - Strain rate

During solidification, the first solidified material induces, due to shrinkage, stress or pressure on the hot spot. When the hot spot itself solidifies completely, its own shrinkage is accommodated by the surrounding thin sections in which tensile stresses develop. Since the thermal expansion coefficient and the low ductility of a volume element in the solidification interval are set values, the risk of hot tearing can only be reduced if the thin contracting zones are as long as possible. The tensile stress can therefore be distributed over a larger number of liquid films [2,3]. The strain rate is recognized as the determining factor for hot tearing [2].

2.4.4 Grain size - Residual melt distribution

During solidification, a coarse grain size or a columnar structure shows considerable segregation at the grain boundaries; this leads to the formation of deep notches [13] or partial melting [10]. In addition, the mobility of large grains is limited or restrained within the solidifying network and reduces the duration of the mass feeding stage. The free movement (rotation) of the large or elongated grains within the residual eutectic liquid is limited. Indeed, larger grains cause mechanical interactions (coherency) to take place earlier in time; this results in a larger solidification interval.

The equalization of the concentration across the microstructure is difficult to achieve because of the long diffusion paths. Lower hot tearing propensity associated with the extent of grain refining was determined by many different techniques and approaches [6,9, 10,14,29]. It has been mentioned [9] as an explanation that the improved strain properties could be associated with crystal rotation, displacement or slippage.

Hot tearing resistance could only be improved by a reduction in grain size in the case where good wetting conditions exist between the residual eutectic liquid and the solid grain. On the other hand, bridging can take place between the grains in the early stage of solidification if the residual liquid is restricted to the grain corners and edges [16,17,21]. During this particular condition, the matrix can accommodate a considerable amount of strain.

2.4.5 Gas content

Gas content has been the subject of an investigation by Lees [9], who studied many aluminum alloys and found that the effect of dissolved gas was to reduce hot tearing in specific alloys which have a relatively high eutectic content. In fact, gas rejected from solution during solidification reduces the linear shrinkage or contraction [6]. In addition, the gas rejection sets up an internal pressure sufficient to force liquid eutectic into incipient tears. The effect of gas rejection during solidification is stronger on alloys with larger solidification intervals. However, a reversed effect could be that the generated gas pressure forces the replenishing eutectic liquid away from the tip of the tear.

2.4.6 Healing of incipient tear

Hot tearing can be healed if the quantity of eutectic liquid is sufficient during the last stage of solidification. The flow resistance in the interdendritic channels, which are growing with increasing solid fraction, can hinder the healing process of incipient tears [7]. The interdendritic melt transport and the feeding mechanisms during solidification are described by others [15,91]. The dendrite coherency defines the transformation from mass feeding to interdendritic feeding. Flow resistance through the dendrite network is described by the filtration laws [91] (i.e., Kozeny-Carman equation: permeability, Darcy's law: flow through porous media).

2.5 Development of Stresses and Strains

The stresses and strains which might develop when a metal is cooled down from the solidus (or eutectic) temperature, T_s, are briefly described in this section. However, the

complex phenomena occurring in the mushy zone during the solidification process will be neglected. It is assumed that the newly formed solid is free of stress and strain, i.e., the solidification shrinkage was accommodated properly by the proper feeding mechanisms.

Consider first the simple thermo-elastic situation (Figure 50) to illustrate the change taking place during cooling. It is assumed that the solid previously formed is already at room temperature, T_o. Cooling of the newly formed solid layer from T_s to T_o, would normally generate a thermal contraction ΔL given by $\alpha(T_o - T_s)$, ($\Delta L < 0$), where L is the length of the plate and α the linear coefficient of thermal expansion. Without the base material, this contraction would correspond to a thermal strain (Figure 50b) given by $\varepsilon^{th} = -\alpha(T_s - T_o)$. If the already cold material cannot deform, then the overall deformation of the newly formed layer must be zero. In other words, the elastic deformation ε^{el} must compensate for the thermal deformation estimated before ($\varepsilon^{el} = -\varepsilon^{th}$) and residual stresses will build up (Figure 50c). In this ideal elastic case, the residual stress will be given by $\sigma = E\varepsilon^{el} = E\alpha(T_s - T_o)$, where E is Young's modulus.

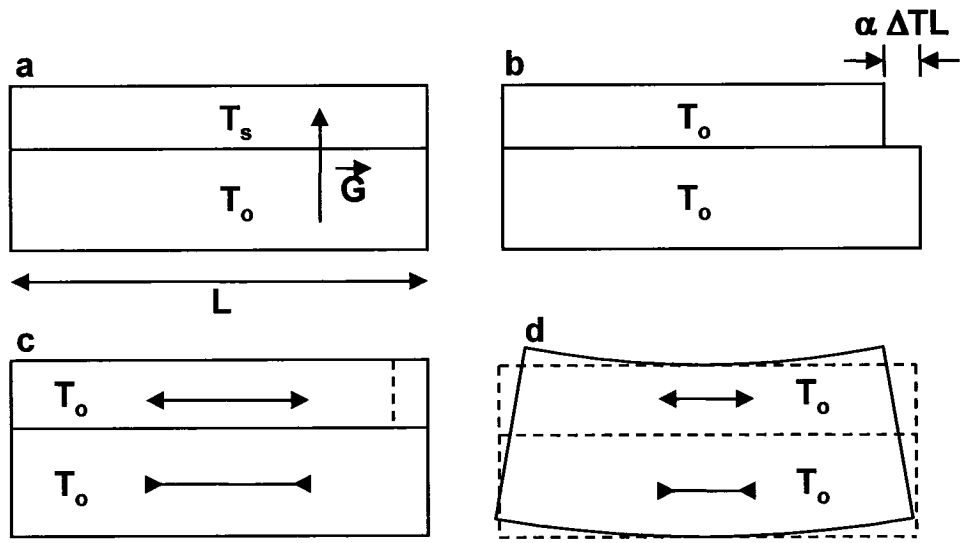

Figure 50: One-dimensional thermo-mechanical situation

Consequently, the surface layer is in tension whereas the base material is in compression. In the case where the plate and the new surface layer are allowed to deform, both deformation and residual stresses will be observed (Figure 50d). This non-symmetric temperature situation induces a bending of the test specimen as a result of the equilibrium of both forces and momentum.

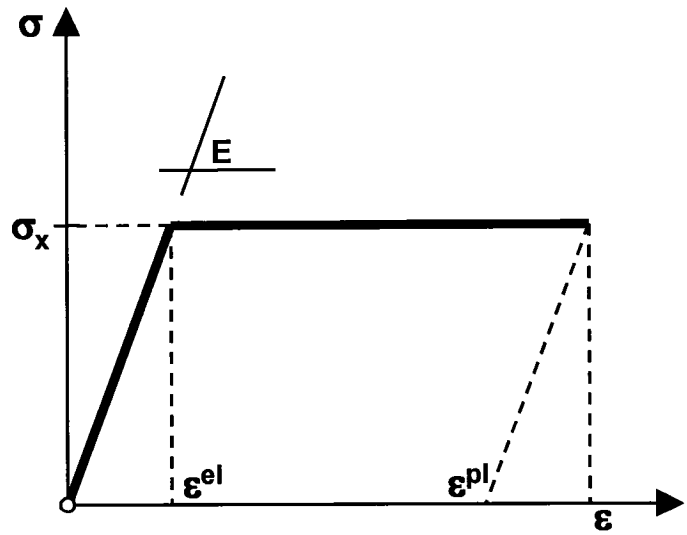

Figure 51: Ideal visco-elastic behaviour of a material

Creep mechanisms (nearly-instantaneous plasticity is included in this definition) will tend to relax stresses. For example, if the new layer has the ideal elastic-viscous behaviour (Figure 51) while the base plate cannot deform, it will have a final residual stress given by the yield stress limit, σ_Y (providing this limit was reached during cooling). The remaining deformation given by $\alpha(T_s - T_o) - \sigma_Y/E$ will be accommodated by plastic strains (i.e., slight change in the thickness of the newly formed layer).

In a general situation, the strain tensor $[\varepsilon]$ or the strain rate tensor $[\dot{\varepsilon}]$ of the material can be decomposed into four components [92] given by Equation 9.

$$[\varepsilon]=[\varepsilon]^{th}+[\varepsilon]^{el}+[\varepsilon]^{pl}+[\varepsilon]^{tr} \text{ or } [\dot{\varepsilon}]=[\dot{\varepsilon}]^{th}+[\dot{\varepsilon}]^{el}+[\dot{\varepsilon}]^{pl}+[\dot{\varepsilon}]^{tr} \qquad \textbf{Equation 9}$$

where the suffix *th*, *el*, *pl*, and *tr* are the thermal, elastic, plastic and transformation contributions to strain or strain rate, respectively. The first three components of the strain tensor are associated with the simple one-dimensional situation (Figure 50). The last component is the contribution associated with the volume change during solid state transformation (e.g., austenite-ferrite transformation).

The thermal strain is a diagonal tensor given by Equation 10.

$$[\dot{\varepsilon}] = \alpha \dot{T} [I] \qquad \textbf{Equation 10}$$

where $[I]$ is the identity tensor and $\dot{T}$ the cooling rate. The elastic strain can be related to the stresses using the elastic tensor $[E]$ (Hook's law) given by

$$[\sigma] = [E][\varepsilon]^{el} \qquad \textbf{Equation 11}$$

The strain rate component related to phase transformation has the same diagonal form as the thermal strain rate. In this case, the evolution of the volume fraction of the phase transformed, $\dot{f}^{tr}$, replaces the cooling rate and is given by Equation 12.

$$[\dot{\varepsilon}]^{tr} = \frac{1}{3} \dot{f}^{tr} \frac{\Delta V^{tr}}{V} [I] = \frac{1}{3} \dot{f}^{tr} \Delta\varepsilon^{tr} [I] \qquad \textbf{Equation 12}$$

where $\Delta\varepsilon^{tr}$ is the normalized volume change associated with solid state transformation. Finally, the plastic strain rate is supposed to occur through creep mechanisms. It can be related to the deviatoric part of the stress tensor, $[s] = [\sigma] - 1/3\ [\sigma]\ [I]$, using a Norton-Hoff law (Equation 13):

$$[\varepsilon]^{pl} = A \left(\frac{\sigma_{eq}}{\sigma_Y} - 1 \right)^{1/m} \frac{3\ [s]}{2\ \sigma_{eq}} \qquad \textbf{Equation 13}$$

where "A" and "m" are two parameters (fluidity and strain rate sensitivity coefficient [13]), σ_{eq} is the von Mises equivalent stress (Equation 14):

$$\sigma_{eq} = \sqrt{\frac{3}{2} \sum_{i,j} s_{ij}} \qquad \textbf{Equation 14}$$

The Equations 8 to 14 have to be complemented by the equation describing the equilibrium of forces (Equation 15):

$$div[\sigma] + \rho g = 0 \qquad \textbf{Equation 15}$$

where ρg is the volumetric force associated with gravity. Providing the appropriate boundary conditions and the cooling history, Equations 8 to 15 allow the calculation of deformation and the residual stresses of any domain cooled from high temperature. Such calculations were used by Drezet [85,86] for the determination of stresses during Direct Chill (DC) casting of aluminum alloys.

2.5.1 Strain Concentration

Pellini's theory may be quantified by the following [15] simple steps. Consider a casting in which both ends are restrained from moving. During cooling from the liquidus temperature, T, the casting having a length, L, and a coefficient of thermal expansion, α, will contract by $\alpha\Delta TL$. If this contraction is concentrated over a hot spot of length l, then the thermal strain in this region is given by $\varepsilon^{th} = \alpha\Delta TL/l$. It is clear that because the deformation is assumed to occur preferentially in the weakest part of the casting, the thermal contraction is magnified by a factor of L/l in the hot spot regions.

In addition, it is also necessary to consider the number of grain boundaries on which the total amount of strain will be acting. The finer the grain size is, the more widely distributed will be the strain. Assuming that the average grain size is, ϕ, then the number of grains in the length, l, of the hot spot is, l/ϕ. The strain acting at each grain boundary is given by $\varepsilon_b = \alpha\Delta TL\phi/l^2$. This simple quantification indicates clearly that reduced temperature differences, smaller overall length between hot spots, and finer grain size all contribute to reducing the strain.

2.5.2 Stress Concentration

Guven and Hunt [93] have measured the stress in solidifying Al-Cu alloys. Although the stresses are small, they are real and a release of stress is shown each time a crack forms. Another stress which might be present could be hydrostatic tensile stress in the liquid phase. However, the hydrostatic stress may contribute to the nucleation of a pore that would assist in the nucleation of a tear. Nevertheless, it has been mentioned [15] that the presence of hydrostatic stress is clearly not a necessary condition for the formation of a tear. Hot tearing is the result of uniaxial tensile stress. It is important to

mention also that because of the creep of the solid at high temperatures, any stress will be dependent on the rate of strain. In fact, the faster that strain is forced into the solid, the higher is its resistive stress.

2.5.3 Hot tearing model based on a critical deformation rate

A new criterion was developed by Rappaz [95] and is based upon a mass balance over the liquid and solid phases. This criterion is most probably the only one taking into account the complex interaction between the tensile deformation and liquid /solid interactions. This model is based on the same principle as the one presented by Feurer [94] which considers a lack of feeding during the solidification and the deformation related to shrinkage and/or applied by the process, e.g., constrained casting. It basically stipulates that a hot tear initiates when the pressure difference generated by the overall mechanical and shrinkage deformation reaches a critical value equal to or greater than the pressure required to generate a cavity. Figure 52 shows the schematic formation of a hot tear between the columnar grains as a result of localized strain with the pressure in the interdendritic liquid during solidification.

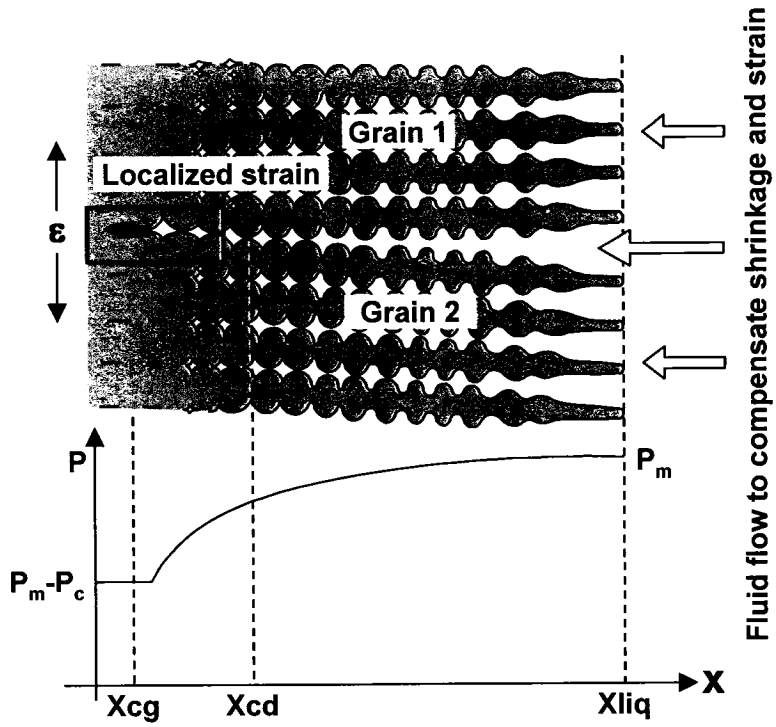

Figure 52: Schematic of the formation of a hot tear between columnar dendrites (Rappaz [95])

The dendrites are assumed to grow directionally in a given temperature gradient (*G*) and with a velocity (*V*) equal to the speed of the liquidus isotherm. The dendritic network is submitted to a tensile deformation rate ($\dot{\varepsilon} = d\varepsilon / dt$) perpendicular to the growth direction. The flow of liquid should compensate for the overall deformation when there is no hot tear. The liquid inflow is related to the pressure gradient in the liquid using the well known Darcy's law that considers the permeability of the mushy zone.

The liquid must be able to feed the zone experiencing deformation to prevent hot tearing. Consequently, during solidification and deformation, the pressure (Figure 52) decreases from the metallostatic pressure, P_m, at the dendrite tips. If the pressure falls below a critical pressure or cavitation pressure, P_c, a void may form (hot tear initiation). Therefore, a hot tear will appear when the critical pressure is reached according to the following:

$$\Delta P_{max} = \Delta P_{\varepsilon} + \Delta P_{sh} < \Delta Pc = P_m - P_c \qquad \textbf{Equation 16}$$

where ΔP_{ε} and ΔP_{sh} are the pressure drop coming from the imposed deformation and the shrinkage, respectively.

Considering the pressure gradient in the liquid obtained from Darcy's law along with the Carman-Kozeny [15,91] approximation and that the deformation is uniform, the following expression is obtained.

$$\Delta P_{max} = P_L - P_O \qquad \textbf{Equation 17}$$

$$\Delta P_{max} = \frac{180}{\lambda_2^2}\frac{(1+\beta)\mu}{G}\int_{T_S}^{T_L}\frac{E(T)f_S(T)^2}{(1-f_S(T))^3}dT + \frac{180}{\lambda_2^2}\frac{v_T\beta\mu}{G}\int_{T_S}^{T_L}\frac{f_S(T)^2}{(1-f_S(T))^2}dT \qquad \textbf{Equation 18}$$

where :
- μ: Liquid viscosity
- β: Shrinkage factor
- λ_2: Secondary dendrite arm spacing (SDAS)
- T_L: Temperature at the dendrite tips
- T_S: Temperature at the dendrite roots

$E(T)$: Cumulated deformation rate

P_L and P_O are the pressure at the tip and at the roots of the dendrites, respectively, over which the expression is integrated, i.e., over the entire length of the mushy zone. The integral over the length of the mushy zone has been replaced by the temperature to introduce the temperature gradient (G), f_S and E are two functions of T as given below.

By combining, Equations 16 and 17 the maximum deformation rate ($\dot{\varepsilon}_{p,\max}$) before a hot tear nucleates at the roots of the dendrites can be obtained,

$$F(\dot{\varepsilon}_{p,max}) = \frac{\lambda_2^2}{180}\frac{G}{(1+\beta)\mu}\Delta P_c - \nu_T \frac{\beta}{1+\beta}H \qquad \textbf{Equation 19}$$

with

$$F(\dot{\varepsilon}_p) = \int_{T_S}^{T_L} \frac{E(T) f_S(T)^2}{(1-f_S(T))^3}\, dT\,; \qquad \textbf{Equation 20}$$

$$E(T) = \frac{1}{G}\int f_S(T)\,\dot{\varepsilon}_p(T)\, dT\,; \qquad \textbf{Equation 21}$$

and,

$$H = \int_{T_S}^{T_L} \frac{f_S(T)^2}{(1-f_S(T))^2}\, dT \qquad \textbf{Equation 22}$$

Using these equations, it is possible to establish the maximum strain rate that can sustain the mushy zone (semi-solid) before a void is nucleated at the roots of the dendrite. The hot tearing phenomena will take place when the strain rate is larger than the maximum established. Using the above approach, one can derive a hot cracking sensitivity index (HCS) of the alloy in terms of the maximum strain rate at the deepest part of the mushy zone before a void is formed, i.e., a hot tear is initiated. The HCS index is assumed to be proportional to $1/\dot{\varepsilon}_{p,\max}$. The HCS index is one of the most used or referred to in the literature so far and is able to reproduce the well publicized λ-curve.

The main limitations associated with the present criteria are:

a) predicting the void formation (hot tear initiation) and not propagation

b) that the cavitation pressure is according to capillarity force, i.e., $\sigma = 2\frac{\gamma}{r}$

c) assuming that the deformation of the solid network is known

d) no contraction of the solid phase

e) solid fraction limit is 0.98 if less than 2 percent eutectic form

2.5.4 Hot tearing model based on a stress limit

A model based on the maximum stress limit was first developed by Drucker [96] to analyze the mechanical response of an idealized semi-solid body. The body was assumed to be made of equally spaced regular hexagonal cylinders representing the columnar structure of the primary solid phase. Drucker [96] derived an expression (Equation 23) for the average stress at the onset of deformation ($\varepsilon = 0$) in terms of strain rate, viscosity and fraction solid.

$$\sigma = \frac{\sqrt{3}\mu\dot{\varepsilon}a^3}{h^3} \qquad \textbf{Equation 23}$$

The expression given by Drucker [96] is able to predict the stress as a function of the strain rate as given by the following:

$$\frac{h}{a} = \sqrt{3}\left(\frac{1-f_S^m}{f_S^m}\right) \qquad \textbf{Equation 24}$$

Figure 53 shows the idealized structure at different strain levels used to derive the model associated with the resistance of the liquid film. The model from Drucker [96] was extended by Lahaie [99] to predict the average stress at different levels of strain (Equation 25). In order to physically model the deformation of a semi-solid, an idealized microstructure was used.

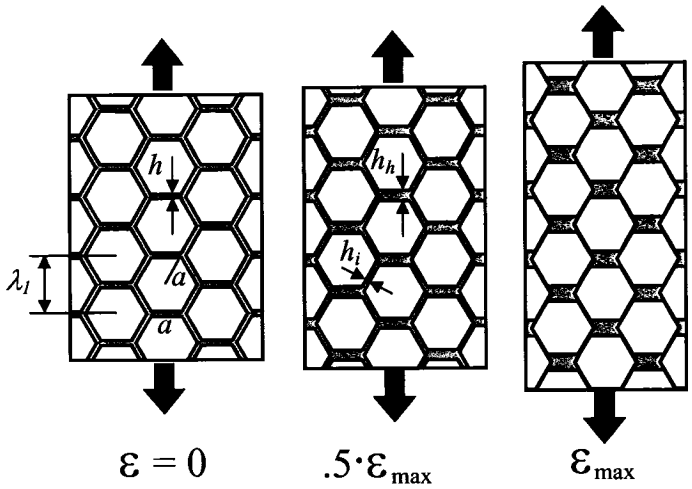

Figure 53: Schematic of the idealized microstructure with h<<a [96,99]

The microstructure is assumed to be composed of solid and mechanically rigid hexagonal grains of size a with a uniformly distributed viscous liquid having a thickness h separating the grain network (Figure 53).

During the deformation, the idealized grain is not deformed and the liquid migrates from the inclined channel into the horizontal ones. The structure is completely locked when the maximum strain, ε_{max}, is reached. When a tensile strain rate, $\dot{\varepsilon}$, is applied, the semi-solid body will deform by local viscous flow of the intergranular liquid. The average tensile stress, σ generated by this process is given by:

$$\sigma = \frac{\mu\dot{\varepsilon}}{9}\left(\frac{f_S^m}{1-f_S^m}\right)^3\left[\left(1-1/2\left(\frac{f_S^m}{1-f_S^m}\right)\varepsilon\right)^{-3}+2\left(1+\left(\frac{f_S^m}{1-f_S^m}\right)\varepsilon\right)^{-3}\right] \qquad \textbf{Equation 25}$$

where μ is the Newtonian viscosity of the liquid, ε is the tensile strain, f_S is the solid fraction and m represents a microstructural parameter having the values of 1/2 and 1/3 that represent the columnar and equiaxed microstructures, respectively. This viscous flow mechanism will terminate at a maximum strain, ε_{max}, such as defined by:

$$\varepsilon_{max} = \frac{2}{\sqrt{3}}\left(\frac{h-h_{lim}}{a}\right) \qquad \textbf{Equation 26}$$

where $h_{\lim}$ is the limiting film thickness on the inclined channels (Figure 53). At this point, the liquid films in the horizontal channels will be constrained and the semi-solid will deform by dilation according to the following equation:

$$\sigma = \frac{2 f_S^m K_T^{-1} \varepsilon}{3\left(1+(\varepsilon_{max}-1) f_S^m\right)} \qquad \textbf{Equation 27}$$

where K_T is the isothermal compressibility of the liquid. As the stress builds up in the semi-solid body, there will be a competition between the deformation mechanisms described previously and fracture processes such as hot tearing. The criterion for fracture by hot tearing was based on the force necessary to separate the two solid surfaces connected by a capillary liquid film. The criterion is given by

$$\sigma_i = \frac{4\gamma_{l/g}}{3h} \cdot \left(1+\left(\frac{f_S^m}{1-f_S^m}\right)\varepsilon\right)^{-1} \qquad \textbf{Equation 28}$$

where $\gamma_{l/g}$ is the surface tension of the liquid/gas interface.

This model gives the hypothesis that all the deformation is accommodated by the liquid and no re-arrangement of the dendrites and no liquid inflow are proposed. In addition the only metallurgical parameter used in the equation is related to the grain structure which is either columnar or equiaxed. Other metallurgical criteria should be added to better understand the close relationship with tensile strength resistance. The model shows that the stress evolution is closely related to the liquid fraction and film thickness.

2.5.5 Summary of the literature survey

The shrinkage-brittleness theory was first advanced by Verö [7] and stipulated that tearing was caused by the contraction strains of the primary dendrites during cooling between the liquidus and solidus. The first new theory to explain the mechanisms of hot tearing is undoubtedly attributed to Pellini [2] and co-workers [3]. They suggest that hot tearing is caused by localized strains, generated by thermal gradients that tend to pull

apart solid masses of material separated by essentially continuous films of liquid (segregated residual melt).

The generalized theory proposed by Borland [5,16,17] attempts to explain the mechanisms of hot tearing as a combination of the "Shrinkage-Brittleness Theory" and the "Strain Theory". The main objective was to modify and extend both theories. Basically, the generalized theory suggested that the distribution of liquid is largely influenced by the solidification mode, ratio of the interphase (solid-liquid) and intercrystalline boundary energies and the effect of solute elements. The most important reason for determining alloy susceptibility to hot tearing is first to allow theories to be assessed, and then to enable predictions to be made about the alloy behaviour in industrial casting and welding situations.

In general, the test methods are designed to induce stresses by external factors in order to produce hot tearing. These factors are: a) restraint of metal contraction caused by moulds or cores, b) restraint of contraction caused by the casting, and c) temperature gradients or "hot spots" operating in conjunction with restraint of contraction.

Ohm and Engler [62-65] represents the first and only documented attempts to measure the stress and strain at the surface of a casting chilled by a metallic mould. However, there are needs to simulate more precisely the phenomena occurring in vertical DC casting such as the heat transfer conditions, the mould filling stage, the metal head, the horizontal solidification and associated solutal convection in order to reproduce the associated conditions and microstructural features. This original approach is the subject of the present work which is presented in more details in the following chapters. It is worth to note that in the light of the tensile property results from the literature, it seems that when the liquid phase content is typically below 15% and above a certain level, a stress in the order of 1 MPa and elongations generally less than 1% are expected in metallic systems. Constitutive relationships were proposed by many authors to correlate their data but most ignored the influence of strain in the semi-solid range. As pointed out by Martin et al [69], the introduction of strain effects is desirable to perform predictions in situations like continuous casting, where strains may not be sufficiently high to induce failure. Considering the very low strains obtained at failure when fraction liquid is typical to what is encountered in hot tearing situations, it is clear that predictions of failure will require constitutive relationships including strain and covering the loading stage.

Attempts to predict hot tearing susceptibility as a function of composition for binary alloys is considered to be the most useful work. However, there are relatively few usefully predictive models and it is difficult to derive a satisfactory theoretical description from decades of research on hot tearing (e.g., lambda curve by Feurer [75]). An advanced formulation of a hot tearing criterion is given by Flender [71] after their studies on computer simulation and modeling of hot tearing, the behaviour of the residual liquid, the mobility of the grain, and the melt system under stress.

Mathematical models that predict the evolution of temperature, stress, and strain fields in metals have become an important tool in obtaining a better understanding of the processes and in optimizing them. An approach was proposed by Chandra [75,77] for the prediction of hot tears in castings. The proposed methodology is divided into several parts (grain size, thickness of the liquid film, and fracture criterion). Yet another constitutive equation that described the hot tearing mechanisms is given by Rappaz [95]. The latter also propose a hot tearing criterion based on a cavitation threshold that creates a defect on which hot tears do initiate. The calculation methods can be made significantly more difficult by taking into account factors such as, phase transformation, segregation of alloying and trace elements, grain size and distribution, and wetting. However, it is recognized that the model from Rappaz [95] represents one of the most classic models that take into account the liquid movement and solidification contraction.

The present model derived from Lahaie [99] shows that the stress evolution is closely related to the liquid fraction. It gives also the hypothesis that all the deformation is accommodated by the liquid and no re-arrangement of the dendrites and no liquid inflow are proposed. In addition the only metallurgical parameter used in the equation is related to the grain structure which is either columnar or equiaxed. Nevertheless the model can be used to predict the onset of hot tearing in a similar way to the Rappaz [95] model. Continuous improvement of these phenomenological models and relationships with more precise metallurgical phenomena could certainly improve them.

Chapter 3: DCSS Experimental Procedure

3.1 Introduction

The majority of the tests described in Chapter 2 are related to the bulk of the alloy and are not concerned with the problem of shell zone formation and characteristics. In addition, these approaches do not take into account the real and unique features of the solidification process during DC casting such as the cooling rate, microstructure evolution, or stable/metastable phase formation. In fact, the definition of the true hot tearing temperature and the correlation of stress direction and crystal growth direction or grain boundary orientation become difficult. Figure 54 shows a diagram of the nucleation and crystal growth of commercially pure aluminum in a DC casting [112]. The primary nucleation of crystals takes place upon contact of the molten metal with the mould wall. The crystals that are formed first are equiaxed. The latent heat resulting from the nucleation and grain growth causes recalescence and no new nucleation sites are formed. Crystals with a favourable orientation grow against the heat flow in a columnar fashion (coarse and elongated grains).

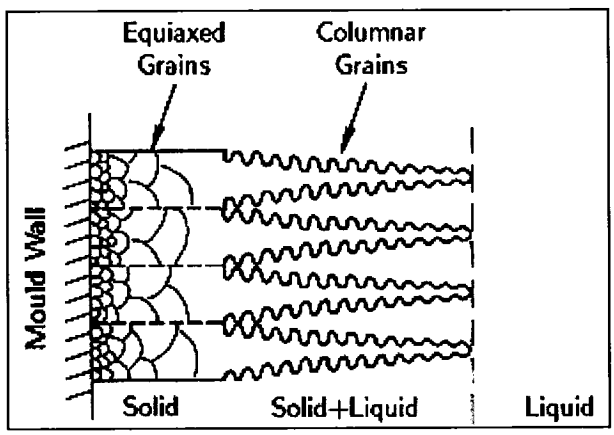

Figure 54: Diagram of Solidification of Commercially Pure Aluminum in a DC Casting [112]

The need to define both the precise dependence of hot tearing on the alloy system and process parameters and the mechanisms responsible for this dependence requires an experimental approach which is able to reproduce and/or simulate attributes

(i.e., microstructure, mechanical quantities) encountered during DC casting of an aluminum ingot.

The new approach consists of solidifying a volume element reproducing the shell zone of a DC cast ingot and measuring its mechanical resistance as a function of physical (e.g., cooling rate, superheat) and chemical parameters (e.g., alloying elements, trace elements, grain refiner and modifier). The objective is to explain the mechanisms responsible for the change in the mechanical resistance to hot tearing.

The solidification apparatus is built to simulate the primary solidification taking place during DC casting. The experimental concept is based on the solidification of a volume element that produces a similar microstructure observed at the surface of a DC ingot. The novelty consists of having a pool of liquid metal maintained at a specific temperature prior to solidification. The solidification unit rotates to make liquid metal contact the chill plate. This allows better control of metal superheat and produces a smooth solidified surface. The unit is built to simulate an air gap (heat accumulation), metal level (metallostatic head) and to mimic mould filling (container rotation) observed during DC casting.

The force acting on the solidifying material is essentially tensile with a tensile stress perpendicular to the heat extraction. This ensures that the tensile stress is applied in a direction also perpendicular to the growth axis of the columnar crystals which contribute to the mechanical strength of the shell.

3.2 Experimental Set-Up

This novel experimental approach was developed specifically to study the surface hot tearing during DC casting of aluminum. The experimental set-up is dubbed DCSS for Direct Chill Surface Simulator. The DCSS acronym will be used throughout the thesis to refer to the experimental set-up. The DCSS was developed to better quantify the hot tearing susceptibility of aluminum alloys and to assess their castability as a function of alloying element addition and grain refiner. The main goal was to obtain quantitative measurements by providing fundamental information such as mechanical properties. The latter are essential to improve mathematical models and to predict and develop more reliable hot tearing criteria.

The DCSS is composed of a conventional horizontal tensile testing machine (Tinius-Olsen™) on which a unique solidification unit is installed (Figure 55). Basically, the solidification unit consists of a specifically designed container of refractory material and a chill plate.

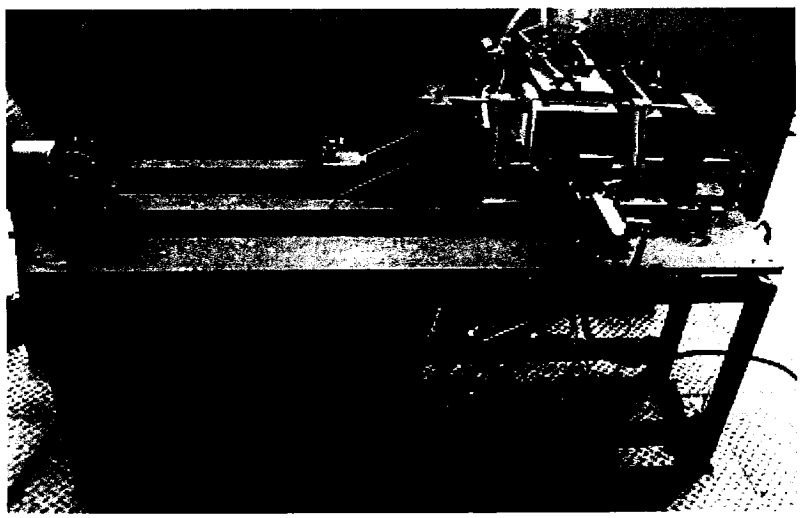

Figure 55: DCSS Unit built on a Tinius Olsen™ horizontal tensile testing machine

The DCSS was designed to process a representative volume of aluminum (approximately 2 kg) and to record the mechanical resistance of the shell zone during deformation and as it solidifies. Temperature history of the solidifying metal is also recorded to determine physical and metallurgical values (e.g., temperature gradient, cooling rate, solidification front velocity). The thermocouples are inserted and secured into the container base during the initial preparation. The temperature history is recorded at different positions from the surface towards the centre of the casting. Three thermocouples are typically located at 5, 10, and 15 mm. Their exact positions are determined after the experiments using X-ray or during metallographic examination. Figure 56 shows an X-Ray of a torn sample from which the exact thermocouple positions are determined. The thermocouple positions were determined for each experiment and used in the numerical model to derive the temperature profile and solid fraction distribution.

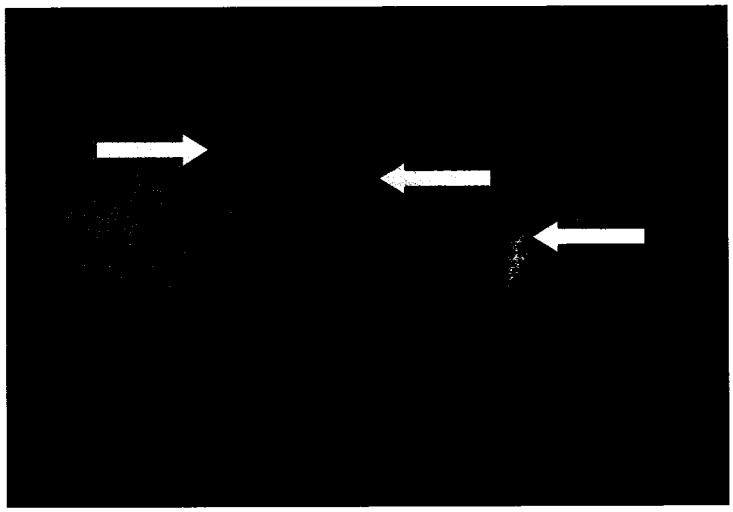

Figure 56: X-ray indicating each thermocouple position (arrows)

The experimental concept includes a better metal temperature control, a more uniform chilled surface, and the capability to instantaneously record temperature and load measurements. Other features of the experimental set-up include a computer interface program to adjust the testing parameters and experimental data acquisitions, e.g., temperature and load. Figure 57 shows a specific window of the computer interface program and buttons to access other menu and adjust parameters accordingly.

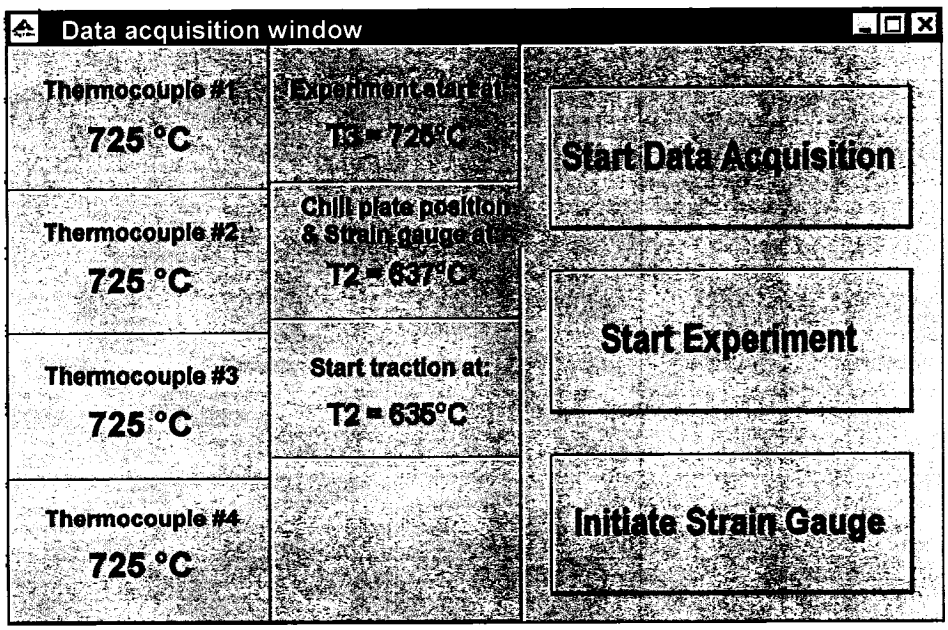

Figure 57: Computer control interface (Data acquisition window)

The criteria for starting the tensile test are based on previously determined thermal and metallurgical values (solid fraction vs. temperature, solidification front velocity, etc.).

The specific criteria are entered into a dedicated control interface program, which controls the solidification and loading sequence. This ensures optimum repeatability for starting temperature by eliminating bias associated with manual operation. The temperature and load data are acquired simultaneously.

The DCSS is engineered to allow anchors to be positioned and used to apply and measure tensile stress. The chill plate has similar characteristics as the primary cooling zone of a conventional DC casting mould (i.e., material, cooling intensity, microstructure features). Figure 58 shows a diagram of the experimental approach with anchors positioned in the sample. The apparatus integrates a directional solidification unit into a horizontal tensile testing machine. The solidification unit is composed of a refractory container closed in one direction by an aluminum chill plate, which is water cooled and whose surface is prepared to simulate the primary cooling intensity of a conventional DC casting mould.

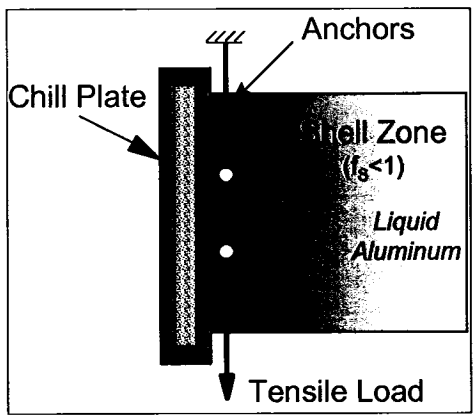

Figure 58: Diagram of the Experimental Concept

The inner lateral walls of the container are covered with ceramic fiber blankets (Koawool™), which allow axial displacement of the test specimen with a minimum of interference. This is made possible because of the small displacement experienced during the test and the fact that the ceramic fiber blankets do not oppose a high mechanical resistance to compression in comparison to the stresses applied in the semi-solid material. Figure 59 presents a diagram of the refractory container with the ceramic fiber blankets and the two anchors used to transmit the force to the solidifying specimen.

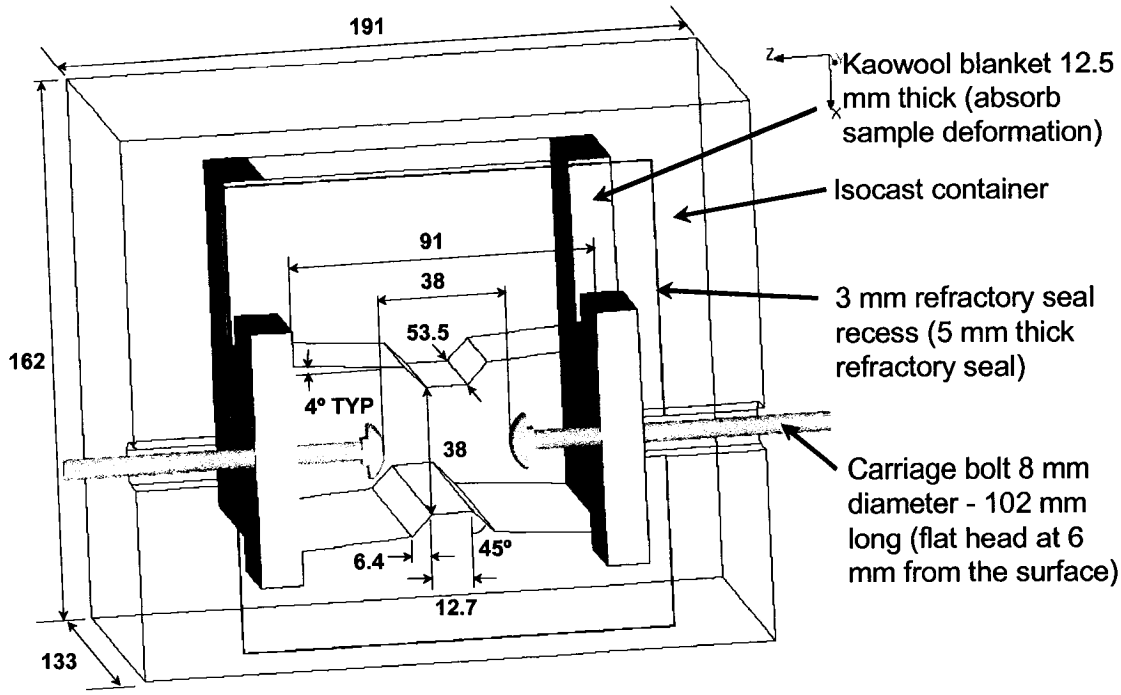

Figure 59: Refractory container with anchors and ceramic fiber blankets (mm)

The container is placed in a pre-heating furnace (Figure 60) until it reaches approximately 725 °C before filling it with superheated molten metal (approximately 100 °C above the liquidus temperature).

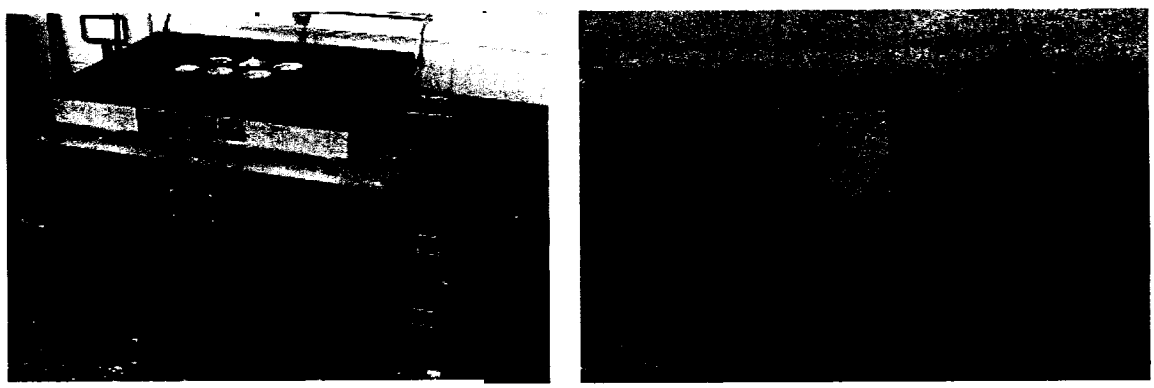

Figure 60: Pre-heating furnace (a) and container (b)

The container and its content remained in the pre-heating furnace until the temperature was stabilized at approximately 25 °C above the testing temperature (750 °C). Preliminary tests indicate that this procedure permits the superheat temperature to be kept within ± 5 °C which allowed enough time to perform the necessary manipulation. As

a matter of fact, the container and its content are transferred from the pre-heating furnace and positioned between the jaws of the tensile tester.

The anchors that will be frozen-in during solidification are carefully positioned (Figure 61). The anchors were installed in their holders to touch the melt prior to installing two small pieces of ceramic fiber blanket that sealed the two small openings by which the anchors reach the jaws. A thin ceramic fiber seal (approximately 5 mm) was positioned on top of the container to prevent liquid metal leakage.

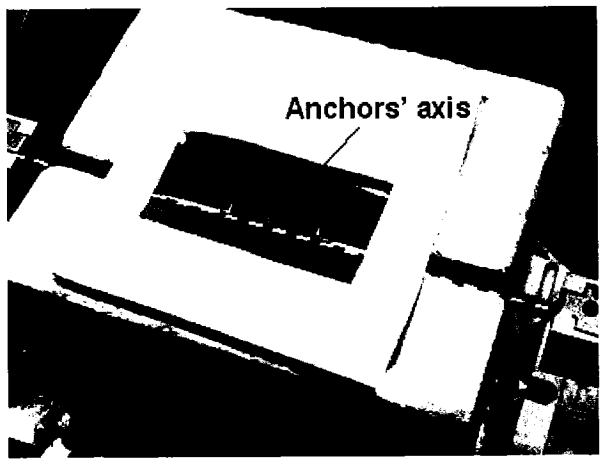

Figure 61: Anchors position and alignment along their axis

The chill plate was sited on top of the ceramic seal to close the container completely and prevent any leakage. Solidification is not initiated at this moment because the chill plate is not yet in contact with the liquid metal. In fact, the solidification unit is designed to rotate 90° around the anchors to put the metal in contact with the chill plate. The rotational motion makes the metal contact the chill plate progressively and simulates the mould filling behaviour encountered during the DC casting operation.

The rotation of the container is instigated automatically when the temperature of the metal at 10 mm from the surface reaches a pre-set value of 725 °C. This causes the liquid metal to contact the chill plate on which solidification begins. The solidification front moves horizontally. The triggering temperature can be easily changed in the control program. Figure 62 shows a diagram of the solidification unit after a 90° rotation as well as the metal head simulated by the calculated volume of liquid metal in the L-shape design. The metal head used during all experiments was approximately 35 mm at the

centre of the test sample, i.e., at the centre of the chill plate in contact with the liquid metal.

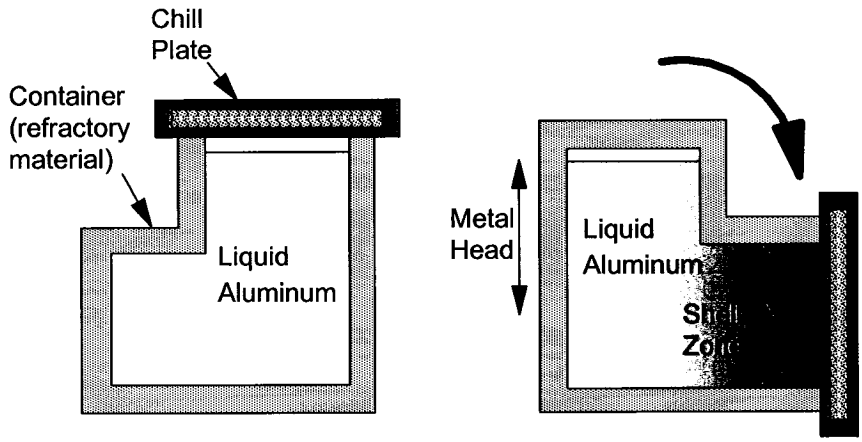

Figure 62: Diagram of the Solidification Unit after a Rotation of 90°

The solidification lasts for a few moments until the melt reaches another triggering temperature that makes the chill plate slide automatically upward to position precisely a small window (1 cm high by 9 cm wide) that exposes the cast surface. The chill plate completely surrounds the window and the solidification is not interrupted during this stage. A limit switch is located at the top of the rail on which the chill plate slides up and down. This switch is used to send a signal that causes the strain gauge probes to be positioned automatically on the cast surface. This arrangement allows the strain to be measured in real time during solidification.

Immediately after the strain gauge is in place, a tensile force, caused by the carriage bolt moving at a constant rate of displacement, is applied on the solidifying shell. The displacement is triggered by a temperature, given by the thermocouple positioned at 10 mm from the surface, corresponding to a solid fraction of 0.95. This temperature related criteria was chosen to ensure that the solid fraction at the surface of the sample remains below unity or above the non-equilibrium solidus.

All temperature criteria used for the different triggering needs were previously determined from thermal analyses of the Al-Si binary alloys. Figure 63 shows the window in the chill plate and the strain gauge equipped with long rods (arrow) to reach the sample surface. The force is measured via the tensile tester load cell measuring the torque, from which the axial force is calculated according to the lever arm's length.

Figure 63: Chill plate with (a) window and, (b) extensometer (strain gauge)

3.3 Testing Procedure

It is worth mentioning that the present section describes the testing procedure and that details regarding the experimental set-up can be found in the appendix section. The tests were conducted by first pouring the melt at 750 °C into the refractory container previously preheated to approximately the same temperature. The tests were conducted on Al-Si binary alloys and three different alloys were tested, i.e., Al-0.5 wt% Si, Al-1.5 wt% Si, and Al-2.5 wt% Si. Figure 64 shows a diagram of the Al-Si phase diagram with the aluminum-rich corner. These compositions were selected to cover the hypoeutectic range of the aluminum binary system where it is well known [75] that the hot tearing sensitivity changes drastically.

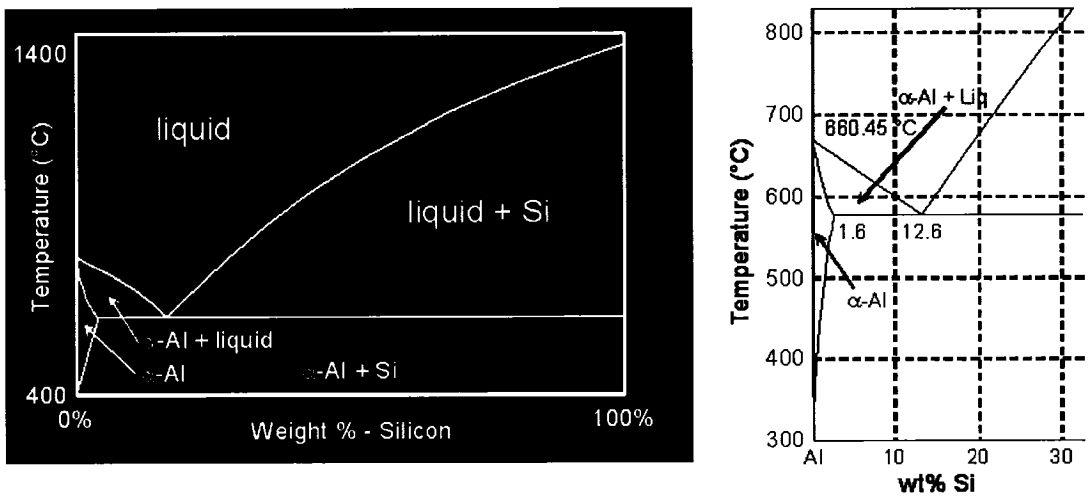

Figure 64: Al-Si phase diagram with the Al-rich corner (right-hand-side)

The alloys were prepared using commercial purity aluminum (99.97 wt% Al) with no grain refiner addition. A sufficient quantity of alloys was prepared in advance to minimize manipulation but also to ensure similar chemical compositions between tests. Approximately 15 kg of Al-Si alloy was melted in a small holding furnace and the container, previously prepared and assembled, was placed in the preheating furnace.

The liquid metal was poured inside the container already placed inside the pre-heating furnace. The container and the liquid metal remained in the pre-heating furnace for a sufficient time to homogenize the temperature. After the target temperature is reached, the container and the molten aluminum was transferred and positioned precisely between the tensile testing jaws.

The melt cooled slowly mainly by conduction through the refractory wall. The unit was rotated 90-degrees to begin solidification when the melt reached the target temperature measured at 10 mm from the surface. Tensile testing started when the temperature at the thermocouple located at 10 mm from the chill plate reached a preset value representing a solid fraction of 0.95 determined from thermal analyses. According to the alloy systems, the preset values selected for the Al-Si experiments were 627 °C (Al-0.5%Si), 573 (Al-1.5%Si), and 572 °C (Al-2.5%Si). The rate of displacement of the actuator was 0.16 mm/s. Other tests with Al-1.5 wt% Si were performed at a different displacement rate to study the impact of the strain rate on the resulting resisting load (tensile strength). The rates of displacement of the actuator were 0.35, 0.72, and 1.39 mm/sec. After the tests, the specimens were investigated by cutting the surface to reveal the torn section and to estimate the load bearing area. This was used later to determine the mechanical resistance (i.e., engineering strength given by the force over the area, F/A) of the solidifying alloys. On some occasions, the torn surface was not visible because of liquid inflow during testing. However, comparison between the section obtained at 10 mm from the surface (i.e., solid fraction of 0.95) and the torn surface shows similar results (approximately ±10% difference). Consequently, the section obtained from the temperature measurement and the exact thermocouple position (X-Ray) was used. In addition the stress-strain curves were determined to compare at different straining conditions the resulting resisting strength of the material being tested.

Chapter 4: Experimental Solid Fraction Determination

Knowledge of the solid fraction evolution as a function of temperature and/or time is of tremendous importance in the study of hot tearing. In fact, the complex interactions between the solid phase and the liquid phase distribution will inevitably reach a critical solidification interval. During this critical solidification interval, the strain and stress accommodated by the microstructure could promote incipient hot tear resulting from grain de-cohesion. Further thermo-mechanical influence would promote the propagation of the hot tear until, in some case, the complete separation of the cast piece or casting occurs.

Consequently, the solid fraction determinations are mandatory for the development of models that best describe the hot tearing behaviour. The solid fraction can be determined by various methods. The most conventional method is from cooling curves analyses, where the temperature history of a specific alloy is recorded and analyzed. The cooling curve is the fingerprint of the alloy and can be used to define the entire solidification path (product reaction for each phase) from liquid to solid. Another way of estimating the fraction of solidifying phases uses mathematical models. Nevertheless, the basis for accomplishing good results with thermodynamic modeling is the quality of the thermodynamic database of individual substances. The assumptions made also contribute to some errors and validation should be done with precise thermal analysis and phase characterization of the material.

In the present work, the solid fractions were determined using a thermal analysis apparatus and results compared against both the Gulliver-Scheil model (no back-diffusion) and the Brody-Flemings expression (diffusive term). The solid fraction determination using these models assumes a unique solidification path related to the temperature field only, even though it can depend also on the cooling rate due to back-diffusion. The main goal was to determine the closest match with the experimental results. The model that showed the best fit was used in the hot tearing theoretical model and for the probabilistic microstructure model to derive the relaxation coefficient (RC). In fact, the use of a thermodynamic model greatly facilitates the solid fraction determination for different alloy system.

It should be noted that the thermal history and metallurgical parameters can be extracted from experimental data, and better describe the solid fraction evolution during the time interval of solidification. This is crucial information that further refines existing numerical models and improves predictives capability.

4.1 Thermal Analysis

The thermal analyses of the three aluminum-silicon alloys were performed using a standard apparatus that was first described by Backerud [112]. Figure 65 shows the apparatus which consists of a perforated cylinder made to hold a small steel cup (approximately 100 g of liquid aluminum) in its cavity. The perforated cylinder is used to force air into the cavity and change the cooling rate of the sample. The cooling rates could be varied from approximately 0.1 to 5 °C/sec. A cooling rate of 1-2 °C/sec has been used in this work to determine the solid fraction. This represents the average cooling rates observed in the shell zone of the DC cast ingot at approximately 5-10 mm from the surface.

Two thermocouples are used in order to determine the temperature gradient and the coherency point. The latter indicates the temperature at which the microstructure starts to bridge and develop some mechanical resistance. Owing to the fact that the coherency point is the beginning of the bridging between dendrites, it is still too early in the solidification process for hot tears to develop.

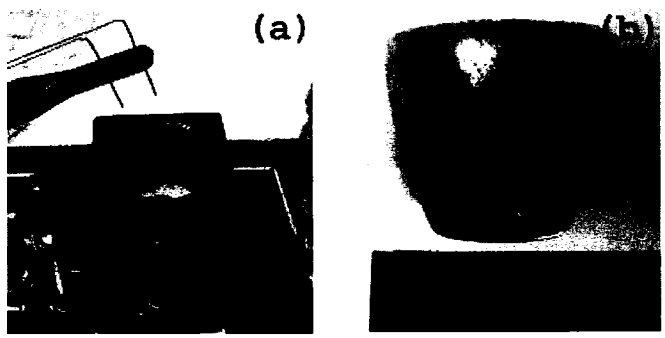

Figure 65: Thermal analysis (a) set-up and (b) sample

This was observed during the DCSS experiments where strength started to develop at a solid fraction above about 0.95. This is far from the coherency point determined from the

twin thermocouples used in the set-up. The coherency point is derived from the maximum temperature difference recorded between the thermocouple positioned near the wall and the one at the centre of the sample.

Two K-type thermocouples (1/16 "-diameter, shown on Figure 65) were mounted on a holder that can be precisely positioned (radial and vertical) in the melt. One thermocouple is located at the exact centre of the small steel crucible and the other is placed very close to the wall. The technique allows precise measurements of the temperature evolution during solidification. The resulting curves are used to derive the solid fraction and other values such as the coherency point.

4.1.1 Thermal analysis curves

The experimental solid fraction values were determined by thermal analyses and used as inputs in the numerical model, ProCAST™, to better reproduce the thermal fields in the solidifying section. This gives also the solid fraction evolution in the solidifying section that can be compared with interrupted experiments and physical values such as solid front position can be calculated. The results obtained with the thermal analyses were compared with different thermodynamic models. The Brody-Flemings expression (Scheil-modified equation) gave the best match and therefore was selected to be incorporated and used in the analytical models (cellular automata, and the thermo-mechanical models). This approach is easier and faster to compute the solid fraction when the alloy system permits it (binary alloys) or is changed to make a sensitivity analysis on variables (e.g., alloy composition).

The solid fraction was determined from the cooling curves by using a three step approach: i) the first derivative of the cooling curve is calculated, b) a zero-curve is computed between the beginning and the end of solidification, and c) the solid fraction is determine from the integral of the area contained between the zero-curve and the cooling curve. The derivative allows identifying not only the solidification boundaries but also the position of possible reaction compounds (solidification path). Figure 66 shows an example of the cooling curve along with the first degree derivative and the zero-curve.

Figure 67 shows the solid fraction curves obtained from the thermal analyses of the Al-0.5%Si, Al-1.5%Si and Al-2.5%Si, respectively. The change in the liquidus temperature

as well as the inflection point for each system can be seen. In addition the increase in the solute content (Si) caused the isothermal eutectic plateau to be longer (higher eutectic portion) before reaching unity (i.e., completely solid).

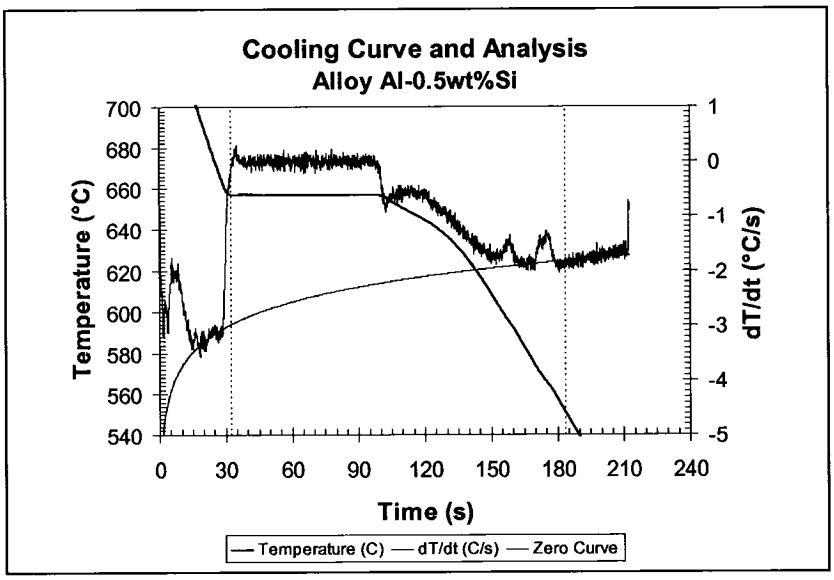

Figure 66: Example of the cooling curve and subsequent treatment (derivative)

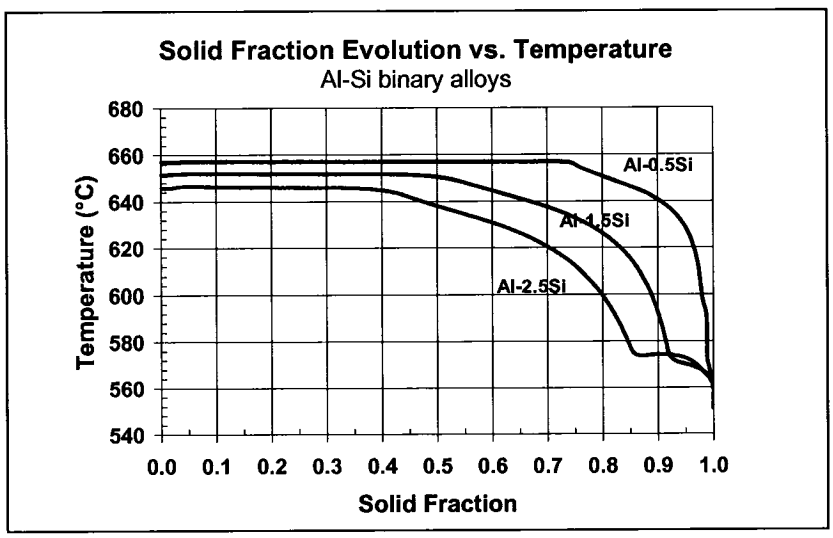

Figure 67: Solid fraction determined from thermal analyses

From the information that can be extracted from the cooling curves, the coherency point is of certain interest. Indeed, the coherency temperature gives information regarding the feeding behaviour of the alloy. Figure 68 shows the coherency point given by the largest temperature difference (i.e., peak of the dT curve) reading between the centre and the

wall thermocouple. The temperature at which dendrites begin to interact will affect the overall capacity to eventually feed any incipient hot tear.

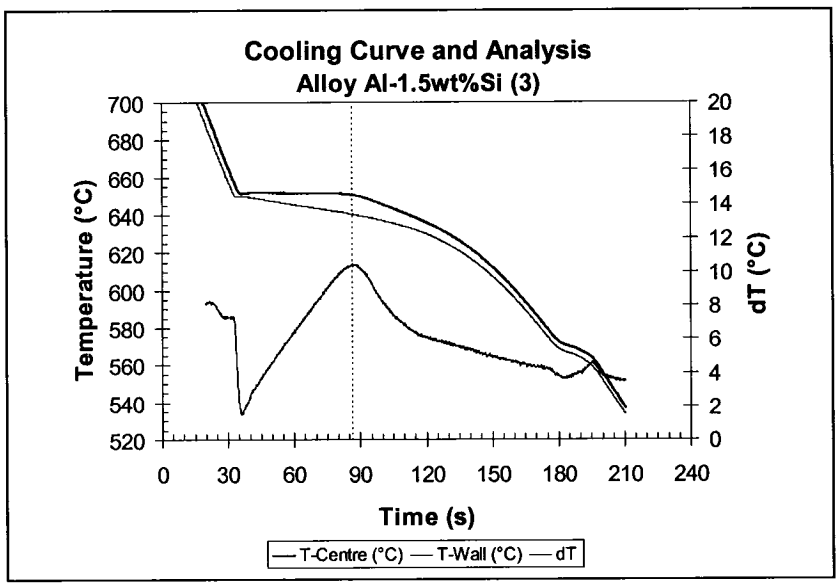

Figure 68: Cooling curves and coherency point (ΔT peak)

Figure 69 shows the coherency temperature as a function of the silicon concentration. It is seen that the coherency temperature for a given alloy corresponds to a different solid fraction. The latter will change the feeding mechanism that takes place during the solidification.

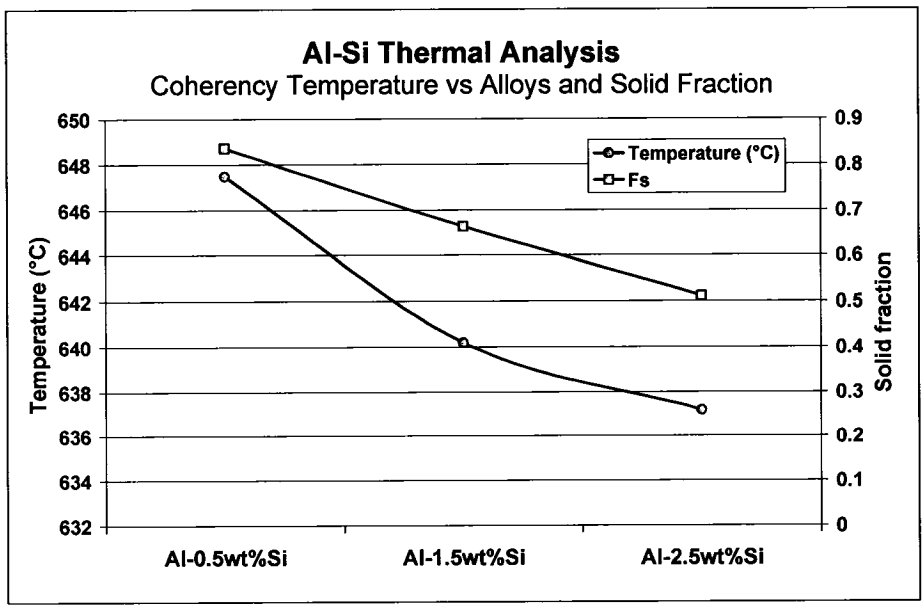

Figure 69: Coherency temperature vs. alloy systems

The corresponding solid fractions for each coherency temperature imply mass and liquid feeding ($0.4 < f_S < 0.9$). However, one can say that the feeding mechanism will be affected depending on the temperature interval at the coherency point.

Figure 70 shows that the Al-1.5wt%Si exhibits the largest temperature difference at the coherency point. This corresponds also to the alloy showing the highest hot tearing propensity. A larger temperature difference indicates a tendency to have more solid network bridging that might prevent liquid movement and feeding during the critical stage.

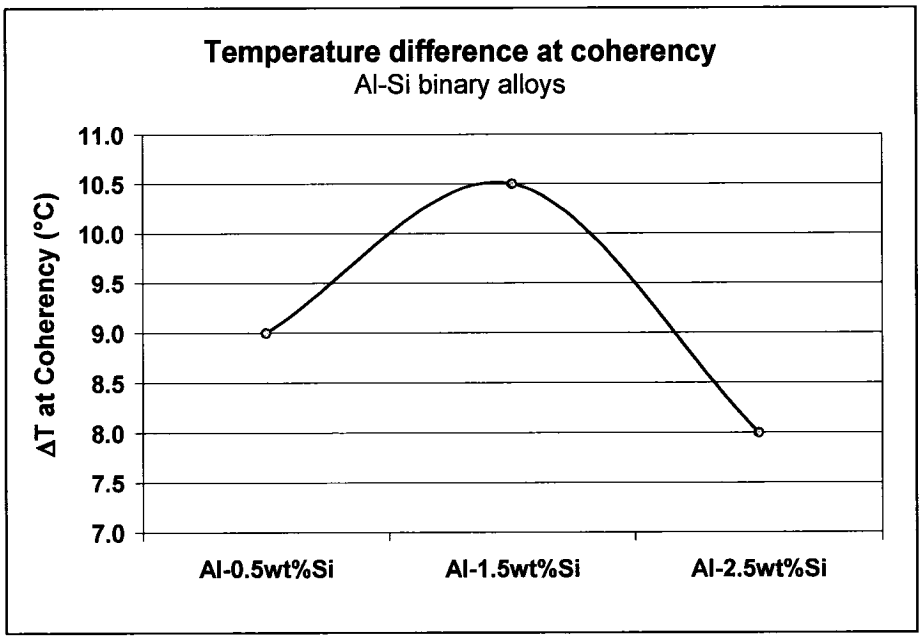

Figure 70: Temperature difference at coherency point

4.2 Lever rule

During extremely slow cooling, thermodynamic equilibrium allows a complete diffusion of all solute elements and the phase composition is homogeneous. For equilibrium solidification described by the lever rule and with linear liquidus and solidus lines (Figure 71) the partition coefficient can be determined by $k = C_S / C_L$ where C_S and C_L are the equilibrium solute composition of the solid and liquid in weight percent, respectively.

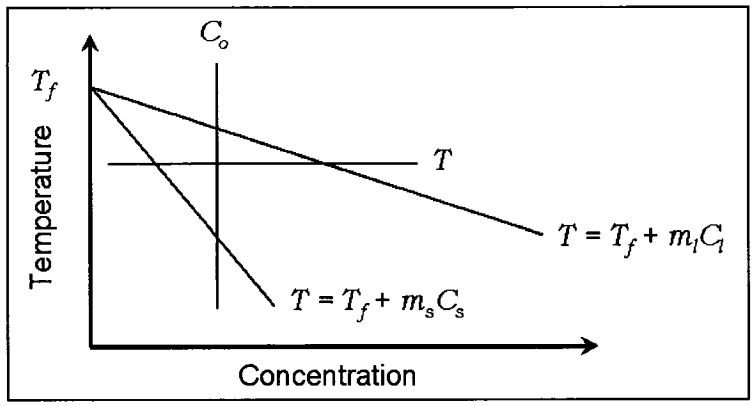

Figure 71: Portion of a phase diagram

The partition coefficients for aluminum alloys are generally below unity (k<1), this implies that the liquid is always enriched during solidification, i.e., the liquid is richer in solute elements than the solid primary phase. Consequently, the solid fraction transformed (f_S) is given by:

$$C_S = \frac{k\ C_o}{f_S\ (k - 1) + 1} \qquad \textbf{Equation 29}$$

where k is the partition coefficient and C_o is the composition of the original liquid alloy. This can be rearranged to obtain:

$$f_S = \left(\frac{1}{1 - k}\right)\left(\frac{T_L - T}{T_f - T}\right) \qquad \textbf{Equation 30}$$

where T is the temperature below the liquidus and T_L and T_S are, respectively, the equilibrium liquidus and solidus temperatures.

However, this condition is not representative of the solidification encountered during DC casting of sheet ingots. A complementary limiting case to equilibrium solidification is to assume that there is virtually no back diffusion (i.e., solute diffusion in the solid phase is small enough to be considered negligible) and that diffusion in the liquid is fast enough to assume that diffusion is complete. There is also a complete mixing in the liquid which has a uniform composition C_L. This relation is the Gulliver-Scheil equation or more simply known as the Scheil model.

4.3 Gulliver-Scheil model

The Scheil model describes relatively well the solid fraction evolution in the case of unidirectional solidification such as experienced in the DCSS unit. For simple binary alloys, the Scheil equation, also known as the non-equilibrium lever rule, can be used for the analytical determination of the weight solid fraction as a function of temperature. The results can been used to obtain high quality input for casting simulations. Figure 72, shows a diagram of the solidification front (solid/liquid) with the corresponding change in solid fraction and concentration after an interval of solidification.

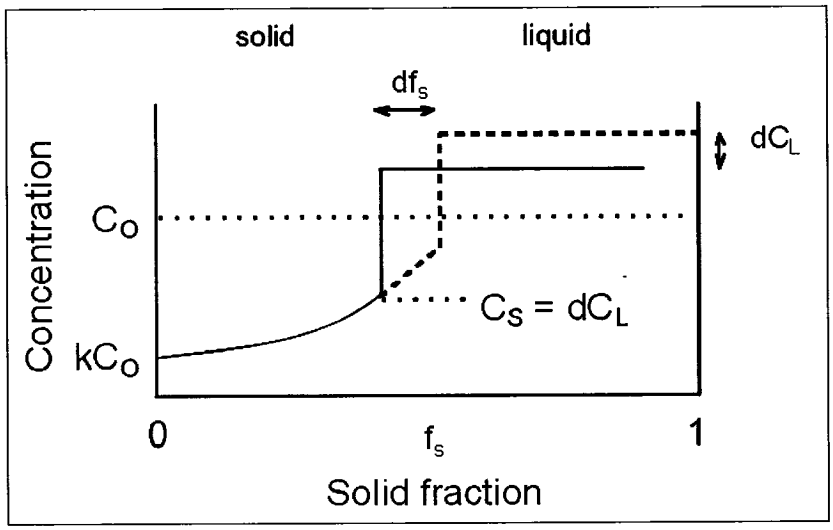

Figure 72: Solidification front moving with complete mixing in the liquid after an interval of solidification (dashed line)

The conservation of solute requires that for a solid fraction, f_S, that has solidified the change is given by:

$$(C_L - kC_L) df_s = (1 - f_s) dC_L \qquad \textbf{Equation 31}$$

and integrating according to the following:

$$\int_0^{f_S} \frac{df_s}{(1 - f_s)} = \int_{C_O}^{C_L} \frac{dC_L}{C_L(1 - k)} \qquad \textbf{Equation 32}$$

The resulting relationship is known as the Scheil Equation.

$$C_S = k\, C_O (1 - f_S)^{(k-1)} \qquad \textbf{Equation 33}$$

The integration from T to T_L will result in the classical Scheil equation:

$$f_s = 1 - \left(\frac{T_f - T}{T_f - T_L} \right)^{\left(\frac{1}{1-k}\right)} \qquad \textbf{Equation 34}$$

where T_L and T_f are the liquidus temperature and the melting temperature of the pure aluminum, respectively.

Thermodynamic database software such as ThermoCalc™, can be used to determine the weight solid fraction in simple and complex multi-component alloy systems. Figure 73 shows the solid fraction determination using the ThermoCalc™ and the Scheil model. The results show the limitations associated with the model where a straight line is drawn when the eutectic temperature is reached. Consequently, this renders difficult any quantitative approach based on the knowledge of the solid fraction evolution to characterize and understand the hot tearing phenomena especially in the solid fraction region ranging between 0.95 and 1.

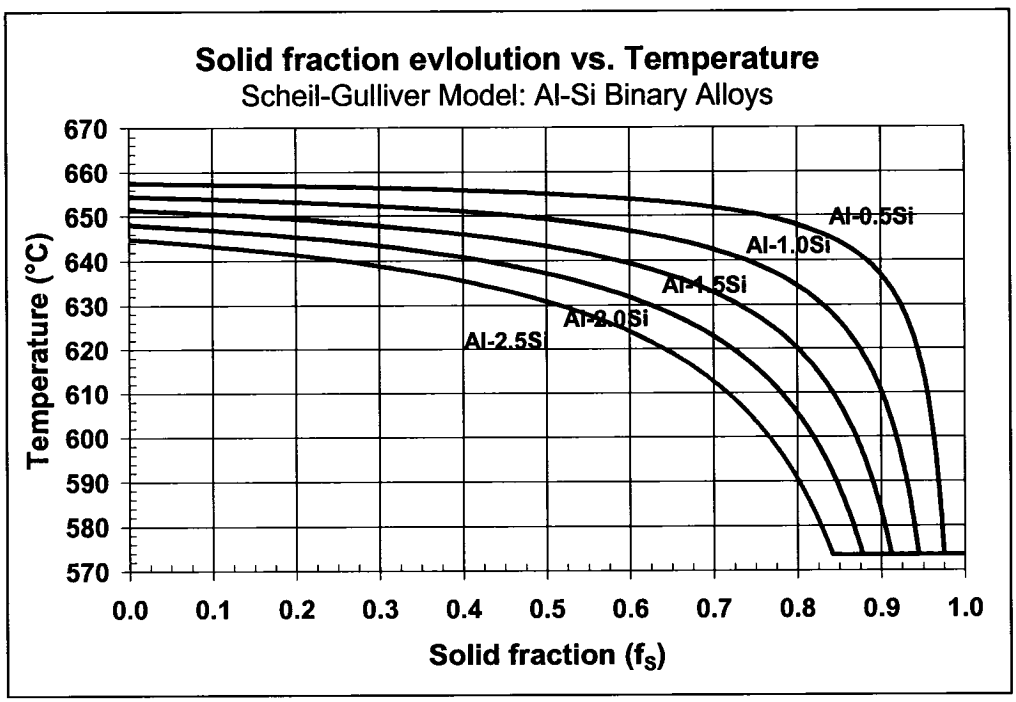

Figure 73: Solid fraction from the Scheil model

Figure 74 shows the impact of back-diffusion on the resulting solid fraction evolution. It can be seen that there is some discrepancy between Dictra™ (Aluminum database from Alcan International Ltd) results and the thermal analysis in the solid fraction ranging from 0 to 0.95. However, the fit is much better in the zone of interest for hot tearing phenomena (i.e., solid fraction above 0.95).

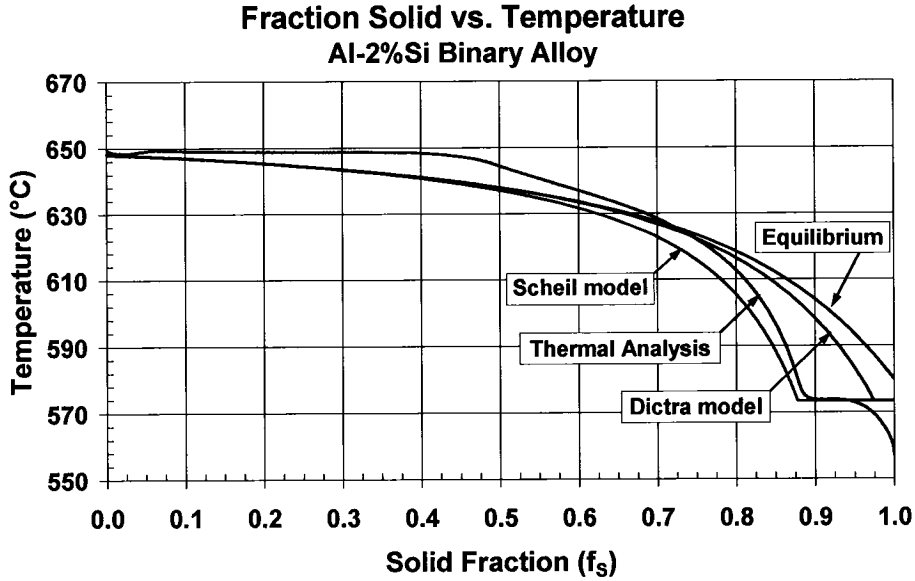

Figure 74: Difference in solid fraction obtained from different methods

The use of models (e.g., Dictra™) that deals with back diffusion greatly reduces the discrepancy between the thermal analysis and the mathematical results, especially in the high solid fraction region. The DICTRA™ calculation was performed using a cooling rate of 1.5 °C/sec and a driving force of 1E-5. The driving force is a variable (DGM) from DICTRA™ related to the temperature gradient according to Equation 35.

$$DGM = \frac{M}{R} \cdot \left(\frac{L \cdot \Delta T}{T \cdot T_m} \right) \qquad \textbf{Equation 35}$$

where;

M : Molar mass, (g/mole)

R : Perfect gas constant (J/K/mole)

L : Latent heat (J/g)

ΔT : Thermal gradient (K)

T : Temperature (K)

T_m : Melting temperature, (K)

Consequently, the mathematical treatment used in the present work is based on the Brody-Flemings expression. The Brody-Flemings expression is basically the standard Scheil equation to which a diffusion term has been added and adjusted to fit the thermal analyses results obtained from the cooling curves. Equation 36 below is the well known expression proposed by Brody-Flemings. This equation takes into account the diffusion in the solid state.

$$f_S = \frac{1}{(1-2\alpha k)}\left\{1-\left[\frac{T_m - T}{T_m - T_L}\right]^{\left[\frac{(1-2\alpha k)}{(k-1)}\right]}\right\} \qquad \textbf{Equation 36}$$

In addition, the coefficient, α, can be adjusted accordingly to better represent the solid fraction evolution during solidification. It should be noted that in the case of no diffusion, i.e., α=0, the Brody-Flemings equation becomes the Scheil equation.

4.4 Solid fraction evolution of commercial alloy systems

Figure 75 shows the thermodynamic calculation of the solid fraction for three different commercial alloys. The traditional derivations of the Scheil and Brody-Flemings equations have severe restrictions when applied to multi-component alloys. It is not possible to derive this equation, using the same mathematical method, if the partition coefficient, k , is dependent on temperature and/or composition.

The binary Scheil-type (Equation 34) is applicable only to dendritic solidification and cannot, therefore, be applied to eutectic alloys. Further, it cannot be used to predict the formation of intermetallics during solidification. Using ThermoCalc™, all of the above disadvantages can be overcome, reducing the need to perform exhaustive thermal analyses. However, the latter becomes necessary, especially in the higher solid fraction range (>0.95) when building coupled thermo-mechanical and microstructure models with

predictive hot tearing capability. This is not part of the present work where the study is more focused on mechanical measurements and hot tearing trends.

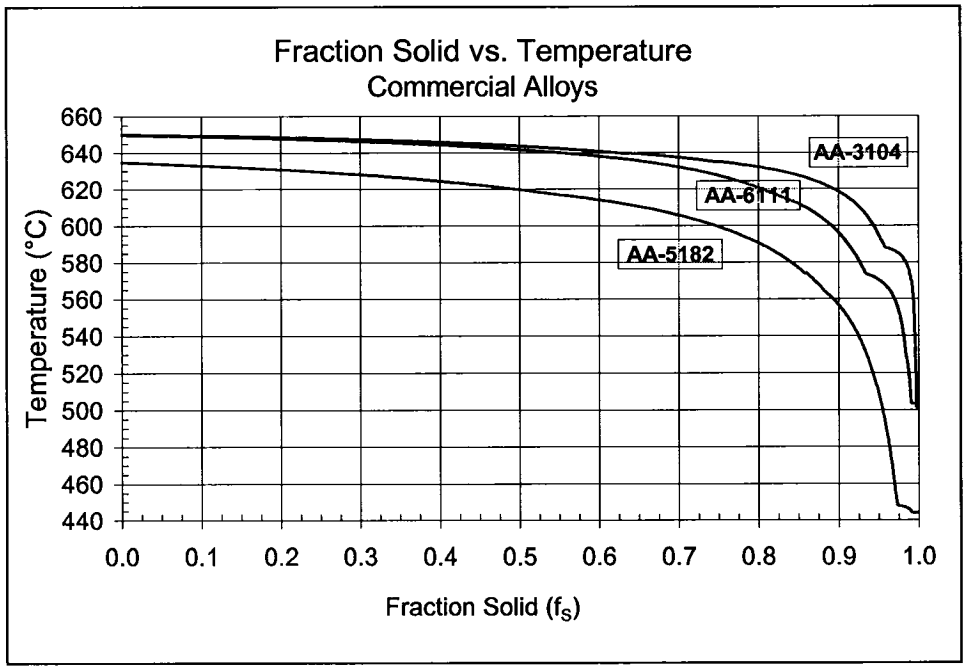

Figure 75: Solid fraction of different commercial alloys

4.5 Volume solid fraction

The change in the quantity of solid is expressed as the weight solid fraction (f_S) or volume solid fraction (g_S). In the present work the volume solid fraction is used for the theoretical model and defined according to Equation 37 below.

$$g_S = \frac{f_S}{f_S + (1 - f_S) * \left(\frac{\rho_S}{\rho_L}\right)} \qquad \textbf{Equation 37}$$

where f_S is the weight solid fraction and ρ_S / ρ_L is the ratio of densities in the solid and liquid phase, respectively, and depends on the composition and temperature of the phases. It is assumed in the present work that the solid and liquid densities are constant but not equal.

Chapter 5: DCSS Experimental Conditions

Numerical simulations were done to verify different aspects related to the DCSS testing procedure. First, the impact of the pre-heating time of the refractory container on the initial temperature was verified to ensure proper testing procedure and test repeatability. Second, the influence of the container rotation speed on the metal free surface movement was simulated to identify the speed that ensures minimum turbulence. This was done also to determine the impact of the liquid metal momentum on the overall heat flux. Third, the extent of heat transfer between the chill plate and the solidifying metal was assessed to determine the sensitivity of the metal/chill plate contact and its impact on solid fraction evolution and distribution across the mushy zone.

The numerical modeling gave many advantages for understanding overall temperature and flow behaviour. Yet another advantage was the ability to improve the testing procedure based on initial parameters and simple temperature measurements.

The modeling work used thermal data obtained from standard testing set-up and conditions using a binary Al-1.5wt% Si. However, no load was applied during tests planned to collect thermal history data only (model input). This preliminary work was intended to identify or confirm that the initial conditions were appropriate.

5.1 Container pre-heating

The heating of the ceramic container (Isocast™) was simulated using the radiative module of the ProCAST™ software package. The container was assumed to be positioned at the center of a plane 25.4 mm above the bottom of a virtual box representing the inner furnace dimensions of 508 x 254 mm x 254 mm. The temperature of the furnace wall was assumed to be uniform and set to 752 °C (i.e., 2 °C above the target temperature to compensate for the typical furnace controller fluctuations). The initial container temperature was assumed to be 20 °C (room temperature).

Figure 76 to Figure 79 show the isotherms generated at approximately 3, 7, 15, and 32 minutes, respectively, within the refractory container material.

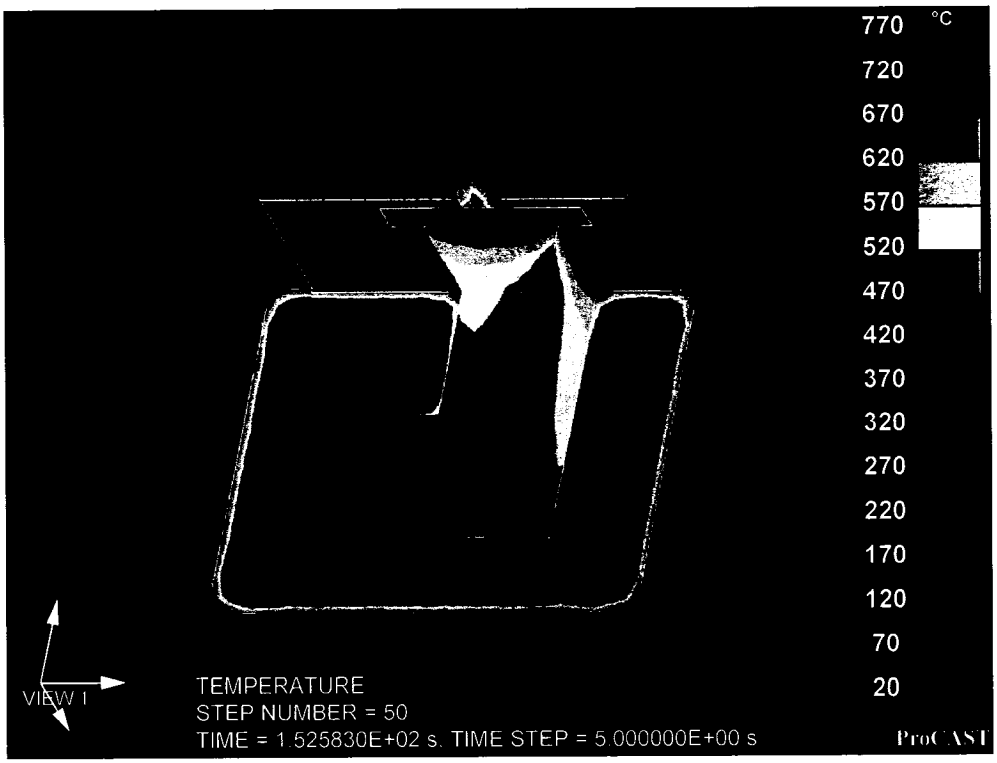

Figure 76: Isotherms after approximately 3 minutes

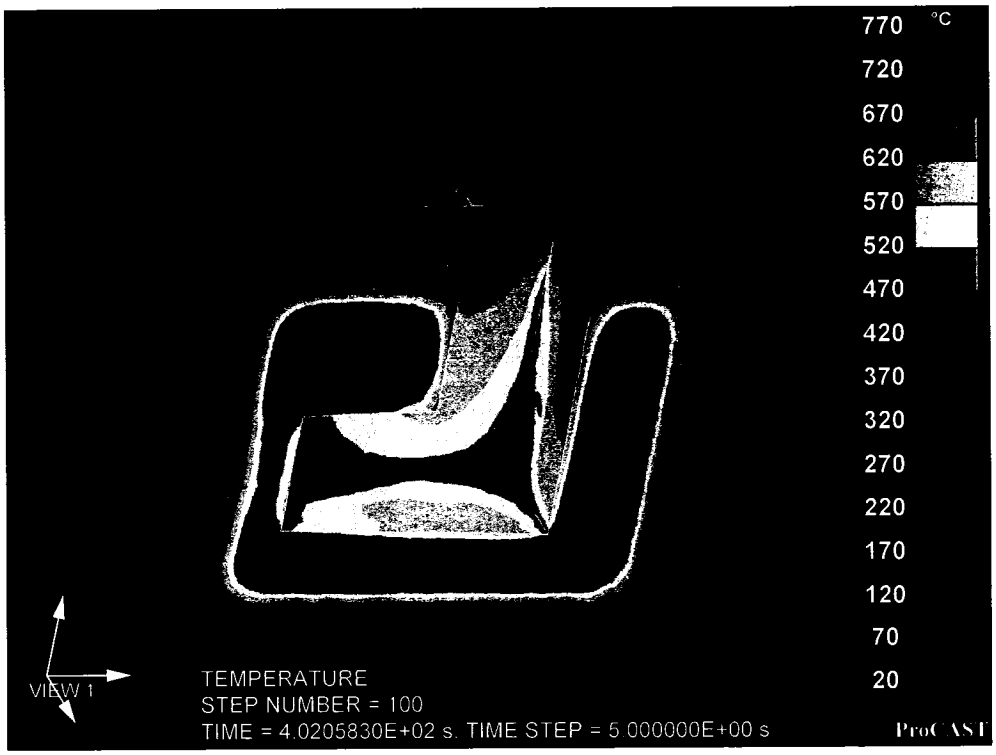

Figure 77: Isotherms after approximately 7 minutes

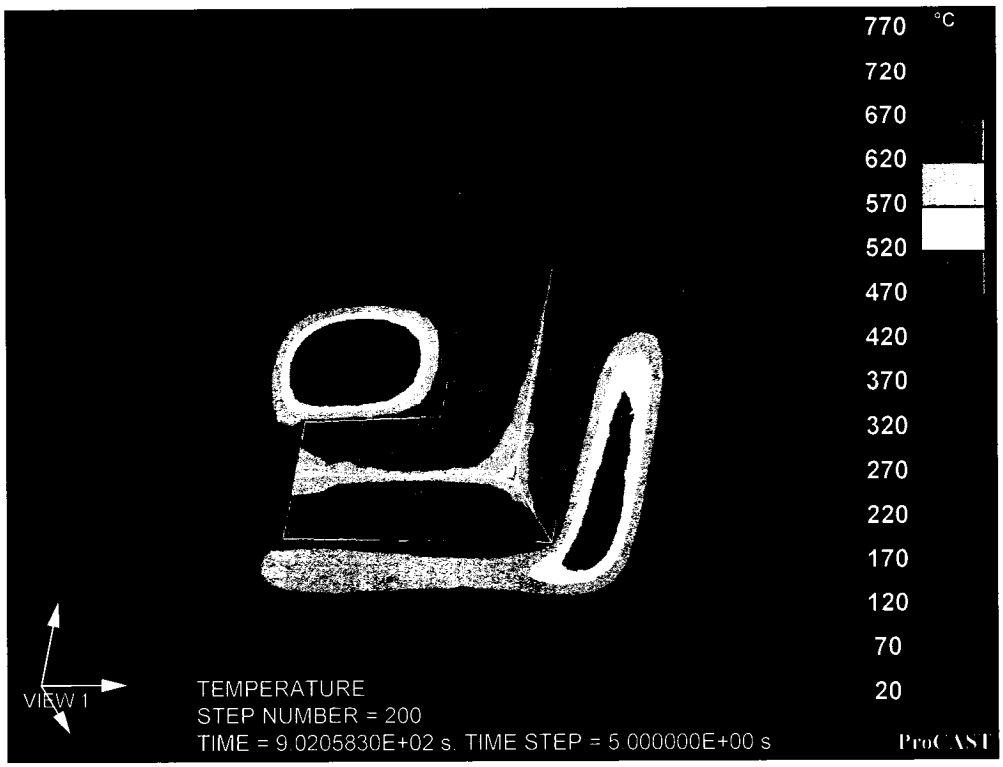

Figure 78: Isotherms after approximately 15 minutes

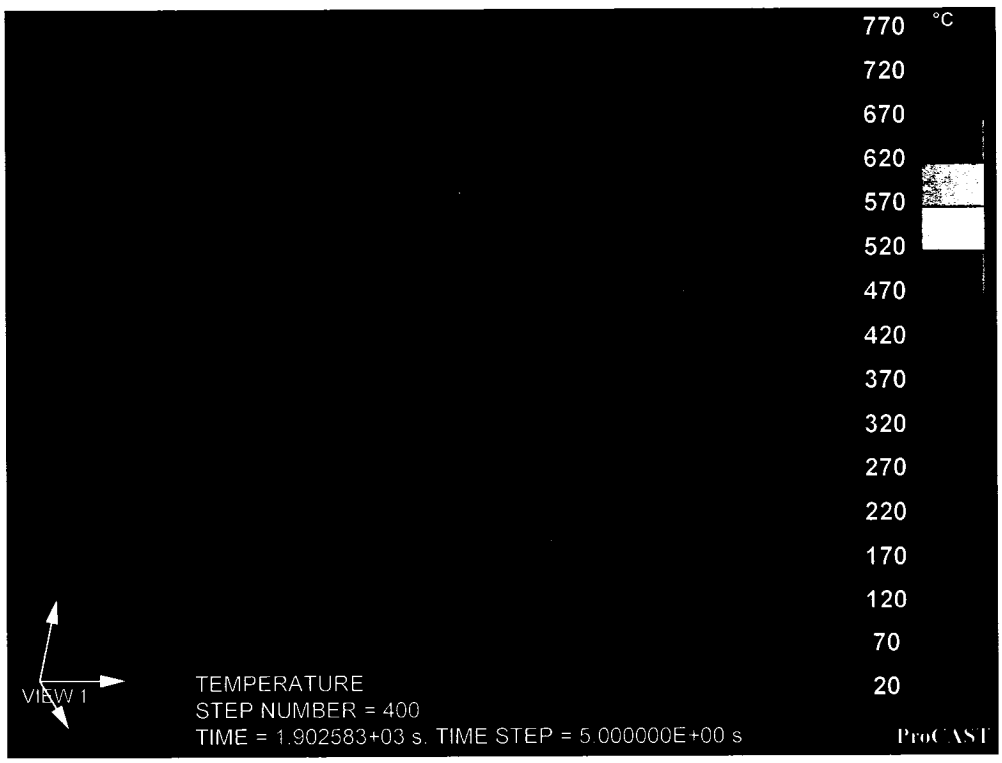

Figure 79: Isotherms after approximately 32 minutes

Figure 80 shows the temperature as a function of time for a point located inside the coldest zone found on the container. It can be seen that a minimum time of 70 minutes is required to obtain a prescribed temperature of 750 °C. It should be noted that this point represents the coolest zone; this means that a uniform temperature condition is achieved after this delay.

Therefore, based on the modeling results the pre-heating was set to 2 hours to achieve a uniform temperature throughout the refractory container and to minimize temperature loss during pouring the liquid metal.

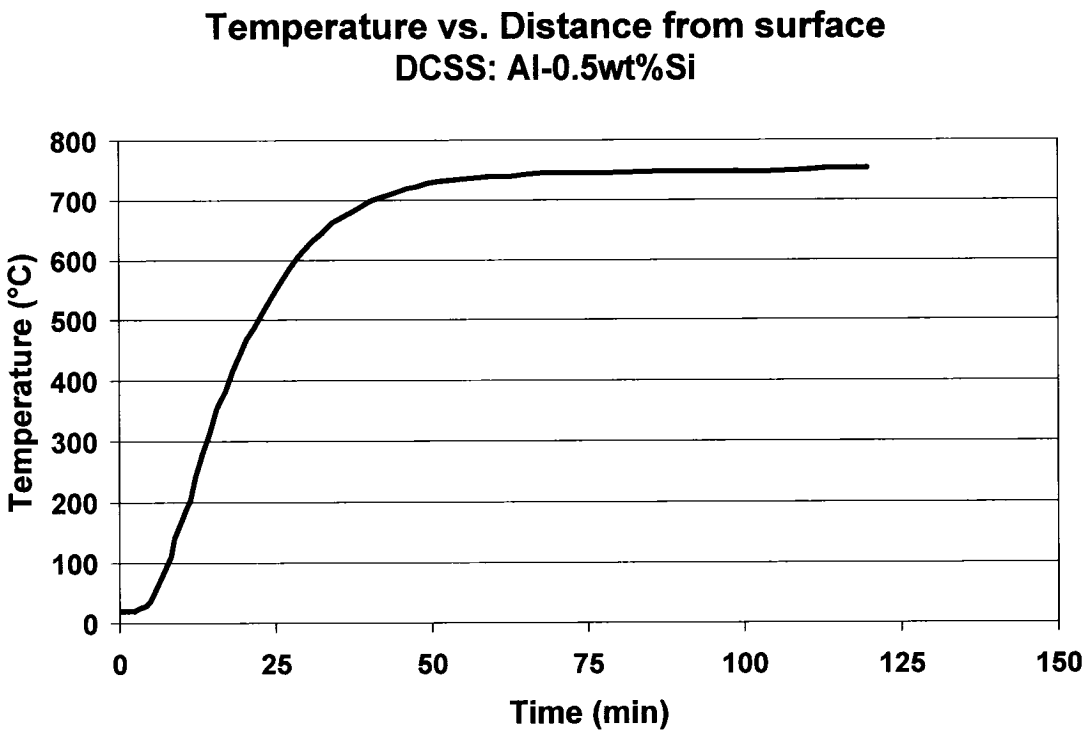

Figure 80: Calculated Heating Curve of the Refractory Container

5.2 Container rotation time and free surface

The rotation speed of the container and its impact on the free surface was simulated using the fluid flow and thermal modules with ProCAST™. The first objective was to analyze the free surface turbulence and to visualize the liquid metal behaviour resulting from the rotation. The second objective was to determine the impact of the rotation speed on the thermal history. Indeed, a fast rotation will cause excessive turbulence and

affect the thermal field and the resulting microstructure. In addition, a very slow rotation will make the solidification front grow unevenly (i.e., wedge-type section) with a thicker section at the bottom (first contact with the chill plate) and thinner at the top (last contact with the chill plate).

The main elements composing the test specimen included the refractory container, the isolating materials, the chill plate with water cooling channels, the anchors and the liquid metal. A planar symmetry was assumed at mid-position perpendicular to the anchors' axis (Figure 61).

The boundary conditions used for the thermal simulation were natural cooling for all external surfaces and a heat transfer coefficient of 42 $W/m^2/K$ with an ambient temperature of 24 °C. Convective heat transfer coefficient was used at the water and the inner wall interface. The convective heat transfer coefficient was obtained from basic heat transfer theory using the dimensionless Nusselt number. The heat transfer coefficient used was 8,000 $W/m^2/K$ and the average water temperature was set to 18 °C. The rotation time is the time required to turn the refractory container 90° around the axis of the anchors from the initial position (Figure 81). Two fluid flow simulations were performed with rotation times of 0.5 and 1 second to evaluate the impact of this parameter on the turbulence generated inside the container. Figure 82 to Figure 86 show the resulting liquid metal movement experienced using the fastest rotation time of 0.5 second and the growing solidification front expressed as solid fraction evolution ranging.

Figure 81: Initial condition at time=0 sec

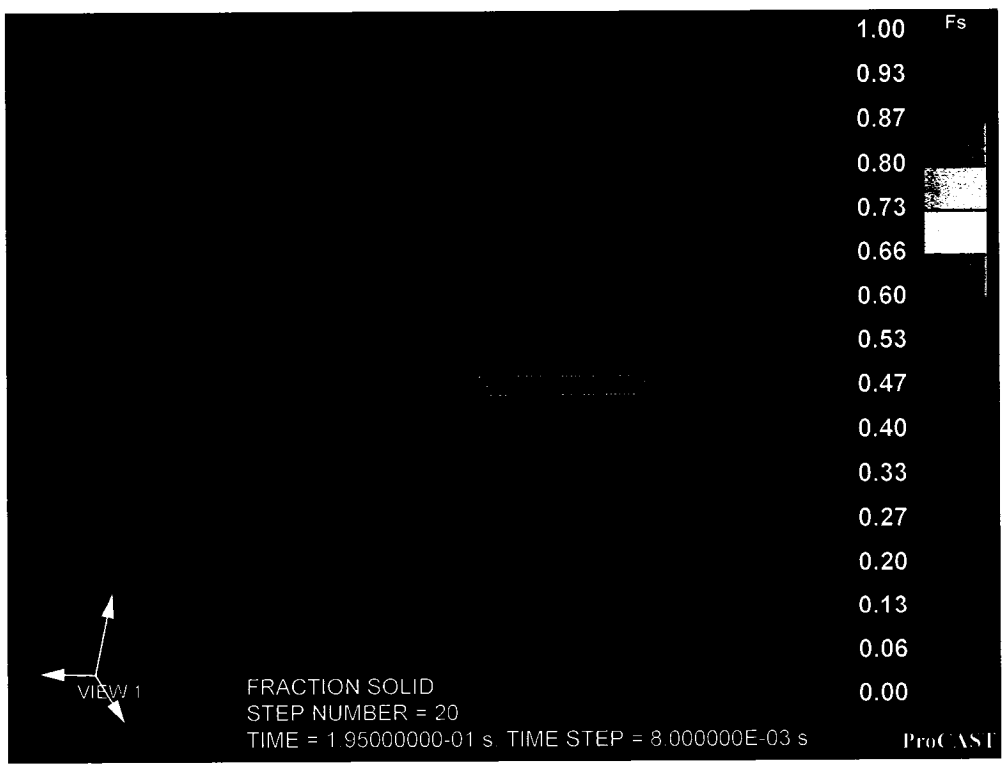

Figure 82: After approximately 0.25 second

Figure 83: After approximately 0.5 second

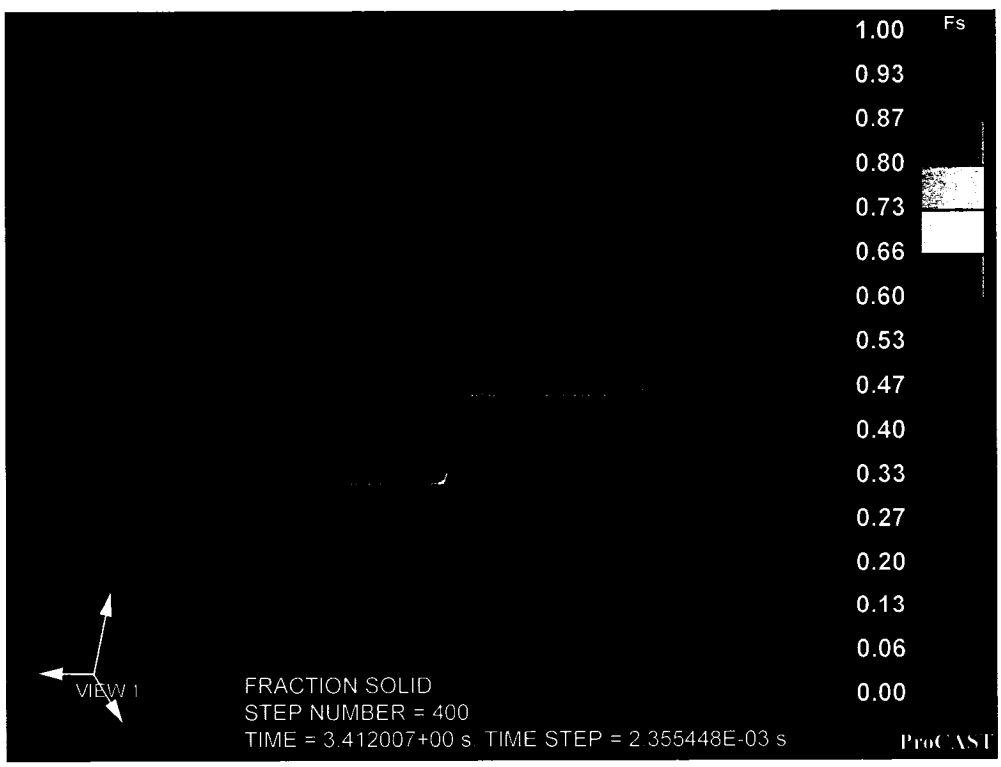

Figure 84: After approximately 3.5 seconds

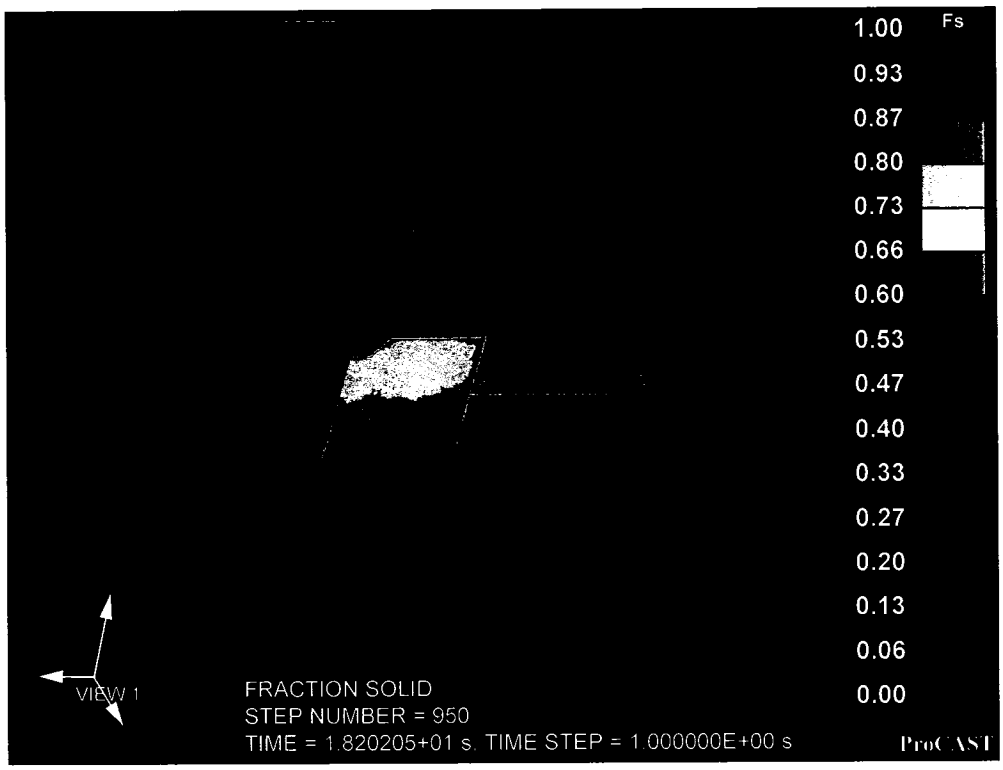

Figure 85: After approximately 18 seconds

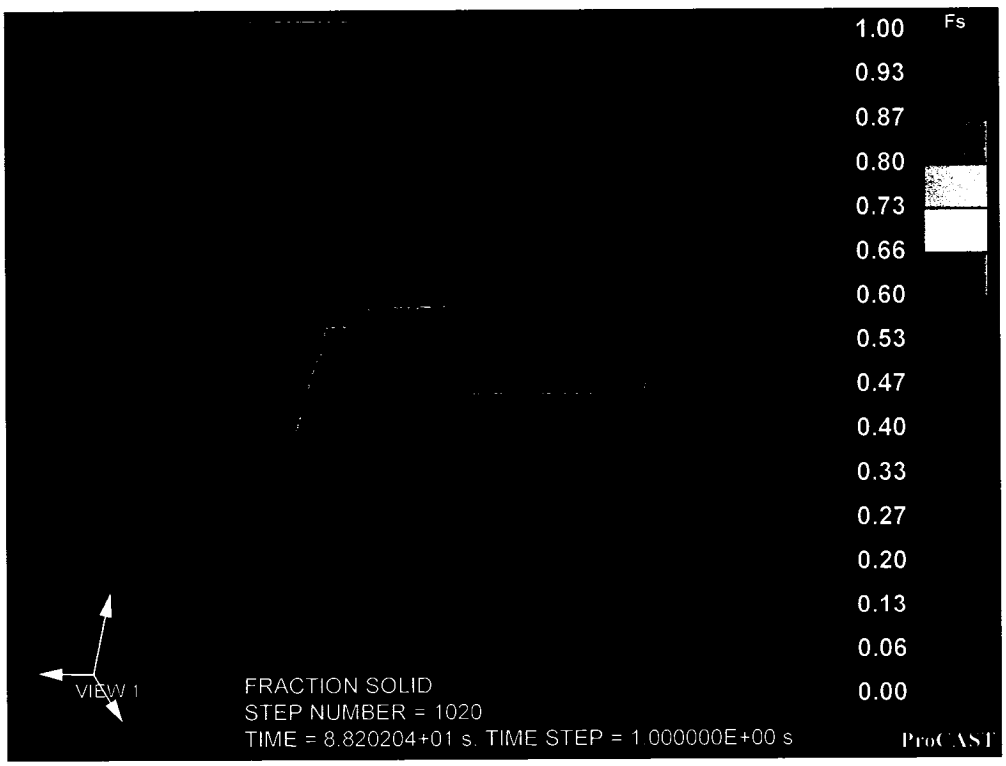

Figure 86: After approximately 88 seconds

It can be seen that the liquid free surface is relatively smooth and gradually touches the chill plate without overlapping or air pocket entrapment. Considering that the present simulation using 0.5 second, i.e., faster rotation, indicated no major problems associated with air pockets or entrapment (oxide generation), then it is obvious that a slower rotation speed could only improve the present results.

Consequently, the DCSS rotation time was set to a slower rotation time of 1 second (twice as slow) to ensure minimum turbulence. The selected rotation time of 1 second was also the minimum delay required for smooth operation with the DCSS air actuator. This condition was tested experimentally and results confirm the absence of thick oxide films at the surface even after validation test with high magnesium alloy (Al-4.8wt%Mg).

Nevertheless, the convective current within the liquid metal also affects the local temperature gradient. Figure 87 shows the resulting cooling curves obtained from two different rotation times.

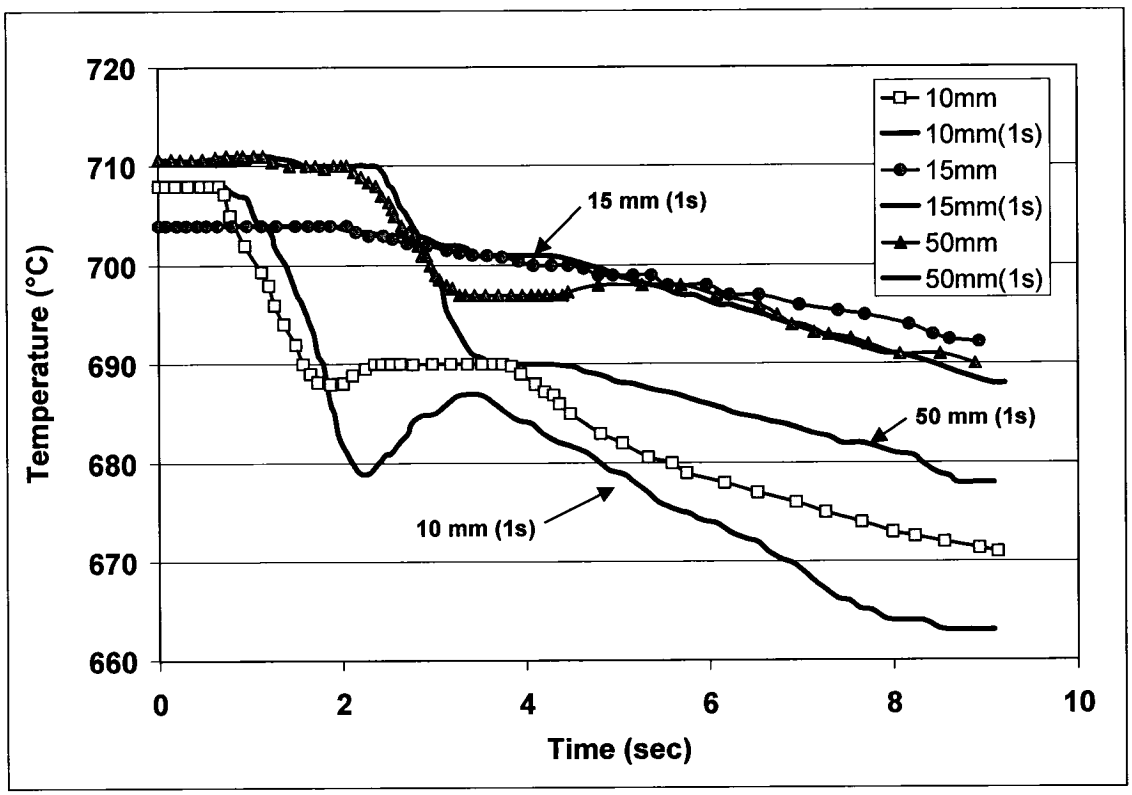

Figure 87: Calculated cooling curves from measurements at 0.5 and 1 second rotation time (AA5182 alloy)

It can be seen that the impact of the convective flow on the thermal history is important near the surface (less than 10 mm) and much deeper (50 mm) within the bulk. It should be noted here that the phenomenon associated with liquid metal superheat was not considered in the present modelling. Nevertheless, the rotation speed could play an important role on the solidification undercooling which is based mainly in this case on the cooling rate. In fact, the slow rotation could generate a less intimate contact between the liquid metal and the chill plate because of the lower momentum and metal head.

This might hinder the formation of pre-dendritic nuclei [66,104] at the interface and lead to a greater undercooling. On the contrary, a faster rotation speed could promote an intimate metal/chill plate contact (momentum and metal head) and therefore the formation of pre-dendritic nuclei resulting from a lower undercooling. It should be noted here that the temperature differences at the beginning of the cooling curves were induced by the initial conditions after the waiting period.

Considering that hot tearing is particularly sensitive to surface and sub-surface temperature gradients and microstructure evolution, it is essential to control this particular aspect to ensure good repeatability. The fluid flow simulations show that the rotation of the container had to control and improve the repeatability of the tests. A rotation time of 1 second makes the liquid move smoothly toward the surface and turbulence effects are small and almost negligible. Consequently, this value was selected and kept constant for all tests to minimize possible bias.

In addition, the rotation of the container makes the solidification front start from the bottom to the top of the section thus generating a slightly angled solidification front (Figure 88). However, this should not influence the results since the load is applied perpendicularly to the growing microstructure. In addition, it simulates the DC casting mould filling during the initial stage and the characteristic shell zone.

These tests were also used to determine the solidification front velocity between approximately 0 to 20 mm from the chill plate (typically 0.4 mm/sec). Figure 88 shows the cast sections along with the drawings representing the overall profiles where t_{chill} represents the time during which the liquid metal was in contact with the chill plate and w_{front} the width of the solidification front at the centre of the cast section.

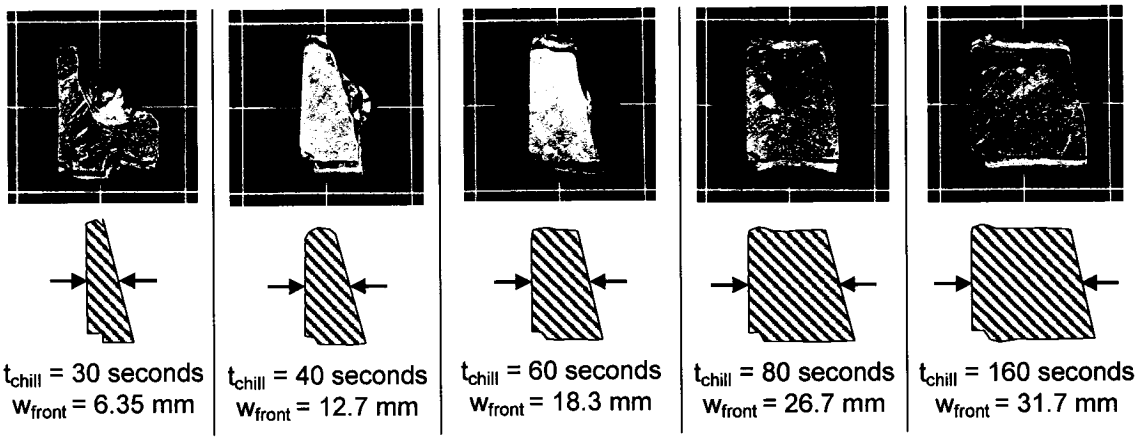

Figure 88: Casting sections obtained from interrupted solidification (1 square = 25 mm)

The average distance from the chill plate was measured at the middle of each section as indicated by the arrows. The solidification front velocity obtained from these experiments and from the thermocouple measurements was used in the different models presented in this work.

5.3 3D Thermal Model

The 3D thermal model was essentially identical to the above mentioned model except that the simulations were dedicated to studying the impact of the heat transfer coefficient at the interface (HTC). The thermal resistance due to air gap formation and/or surface conditions (e.g., roughness, lubricant) will modify the resulting HTC.

During testing, a poorly controlled surface condition will contribute dramatically to the variability of the HTC; this could introduce more variation in the cooling conditions and affect the mechanical response of the solidifying material. More specifically, simulations were made in order to quantify the impact of HTC variability on the solid fraction evolution and distribution across the shell zone to select the most appropriate conditions.

5.4 Heat Transfer Coefficient (HTC)

Figure 89 shows the HTC used in the numerical simulations. These HTC values are typically associated with the primary cooling conditions of DC casting.

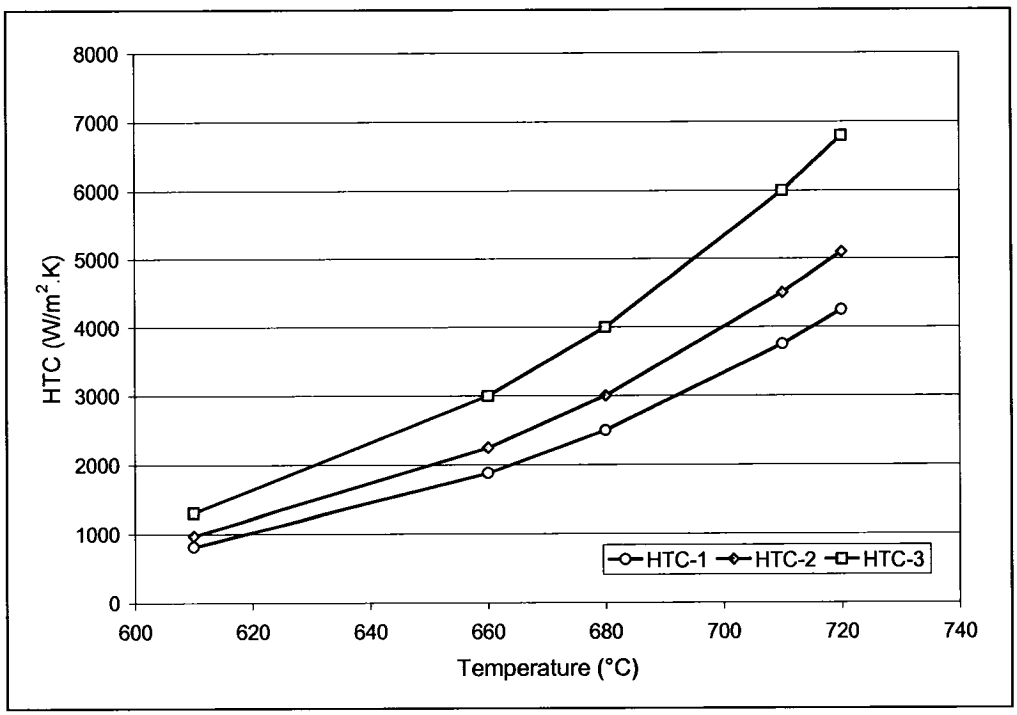

Figure 89: Theoretical HTC curves (AA-6111)

Knowing the potential test sensitivity to the HTC variation, it was important to better fit the cooling curves to predict the solid fraction distribution. The ultimate goal will be to obtain the effective test section, based on solid fraction, at the exact moment the load is applied and to derive the stress distribution over this section. In fact, the test section is used to calculate the stress applied on the test specimen. The best modeling approach is to use an inverse thermal model to determine the specific HTC evolution by tracking the experimentally obtained cooling curves. Unfortunately, the inverse thermal model was not available to perform this task during this work. Consequently, the HTC were adjusted manually in ProCAST™ to fit the experimental curves and the solid fraction distribution in the test section.

5.5 Cooling Curves

Figure 90 shows the calculated cooling curves at 10 mm below the surface using the HTC curves (Figure 89).

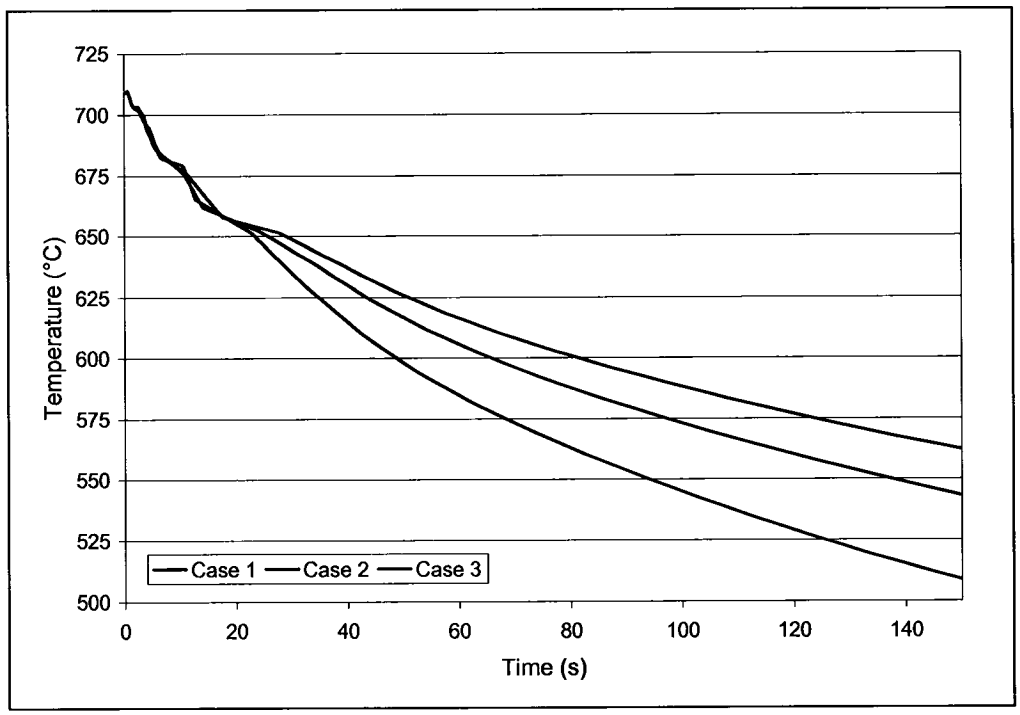

Figure 90: Calculated cooling curves at 10 mm below the surface (AA-6111)

In the DCSS testing procedure, the tensile loading is started when the temperature at 10 mm below the surface reaches a pre-determined value. Depending on the HTC, that condition is met at different times as deduced from the cooling curves presented in Figure 90. This time ranges from 48 to 80 seconds as a function of the HTC used. It is worth mentioning that these time delays could be encountered during the experimental tests performed under poorly controlled surface conditions.

5.6 Thermal Gradient

Figure 91 shows the temperature gradient across the shell zone for the three HTC curves when the temperature reaches 600 °C at 10 mm from the surface in each case. It can be seen that the surface temperature ranges from approximately 564 °C to 575 °C. Similarly, the bulk temperature is also affected due to the different heat flux experienced

at the time when the tensile load is applied. Notice that the temperature at a distance of 10 mm is the same for the 3 cases since this was the condition for the beginning of tensile loading.

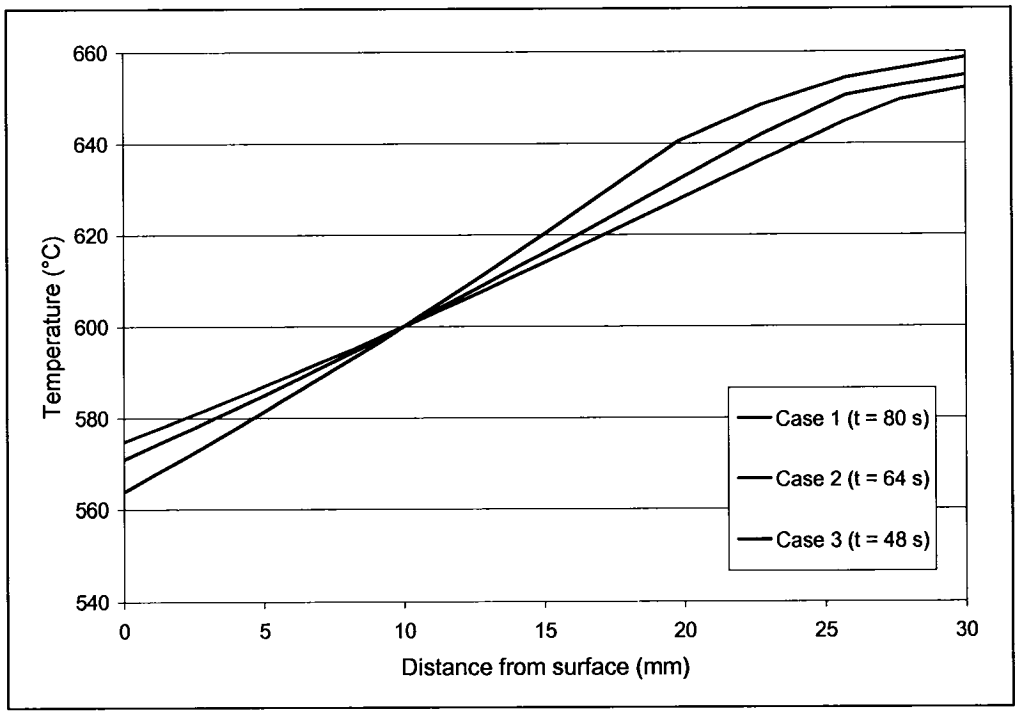

Figure 91: Calculated temperature gradients at loading condition (AA-6111)

The impact of the variability of the contact heat transfer coefficient (HTC) was assessed and quantified in terms of temperature gradient and solid fraction distribution. In fact, the HTC determined the overall heat flux and therefore the thermal gradient and the solid fraction distribution across the mushy zone.

5.7 Solid Fraction

Basically the average stress is derived from the measured load divided by the effective test section. The latter can be estimated from the solid fraction distribution as a function of the distance from the surface. The critical solid fraction above which the semi-solid material has a measurable mechanical resistance by the DCSS is expected to be above 0.95. The load recorded by the DCSS could be different because of the slightly different effective test section. The time of tensile loading sometimes differed substantially from one test to another depending on the overall conditions (metal temperature, mould

surface, lubricant, etc). As a consequence, the maximum force required to create hot tearing might be different should the time of testing be delayed and/or the initial solid fraction and temperature gradient conditions differs. A deeper effective shell when the conditions change could result in a different maximum load.

Consequently, it was essential to measure the temperature evolution during every test and ensure that the solid fraction during the initial loading was above 0.95 and below unity to remain in the semi-solid state (i.e., hot tearing condition). In addition, it was necessary to have the isotherms parallel from surface to bulk to generate a more uniform section while targeting a temperature gradient between 2 to 3 °C/mm. This was made possible by keeping good control of the mould surface conditions to enhance the repeatability and simplify the comparison between tests. Tests that did not fulfill the thermal conditions were simply rejected.

Figure 92 shows the different solid fraction distributions pertaining to the 3 different thermal gradients existing at the time of tensile loading. This indicates that the solid fraction distribution after a waiting time of 48 to 80 seconds does not change too much at the surface. This confirms that the selected criteria prior to applying the tensile load are retained.

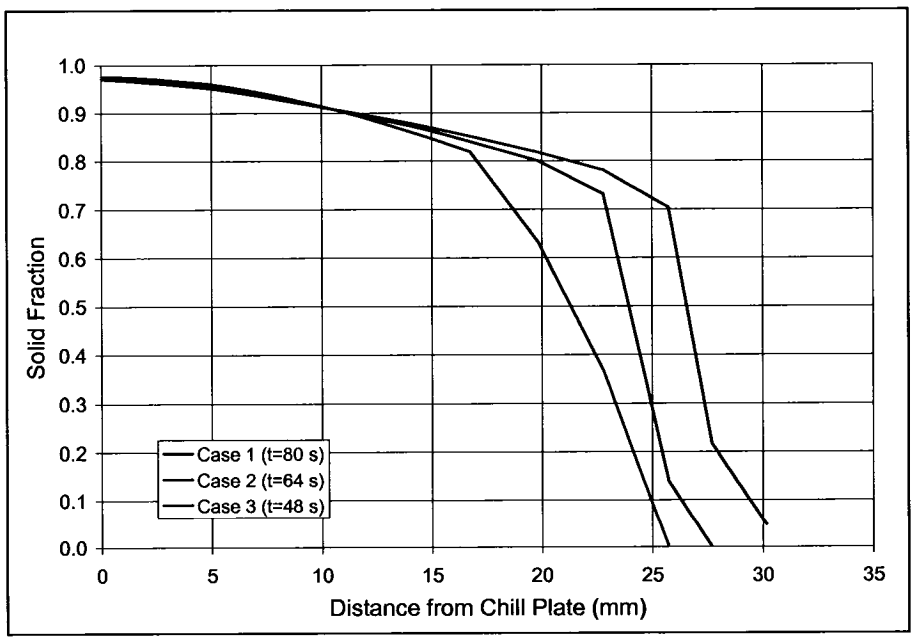

Figure 92: Calculated solid fraction distribution along the distance from the chill plate (AA6111 alloy)

5.8 3D Thermo-mechanical Model

The main objective in this section was to use a mechanical model to determine the overall stress distribution especially at the anchors' heads. The main reason was to understand the cause of premature failure in the initial anchors' head region. In fact, the container was designed to generate a bone-shaped sample and force, upon applying the tensile force, the hot tear to initiate and propagate at the centre of the smaller section. The preparation of each test takes approximately a few hours. Premature fracture at the anchors' heads needed to be eliminated to minimize test rejection and obtained better and valid results.

This was achieved by using a 3D thermo-mechanical model (ProCAST™) under constrained solidification conditions, i.e., without applying external load. The presence of fixed anchors located inside the liquid metal that undergoes solidification creates a condition where the shell is put under tension (constrained). As mentioned above, under ideal conditions, the hot tear must take place between the anchors (reduced section) otherwise the test was meaningless and rejected.

For this particular case, a linear relationship was assumed between the stress and the strain of the test material. The task was to illustrate the stress concentration arising from the solidification contraction and distribution around or near the anchors.

5.9 Impact of anchor design on stress distribution

The anchor used in this work was a standard carriage bolt with a round head. This creates a condition such that a hot tear might initiate and propagate preferentially at or near this region. In order to validate this hypothesis, a numerical simulation was performed to determine the stress distribution. The results confirmed that the anchor design was inappropriate because of the stress concentration at the tip of the bolt head. Figure 93 shows the stress distribution on the cross section located at the middle of the sample from the surface (chill plate) towards the bulk of the liquid. It should be noted that under the present configuration, the stress concentration migrates to the surface of the sample.

Based on these results, the anchor design has been modified such that the top portion of the rounded head was flattened (Figure 94) to minimize stress concentration. The new

design allowed positioning closer to the surface to improve the sensitivity and reproducibility of the DCSS.

The new design has been tested in the field without further numerical modelling. The results indicated that the modifications reduced significantly the occurrence of hot tear near or at the bolt head region. Consequently, this improved the overall DCSS unit performance and minimized the number of tests rejected.

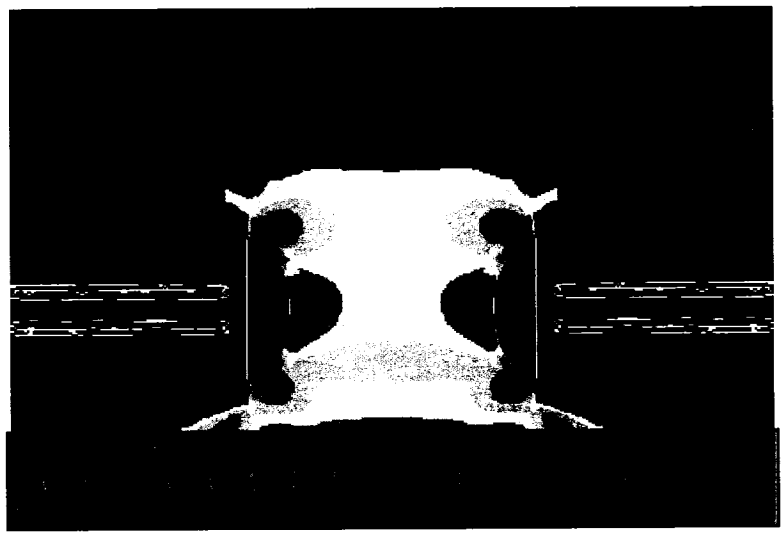

Figure 93: Horizontal stress distribution

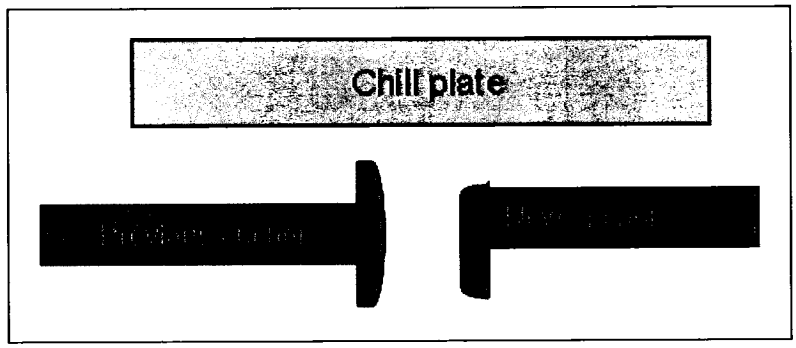

Figure 94: Modification of the anchor set-up to minimize stress concentrations

Chapter 6: Experimental Results: Thermal Behaviour of Al-Si Binary Alloys

The hot tearing mechanism is based on the fact that a liquid portion is present between the dendritic networks upon fracture. Any means used to measure the mechanical properties of a semi-solid material in order to establish the hot tearing propensity must rely on precise measurements. Therefore, it is important to know the thermal conditions that prevail during the test. Surface temperature measurements using contact thermocouples were taken to evaluate the solid fraction at the surface of the sample during testing. Figure 92 shows the two surface temperature measurements along with the calculated average taken once during testing on the Al-0.5wt%Si alloy. It is seen that the average surface temperature in the testing zone (time equal 6 seconds) corresponds to a solid fraction below unity during testing (large arrow).

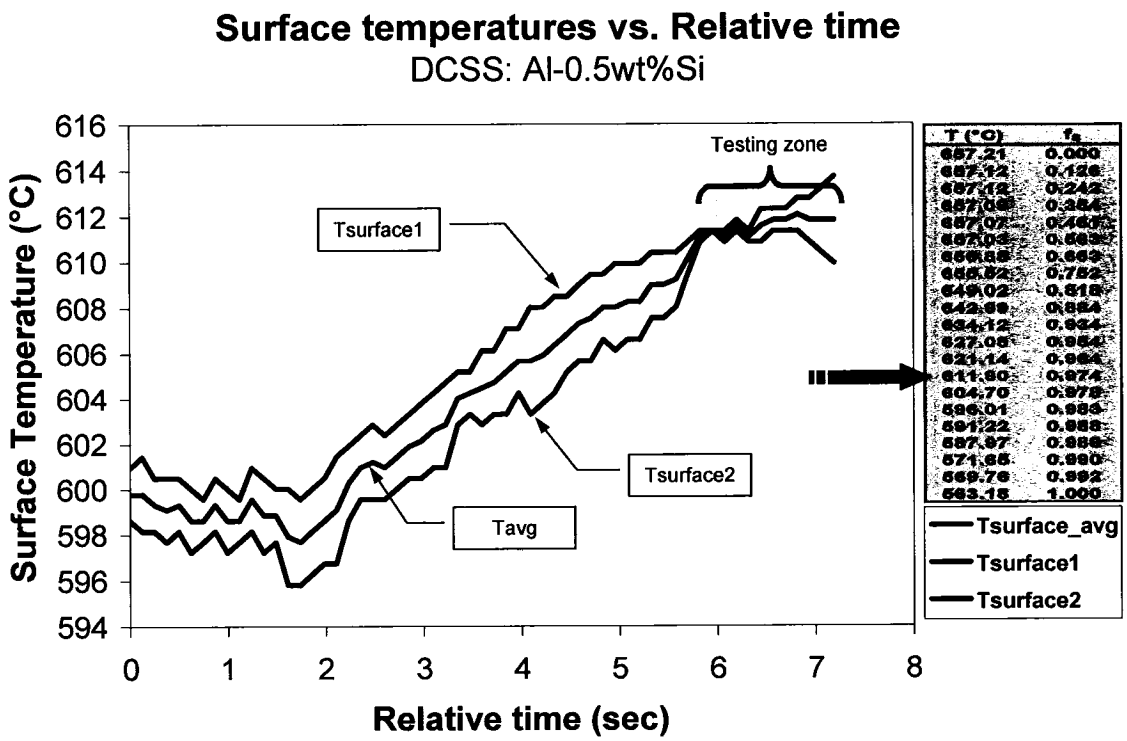

Figure 95: Surface temperature measurements with 2 contact thermocouples

Since precise surface temperature measurements are relatively difficult to acquire, numerical simulations were then performed to validate and predict the surface temperature (inverse model) of the aluminum sample from cast-in thermocouples positioned at 5, 10 and 15 mm from the surface, respectively. This was done specifically to confirm that the mechanical properties were obtained in the temperature or solid fraction range critical for hot tearing (typically 0.95 to 0.99). As mentioned above, the specimens were investigated by cutting the surface to reveal the torn section and to estimate the load bearing area. This was used later to determine the mechanical resistance (i.e., engineering strength given by the force over the area, F/A) of the solidifying alloys. In cases where the torn surface was not visible (liquid inflow) the section was obtained from the temperature measurement (i.e., solid fraction of 0.95) and the exact thermocouple position (X-Ray).

Numerical simulations using ProCAST™ were done to determine the temperature profile inside the test sample and at the surface. The results show that the model fits the experimental data and predict a volume solid fraction less than unity at the surface of the sample during the DCSS testing. The results agree also with surface temperature measured during the test using surface thermocouples. In addition, the data and modeling results indicate that the isotherms are parallel from the surface to the bulk. This contributes also to having conditions that are more repeatable and minimizes bias from test-to-test.

Figure 96 to Figure 101 show the temperature measurements (dotted lines) and the modeling results (smooth lines) that fit the experimental data relatively well. The beginnings of the experiment are indicated on the graphs. It can be seen that the waiting time before testing is different for the Al-0.5Si. This could be attributed to the heat transfer across the refractory container and the chill plate along with the pouring temperature. However, the most critical factor was to proceed with the DCSS testing when the temperature criteria were met, i.e., applying tensile load at a volume solid fraction above 0.95 and below unity at the surface of the sample.

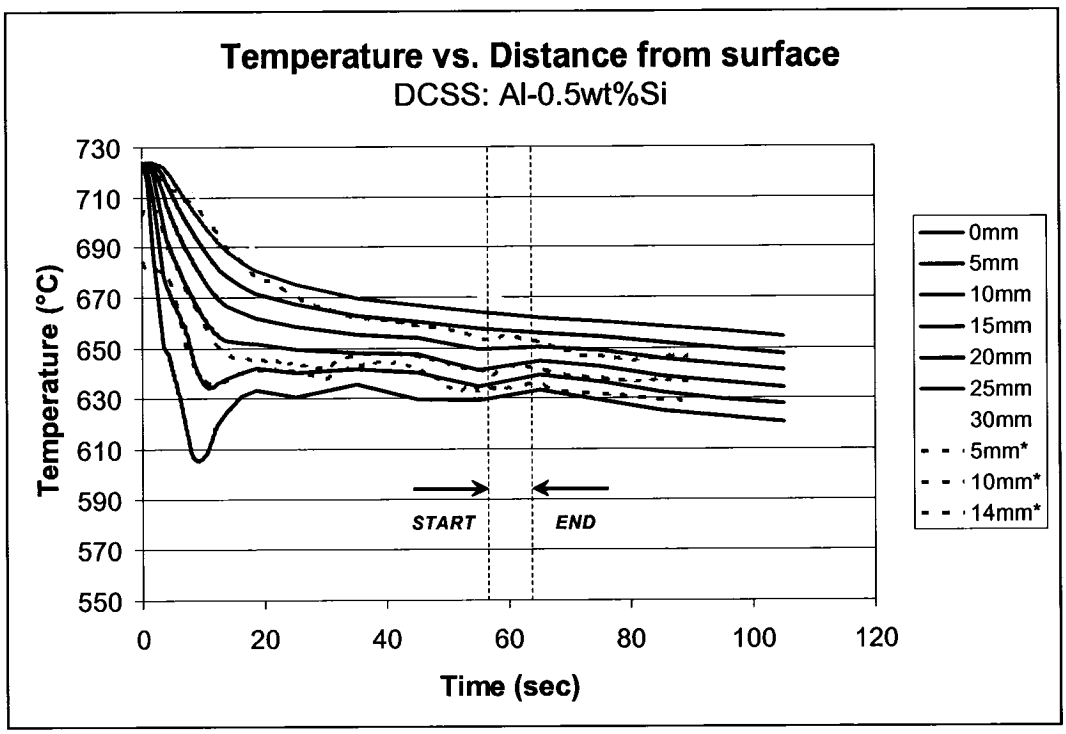

Figure 96: Temperature evolution from the chill plate (Al-0.5Si)

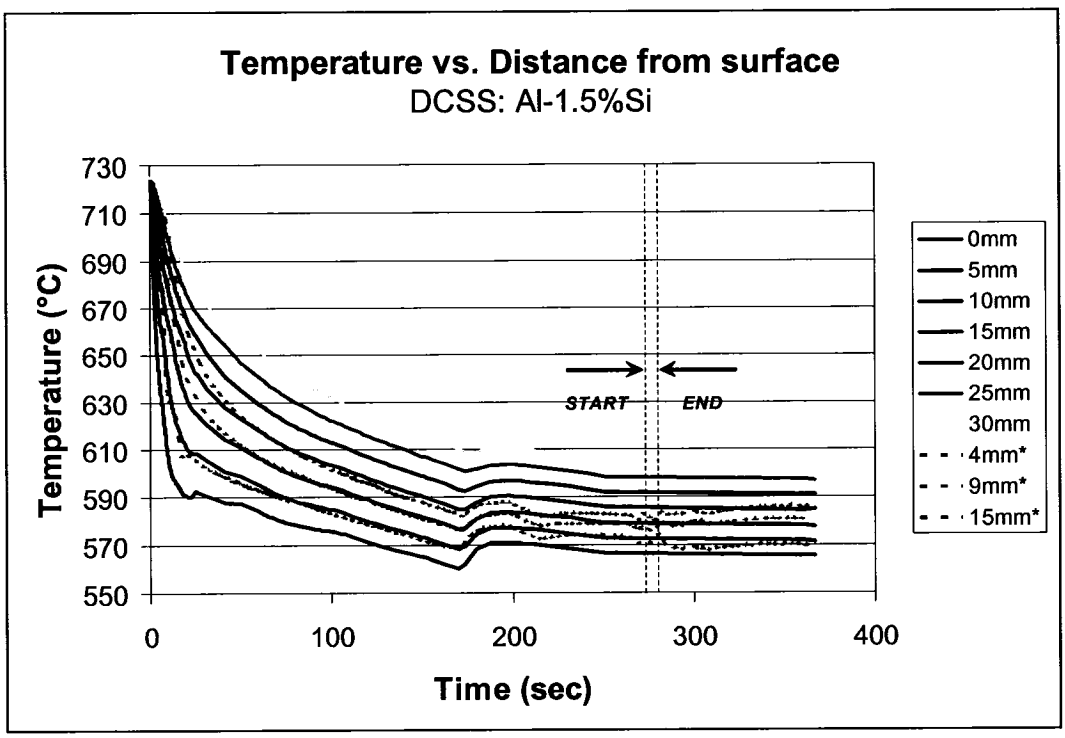

Figure 97: Temperature evolution from the chill plate (Al-1.5Si)

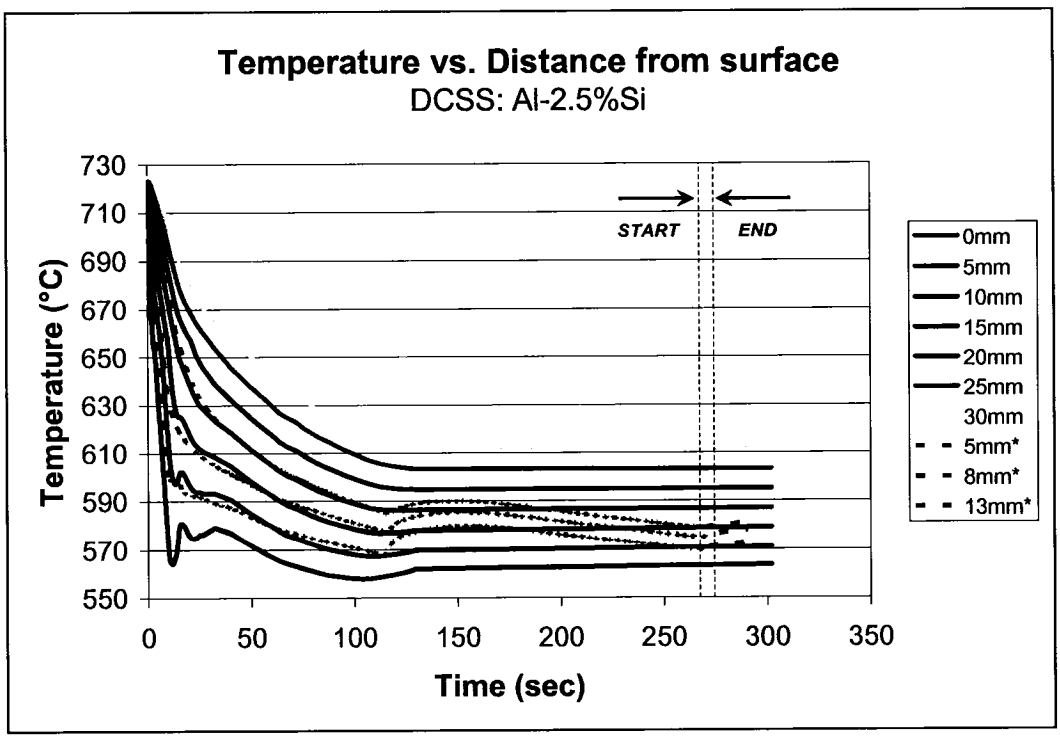

Figure 98: Temperature evolution from the chill plate (Al-2.5Si)

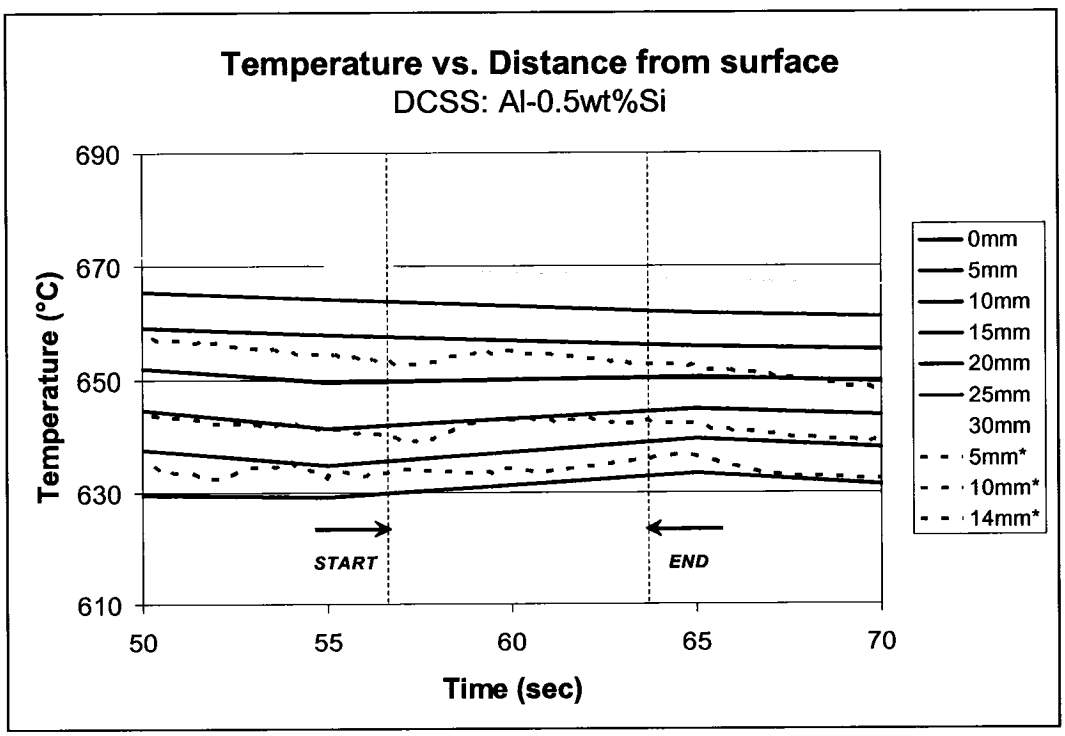

Figure 99: Temperature evolution from the chill plate (Al-0.5Si: zoom)

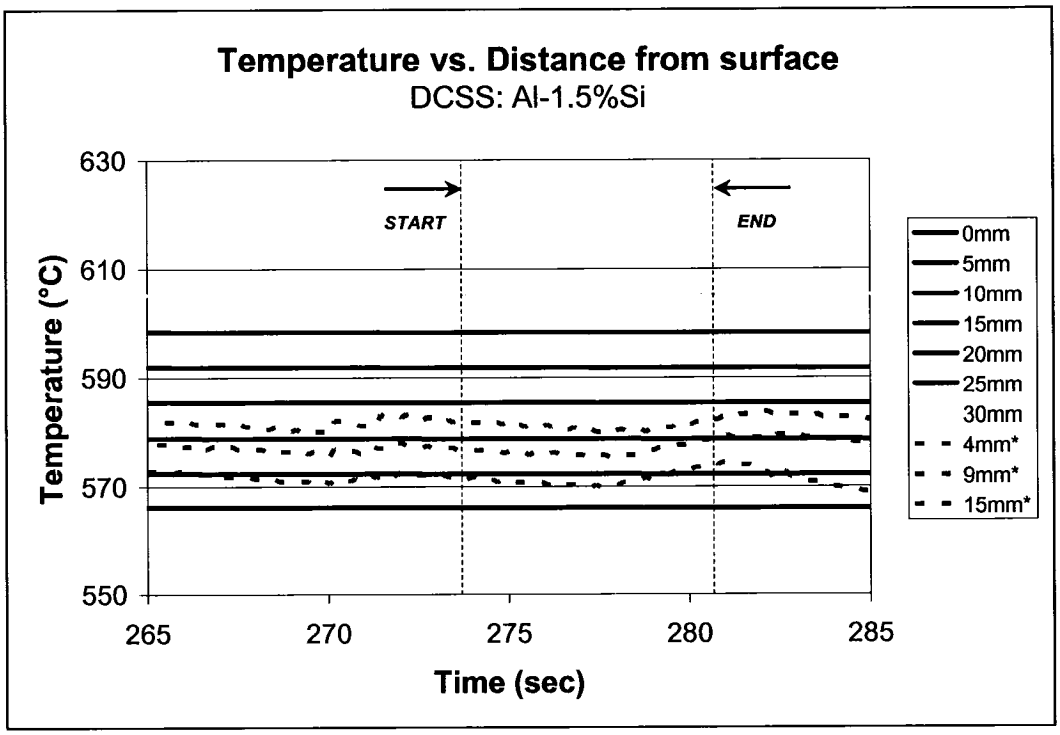

Figure 100: Temperature evolution from the chill plate (Al-1.5Si: zoom)

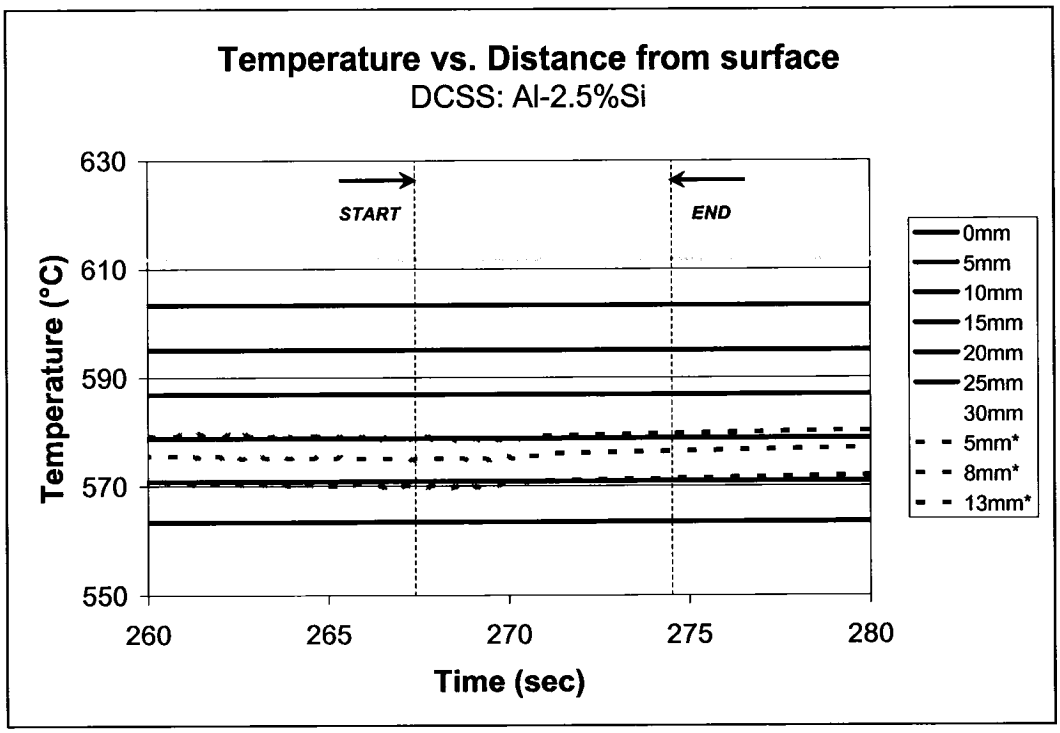

Figure 101: Temperature evolution from the chill plate (Al-2.5Si: zoom)

The temperature profiles were then obtained from the modeling work to determine the solid fraction profile from the surface to the bulk of the sample. This was used to calculate various thermal values such as the temperature gradient and the solidification front velocity. Nevertheless, the most important goal was to ensure that the temperature profile remained in the range corresponding to a solid fraction between 0.95 and unity at the surface.

The latter solid fraction was used as a trigger to apply tensile force on the sample. Figure 102 to Figure 104 show the solid fraction curves obtained from the test samples during solidification of Al-0.5 wt% Si, Al-1.5 wt% Si, and Al-2.5 wt% Si, respectively. It can be seen that all samples met the initial requirements for the solid fraction.

Consequently, all the tests were accepted and used to derive the mechanical properties of the semi-solid Al-Si binary alloys during tensile loading. Figure 105 to Figure 110 show the mapping of the temperature fields and the corresponding solid fractions (ProCAST™).

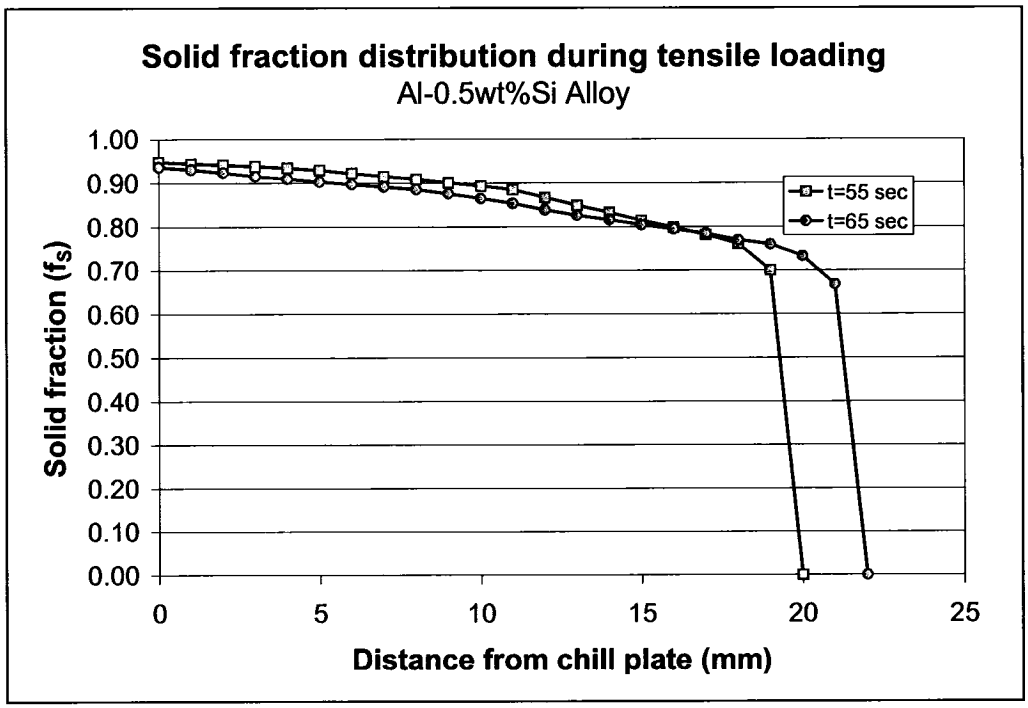

Figure 102: Solid fraction evolution with time and temperature (Al-0.5Si)

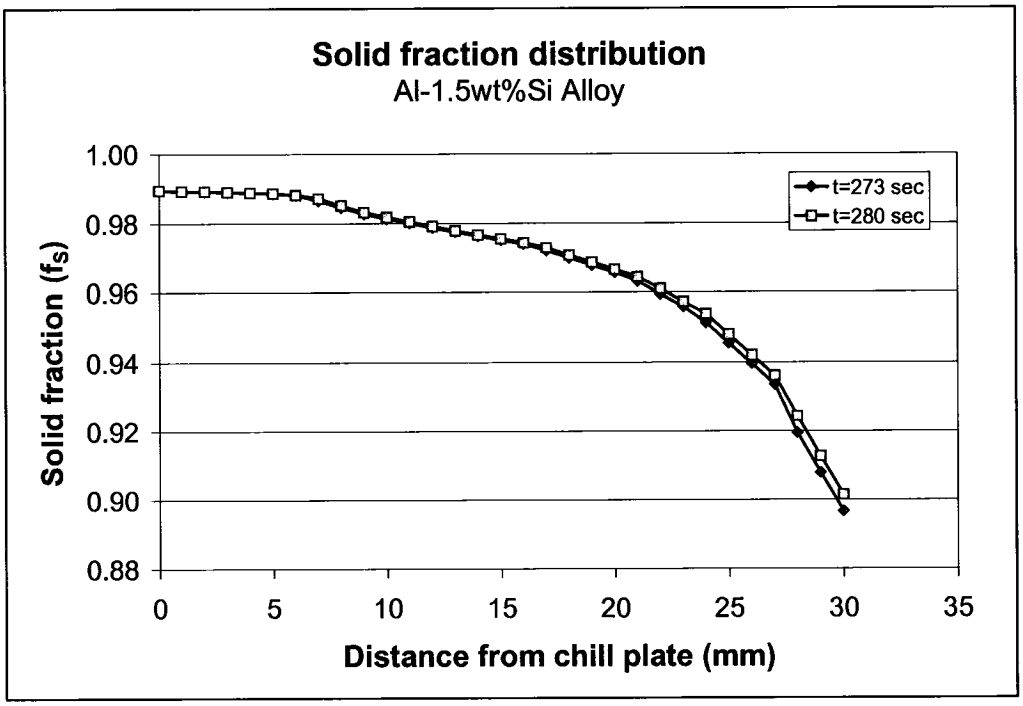

Figure 103: Solid fraction evolution with time and temperature (Al-1.5Si)

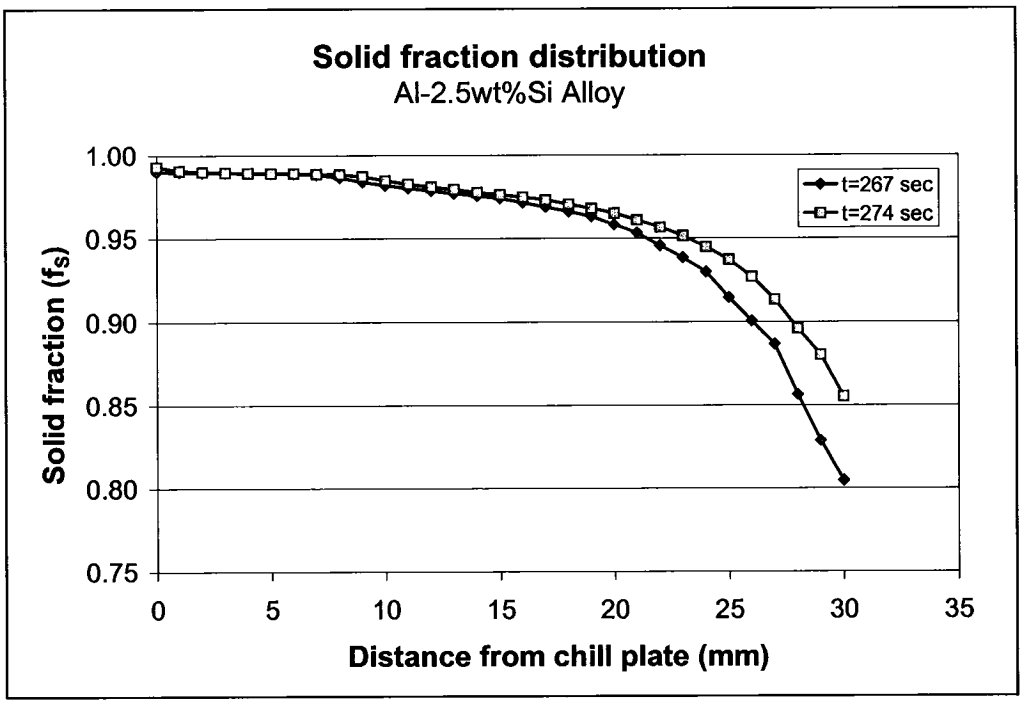

Figure 104: Solid fraction evolution with time and temperature (Al-2.5Si)

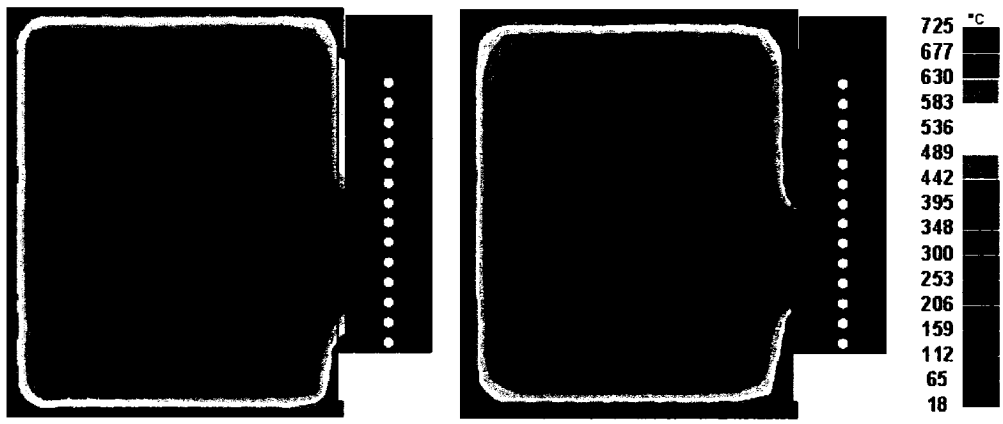

Figure 105: Temperature field evolution before tensile loading (Al-0.5wt%Si)

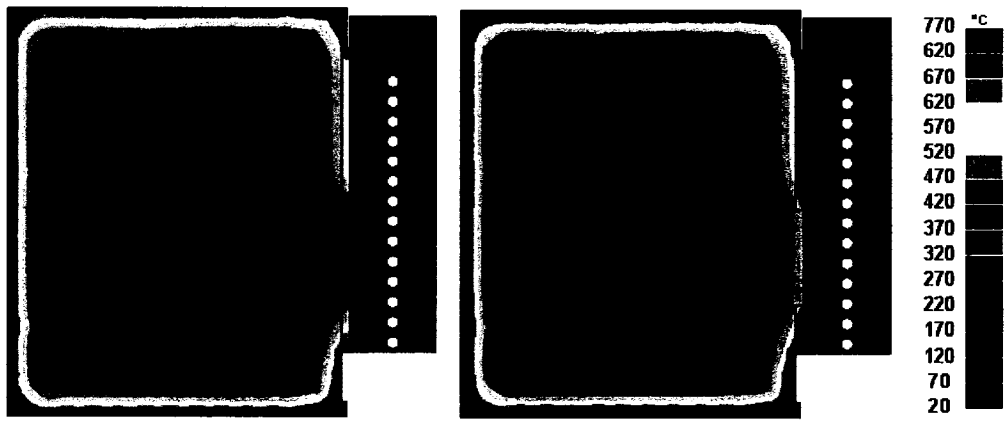

Figure 106: Temperature field evolution before tensile loading (Al-1.5wt%Si)

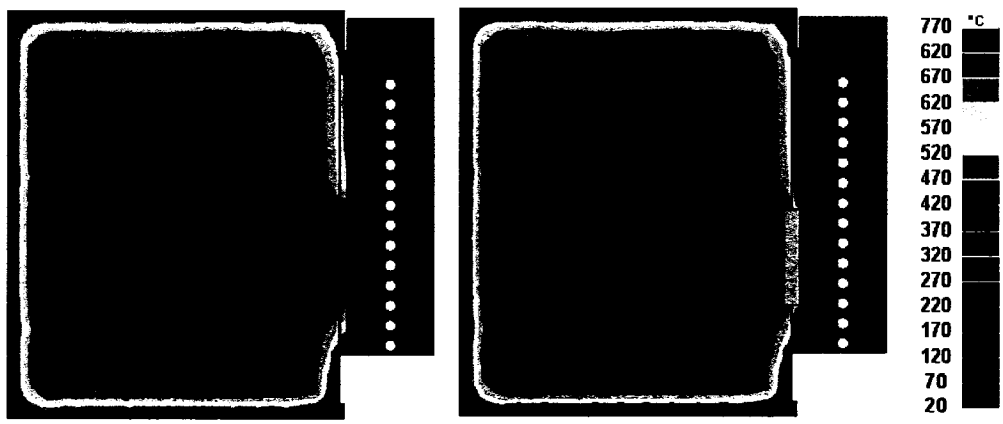

Figure 107: Temperature field evolution before tensile loading (Al-2.5wt%Si)

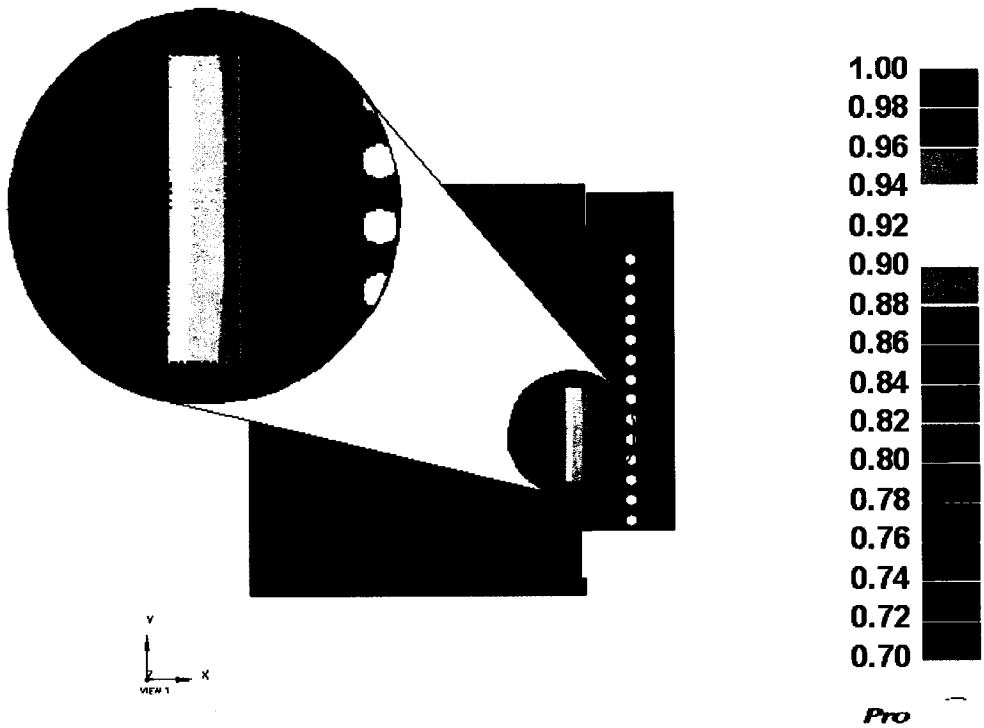

Figure 108: Solid fraction distribution obtained from ProCAST™ (Al-0.5wt%Si)

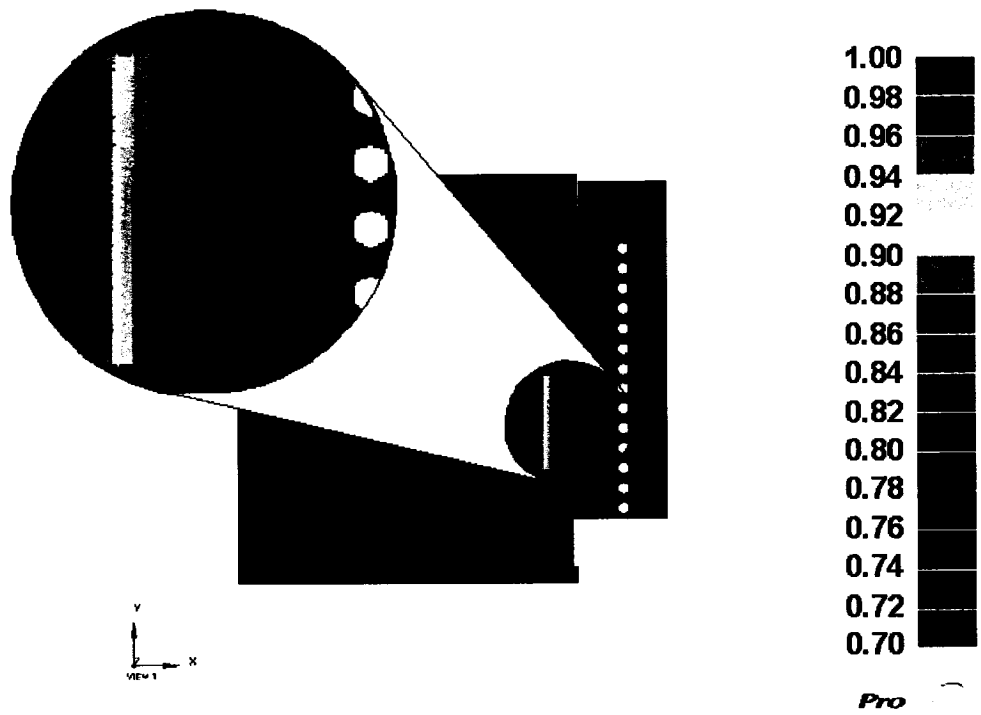

Figure 109: Solid fraction distribution obtained from ProCAST™ (Al-1.5wt%Si)

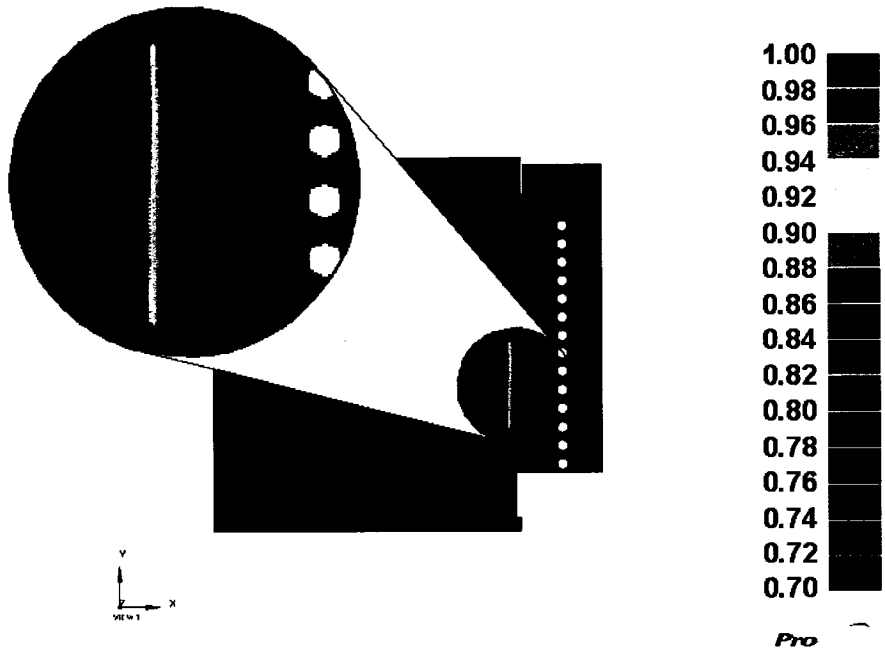

Figure 110: Solid fraction distribution obtained from ProCAST™ (Al-2.5wt%Si)

Numerical modeling shows that the temperature field is such that the solid fraction near the chill plate is below unity and decreases with the position going towards the bulk (liquid).

In addition the temperature distribution during the tensile loading was quite uniform. As explained above this is important since a large difference between loading times will affect the section on which the tensile force is applied. Consequently, the results will be less representative of the material resistance as the section changes. Nevertheless, since there is a variation in the solid fraction from the chill plate to the bulk, the stress will always be distributed along the solid fraction change with higher resistance at the surface. The solid fraction curve evolution is changing according to the isotherms shown in Figure 99 to Figure 101 above.

This approach has been used later to validate the section obtained from the temperature profile and to determine the stress-strain curves. In addition, the torn section was characterized by a grayish and fibrous zone after the sample solidified. The strain was obtained from a strain gauge touching the surface of the sample during the loading. Consequently, the initial gauge length (L_o = 23 mm) and the final gauge length were used to derive the engineering strain or the elongation, i.e., $(L-L_o)/L_o$.

Chapter 7: Experimental Results: Tensile Behaviour of Al-Si Binary Alloys

7.1 Experimental stress-strain curves

The DCSS apparatus has been designed to apply and measure a tensile load and the surface elongation. Consequently, these mechanical values are used to derive the stress-strain curves that best represent the material behaviour during solidification and its capacity to resist hot tearing.

Figure 111 shows the DCSS tensile testing results (stress-strain curves) for the binary Al-Si alloys that were used in this work and compared with the theoretical model. The tests were done under the same experimental conditions under a constant anchor displacement speed that generated a quite similar average strain rate (0.028 s^{-1}). The results show a typical behaviour with strength building up during the first portion of the curve followed by a "creep separation" and the rupture characterized by the sudden change in the slope. The plastic region and the rupture zone are associated with the hot tearing propagation.

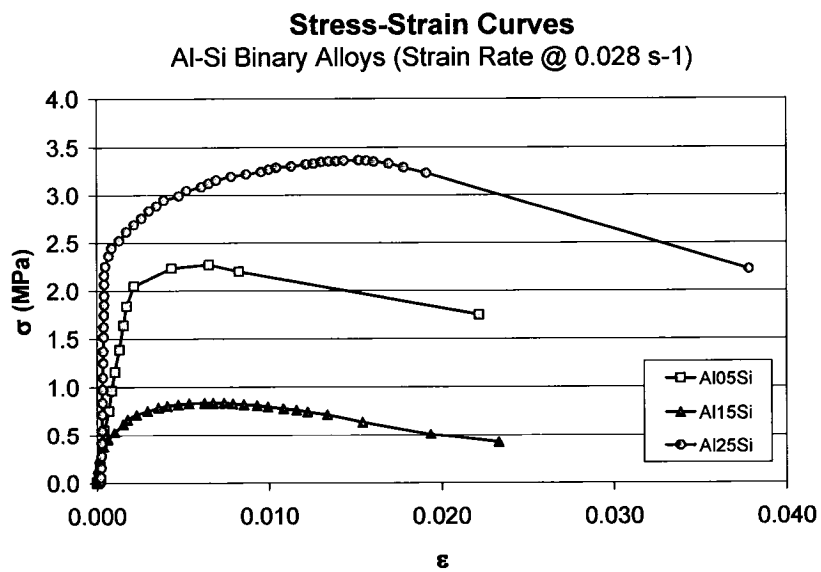

Figure 111: DCSS tensile testing results on binary Al-Si alloys

In this work, the theoretical model attempts to reproduce the characteristic stress-strain curves obtained by the DCSS unit. First, a viscous model is used in the first portion of the curve in combination with a creep law for the visco-plastic region. The hot tearing propagation that is leading to the separation of the microstructure uses a crack propagation coefficient or CPC (Chapter 10:) based on the microstructure to relate the film thickness and stress proportionality. To some extent, the combination of a theoretical visco-plastic model and a microstructure coefficient to explain the hot tear propagation is not common. The CPC is based on the film thickness according to the grain size in the surface and sub-surface region. The grain size has been derived from a cellular automaton that predicts the grain structure based on a nucleation and growth law for each given Al-Si alloys covered in the present study.

The stress-strain curves are the ultimate results that are obtained from the tensile test measurement in the semi-solid state. However, there are many publications by Clyne and Davies [58] and Feurer [75] describing hot tearing sensitivity based on the well-known lambda-curve (Λ-curve). The latter was obtained in different ways mostly related to physical measurements such as direct measurement of the crack length.

The present work allows use of real mechanical quantities (inverse of the maximum stress) to determine and confirm the distinctive Λ-curve previously obtained by others. Figure 112 shows the resulting Λ-curve obtained from the inverse of the maximum stress for the tested binary alloys.

The first approach used the inverse of the maximum tensile load (Langlais [102,103]) obtained from the DCSS measurements. Improvements made on the DCSS unit (strain gauge, computer control, etc.) made it possible to use more standard properties such as the maximum stress to fracture. Owing to the fact that the overall results are comparable, the mechanical quantities used here to derive the Λ-curves are more representative of the material.

It should be noted that the section used to determine the tensile properties were determined from the thermal history of the sample being tested and the investigation of the torn section characterized by a grayish and fibrous zone. As mentioned above, the strain values were measured using a strain gauge touching the surface of the sample

during the loading. The elongation or engineering strain were derived accordingly from the change in the gauge length, i.e., $(L-L_o)/L_o$.

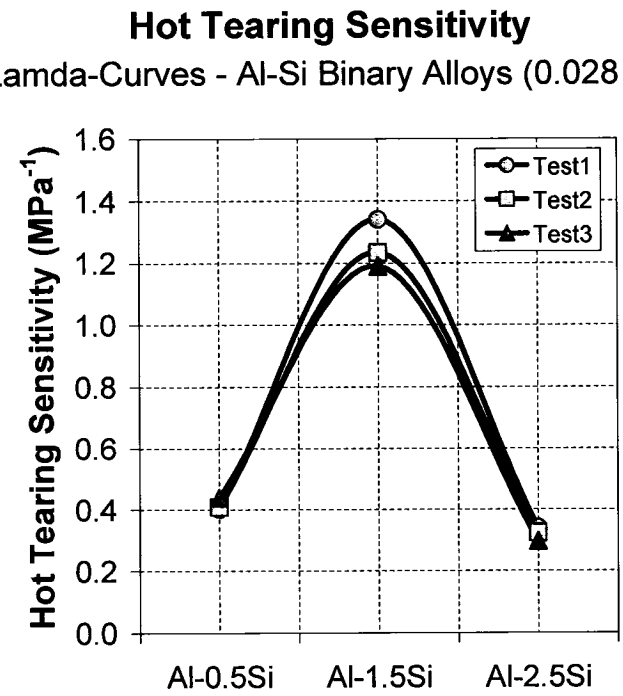

Figure 112: Lamba-curves (smoothed) obtained from DCSS experimental results

7.2 DCSS repeatability

The DCSS unit is an apparatus to measure material properties during solidification. The results depend on many parameters that need to be checked carefully. It also involves the probalistic behaviour related to the pre-dentritic grain formation and growth. Consequently, extra care is required for the preparation of the chill plate surface in contact with the liquid metal. It was shown that the surface roughness of the chill plate influences the number of nuclei and pre-dendritic grain formation (Fortier [104]). The grain size will play an important role in the liquid film distribution and impact the hot tearing behaviour.

The use of a data acquisition system allowed installation of several thermocouples at different locations to verify and accept or reject the test. In fact, all tests that met the temperature criteria with hot tear located between the anchors, i.e., at the centre of the reduced section, were accepted (Figure 113). Rejection of a test was based mainly on

the temperature profiles or gradients in the sample along with data collection points on the DCSS unit to ensure set points are followed (e.g., rotation speed, water temperature, etc.). Hot tears outside the reduced section or at the anchors' heads were automatically rejected even if the thermal criteria were respected. This was done to minimize bias in the results and produce more reliable mechanical values for a given alloy.

Figure 113: Accepted sample with hot tear located at the centre of the reduced section

Figure 114 to Figure 116 show examples of the repeatability obtained with three different tests when all parameters and the set-up are precisely well adjusted. The initial test preparation (i.e., container, metal temperature, insulating material, strain gauge positioning, etc) is crucial to obtain such repeatability. Any mistake during the test preparation could dramatically affect the final results.

It can be seen that the repeatability in the first region (viscous portion) is relatively good. More variation is observed in the peak and the plastic region. The solidifying microstructure is continuously changing with time (i.e., volume solid fraction, morphology). It is therefore impossible to expect perfectly superposed curves from test-to-test. Nevertheless, the present repeatability is more than acceptable knowing the stochastic nature of the solidification process during which the material is being tested.

The analyses of the tensile testing results were performed on these results and the theoretical or phenomenological model was then used to evaluate the impact of specific parameters such as the strain rate, the volume solid fraction and morphology (columnar vs. equiaxed).

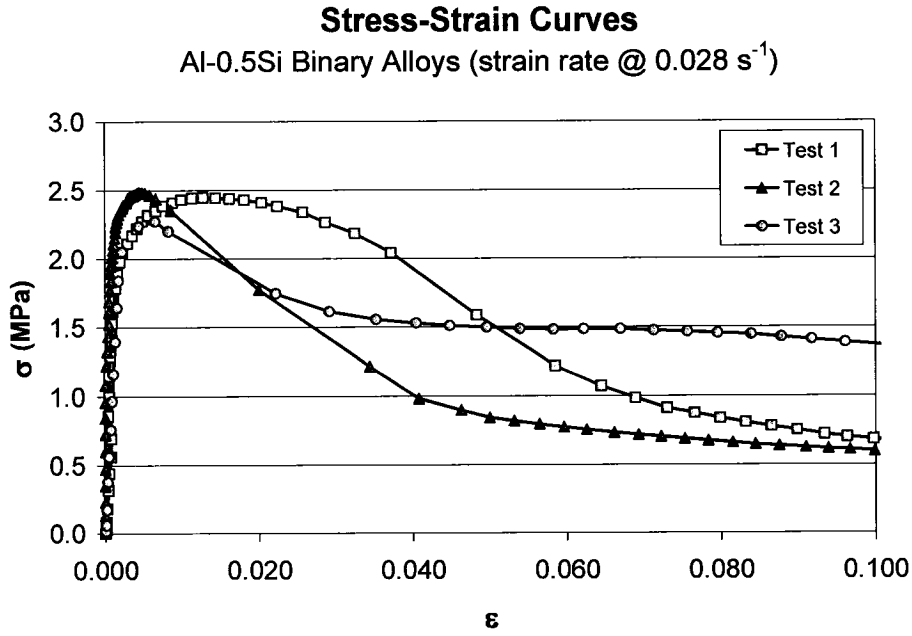

Figure 114: Repeatability on three DCSS test - Al-0.5wt%Si

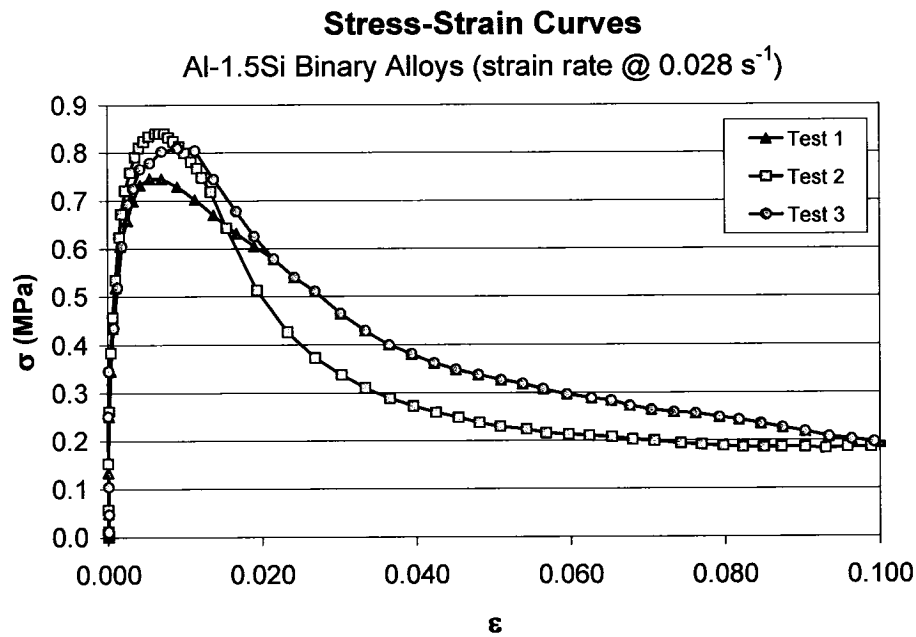

Figure 115: Repeatability on three DCSS test - Al-1.5wt%Si

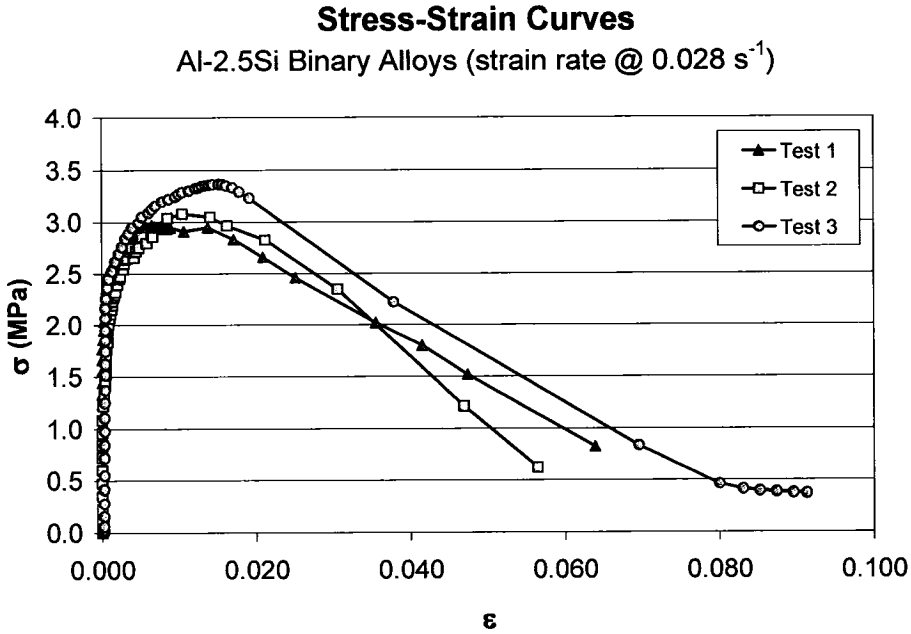

Figure 116: Repeatability on three DCSS test - Al-2.5wt%Si

7.3 Impact of strain rate on stress-strain curves

It must be noted that the maximum stress is intimately related to the strain rate. Indeed, a higher strain-rate will result in a higher reactive stress (Figure 117). Consequently, the relative hot tearing sensitivity will change according to the strain rate used in the experiment. It is important to note here that the strain rate normally varies with time. The DCSS tests were performed using different displacement speeds and the average strain rates were determined from the time versus strain measurements. Consequently, the strain rates presented in this work are, for simplicity, the average of the time-strain curves, i.e., $d\varepsilon/dt$.

It is therefore mandatory to use the same strain rate to perform such analysis. In the case of the ring mould testing, the shape is permanent and the resulting strain rate is basically linked to the solidification rate around the solid core. In this case, the testing parameters (e.g., metal temperature, cooling rate, etc.) need to be the same to improve repeatability and quality of the results.

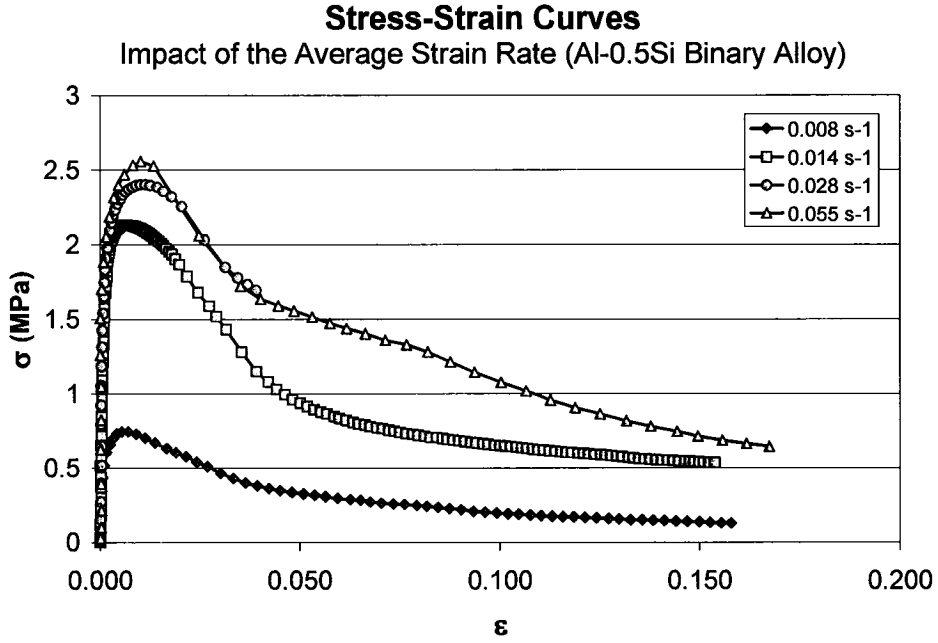

Figure 117: Impact of the average strain rate on the resulting stress

The impact of the strain rate was also evaluated using the microstructure taken from the test samples of the Al-0.5 wt% Si alloy. Figure 118 to Figure 121 show the resulting microstructure response to the imposed strain rate. It can be seen that the material is able to accommodate a certain level of resistive stress to the imposed deformation. As the solidification proceeds at low strain rate, the material can sustain the tensile load with a minimum of hot tear propagation. On the contrary, a higher strain rate does not allow accommodation by grain rearrangement and fluid movement. Consequently, the higher the strain rate, the higher is the resistive stress and the lower is the capacity for the microstructure to accommodate the deformation. The energy is then released by hot tear propagation after the maximum strain is attained. The same analogy applies to DC casting where hot tear propagation is more likely to occur at faster casting speed. One simple solution (at the expense of the production) is to reduce the casting speed to minimize hot tear initiation or to stop their propagation.

It is worth mentioning here that the concept of hot tearing sensitivity using the inverse of the measured stress cannot be applied for the change in the strain rate. This concept was defined to compare alloy families using the same displacement rate.

Figure 118: Strain rate impact on Al-0.5Si @ 0.008 s^{-1}

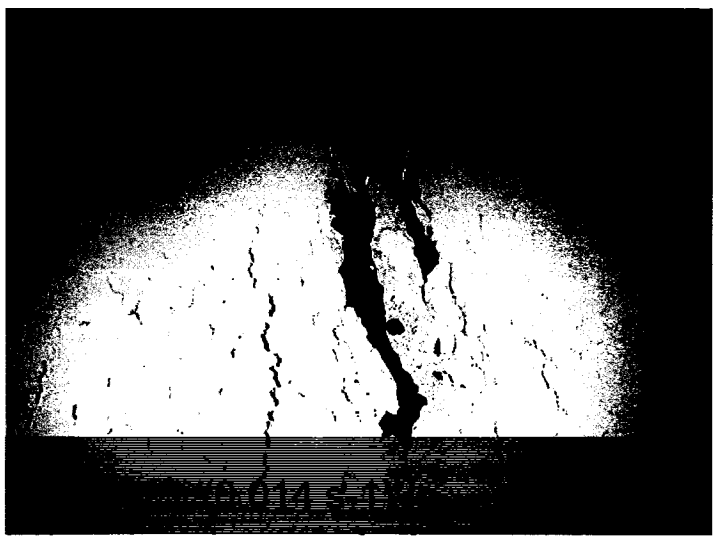

Figure 119: Strain rate impact on Al-0.5Si @ 0.014 s-1

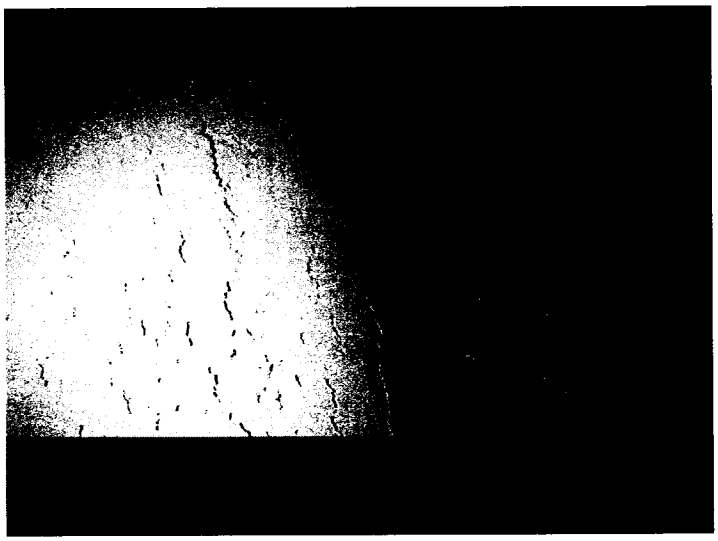

Figure 120: Strain rate impact on Al-0.5Si @ 0.028 s-1

Figure 121: Strain rate impact on Al-0.5Si @ 0.055 s-1

The theoretical model has been used to evaluate the impact of the strain rate on the resulting stress. Figure 122 shows the resulting stress-strain curves. Only the viscous flow portions (green or first shaded area) of the curves are affected by the different strain rates. The present model allows creep (blue or second shaded area) to take place after the volume solid fraction criteria is reached (0.97). Consequently, the final result shows essentially the same behaviour in the plastic region and the macroscopic separation (yellow or last shaded area) or fracture region (after volume solid fraction reached 0.99). It can be seen that the theoretical results are in good agreement with the trend shown by the experimental results, i.e., increasing the strain rate, increases the resistive stress.

The absolute values are relatively similar except for the lowest strain. Again, the discrepancy at the lowest strain between the experimental result and the theoretical results could arise from the difference between reality and the idealized microstructure. In addition, the sample during testing undergoes constant change in the grain structure and morphology.

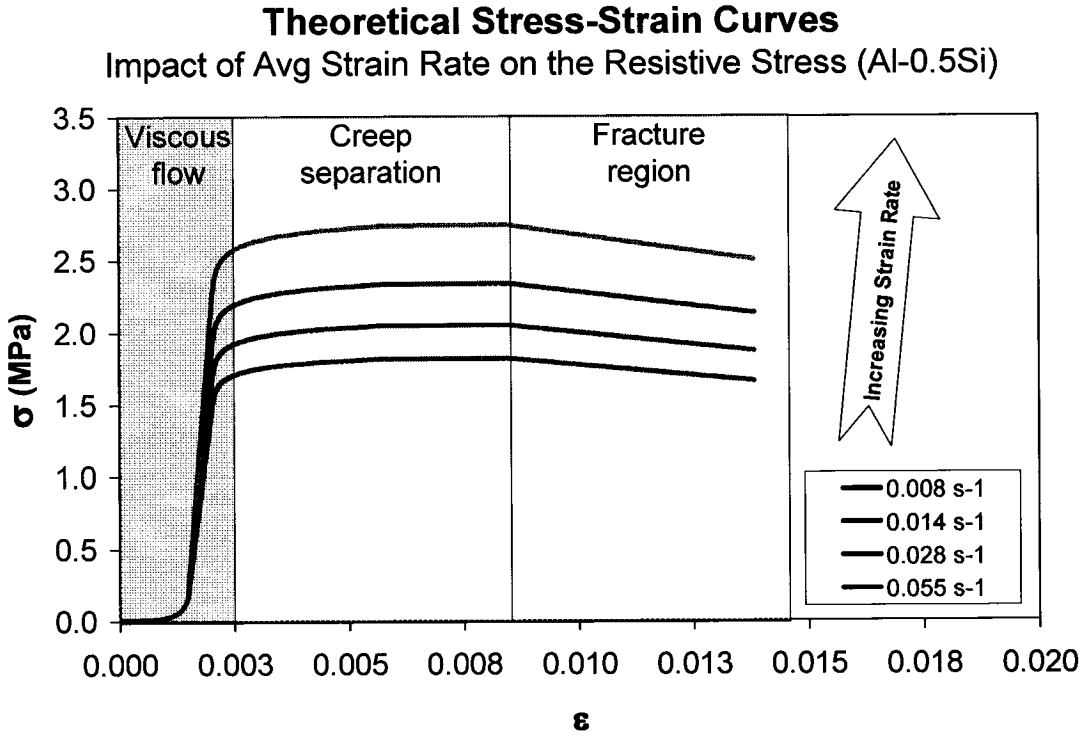

Figure 122: Model results of the impact of the average strain rates on the resistive stress (visco-plastic)

Figure 123 shows the effect of grain size (depicted by the primary arm spacing in the columnar structure) on the resistive stress (stress–to-fracture) for the Al-0.5 wt% Si for a constant volume solid fraction of 0.99. It can be seen that the resistive stress is decreasing rapidly as the grain size increases. The solid fraction and the grain size are determining the initial liquid film thickness, *h*. Consequently, the film thickness, *h*, increases with increasing grain size which results in decreasing the overall strength of the material. The larger grain size will increase the impact which mostly depends on the creep contribution at higher volume solid fraction. It should be noted that the combined effect of the grain size (primary arm spacing) and the solid fraction is shown here while the initial film thickness was calculated according to Equation 49.

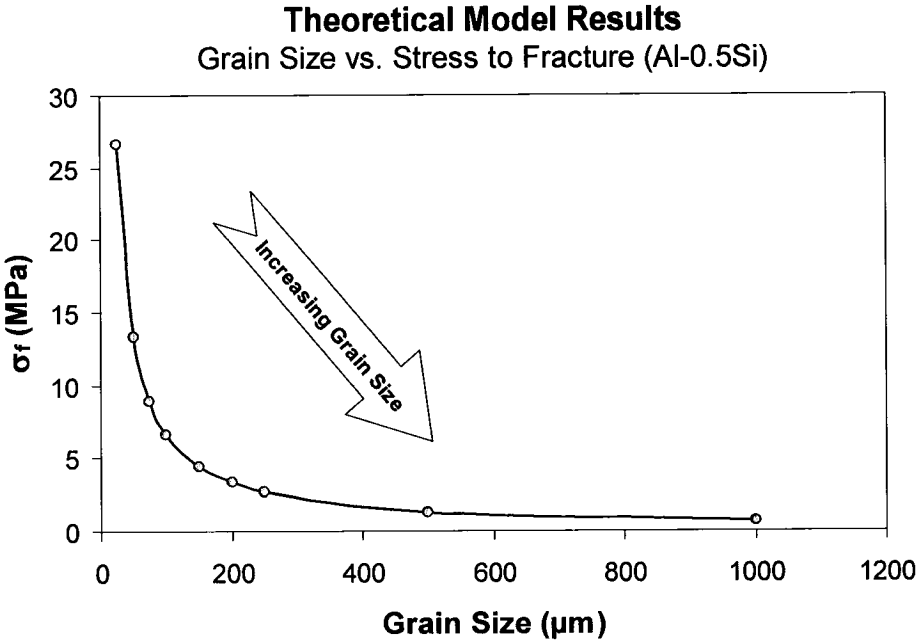

Figure 123: Effect of grain size on stress to fracture (Al-0.5Si)

Figure 124 shows the calculated fracture stress and fracture strain as a function of the volume solid fraction. It is clearly shown that the volume solid fraction is a parameter of importance.

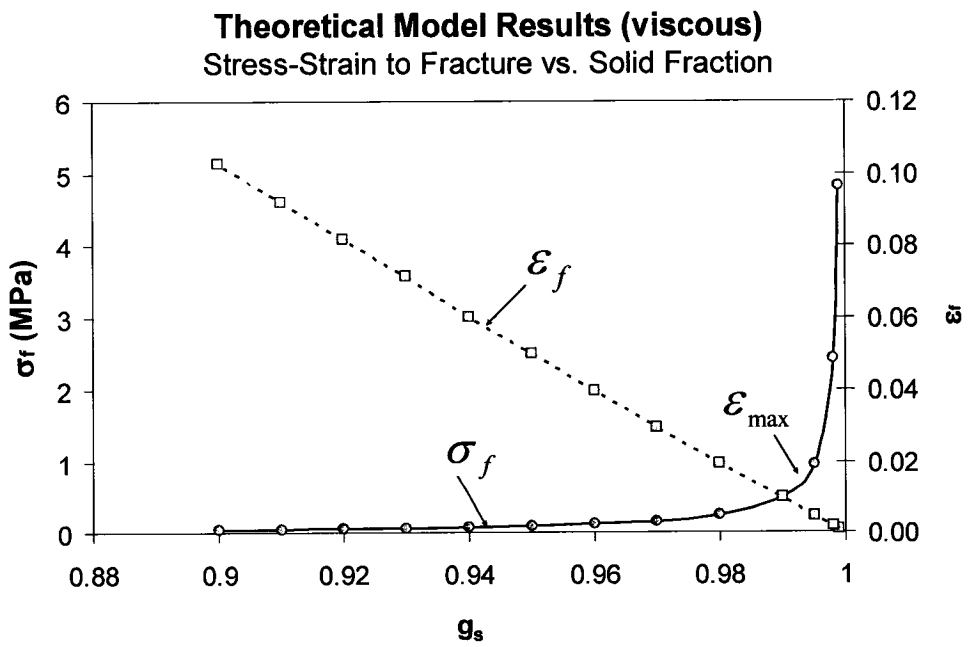

Figure 124: Impact of volume solid fraction on stress and strain to fracture (Al-0.5Si)

This parameter is intimately linked with the film thickness and grain size (primary arm spacing) according to Equation 49. It can be seen that the stress to fracture increases sharply when approaching the maximum strain (ε_{max}). This is similar to the results obtained by Lahaie [99] for the viscous regime.

7.4 Theoretical model vs. DCSS Experimental stress-strain results

Results of the theoretical model indicate that the higher tensile strength is localized at the center of a channel submitted to perpendicular tensile forces. Figure 125 shows the microstructure of the Al-1.5wt%Si alloy with a hot tear that initiated and propagated within the horizontal channel under tensile loading. This confirms the results suggested by the viscous model where the maximum negative pressure (tensile) takes place at the centre of the horizontal channel. This is obtained when the film in the horizontal channel is constrained and further tensile loading creates a void (hot tear initiation). The creation of this void can be affected by other means such as the presence of oxides (nucleation site) or dissolved gas.

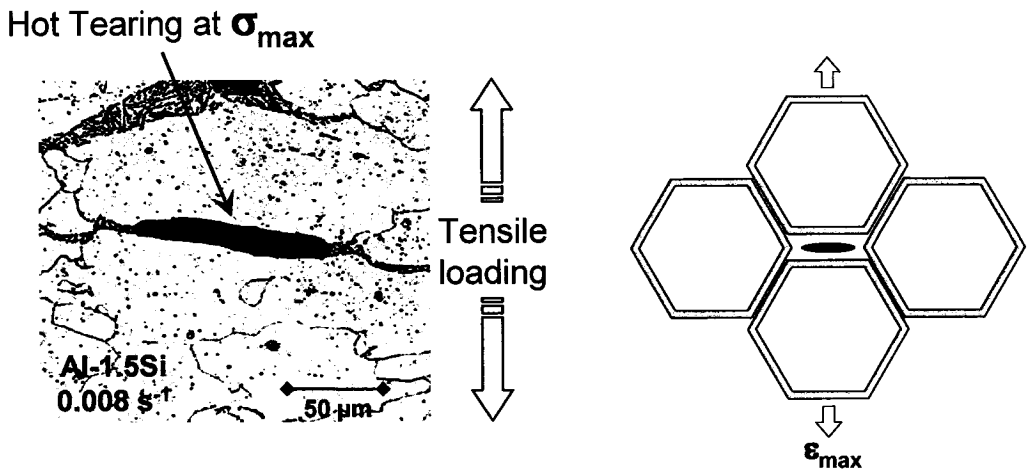

Figure 125: Hot tearing within the horizontal channel and analogy to the ideal model

During solidification of alloys, eutectic liquid is rejected at the grain boundaries. Depending on the solidification path (trace of liquid or solid composition as a function of volume solid fraction, (g_s) a temperature range normally exists in which the solid grains, that form an almost continuous network, trap some of the remaining liquid.

Different studies [5] of the solidification of aluminum castings indicate that the shape and distribution of the liquid phase near the end of solidification has important effects on hot tearing characteristics. The volume of the remaining liquid is usually small (approximately 10% by volume). As solidification proceeds, the remaining eutectic is depleted by the growth of the solid from the grain boundary area of the dendritic network.

Figure 126 to Figure 128 show the DCSS experimental results plotted along with the theoretical model. It can be seen that there is a good agreement between the DCSS results (stress-strain curve) and the theoretical model. The main differences could be associated with the fact that the theoretical model is based on an idealized microstructure using a hexagonal array structure. However, a real aluminum sample that undergoes deformation during solidification shows a much more complex arrangement. The microstructure is composed of a mixture of small and large grains having different morphologies and orientations. This leads to a microstructure where some grains are almost touching each other while some are well surrounded or separated by a thicker liquid film.

It is seen in all cases that upon tensile loading, the microstructure accommodates the load by deformation (strain) until the structure is locked and the liquid films are constrained. At this stage of the deformation, the strength builds up until plastic deformation by solid/liquid movement is taking place. The strength continues to build slightly until it reaches the maximum stress and separation occurs. In the present work, the viscous-plastic model was arbitrarily chosen to cover a volume solid fraction ranging between 0.95 and 0.99. The volume solid fraction below 0.95 was not able to build significant strength.

The creep law appears to fit quite well the plastic portion of the curve. The number of parameters available allowed identification of the proper combination that best described the material behaviour at high temperature. The CPC (Crack Propagation Coefficient) is triggered at the volume solid fraction of 0.99.

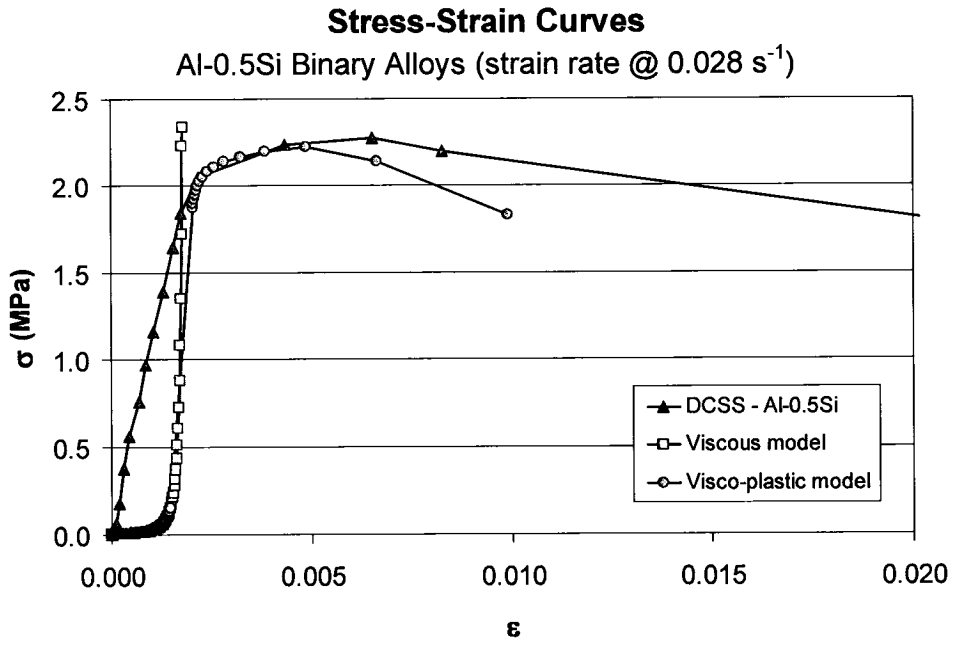

Figure 126: Theoretical model results along with DCSS experimental results (Al-0.5Si)

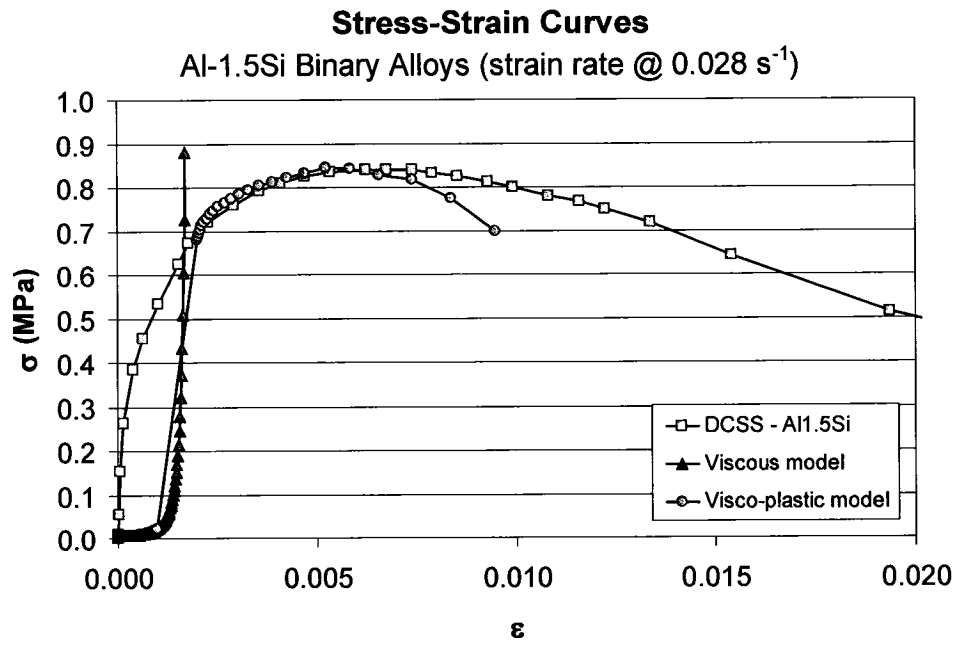

Figure 127: Theoretical model results along with DCSS experimental results (Al-1.5Si)

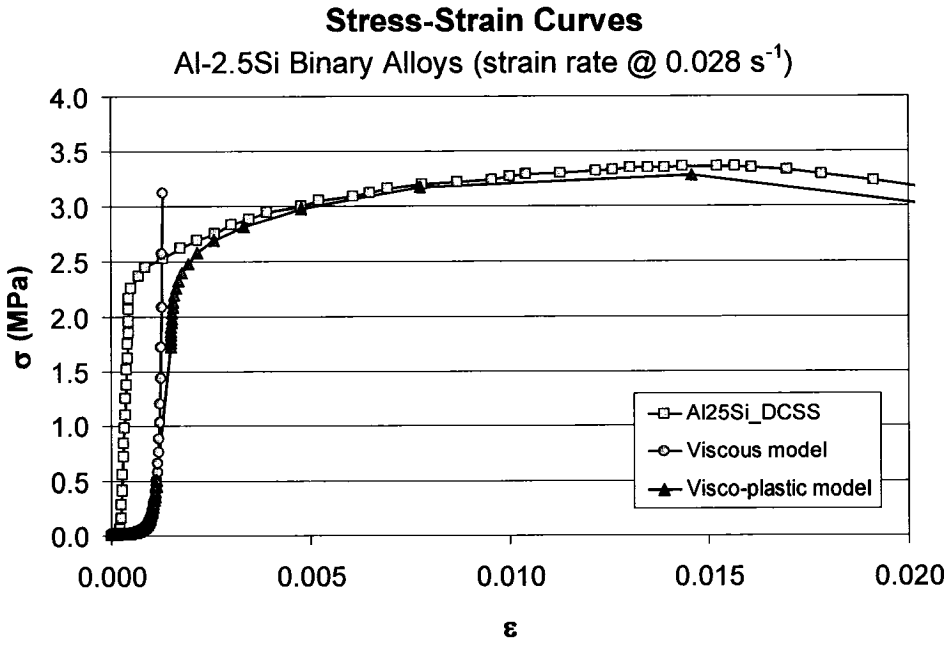

Figure 128: Theoretical model results along with DCSS experimental results (Al-2.5Si)

7.5 Microstructure analyses of the test samples

The microstructure of the tested samples was investigated to confirm the fracture mechanism taking place during the test and to identify characteristic features related to hot tearing (e.g., liquid film). The investigation was also made to support the use of a capillary force prior to fracture or separation. In fact, one observed phenomenon during the test suggests the use of capillary force at the maximum deformation.

Surface exudation of eutectic liquid was commonly observed at the surface of the sample just prior to applying the tensile loading (Figure 129). As soon as the deformation of the semi-solid body begins, this eutectic liquid is sucked back inside the interdendritic channels. The small interdendritic channels are communicating with the surface and are stretched open by the anchors' displacement (strain). This creates a suction to compensate for the solid being pulled away (conservation of mass). This suggests also that the hot tearing is certainly initiating from the ingot surface and propagating inward.

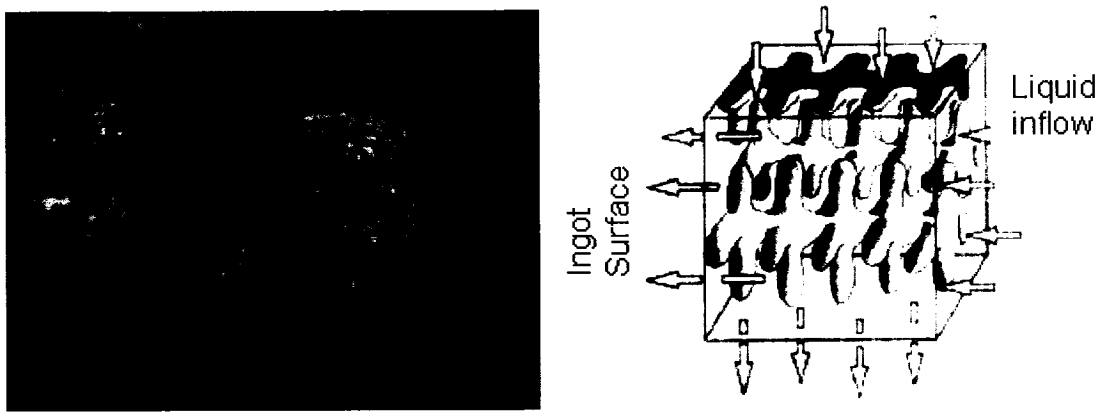

Figure 129: Liquid exudation at the surface of the sample and schematic representation

Figure 130 shows a diagram explaining the surface exudation formation and liquid movement upon straining the structure. This suggests that the fracture criterion can be estimated from the stress needed, when the liquid film is constrained (i.e., no inflow), to separate two plates bonded by capillary force. This has been reported in the literature and was used in the present work to express the fracture stress at high solid fraction (>0.99). The tensile stress will decrease as the separation distance, h, is increasing. This behaviour was used to depict the catastrophic fracture propagation in the theoretical model.

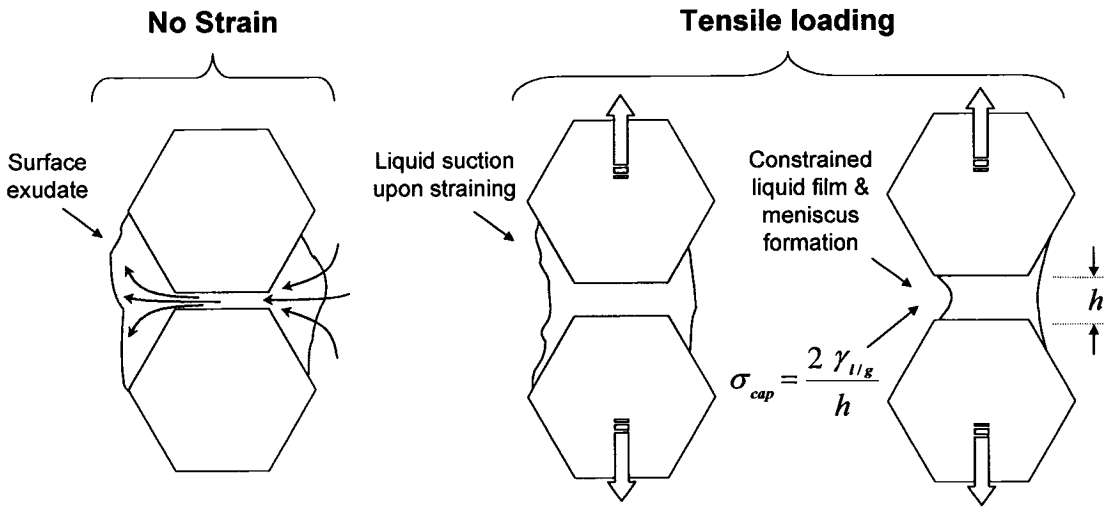

Figure 130: Diagram of the surface liquid exudates and meniscus formation (hot tear initiation)

Further microstructure investigation allowed confirmation of the above described hot tearing mechanism at the surface of a DC ingot. It can be seen that the hot tear initiated

and propagated from the surface. Generally, the mechanism is similar for all alloys except that some variant is observed depending on the solidification range of the alloys. In fact, the present investigation using three different Al-Si binary alloys shows that liquid migration can play an important role to prevent or heal incipient hot tears. Figure 131 to Figure 133 show the behaviour of the eutectic liquid upon hot tearing using the same strain rate. The low solute content alloy (Al-0.5Si) can accommodate the tensile loading from a continuous resistive stress from the constrained liquid film (low eutectic liquid volume available). On the other hand, the Al-1.5Si alloy has the largest solidification range and a fair amount of eutectic liquid.

Figure 131: Surface hot tear on Al-0.5Si alloy

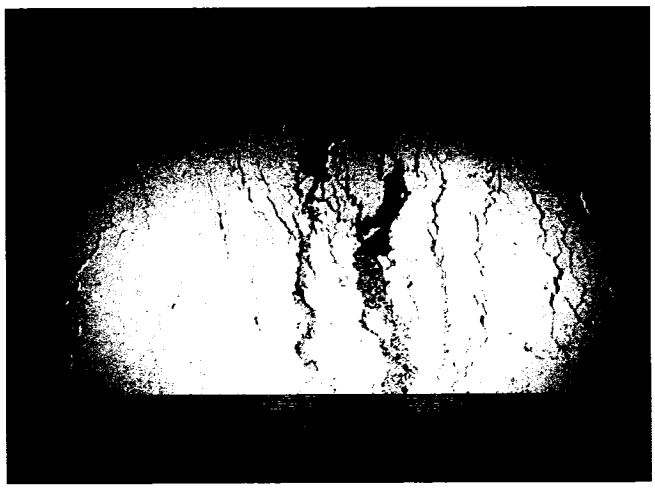

Figure 132: Surface hot tear on Al-1.5Si alloy

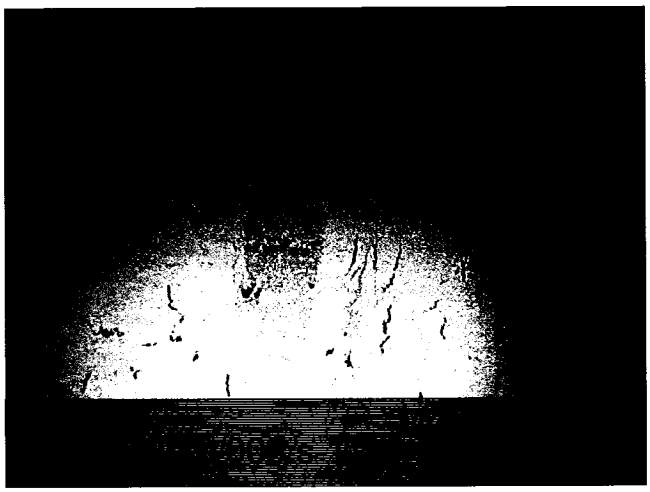

Figure 133: Surface hot tear on Al-2.5Si alloy

During straining, it is observed (Figure 132) that numerous incipient hot tears appear in the sample. As soon as the liquid films are constrained, hot tears initiate and propagate towards the bulk. At this point, the eutectic liquid moves towards the surface (mass conservation) to fill any hot tears.

However, the number of incipient hot tears is such that the eutectic liquid volume is not sufficient to feed them all. Consequently, this makes the Al-1.5Si alloy the weakest among the three alloys tested.

In the case of the Al-2.5 wt% Si alloy, the solidification range is smaller than the Al-1.5Si and there is a larger amount of eutectic liquid available compared with the other two. This makes the alloy behave differently when submitted to a tensile load. Figure 133 shows fewer hot tears generated in the strained sample. The large amount of eutectic liquid is immediately rushed towards the hot tears that have initiated during the tensile loading and further propagation is prevented (hot tear healing).

The microstructures show the eutectic liquid behaviour on the different binary alloys submitted to tensile loading. The larger solidification range of the Al-1.5wt%Si shows to some extent the mechanism taking place during the tensile loading. It can be seen that many channels opened up at various locations followed by the migration of the eutectic liquid towards the incipient hot tears. The eutectic liquid is in a relatively smaller portion compared with higher solute rich alloys (Al-2.5 wt% Si) and not able to back fill the numerous channels. Consequently, the probability of having an incipient hot tear propagate under the load is larger for this alloy or an alloy showing similar behaviour. On

the contrary, the Al-2.5Si contains more eutectic liquid available to migrate towards the incipient hot tears. In addition, it appears that the strain was more localized. This might also play an important role during the tensile loading of the microstructure. In fact, the liquid movement is migrating towards the same critical spots (volume conservation) that heal and stop the hot tear propagation. As the eutectic liquid is moving towards the surface (colder area) it wets and solidifies almost instantaneously upon reaching the solidus temperature. This process can accommodate further strain and stress before complete separation takes place.

Figure 134 to Figure 136 show the characteristic microstructure skew caused by thermal convection in the liquid also emphasized by the rotational force of the container. These figures also show the change in the microstructure scale between the surface and the sub-surface. This change in the microstructure scale is the basis of the proposed crack propagation coefficient (CPC). It appears that the effect is more pronounced in the higher solute concentration alloy (Al-2.5wt%Si). This could be related to the solid/liquid interface disturbances that have affected both the constitutional undercooling and growth direction. Indeed, the liquid movement induced by thermal convection and by the rotation (forced convection) caused the columnar grain to grow with a certain angle.

However, it is believed that this particular microstructure orientation might have a minimum impact on the final results. In fact, all samples were subjected to a similar convective current (same rotational speed for the container).

Figure 134: Typical skewed microstructure caused by thermal convection (Al-0.5wt%Si)

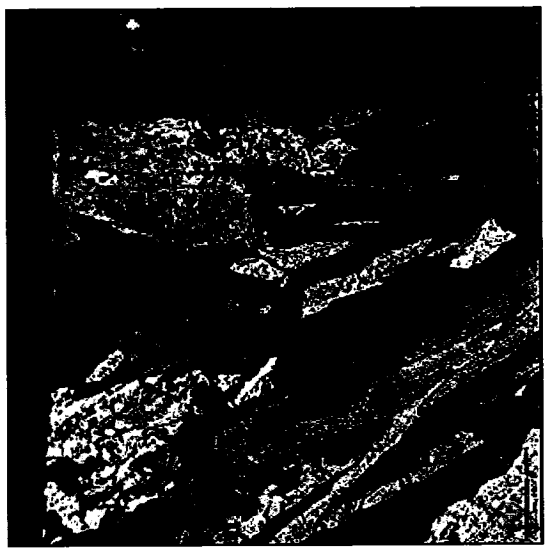

Figure 135: Typical skewed microstructure caused by thermal convection (Al-1.5wt%Si)

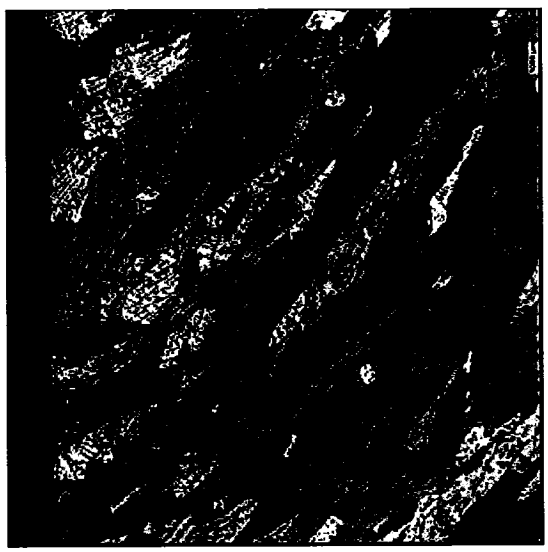

Figure 136: Typical skewed microstructure caused by thermal convection (Al-2.5wt%Si)

The higher solute alloy (Al-2.5 wt% Si) shows a somewhat more skewed microstructure. Nevertheless, the columnar grains were growing in the opposite direction from the heat flux (chill plate) and remained perpendicular to the tensile loading.

Figure 137 shows that upon separation of the microstructure under the tensile loading, all individual grains were separated along the grain boundaries without noticeable deformation. This suggests that a liquid film was still present during the tensile loading of the samples; this is typical of a hot tear which takes place at temperature above the non-equilibrium solidus (higher cooling rate will suppress the solidus line). Scanning Electron

Microscopy (SEM) allowed study of the torn surfaces of the samples in much more detail.

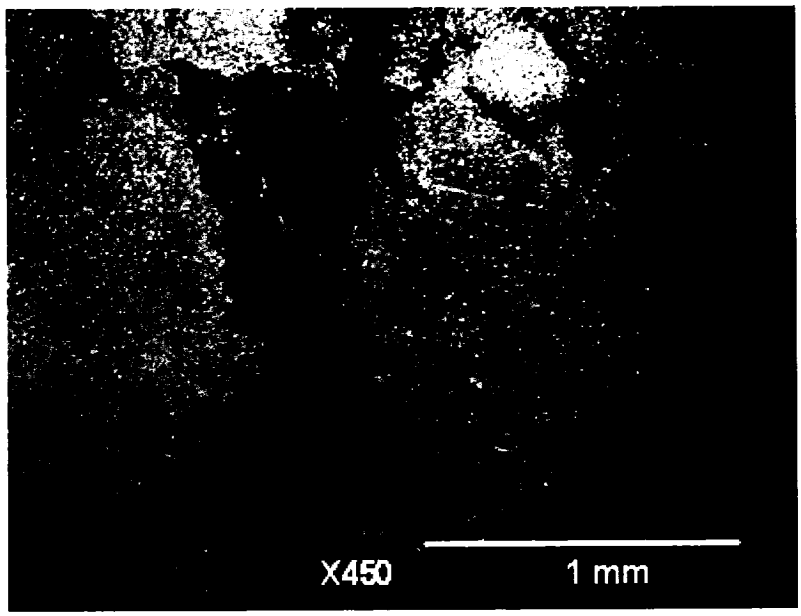

Figure 137: Individual grain separation upon tensile loading (Al-1.5wt%Si)

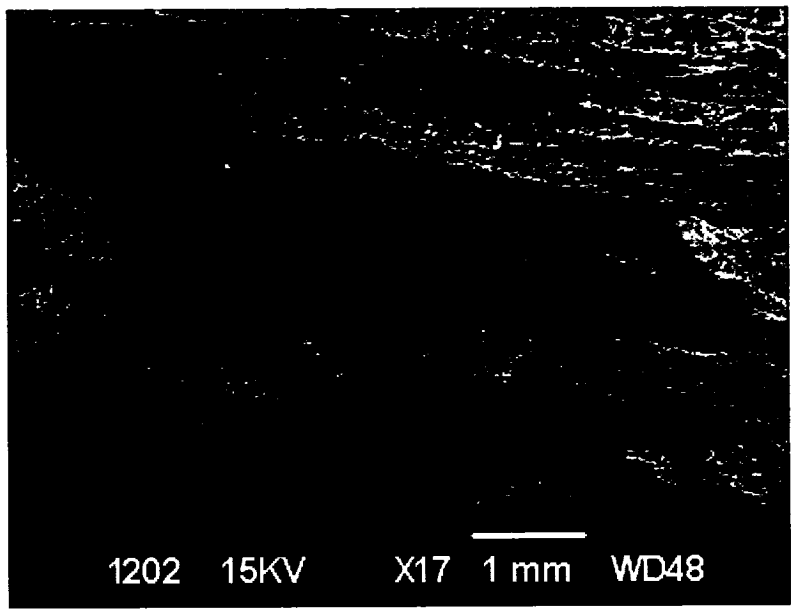

Figure 138: Fracture zone with fibrous-like structure (Al-1.5wt%Si)

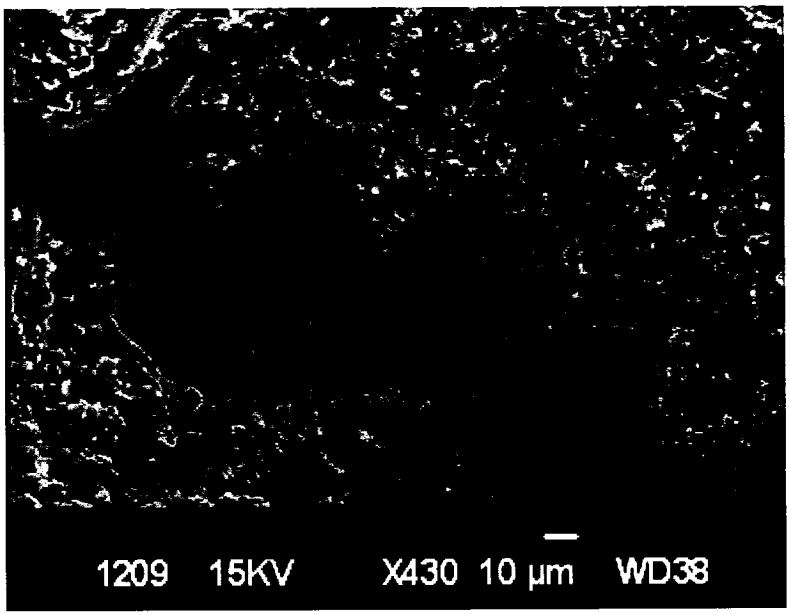

Figure 139: Fibrous-like structure with hot tear and liquid film (Al-1.5wt%Si)

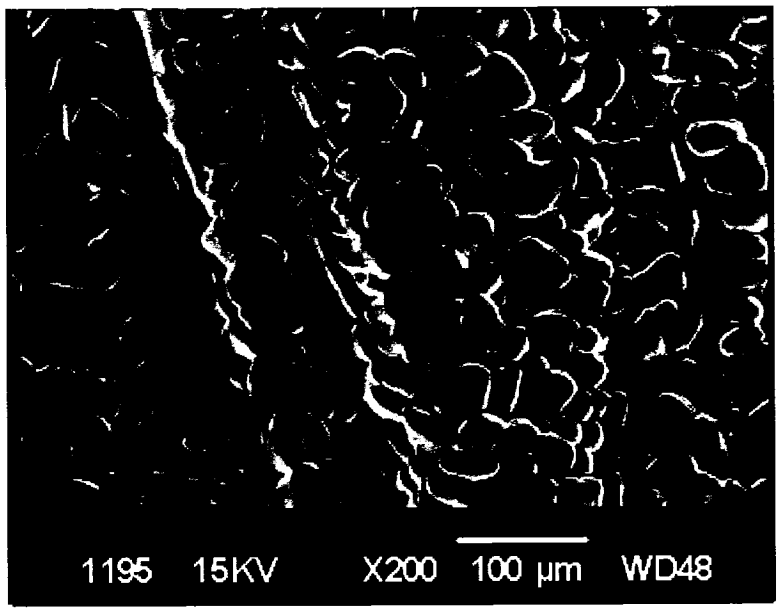

Figure 140: Typical hot tear showing the dendritic skeleton (Al-1.5wt%Si)

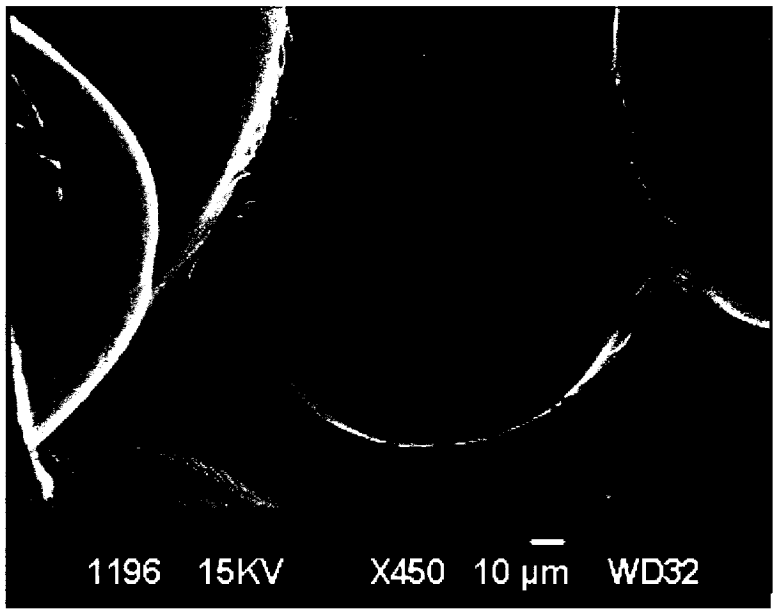

Figure 141: SEM picture confirming the presence of a liquid film upon tearing

Figure 138 shows the fibrous-like microstructure which represents the columnar grain separated from each others at rupture under the tensile strength. Figure 139 indicates that the hot tear microstructure is clearly separated with virtually no solid deformation. Figure 140 shows the characteristic structure observed on the torn surface where the dendrite trunk is shown with the secondary arms (rounded structure). Figure 141 demonstrates at higher magnification that a constrained liquid film was present upon separation. Its presence is confirmed by the characteristic wrinkles of the oxide films trapping the liquid underneath. It is seen also that the liquid was surrounding the grain structure and localized, after tearing the material, at the interface of neighbor grains or dendrites.

Chapter 8: Experimental Results: Industrial Applications of the DCSS Unit

The DCSS has been used as a tool to evaluate the hot tearing susceptibility associated with alloy castability as a function of alloying element addition and grain refiner practices based on quantitative measurements. The DCSS provided also fundamental information such as mechanical properties (stress-strain relationship) required to improve mathematical model predictability and to develop more reliable hot tearing criteria. The results below show some examples of the DCSS results used to support specific R&D activities on DC casting and alloy development program at the Arvida Research & Development Centre (Alcan).

8.1 Castability prediction for commercial alloys

The DCSS was able to rank commercial alloys in terms of their maximum tensile strengths (hot tearing resistance). The ranking was compared against low solute content aluminum alloy (AA-1050). The results showed that the resistance to hot tearing decreases as follow: AA1050 > AA-3104 > AA-5182 > AA-6111. Figure 142 shows the results presented as the inverse of the maximum tensile strength to fracture and dubbed HTS for Hot Tearing Susceptibility coefficient.

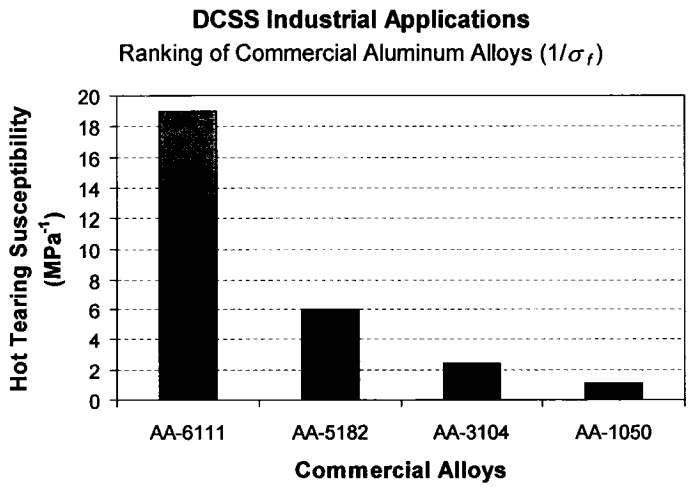

Figure 142: Ranking of commercial alloys using the DCSS

The DCSS unit was used successfully to rank commercial alloys and suggested that AA-6111 automotive alloy is the most sensitive to cast among the selected ones. DC casting production of the AA-6111 alloy variant tested with the DCSS confirmed the hot tearing sensitivity compared with standard production alloys (e.g., AA-3104). The present results were obtained according to the DCSS procedures and set-up described above.

8.2 Impact of copper addition on AA-6111 alloy

The determination of the global impact of copper addition in a AA-6111 automotive alloy was determined using the DCSS unit. The results (Figure 143) suggest that the castability of the AA-6111 alloy decreases significantly with copper addition as indicated by the higher HTS with increasing level of copper. It should be noted also that the addition of a specific alloying element might create a combined effect that could be discriminated using a proper design of experiment with the DCSS. The results are presented using the inverse of the maximum tensile stress to fracture to determine the hot tearing susceptibility index.

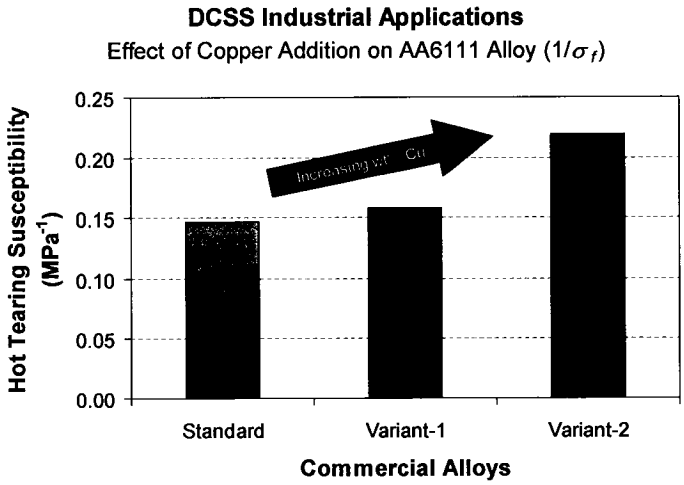

Figure 143: Impact of copper addition on AA-6111 alloy

8.3 Impact of grain refiner addition on AA-1050 alloy

The technique was also used to evaluate the impact of grain refiner on the hot tearing resistance. One specific example is given below (Figure 144) where it is possible to

differentiate the material behaviour with small grain refiner addition (2 ppm TiB_2) for AA-1050 alloy.

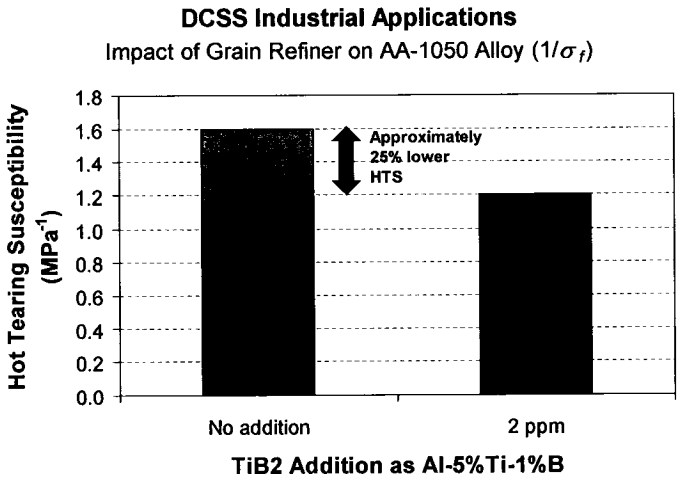

Figure 144: Impact of grain refiner addition (AA-1050)

8.4 Impact of AA-5182 alloy composition change on HTS

The ranking of different AA-5182 alloy variants using the DCSS apparatus indicated that small changes (5-10%) in the alloy chemistry can modify substantially the alloy hot tearing sensitivity index (Figure 145). The tendency indicates that the variants No.2 and No.3 offer less resistance to strain and consequential stress during solidification.

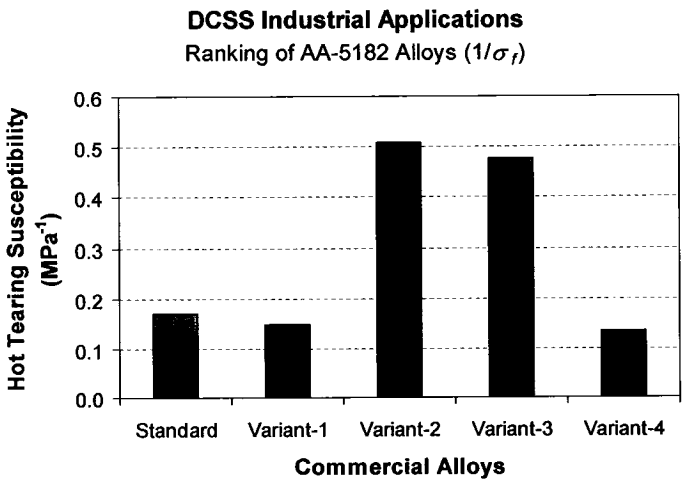

Figure 145: Effect of alloy composition change on HTS (AA-5182)

The results were confirmed during large scale DC casting of sheet ingot where attempts to cast variants No.2 and No.3 required major changes in the casting practices to prevent hot tearing. The main change was related to the casting speed which is a direct relation with the strain rate known to affect the strength to fracture during DCSS experiments.

Chapter 9: Theoretical Model for Hot Tearing

9.1 Theoretical Model

The present work proposes an improved version of the model initially developed by Drucker [96] and later extended by Lahaie [99] to predict the average stress at different levels of strain. Drucker [96] analyzed the mechanical response of an idealized semi-solid body (Figure 146). The body was assumed to be made of equally spaced regular hexagonal cylinders representing the columnar structure of the primary solid phase. Drucker [96] derived an expression for the average stress at the onset of deformation in terms of strain rate, viscosity and fraction solid.

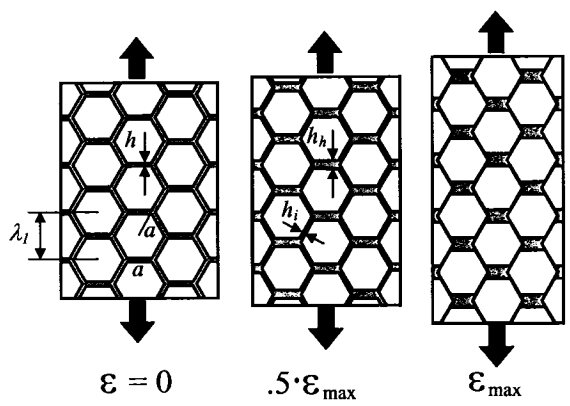

Figure 146: Schematic of the deformation of a semi-solid body

It should be noted that the development made by Drucker [96] follows from the zero relative motion condition, i.e., no strain. On the contrary, the analysis performed by Lahaie and Bouchard [99] included a non-zero strain consideration. Nevertheless, the model did not take into account some important metallurgical features that best describe the solidifying material (e.g., dendrite arm spacing) and the crystallographic representation was not complete (i.e., fully symmetrical) which made the final mathematical expression somewhat more complicated. Consequently, the model presented in this work includes important metallurgical features along with a much more symmetric and representative compact structure in 3D using a rhombic-dodecahedra crystal. More details about the complete mathematical development and relationships are found in Appendix I.

In fact, the physical model of the grain boundary is idealized by using an array of hexagons with edges of size, a, surrounded by a continuous liquid film thickness, h. This assumption suggests that the dendrite trunk arrangement is a close-packed hexagonal. This approach was first presented by Drucker [96] and later by Campbell [15] and also by Lahaie [99] to conceptualize hot tearing mechanisms and analyze the impact of various contributive parameters. The present work will use the basis of this physical model as it idealizes simply the development and growth of the microstructure. Figure 147 shows the physical correspondence of the model to the hexagonal microstructure.

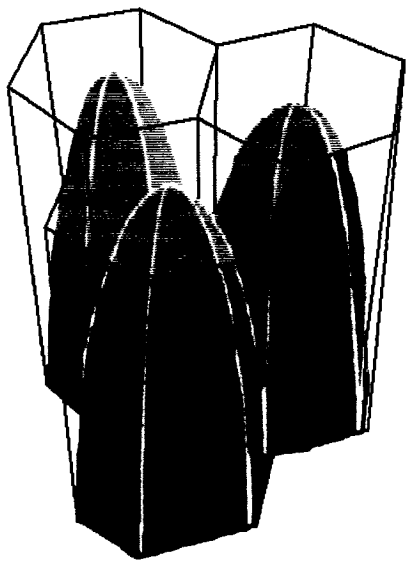

Figure 147: Diagram of the close-packed hexagonal arrangement of the dendrite trunks

Other quantities such as the growth velocity, V and the temperature gradient, G were determined from the experimental results and used in a probalistic model (cellular automata) to simulate the microstructure near the surface of the chill plate. The present work is intended to explain analytically the mechanisms that deal with the contribution of thermal, mechanical and fluid flow. The main objective is to identify the specific contribution of various parameters on hot tearing propensity. The liquid movement caused by solidification contraction and the imposed strain would impact to a certain extent the hot tearing mechanism. However, these aspects were not included in the present work since it is believed that the surface hot tears observed at the surface of the DC cast ingot involve other mechanisms. Actually, the liquid movement from the surface

was frequently observed during the DCSS experiments (Figure 129). This suggests that only this segregated liquid (exudates) plays a role during the first stage of the surface deformation (small strain).

The maximum stress builds rapidly to reach the maximum stress causing the separation of the microstructure. The fracture stress, at this stage, is governed by the surface tension of a thin liquid film constrained between two horizontal plates. Nevertheless, a more complete analysis would have dealt with complex coupled phenomena that can be addressed only by mathematical models and proper constitutive laws. The coupled phenomena would have involved the contribution from thermal, mechanical, fluid flow and microstructural evolutions but this was not within the scope of this work.

In addition, to the rationalized model, a creep law is added to describe the plastic behaviour of the stress-strain curves obtained from the experiments. Finally, a propagation coefficient is suggested based on the predicted microstructure obtained from a cellular automaton (probalistic model) to depict the typical material behaviour during the complete separation (i.e., propagation and separation). The general expression (see Appendix I for the complete mathematical development) for the viscosity-induced stress can be re-written as below:

$$\sigma_{visc} = \frac{\mu\dot{\varepsilon}}{9}\left[\left(1 - g_s^m - \frac{\varepsilon}{2}\right)^{-3} + 2\left(1 - g_s^m + \varepsilon\right)^{-3}\right] \qquad \textbf{Equation 38}$$

where g_s is the volume solid fraction, m a microstructure factor, μ the viscosity of the liquid phase, ε the uniaxial strain and $\dot{\varepsilon}$ the uniaxial strain rate. The strain was defined (see Appendix I) to take into account the film thickness and the primary arm spacing as:

$$\varepsilon = \frac{h_h - h}{\lambda_1} \qquad \textbf{Equation 39}$$

As mentioned above, the primary arm spacing λ_1 has been added to the model to define the strain. The term λ_1 is the center-to-center distance between two adjacent grains and by definition represents the grain size. It is therefore more representative of the microstructure under the tensile stress. In addition, the primary arm spacing λ_1 is related to the channel thickness h and the volume fraction solid g_s.

The idealized equiaxed grains in a spatial representation are shown in Figure 148. The three equally spaced rhombic dodecahedra show similarities with the hexagonal structure when looking at the trunk of the columnar structure (Figure 147). The solid fraction evolution in the theoretical model is defined according to Figure 149.

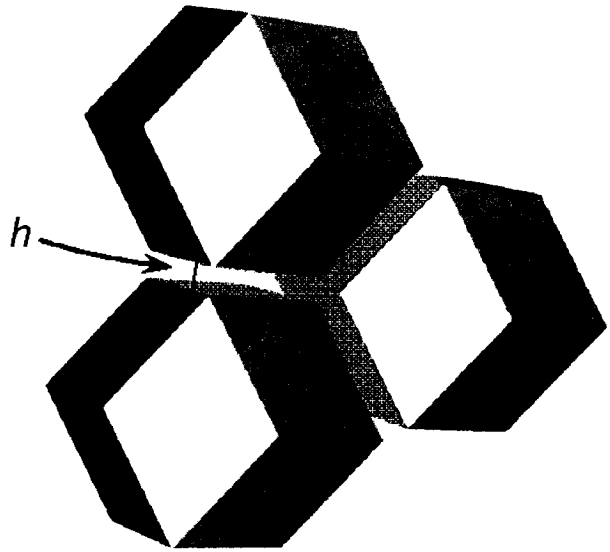

Figure 148: Rhombic-dodecahedra separated by a liquid film of thickness, h

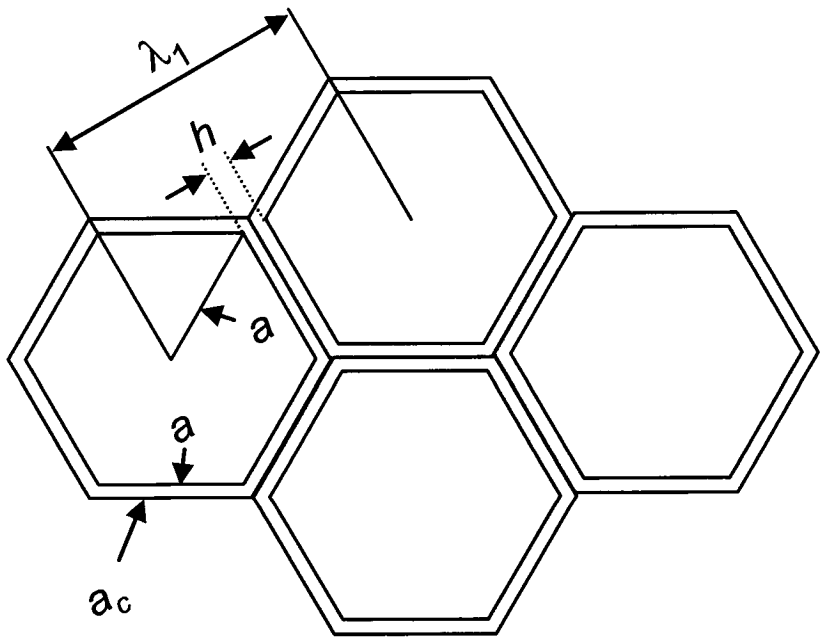

Figure 149: Hexagonal grain showing the liquid film solidification

The volume fraction solid for equally spaced hexagonal prisms, is given by:

$$g_s = \left(\frac{a}{a_c}\right)^2 \qquad \textbf{Equation 40}$$

where

$$a = \frac{\lambda_1 - h}{\sqrt{3}} \qquad \textbf{Equation 41}$$

and

$$a_c = \lambda_1 / \sqrt{3}\,. \qquad \textbf{Equation 42}$$

Solving for *h*, one obtains:

$$h = \lambda_1\left(1 - g_s^{\,1/2}\right) \qquad \textbf{Equation 43}$$

Figure 150 shows the rhombic dodecahedron arrangement composed from a cube of edge length a_c , upon which is affixed a square pyramid of height ½ a_c on each of the six faces.

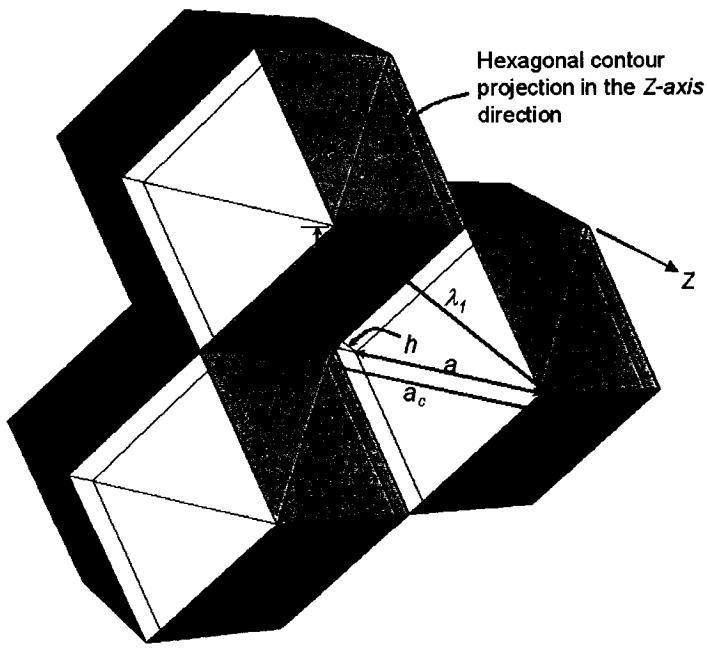

Figure 150: Diagram of the packed hexagonal grains projection towards the Z-axis

The parent cubes are shown in Figure 150 when looking at the line at the base of the pyramid of three rhombic dodecahedra. The volume of the rhombic dodecahedron is equal to $2a_c^3$. This includes the volume of the parent cube (a_c^3) and the volume of the six square pyramids, each having a volume equal to $a_c^3/6$.

In order to calculate g_s for equally spaced rhombic dodecahedra, one can consider that the space is filled with rhombic dodecahedra having a parent cube edge length a_c , each enclosing a smaller and centered (solid) rhombic dodecahedron having a parent cube edge length *a*. This is the same analogy to a sphere having a radius r1 that *grows* to a new radius r2. The change in volume is given by the ratio of the radii to the cube. For this arrangement the volume fraction solid is given by:

$$g_s = \left(\frac{a}{a_c}\right)^3 \qquad \textbf{Equation 44}$$

Figure 148 shows that the liquid channel thickness *h*, and the primary arm spacing λ_1 are connected with the parent cube edge lengths. According to this figure, we have the following relationships:

$$a_c = \lambda_1/\sqrt{2} \qquad \textbf{Equation 45}$$

$$h^2 = (a_c - a)^2 + (a_c - a)^2 \qquad \textbf{Equation 46}$$

$$a = \frac{\lambda_1 - h}{\sqrt{2}} \qquad \textbf{Equation 47}$$

Solving for *h*, one obtains:

$$h = \lambda_1\left(1 - g_s^{1/3}\right) \qquad \textbf{Equation 48}$$

Therefore, assuming a microstructure made of equally spaced hexagonal cylinders (m = 1/2) or equally spaced rhombic dodecahedra (m = 1/3), the channel thickness can be expressed by Equation 49.

$$h = \lambda_1\left(1 - g_s^m\right) \qquad \textbf{Equation 49}$$

The factor *m* takes a value of ½ for equally spaced hexagonal cylinders (columnar microstructure) and 1/3 for equally spaced rhombic dodecahedrons (equiaxed microstructure). Even though Equation 49 is exact for a microstructure composed of equally spaced rhombic dodecahedrons, the applicability of Equation 38 has not been validated so far and therefore the present analysis will involve the 2D case only where *m* =1/2.

9.2 Creep Law

The improvement made to the viscous model in the present work allowed better visualization of the role of the primary arm spacing and the impact of a more appropriate crystal structure on the final mathematical notation. However, the theoretical model could not reproduce the stress-strain curves generated by the DCSS unit especially in the plastic portion and the propagation of the hot tear. In fact, the real metallurgical microstructure shows a complex morphology that is not equally spaced or perfectly oriented in space. Consequently, strain accommodation of the network should involve some sliding and pushing of the grains (Figure 151). As the strain increases, the grain boundaries become more and more subjected to friction sliding and oppose a higher resistance than a fully lubricated sliding condition (liquid surrounding the grains).

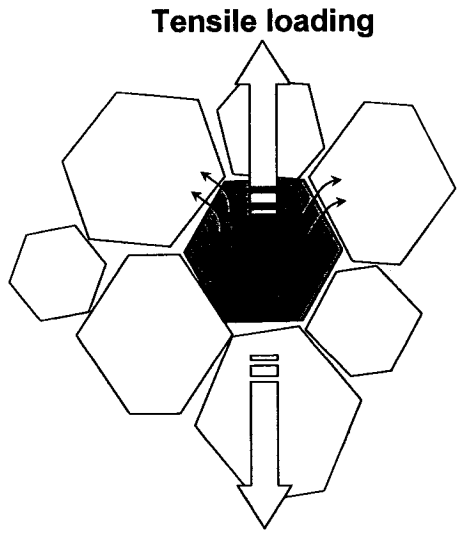

Figure 151: Diagram of grain sliding touching and pushing upon tensile loading

This results in a gradual increase of strain with stress. Figure 151 suggests the mechanism that might occur during the tensile loading.Some grains are taking more loading force and push away others that are less constrained within the network. This rearrangement still take place at a relatively low strength since virtually no deformation is observed on the torn surfaces.

Nevertheless, a close look at the microstructure (Figure 152) shows apparent mechanical locking or welding that certainly contributed to some extent to the overall strength of the material.

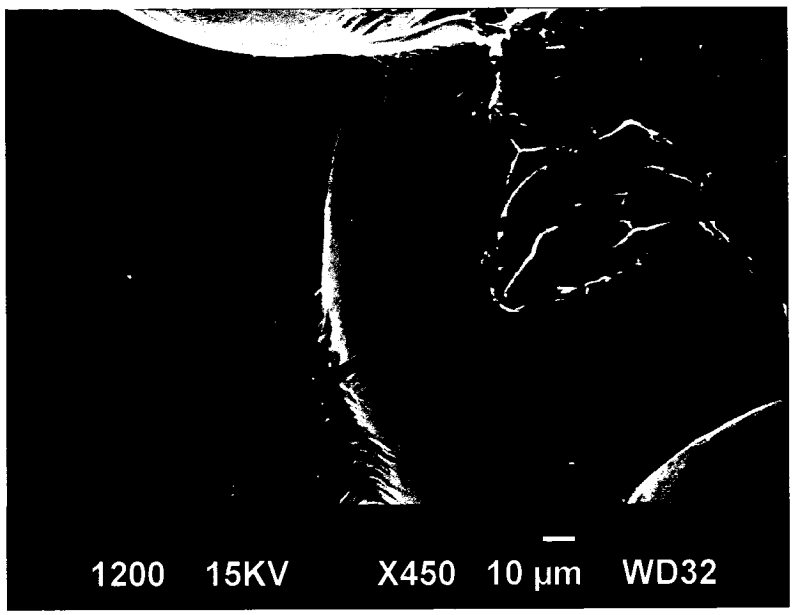

Figure 152: Hot tear from the DCSS experiment showing a torn surface (arrow) on a dendrite arm initially surrounded (wrinkle) by the eutectic liquid (Al-1.5wt%Si)

Indeed, Figure 152 shows a dendrite surface zone where an intimate contact has been broken or torn. The wrinkles observed on the dendrite arm surface indicate that liquid was present during the tearing process. The interface compatibility between the liquid and the solid is such that the remaining eutectic liquid welds the structure upon solidification. Therefore, based on the DCSS results and the microstructure investigation, a more complete model is proposed using the following two main mechanisms, a) a viscous flow, and, b) a creep behaviour to sustain the high temperature deformation at slightly higher stress.

The first portion of the model deals with the viscous behaviour during deformation of a semi-solid material but cannot alone explain the stress at higher deformation. In order to better describe the material behaviour in the plastic region, a typical creep law was added to the model based on a specific solid fraction ranging from 0.97 to 0.99. After this solid fraction is reached, a microstructure coefficient is used to explain the rapid and catastrophic propagation and the complete separation. The microstructure coefficient is dubbed CPC for *Crack Propagation Coefficient*. The latter is based on the fact that the solid fraction and grain morphology form a tight interdendritic bridging such that no flow is possible, i.e., all liquid films are constrained. Upon reaching the maximum stress and strain, the catastrophic rupture and propagation is believed to be the result of the distribution of the tensile load over a uniformly and geometrically distributed thicker liquid film. Consequently, the maximum fracture strength, σ_{cap} (Equation 53) is rapidly inversely proportional to the change in the film thickness to which the maximum load is applied. The proposed CPC is covered in more detail in the section related to the microstructure modeling using a cellular automaton (Chapter 10:).

However, this proposed theory assumed that the local solid fraction is variable and depends on the strain, ε because of the liquid segregation and inflow that might also affect the local temperature.

The creep law applied in the present work considered the dependence of a dissipation potential for the visco-plastic deformation that is a function of the volume solid fraction and deformation. One of the possible forms of this dependence is given by a hyperbolic sinus type semi-empirical power-law as proposed by Sellars and Tegart [105] for creep deformation (Equation 50).

$$\dot{\varepsilon} = \beta \, exp\left(-\frac{Q}{RT}\right)\left[sinh(\alpha\sigma)\right]^n \qquad \textbf{Equation 50}$$

The terms in the creep law are:

$\dot{\varepsilon}$: Strain rate, (s^{-1})

β, α, n: Representative material constants that fits the experimental results

σ_c: Critical fracture strength (MPa)

Q: Activation energy that fits the experimental results, (kJ/mol)

R : Perfect gas constant, (J/K/mole)

T : Temperature, (K)

This creep law is recognized [106,107,108] to fit the experimental results relatively well over a wide range of strain rates (10^{-8} to 10^{2} s^{-1}) or stresses for high temperature deformation of various metals and in particular for aluminum and its alloys.

The creep law was derived as a function of time to determine the strain and the stress at different temperatures and then applied to the volume solid fraction ranging between 0.97 and 0.99. The total strain corresponds to the maximum strain obtained from the viscous flow model and the plastic strain (creep). In other words, the activation of the third creep stage (Figure 153) normally termed plastic in this work takes place when the solid fraction is between 0.97 and 0.99, i.e., when $\varepsilon = \varepsilon_{0.97}$ and $\varepsilon = \varepsilon_{0.99}$.

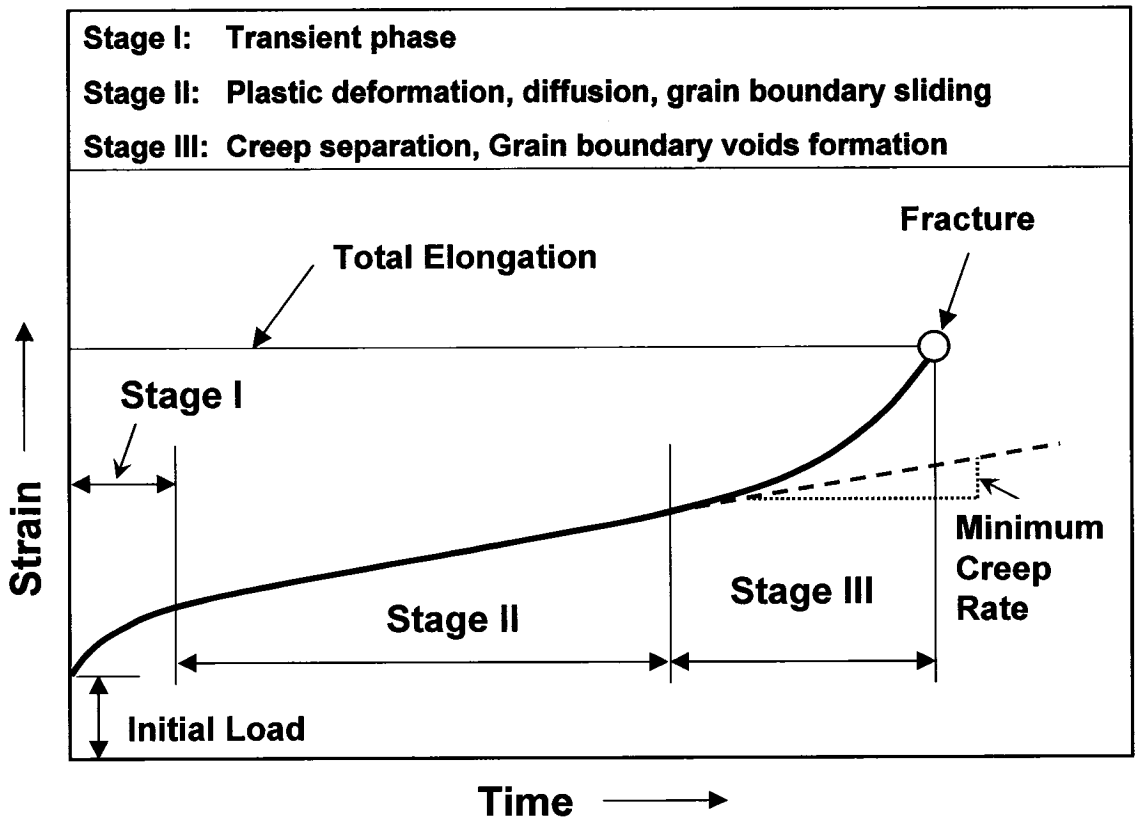

Figure 153: Diagram showing the three creep regimes proposed in this work

However, the validity of this type of creep law must be done over a larger range of temperature and strain rate in the second stage (Stage II). In the case of the DCSS,

these two variables are quite similar. It is assumed that hot tearing or fracture takes place when the solid fraction is greater than 0.95 (i.e., f_s (ε) >0.95). Consequently, in the present context the term "Creep Separation" is proposed as a stage close to the third creep stage (Stage III) during which there is formation of voids. It is recognized [113] that grain boundary sliding stimulates nucleation of grain boundary voids.

Table 1 below shows the creep parameters used for the different binary alloy systems. This volume solid fraction criterion was arbitrarily chosen based on values stipulated in the literature but also measurements taken on the microstructure at high magnification (SEM). This confirmed the presence of a thin film of a few microns surrounding the grains prior to separation (Chapter 7:, Figure 141).

Table 1: Creep law parameters for each Al-Si binary alloys

Parameters	Al-0.5Si	Al-1.5Si	Al-2.5Si
α (MPa-1)	0.09	0.08	0.08
n	4.7	4.7	4.7
Q_a (kJ/mole)	190	196	196
ln(β)	43.6	48	48
β	8.61E+18	7.02E+20	7.02E+20
R (J/K/mole)	0.008314	0.008314	0.008314
$\dot{\varepsilon}$ (s^{-1})	0.026	0.026	0.026

These parameters allowed reproduction of the plastic portion of each stress-strain curve in good agreement with the experimental results. It is interesting to note also that the apparent activation energies for all Al-Si binary alloys are significantly higher than the self-diffusion energy of pure aluminum ($Q_a \cong 150 KJ/mole$). This suggests that the deformation process of the selected Al-Si binary alloys is not controlled by diffusion for the present experimental strain rate and temperature.

In the present work, it is assumed that the creeping mechanism takes place when the local volume solid fraction is between 0.97 and 0.99. It is assumed also that only two mechanisms are present based on the change in the film thickness, h. The thickness of the liquid film, h, was transposed into volume solid fraction where the viscous flow is

suggested to operate between a volume solid fraction of 0.95 and 0.97 and the creep law from 0.97 to 0.99.

Consequently, the average stress will be given by the following statement:

$$\sigma_{avg} = \int_{g_s^{0.95}}^{g_s^{0.97}} \sigma_{visc}\, dg_s + \int_{g_s^{0.97}}^{g_s^{0.99}} \sigma_{creep}\, dg_s \qquad \textbf{Equation 51}$$

In the above equation, σ_{visc} is the viscous strength component of the stress given by Equation 38 and σ_{creep} is deduced from the creep law given by the Equation 50. The total strain is assumed also to have only two components, i.e., the viscous and the creep contributions, respectively.

$$\varepsilon_{total} = \varepsilon_{visc} + \varepsilon_{creep} \qquad \textbf{Equation 52}$$

Finally, it is proposed that when the maximum stress is exceeded, Equation 53 will predict the complete separation and represent a fracture criterion for a semi-solid body with constrained capillaries at its free surface.

$$\sigma_{cap} = \frac{2\,\gamma_{l/g}}{h_{cap}} \qquad \textbf{Equation 53}$$

This approach has been used previously [27,95,99,109] to determine the fracture stress during hot tearing. Indeed, the critical fracture strength, σ_{cap} represents an inherent property of the microstructure. The results obtained were in the range of 0.1 to 10 MPa and correspond quite well to the experimental DCSS results. It should be mentioned here that the hot tearing observed during DC casting of sheet ingot is a surface or sub-surface defect. Consequently, the present fracture criterion should describe the hot tearing based on numerous observations made during casting, the DCSS results (surface liquid exudates back flow upon applying the tensile load) and microstructure investigations showing hot tears open to surface (Figure 154, Figure 118, Figure 120). This fracture stress was used in the creep law to determine the last creep stage after the viscous flow regime ended upon reaching a volume solid fraction of 0.97. In fact, it is

assumed that the end of the visco-plastic regime corresponds to a solid fraction of 0.97 followed by "Creep Separation" (Figure 153) for solid fraction above 0.97.

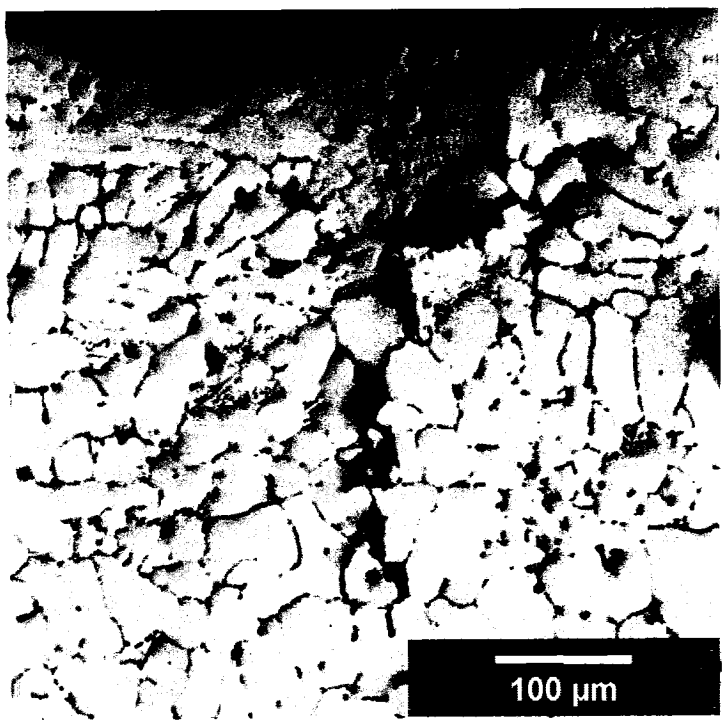

Figure 154: Typical hot tear at the surface of a DC cast ingot

The DCSS experimental results of the Al-Si binary alloys showed that the strength is built almost immediately after the tensile load or force was applied. The model suggested in the present work reproduced the stress-strain behaviour of the DCSS experimental results as presented in Chapter 7:.

Chapter 10: Cellular Automaton and Crack Propagation Coefficient (CPC)

The microstructure evolution during solidification plays a major role in the hot tearing phenomena. As a general rule, the hot tearing susceptibility increases as a function of the grain size and morphology. Consequently, predicting the microstructure of a given alloy during solidification gives insights to determine key parameters related to the hot tearing phenomena. In this work, a model microstructure that includes the mechanisms of heterogeneous nucleation and grain growth was applied for two purposes, a) to simulate the pre-dendritic surface microstructure (i.e., nucleation sites) obtained during the experiments and, b) to derive a crack propagation coefficient (CPC). In fact, the CPC will be used to simulate more specifically the stress-strain curves zone indicating the microstructure de-cohesion (visco-plastic zone) as seen during the DCSS experiments.

The model is based upon a 2D cellular automata technique. This method based on a finite element using a 2D cellular automaton has been proposed by Rappaz [97,98] to model microstructure. However, Brown and Spitle [100] have developed the approach based on a probalistic concept. These authors have adapted to the case of solidification, the Monte Carlo procedure which has been developed by Srolovitz [101] for treating grain growth.

The modeling uses a matrix with a number of cells having the same dimensions. The cells are attributed with different properties such as the state (liquid or solid) and the crystallographic orientation. The cell properties evolve according to the nucleation and growth laws.

10.1 Nucleation law

Figure 155 summarizes this nucleation model which assumes a continuous dependence of n(t) to temperature (T). The initial nucleation site density is represented by n_O and is directly related to the size of the matrix described in the cellular automaton (CA) model (Appendix VIII).

The nucleation rate assumes a Gaussian distribution with respect to the undercooling ΔT where ΔT_n represents the average undercooling and ΔT_σ the solutal undercooling termed standard deviation in the CA model. At a given undercooling, ΔT, the grain density is given by the integral of the nucleation site distribution from 0 undercooling to ΔT. The number of nuclei, n, within the liquid is given by the integral of the distribution.

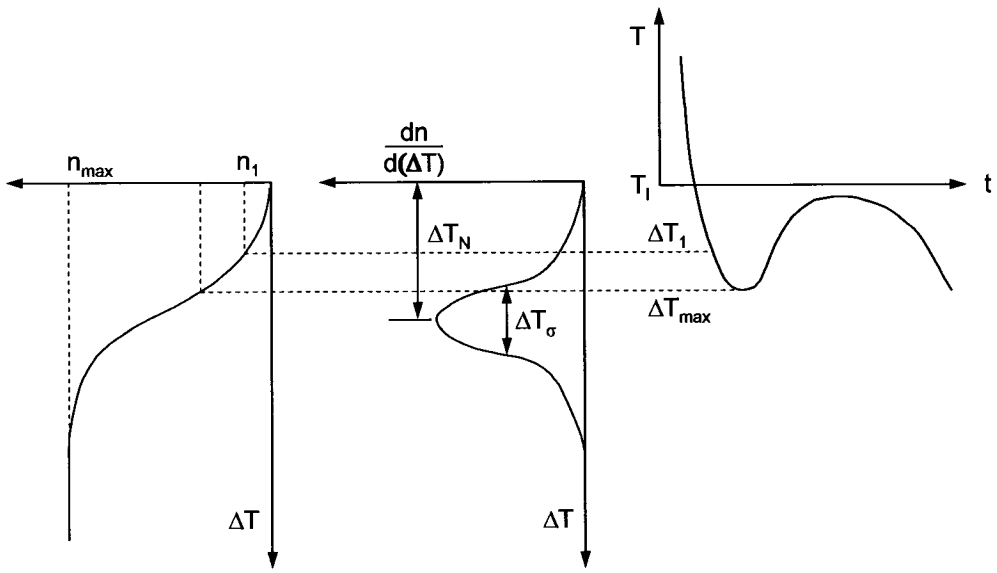

Figure 155: Nucleation model giving the nuclei density distribution probability (Gaussian)

$$\dot{n} = \frac{dn}{dT} = \frac{n_o}{\sqrt{2\pi}\,\Delta T_\sigma} \exp\left(-\frac{(\Delta T - \Delta T_n)^2}{2(\Delta T_\sigma)^2}\right) \qquad \textbf{Equation 54}$$

These parameters have been adjusted in the cellular automaton model to reproduce as closely as possible the surface and sub-surface microstructures of the DCSS samples.

10.2 Growth law

The growth law is derived from the solid and liquid concentration at the liquidus temperature of the alloy (C_S, C_L), the partition coefficient (k), the distribution coefficient (p), the temperature difference between the liquidus and the solidus (ΔT_{L-S}), and finally the undercooling (ΔT).

$$k = \frac{C_S}{C_L} \qquad \textbf{Equation 55}$$

$$p = 1 - k \qquad \textbf{Equation 56}$$

$$\Omega = \frac{\Delta T}{p\Delta T + k\Delta T_{L-S}} \qquad \textbf{Equation 57}$$

$$V = \frac{\Omega^2 D_L}{\pi^2 G} \cdot \frac{k\Delta T_{L-S}}{1 - \Omega p} \qquad \textbf{Equation 58}$$

Table 2: Growth law parameters (Al-Si alloys)

Parameters	Al-0.5Si	Al-1.5Si	Al-2.5Si	Units
C_S	0.5	1.5	2.5	%Si
C_L	0.065	0.195	0.325	%Si
ΔT_{L-S}	94	89.4	86.9	K
D_L	3E-9	3E-9	3E-9	m^2s^{-1}
G	9E-8	9E-8	9E-8	$K.m^{-1}$

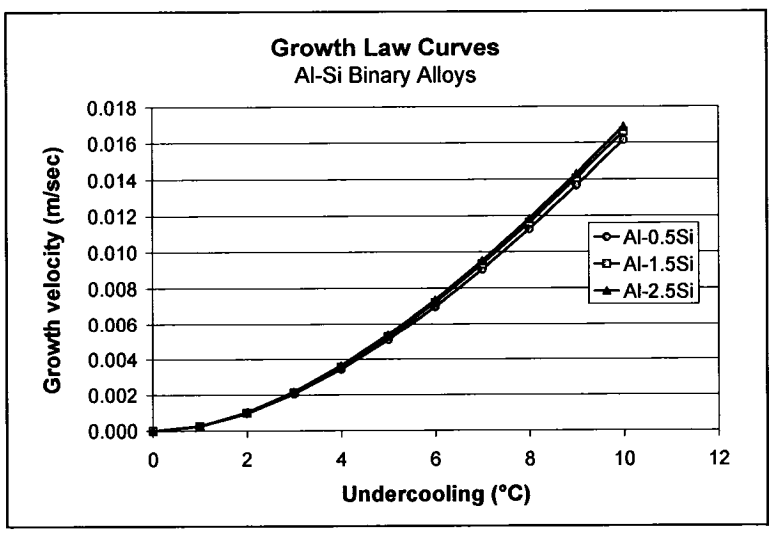

Figure 156: Growth law curves (Al-Si growth parameters)

Table 3: Input variables for the Cellular Automaton model

Parameters	Descriptions	Values
dt	Time interval between each step (sec)	0.005
l	Network step value, cell size (meter)	0.000001
ΔT	Undercooling removed before every iteration (°C)	0.01
SΔTn	Maximum rate for the surface nucleation law	0.2
SΔTs	Standard deviation for the surface nucleation law	0.1
BΔTn	Maximum rate for the bulk nucleation law	2.35
BΔTs	Standard deviation for the bulk nucleation law	0.2
#	Number of cells between surface asperities	4

The cooling rate is simulated by choosing the undercooling and the time step accordingly. A cooling rate of 2°C/sec was selected and represents the average cooling rate measured near the ingot surface during DC casting.

The microstructure model was built to study the impact of various conditions on the resulting microstructure. This approach is believed to ease sensitivity analyses to identify the main governing factors. In fact, the model was able to reproduce relatively well the surface microstructure encountered in the DCSS unit. The change in the surface and bulk nucleation coefficient as well as the surface roughness allowed identification of a general trend for the surface microstructure, namely the grain size and the derivation of the liquid film thickness near the surface. It is difficult to determine precisely the liquid fraction during hot tearing because of the liquid segregation. Consequently, the film thickness was derived from the number of grains (nucleation sites) and the size (primary dendritic arm spacing, λ_1) according to the equation proposed by Upaddhya [77]. Therefore, the results from the microstructure allowed a simple *Crack Propagation Coefficient* (CPC) to be built.

The CPC is essentially based on the change in film thickness on which the maximum fracture stress (load) is applied. Consequently, the strength during the hot tear propagation will change according to the microstructure scale defined by the cellular automaton model. It represents essentially the ratio of the film thickness at the maximum fracture strength (h_{cap}) over the new film thickness obtained from the numerically

generated microstructure (h_{micro}). The maximum fracture strength is described (Equation 53) for a semi-solid body with constrained capillaries at its free surface [109]. It was reported [111] that the tensile stress on the parallel plates decreases as the separation distance increases. In the case of hot tearing, it is assumed that when the maximum strain is reached, the separation is taking place suddenly along the increasing liquid film thickness. In fact, the grain size increases (growth competition, coarsening) from the surface to a few microns towards the bulk. Considering a constant volume liquid fraction at this moment, an increase in the grain size will cause the liquid film surrounding the grains to be thicker (less solid surface area). In reality, liquid segregation and inflow will contribute to increase the local liquid fraction. However, the impacts of these mechanisms are beyond the scope of the present work.

10.3 Microstructure results from the Cellular Automaton

Figure 157 to Figure 160 show the results of the cellular automaton with the parameters used to simulate the microstructure. The results presented here are the Al-0.5 wt% Si. Basically the outputs were similar for the Al-1.5 wt% Si and Al-2.5 wt% Si alloys depending on the nucleation and growth parameters used.

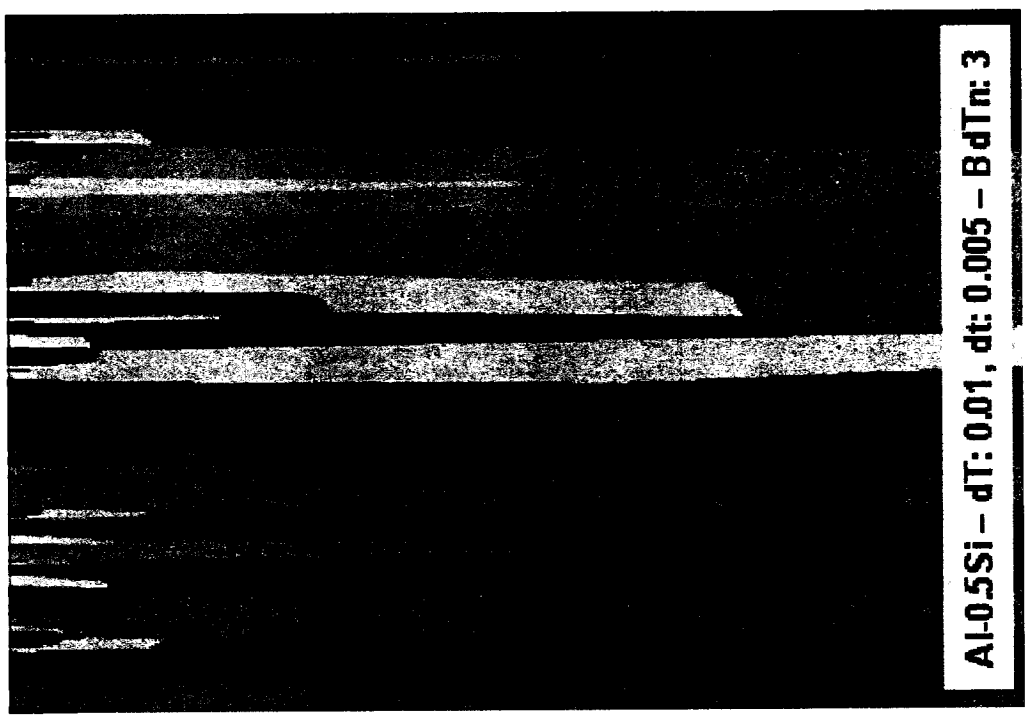

Figure 157: Columnar structure (CA)

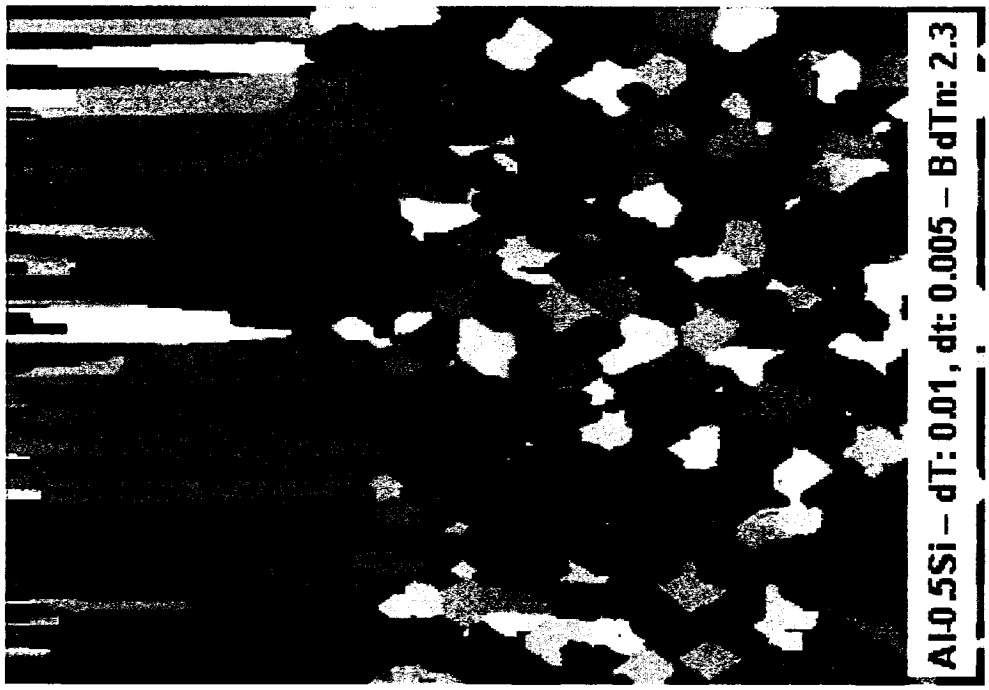

Figure 158: Columnar to equiaxed (CA)

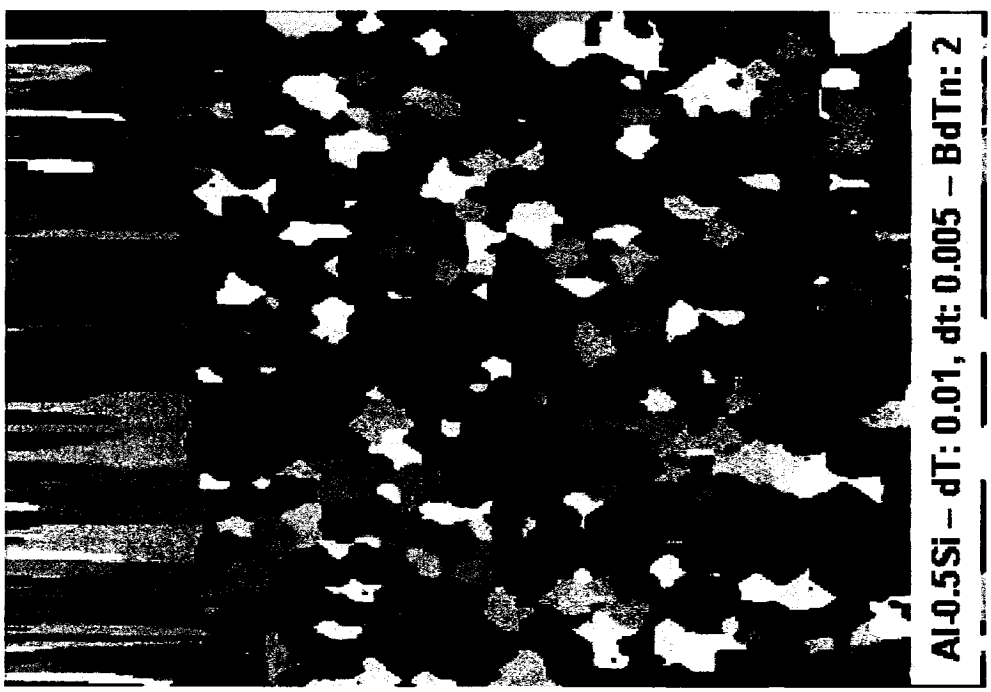

Figure 159: Nearly fully equiaxed (CA)

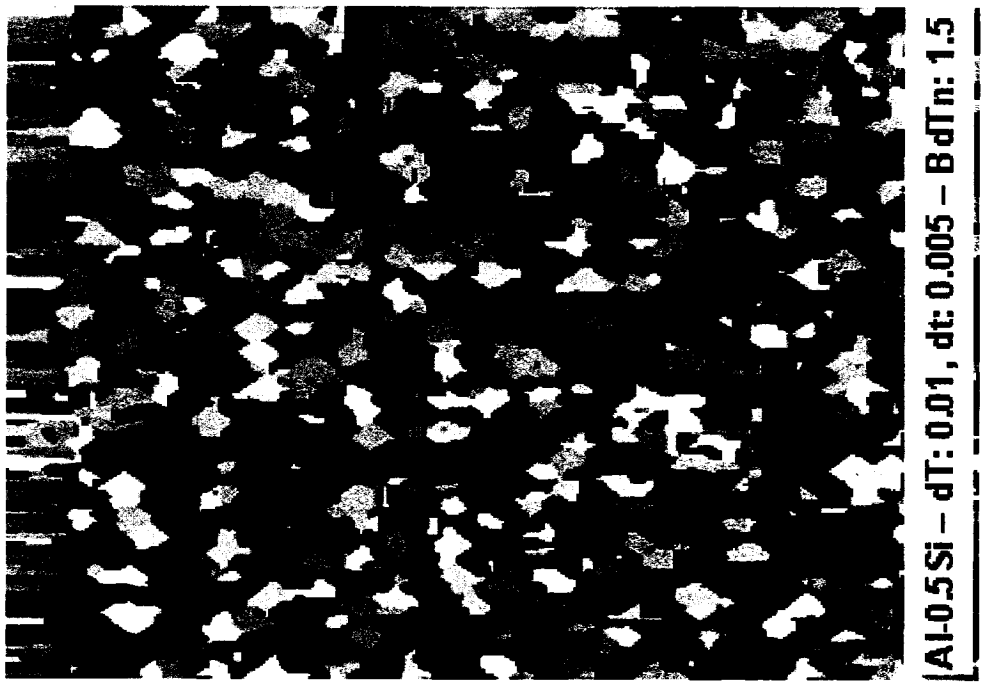

Figure 160: Equiaxed structure (CA)

Nevertheless, the change in the alloy parameters did not affect by much the growth law curves (Figure 156). Consequently, the microstructures generated at the surface were quite similar and essentially driven by the number of nuclei. It is worth mentioning here that it is beyond the scope of this work to reproduce the entire microstructure obtained during the DCSS tests. In fact, the interest was focused on the resulting microstructure at the surface of the cast sample (i.e., at the mould/metal interface).

The latter was kept constant in the model for simplicity. Only the parameters that were changed appear in the legend while the others are found in Table 3. It is seen that the microstructure morphology changes from a columnar to an almost fully equiaxed structure.

The present study is related to surface hot tearing and the microstructures obtained during the experiments are essentially columnar. Therefore, only the columnar microstructure at the very near surface was used to determine the CPC. Figure 161 shows the curve generated from the primary arm spacing (Cellular Automaton) and the change in the film thickness. This represents the Crack Propagation Coefficient (CPC) that could be simplified by a power law with the proper terms describing the microstructure. Since h_{micro} is proportional to λ_1, then h_{cap} is an independent variable (or

linked to other parameters) that could be deduced from Equation 53 using direct measurements of the microstructure. Nevertheless, this section introduces a possibility of explaining the catastrophic failure as indicated by the stress/strain curves using change in the microstructure surface and sub-surface scale and advanced solidification modeling software.

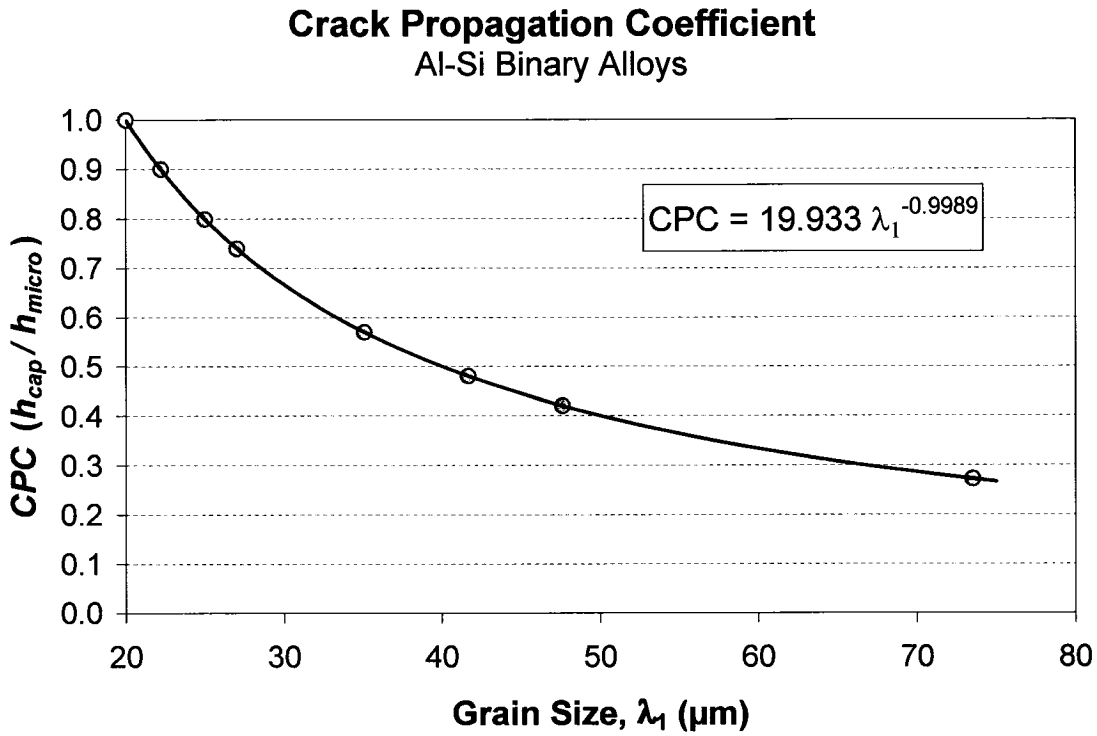

Figure 161: Crack Propagation Coefficient (CPC)

As mentioned above, the CPC corresponds to the ratio of h_{cap}/h_{micro} which generates a coefficient that varies from 0 to 1 and it is applied when the maximum strain (ε_{max}) is attained and the volume solid fraction is 0.99. Equation 59 shows the general form of the CPC where, λ_1, is the primary arm spacing (grain size in columnar structure), and A, a constant obtained from the microstructure analyses.

$$CPC = A \cdot \lambda_1^{-0.9989} \qquad \textbf{Equation 59}$$

The impact of the CPC on the stress is essentially a coefficient which is proportionally related to the change in the film thickness, *h*. Nevertheless, this is not universal since we must generate a certain number of numerical microstructures and extract a representative average of the grain intercepts used to calculate the change in liquid film thickness. The results of this approach suggest a potential way to describe the propagation after the maximum strain is taken by the semi-solid material and the hot tear is initiated.

The process could become more standard by characterizing the surface and sub-surface samples obtained from the DC casting process. The cooling conditions and mould surface conditions are relatively the same for the primary cooling zone and therefore a quite reproducible microstructure is anticipated.

The CPC does not fit all curves for all other alloys but it represents a criterion for the propagation and loss in strength for the alloys covered in the present work. The CPC is also based on true metallurgical features known to affect the semi-solid strength of the material under strain/stress during solidification.

Chapter 11: Conclusions

11.1 Overview

The goal of the present thesis was to understand the hot tearing mechanisms of Al-Si binary alloys. The work has been divided into various parts. The first part was related to the study of the microstructure of the hot tearing zone to be able to understand better its origin during DC casting of sheet ingot. The results of this investigation confirm that hot tearing during DC casting is a surface defect. Consequently, the second part of the work consisted of having a better experimental procedure to study the hot tearing behaviour. Consequently, a novel apparatus capable of reproducing microstructural features encountered during DC casting has been built. The unit was dubbed DCSS for *Direct Chill Surface Simulator.* The DCSS can apply and measure tensile force and surface deformation during solidification. Many tests were done with the DCSS unit to measure the mechanical response of specific alloys subjected to a tensile load during solidification. The ultimate goal was to obtain the stress-strain curves and quantify the alloys in terms of hot tearing sensitivity. A non-negligible aspect of the work was to use numerical modeling to be able to understand better the DCSS approach and identify the testing conditions and parameters.

The third part of the work consisted of explaining the behaviour of the semi-solid material being tested and the relationship with metallurgical and mechanical features. This work consisted of deriving the equation to lead to a representative theoretical or phenomenological model. The model was based on work previously done but adapted with better use of the true metallurgical factor that best characterizes the tested material (Al-Si). The novelty resides in the use of known metallurgical factors combined with a creep law and a crack propagation coefficient (CPC) to better reproduce the typical stress-strain curves. The CPC was derived using a Cellular Automaton that was built to determine a general trend in the microstructure. This trend was transformed into a mathematical equation and used in the model to suggest the catastrophic separation of the microstructure upon reaching the maximum deformation.

The theoretical model has also been used to perform a sensitivity analysis on different parameters to isolate the most critical one.

It turned out that the liquid film thickness and distribution are among all, the most critical parameters. The liquid film thickness is intimately linked with the grain size and the solidification range of the alloy.

The DCSS apparatus has also been used to quantify the hot tearing sensitivity of commercial alloys. The results showed that the DCSS apparatus could be used to evaluate new alloys and their hot shortness prior to large scale casting.

11.2 Main conclusions

- A novel method to assess the hot tearing sensitivity of aluminum alloys has been developed (DCSS) and used successfully to quantify the mechanical behaviour of a material undergoing solidification. The DCSS reproduces the complex metallurgical features observed at the surface of a DC cast ingot and allows application and measurement of the tensile load on the solidifying material. The experimental results such as the stress-strain curves could be used as input to simply rank alloys, determine constitutive laws or to generate data to improve numerical model predictive capability.

- A theoretical model has been adapted and used to explain and reproduce relatively well the general behaviour of the stress-strain curves derived from the DCSS experiments. Indeed, the combination of a viscous flow model along with a creep law allowed better reproduction of the stress-strain curves especially in the creep separation region. This was made possible by using metallurgical values that best describe the material being tested and the use of a creep law along with an original crack propagation coefficient (CPC).

- The proposed hot tearing sensitivity index derived from the DCSS measurements has been used successfully on the Al-Si binary alloys. The well-known Λ-curve was reproduced and indicated that the Al-1.5 wt% Si alloy was the most prone to hot tear.

- The DCSS was proven to be useful in understanding the effect of different variables on hot tearing propensity of aluminum alloys and to save time and effort compared with casting large scale DC ingot.

- The viscous model shows similarities with experimental work except that the starting point and the progressive strength built up are difficult to match precisely. The structure and morphology of the solidifying sample is somewhat different from the idealized structure and the discrepancy arises from those differences. In addition, there is rearrangement of the microstructure during straining and grain boundary movements might have created conditions to further resist local deformation.

- The present technique offers the possibility of obtaining real quantitative measurements to characterize the hot tearing phenomenon. Furthermore, it can be used to rank commercial alloys and improve castability during alloy development.

- The theoretical model proposed in the present work resulted in an understanding of the impact of various parameters such as the liquid film thickness, h, grain size, and the strain rate. It was capable to reproduce the experimental stress-strain curves of a semi-solid material under tensile loading. The model can be further improved by considering the addition of solidification contraction and liquid inflow (Darcy's Law) during deformation. Yet another addition will be to implement solidification along with a segregation model that will consider the effect of microstructural changes during tensile loading.

11.3 Future Investigations

Further investigations to extend the work presented in this thesis would be useful for the industry and can bring much interest for the scientific community. A proposal for experimental work is presented below with some suggestions for modelling.

The DCSS experiments are relatively complex and require much attention to ensure that results are representative. The relationship between industrial DC casting and the DCSS technique is important to ascertain. This knowledge strongly influences the extent to which results obtained in the laboratory can be used to predict the hot tearing during DC casting. In fact, the solidification conditions and the resulting strain and stress encountered during DC casting need to be reproduced precisely. This could be done approximately using the same technique as presented in this thesis but including the impact of secondary cooling (i.e., water quenching). Indeed, the secondary cooling can play an important role during the initial stages of casting such as solid contraction, change in the microstructure scale and impact on solute rich liquid movement and distribution. One aspect that can be investigated further is the combined effects of trace elements, modifiers and grain refining techniques on the characteristics of the liquid film at very high solid fraction (>0.95).

In addition, improvements to the model presented in the present work can include the effect of microsegregation and liquid inflow from the bulk during solidification and deformation of the microstructure. Current results suggest that the liquid film thickness play a major role in the hot tearing mechanism. However it remains to be investigated how the second phase precipitates and morphologies affect the liquid movement and distribution. Even further improvements could consider the effect of convection, solute transport, and grain movement to establish accurate hot tearing predictions.

The investigations presented in this thesis have advanced the understanding of hot tearing by measuring mechanical quantities during solidification. During this investigation, many new questions and potential areas of further work emerged. This revealed that this industrially important and scientifically fascinating subject is yet to relinquish all of its secrets.

APPENDICES

Appendix I. Mathematical Development of the Viscous Model

The analysis is similar to Drucker [96] and Lahaie [99] regarding constrained liquid film, except as mentioned previously, the model was improved by considering the primary arm spacing, λ_1, term which is much more representative of the metallurgical microstructure (Figure I.1 to Figure I.4). In addition, a more uniform and symmetrical crystallographic structure was selected to better represent the idealized structure and simplify the mathematical development. In addition, the crystal structure allowed simplifying the original equation for the volume solid fraction terms. The shape of the dendrites represents a two-dimensional channel, with the wall spacing decreasing gradually in the direction of flow. Given the volumetric flow rate and the local half-height, $\frac{h}{2}(x)$, the objective was to determine the velocity and pressure distribution in the interdendritic channels. First, the pressure distribution within the liquid film thickness h was determined and represents the stress generated on the film during straining the material. The average and maximum stress for the viscous flow regime is described below. Second, a creep law was used for the plastic behaviour experienced during the tensile loading. Indeed, the development made so far on the viscous flow only did not reproduce the overall mechanical behaviour observed during the DCSS tensile testing. Finally, a crack propagation coefficient (CPC) is suggested for the hot tear propagation. The objective of the CPC is to explain the stress-strain behaviour during catastrophic microstructure separation. The CPC is explained in Chapter 10: on the microstructure model with a cellular automaton

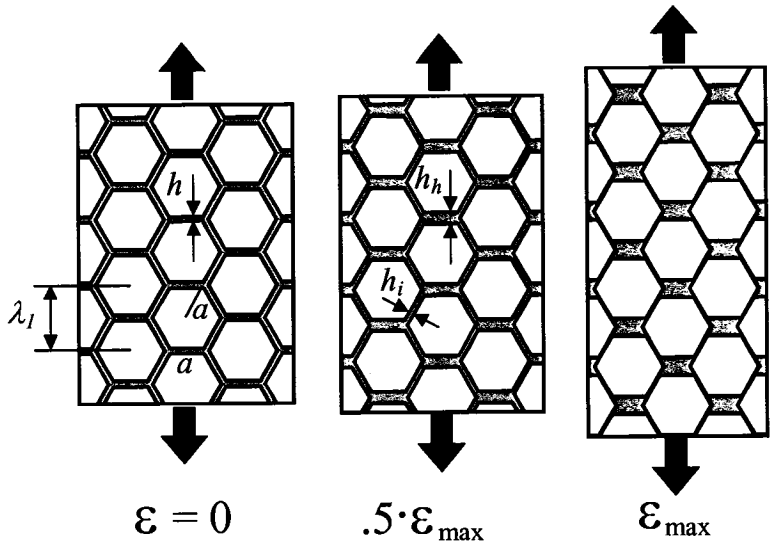

Figure I.1: Schematic of the deformation of a semi-solid body

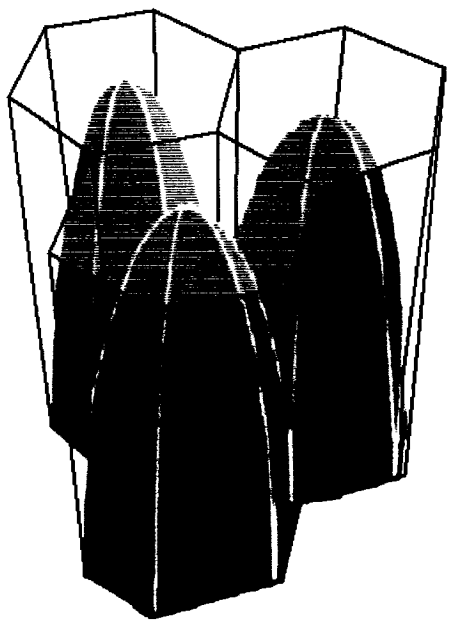

Figure I.2: Diagram of the close-packed hexagonal arrangement of the dendrite trunks

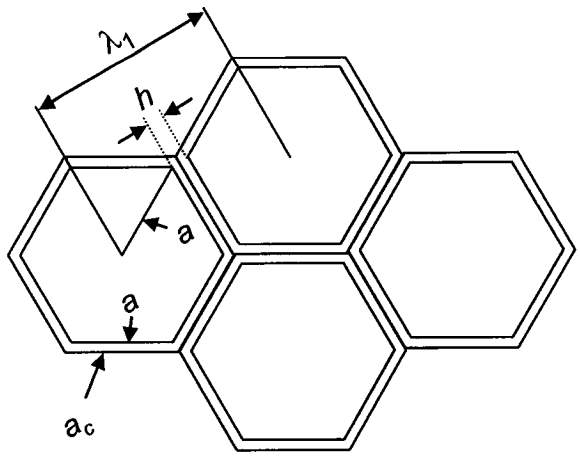

Figure I.3: Hexagonal grain showing the liquid film,*h*, upon solidification

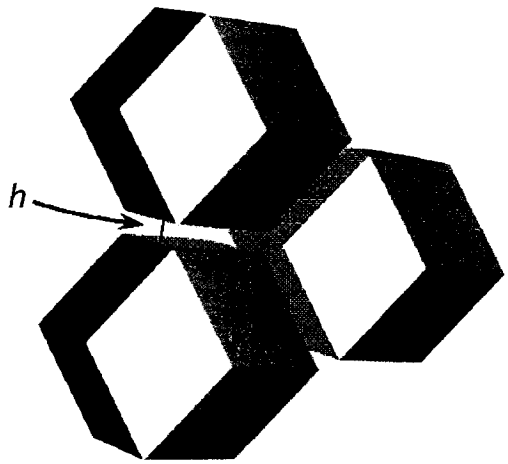

Figure I.4: Rhombic-dodecahedra separated by a liquid film of thickness, *h*

The definitions of the terms are:

h_i: film thickness in the inclined channels

h_h: film thickness in the horizontal channel

a : side dimension of the hexagon

v : velocity of the hexagon (tensile)

λ_1 : primary arm spacing

x and y : symmetrical position

Note: h/a << 1 where "h" is a thin film separating the hexagonal array of the idealized microstructure.

Continuity equation or conservation of volume

The mass conservation in the liquid (where ρ is approximately constant) is given by:

$$\vec{\nabla}\cdot(\rho\vec{v})=0$$

$$\frac{\partial v_x}{\partial x}+\frac{\partial v_y}{\partial y}=0$$

$$\frac{d\langle v_x\rangle}{dx}+\frac{d\langle v_y\rangle}{dy}=0$$

where $\langle v_x\rangle$ and $\langle v_y\rangle$ are the average velocities of the flows.

In the horizontal channel, it is assumed that:

$$\langle v_y\rangle=\frac{y}{(h_h/2)}\cdot\frac{1}{2}\frac{\partial h_h}{\partial t}=\frac{2yV}{h_h}$$

such that:

$$\langle v_y\rangle=\frac{1}{2}\frac{\partial h_h}{\partial t}=V \text{ at } y=\frac{h_h}{2} \text{ and } \langle v_y\rangle=0 \text{ at } y=0$$

We insert $\langle v_y\rangle$ in the mass conservation equation:

$$\frac{d\langle v_x\rangle}{dx}=-\frac{d}{dy}\left(\frac{2yV}{h_h}\right)=-\frac{2V}{h_h}$$

thus:

$$\langle v_x\rangle=\frac{-2V\cdot x}{h_h}$$ Note: In compression, the minus sign disappear.

The last expression can be arranged using the same terminology than Drucker [96] such as the average velocity of the flow in the horizontal channels $\langle v_x\rangle$ becomes w_a and the large V (displacement velocity of the hexagons) becomes v

We are now back to the original expression by Drucker [96] for the continuity or conservation of volume due to the displacement of the hexagons and first expressed by:

$$\underbrace{2vx}_{Volume1} = \underbrace{w_a h_h}_{Volume2}$$

where v is the displacement velocity of the upper and lower hexagons, x, the position from the axisymetric position, w_a, the average velocity of flow in the horizontal channels, and h_h the liquid film thickness. In fact, liquid flowing in long, narrow channels, and in thin films often have these characteristics of being nearly unidirectional and dominated by viscous stresses.

The left-hand-side is the "Volume 1" that represents the volume/time accommodated by flow and the right-hand-side the "Volume 2" that represents the volume/time created by deformation (strain).

The speed of the hexagon (top and bottom) is $2v$, x is the axisymetric position, h_h is the liquid film thickness and the average velocity in the horizontal channel during is given by w_a. If only one hexagon moving then, $v\,x = w_a\,h_h$

Because "v" is negligible in comparison with "w_a" over most of the distance "a". The distribution of "w" through the thickness "h_h" is parabolic. The maximum velocity is $3w_a/2$ and the maximum velocity gradient in the vertical direction is given by:

$$2\frac{\left(\frac{3w_a}{2}\right)}{\left(\frac{h_h}{2}\right)} = \frac{6\,w_a}{h_h}$$

"v" is considered negligible because "h_h" is very small (h_h<<a) and a slow speed "v" will make the liquid film "h_h" to be displaced rapidly.

By definition:

$$\tau = -\mu \frac{dv}{dy}$$

where;

τ is the shear stress

μ is the coefficient of viscosity

(Laminar and incompressible flow)

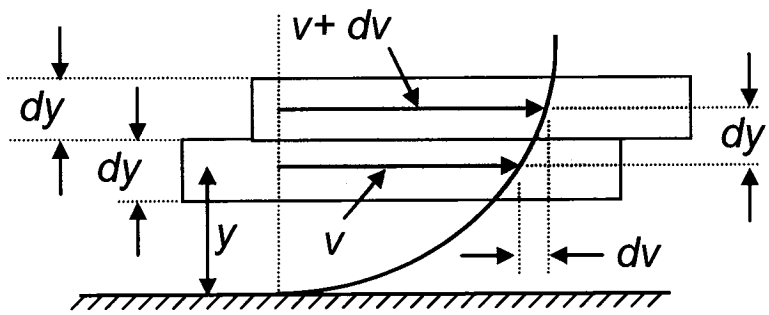

Note: The velocity profile drafted here is for compressive as per the work from Drucker [96]. The sign will be reversed accordingly to adapt it in tensile mode. This will be change at the end of the mathematical derivation process to obtain the maximum and average viscous stress during tensile loading.

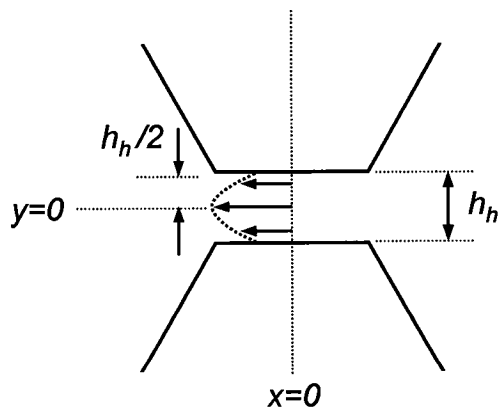

at $\frac{h_h}{2}$ the shear is maximum and at y=0 (centre of the film thickness), the shear is zero.

Film thickness, h

This section explains the relationship between the film thickness and the strain (Figure I.5). The terms h_i and h_h refers to the liquid film thickness in the inclined and horizontal channels, respectively.

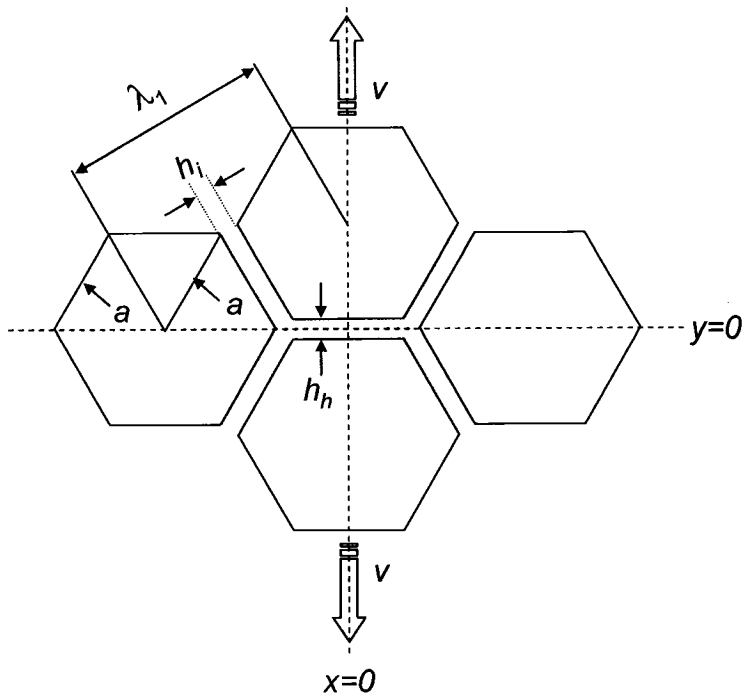

Figure I.5: Hexagonal arrangement and description

The liquid will move from the inclined channel towards the horizontal channel when strain is applied while respecting the volume conservation. The liquid portion is assumed to be constrained until fracture and separation of the idealized microstructure.

The relationship between h_i, h_h, strain (deformation), strain rate, and the primary arm spacing, λ_1, is described below. This will be used for the complete mathematical derivation of the viscous model based on the pressure distribution within the channels.

The film thickness "h" is a function of strain and defined by "h_h" (film in the horizontal channel) and "h_i" (film in the inclined channel). At outset "h_h" and "h_i" are equal to "h". For incompressibility, there is no volume change and the total volume is given by the volume in the inclined and the horizontal channels:

The film thicknesses (Figure I.6) described in this section are also referred to the description made for the *Strain* and *Strain Rate* in the following sections.

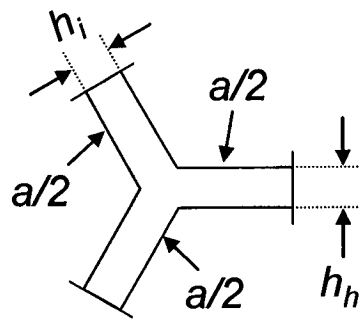

Figure I.6: Liquid film in the inclined (h_i) and horizontal (h_h) channels

$$\underbrace{2\left(\frac{a}{2}\right)h_i}_{\text{volume inclined channel}} + \underbrace{\left(\frac{a}{2}\right)h_h}_{\text{volume horizontal channel}} = \underbrace{3\left(\frac{a}{2}\right)h}_{\text{total volume}}$$

thus;

$$2h_i + h_h = 3h$$

The film thickness in terms of the strain is;

$$\varepsilon = \frac{(h_h - h)}{\lambda_1}$$

Consequently the film thicknesses in the inclined and the horizontal channels can be described as:

$$h_h = \varepsilon \lambda_1 + h$$

or

$$h_h = h\left(1 + \frac{\varepsilon \lambda_1}{h}\right)$$

and;

$$h_i = h - \frac{\varepsilon \lambda_1}{2}$$

or;

$$h_i = h\left(1 - \frac{\varepsilon \lambda_1}{2h}\right)$$

Strain, ε

The strain is also given by the film thickness reduction over the hexagon mid-height (Figure I.7) where;

$$y = \frac{\sqrt{3}a}{2}$$

$$\varepsilon = \frac{(h_h - h)}{\lambda_1} \text{ (by definition)}$$

at $\varepsilon = 0$, $h_h = h$ and, at $h_i = 0$, $\varepsilon = \varepsilon_{max}$

When h_i=0, i.e., no more liquid in the inclined channel, then:

$$\varepsilon_{max} = \frac{2h}{\lambda_1}$$

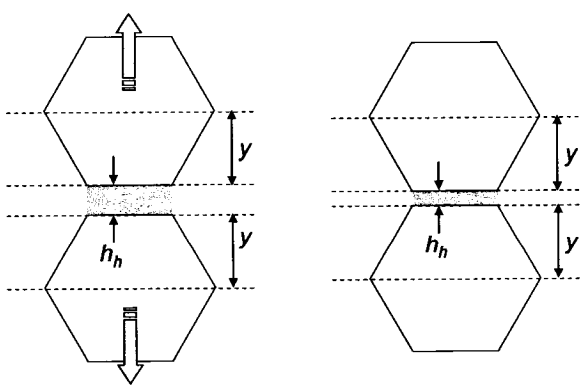

Figure I.7: Change in film thickness for $\varepsilon \neq 0$ and $\varepsilon = 0$, respectively

It should be noted that λ_1 is the distance between the hexagons including the liquid film thickness "*h*" when completely solidified.

Strain rate, $\dot{\varepsilon}$

The relative motion of the hexagon is related to the strain rate. This is the change in strain (displacement) as a function of the film thickness.

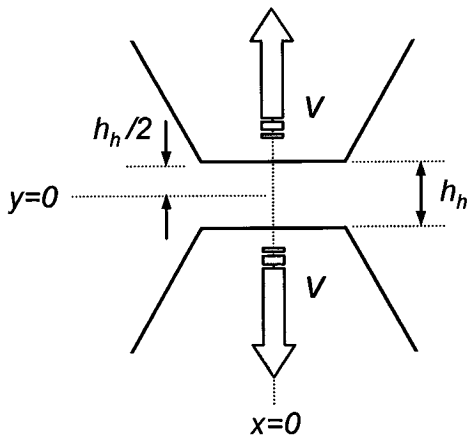

$$\varepsilon = \frac{(h_h - h)}{\lambda_1}$$

and thus:

$$\dot{\varepsilon} = \frac{d\varepsilon}{dt} = \frac{dh}{\lambda_1} = \frac{1}{\lambda_1}\frac{dh}{dt}$$

The change in "*h*" as a function of time represents the speed of the hexagon and given by:

$$v = \frac{dh/2}{dt}$$

Consequently, the relative speed for the two hexagons (opposite direction) is given by:

$$2v = \frac{dh}{dt} \text{ or } dh = 2v\,dt$$

This is the change in "*h*" as a function of time given by the speed of the hexagon. Nevertheless, the relative speed is the displacement of the two hexagons in opposite direction (tensile). The strain rate is the change in the strain with time by the following;

$\dot{\varepsilon} = \frac{2v}{\lambda_1}$ and the strain rate is:

$$\dot{\varepsilon} = \frac{d\varepsilon}{dt}$$

$$d\varepsilon = \frac{dh}{\lambda_1} = \frac{2v\,dt}{\lambda_1}$$

thus, the strain rate as a function of the hexagon speed and the primary arm spacing is given by;

$$\dot{\varepsilon} = \frac{2v}{\lambda_1}$$

Shear stress

From the volume conservation equation;

$$\underbrace{2vx}_{Volume1} = \underbrace{w_a h_h}_{Volume2}$$

$$w_a = \frac{2vx}{h_h} = \frac{2vx}{h\left(1+\frac{\varepsilon\lambda_1}{h}\right)}$$

Note: The maximum velocity gradient in the centre of the horizontal channel ($h_h/2$). At the edge of the hexagon, the velocity is "0" because "v" is negligible with "w_a" over most of the length "a". The distribution of the velocity is assumed parabolic.

$$w = w_{\max}\left(1-\frac{x^2}{L^2}\right)$$

(a parabolic velocity profile)

$\langle w\rangle = \frac{1}{L}\int_0^L w\,dy$ (average velocity)

where;

$\langle w\rangle = w_a = \langle v_x\rangle$ and $L = h_h/2$

$$w_a = \frac{2}{h_h}\int_2^{\frac{h_h}{2}} w_{\max}\left(1-\left(\frac{2y}{h_h}\right)^2\right)\quad dy$$

$$w_a = w_{\max}\int_0^1 (1-z^2)dz$$

$$w_a = w_{\max}\left[z\Big|_0^1 - \frac{z^3}{3}\Big|_0^1\right]$$

$$w_a = w_{max}\left[1-\frac{1}{3}\right] = \frac{2w_{max}}{3}$$

Therefore the maximum velocity at y=0 is given by:

$$w_{\max} = \frac{3w_a}{2}$$

thus;

$$w_x = \tfrac{3}{2} w_a - \tfrac{3}{2} w_a \frac{4y^2}{h_h^2}$$

$$\frac{dw_x}{dy} = \frac{-12w_a}{h_h^2} y$$

and the maximum velocity gradient is given by;

$$\frac{dw_x}{dy} = \frac{-12w_a}{h_h^2} \cdot \frac{h_h}{2} = \frac{-6w_a}{h_h}$$

and,

$\tau = \dfrac{\mu 6 w_a}{h_h}$ at strain=0, h_h=h

and in terms of strain for the horizontal channel;

$$\tau = \frac{12\mu v x}{h_h^2} = \frac{12\mu v x}{(h + \varepsilon \lambda_1)^2}$$

Horizontal pressure gradient

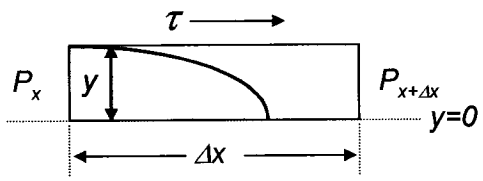

a) $y = \frac{h_h}{2}$

b) high pressure (more compressive) is at the edge

c) lower pressure (more tensile) is at the centre.

$$\frac{\sum Fx}{width} = 0 = P_{x+\Delta x} \cdot y - P_x \cdot y - \tau \Delta x$$

$$\tau \Delta x = \underbrace{(P_{x+\Delta x} - P_x)}_{dP} y$$

where y= $h_h/2$ and h_h is the film thickness in the horizontal channel.

$$\tau = \frac{dP}{dx}\left(\frac{h_h}{2}\right)$$

thus;

$$\tau = \frac{12\mu v x}{h_h^2} = \frac{dP}{dx}\left(\frac{h_h}{2}\right)$$

$$\int_{P_{oh}}^{P} dP = \frac{24\mu v}{h_h^3}\int_0^x x\,dx$$

$$P - P_{oh} = \frac{12\mu v x^2}{(h + \varepsilon\lambda_1)^3}$$

where Poh represents the maximum tensile pressure on the horizontal face, i.e., at the centre or at x=a/2

At this point the sign is positive since pressure increases and more compressive towards the end. The sign is reversed accordingly to simulate tensile or compressive force.

In the inclined channel, we must find v_i which is the separation velocity (or compression).

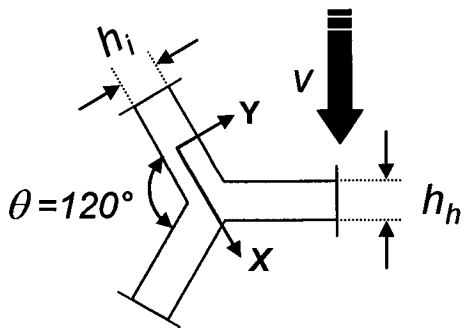

$$v_i = v\cos\theta$$

$$v_i = \frac{v}{2}$$

From the conservation of volume:

$$w_a = \frac{vx}{h_i} = \frac{vx}{\left(h - \frac{\varepsilon\lambda_1}{2}\right)}$$

This is the average flow velocity in inclined channel.

Similarly, the maximum velocity gradient in the inclined channel is:

$$\tau = \frac{\mu dv}{dy} = \frac{-6w_a\mu}{h_i} = \frac{-6vx\mu}{h_i^2} = \frac{-6vx\mu}{\left(h - \frac{\varepsilon\lambda_1}{2}\right)^2}$$

The inclined channel pressure gradient is given by:

$$\frac{dP}{dx}\left(\frac{h_i}{2}\right) = \tau$$

(Note: similar to equation for h_h)

$$\int_{P_{0_i}}^{P} dP = -\int_0^x \frac{12\mu v x}{h_i^3} dx$$

$$P = P_{oi} - \frac{6\mu v x^2}{\left(h - \frac{\varepsilon \lambda_1}{2}\right)^3}$$

Note: Poi is the maximum tensile pressure at the centre of the inclined channel.

At present, we must find the P_{oh} that represents the maximum tensile pressure on the horizontal face, i.e., at the centre. In fact, P_{oh} is the maximum tensile stress σ_{max} at x=0.

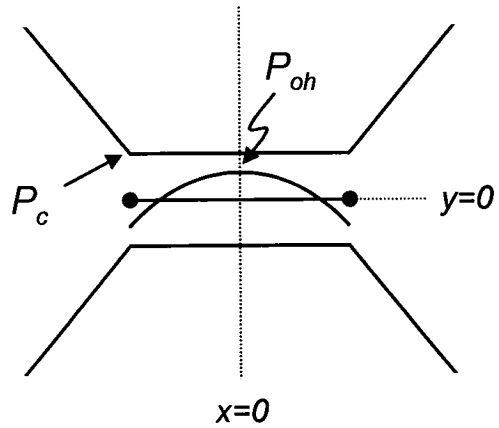

P at corner equal P at $x = \lambda_1 / 2\sqrt{3}$ which equal P_c (Pressure at the corner of the inclined and horizontal channels)

Note: Total stress perpendicular to the face of the inclined channel must be zero.

$$\int_0^x P dx = 0$$

$$\int_0^{\frac{\lambda_1}{2\sqrt{3}}} \left[P_{oi} - \frac{6\mu v x^2}{\left(h - \frac{\varepsilon \lambda_1}{2}\right)^3} \right] dx = 0$$

$$P_{oi} = \frac{\mu v \lambda_1^{\,2}}{6\left(h - \frac{\varepsilon \lambda_1}{2}\right)^3}$$

We now substitute P_{oi} to evaluate P at corner in the following:

$$P_c = P_{oi} - \frac{6\mu v\left(\frac{\lambda_1}{2\sqrt{3}}\right)^2}{\left(h - \frac{\varepsilon \lambda_1}{2}\right)^3}$$

$$P_c = \frac{\mu v \lambda_1^{\,2}}{6\left(h - \frac{\varepsilon \lambda_1}{2}\right)^3} - \frac{6\mu v\left(\frac{\lambda_1}{2\sqrt{3}}\right)^2}{\left(h - \frac{\varepsilon \lambda_1}{2}\right)^3}$$

$$P_c = \frac{-\mu v \lambda_1^{\,2}}{3\left(h - \frac{\varepsilon \lambda_1}{2}\right)^3}$$

Substituting P_c in the P_{oh} equation (horizontal channel) below:

$$P_{oh} = P_c - \frac{\mu v \lambda_1^{\,2}}{(h+\varepsilon\lambda_1)^3}$$

then:

$$P_{oh} = \frac{-\mu v \lambda_1^{\,2}}{3\left(h-\frac{\varepsilon\lambda_1}{2}\right)^3} - \frac{\mu v \lambda_1^{\,2}}{(h+\varepsilon\lambda_1)^3}$$

$$P_{oh} = \frac{\mu v \lambda_1^{\,2}}{3}\left(\frac{1}{\left(h-\frac{\varepsilon\lambda_1}{2}\right)^3} + \frac{3}{(h+\varepsilon\lambda_1)^3}\right) \text{ (negative sign remove for tension)}$$

In fact, P_{oh} is the maximum tensile stress σ_{max} at x=0, and positive sign for tensile, thus we reverse the sign to obtain:

$$\sigma_{max} = \frac{\mu v \lambda_1^{\,2}}{3}\left(\frac{1}{\left(h-\frac{\varepsilon\lambda_1}{2}\right)^3} + \frac{3}{(h+\varepsilon\lambda_1)^3}\right)$$

This equation can be expressed in terms of the strain rate related to displacement speed, *v*, and film thickness, *h*, (see Strain and Strain Rate development section) such as:

$$\sigma_{max} = \frac{\mu \dot{\varepsilon} \lambda_1^{\,3}}{6}\left(\frac{1}{\left(h-\frac{\varepsilon\lambda_1}{2}\right)^3} + \frac{3}{(h+\varepsilon\lambda_1)^3}\right)$$

Similarly, the equation can be expressed in terms of the volume solid fraction based on the following:

$$g_S = \left(\frac{a}{a_c}\right)^3 \text{ and } a_c = \frac{\lambda_1}{\sqrt{3}}, \text{ and } a = \frac{\lambda_1 - h}{\sqrt{3}}, \text{ for } h = \lambda_1(1 - {g_S}^m)$$

$$\sigma_{\max} = \frac{\mu\,\dot{\varepsilon}}{6}\left(\left(1 - {g_s}^m - \frac{\varepsilon}{2}\right)^{-3} + 3\left(1 - {g_s}^m + \varepsilon\right)^{-3}\right)$$

Average stress on the face of the hexagon

The maximum stress is depicted in the figure below as the peak of the parabola while the average stress is distributed along the face from x=0 to $x = \frac{\lambda_1}{\sqrt{3}}$ of the hexagon (straight line).

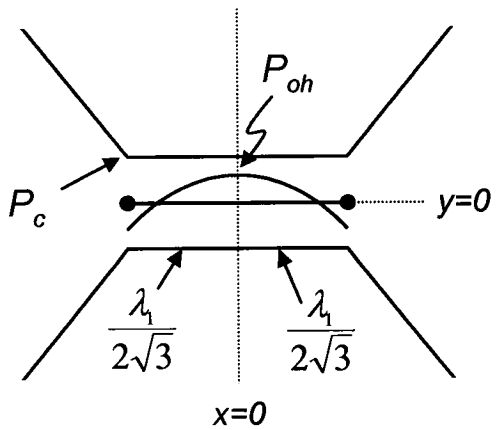

$$P_{avg} = \frac{1}{L}\int_0^L P\,dx$$

$$\sigma_{avg} = \left(\frac{\lambda_1}{2\sqrt{3}}\right)^{-1} \int_0^{\frac{\lambda_1}{2\sqrt{3}}} P\,dx$$

Using the equation below;

$$P = P_{oh} + \frac{12\mu v x^2}{(h+\varepsilon\lambda_1)^3}$$

$$\sigma_{avg} = \frac{1}{\lambda_1/2\sqrt{3}} \int_0^{\frac{\lambda_1}{2\sqrt{3}}} \left(P_{oh} + \frac{12\mu v x^2}{(h-\varepsilon\lambda_1)^3} \right) dx$$

$$\sigma_{avg} = P_{oh} + \frac{\mu v \lambda_1^{\,2}}{3(h+\varepsilon\lambda_1)^3}$$

Using the equation for P_{oh} and substituting it in the average stress we obtain:

$$\sigma_{avg} = \frac{-\mu v \lambda_1^{\,2}}{3} \left(\frac{1}{\left(h - \frac{\varepsilon\lambda_1}{2}\right)^3} + \frac{3}{(h+\varepsilon\lambda_1)^3} \right) + \frac{\mu v \lambda_1^{\,2}}{3(h+\varepsilon\lambda_1)^3}$$

$$\sigma_{avg} = \frac{-\mu v \lambda_1^{\,2}}{3} \left(\frac{1}{\left(h - \frac{\varepsilon\lambda_1}{2}\right)^3} + \frac{2}{(h+\varepsilon\lambda_1)^3} \right)$$

Similarly to the maximum stress, a substitution to obtain the average stress as a function of strain rate.

$$\sigma_{avg} = \frac{-\mu \dot{\varepsilon} \lambda_1^{\,3}}{6} \left(\frac{1}{\left(h - \frac{\varepsilon\lambda_1}{2}\right)^3} + \frac{2}{(h+\varepsilon\lambda_1)^3} \right)$$

Again, the substitution is made to obtain the average stress as a function of solid fraction.

$$\sigma_{avg}=\frac{-\mu\dot{\varepsilon}\lambda_1^3}{6}\left(\frac{1}{\left(\lambda_1(1-g_s^m)-\frac{\varepsilon\lambda_1}{2}\right)^3}+\frac{2}{(\lambda_1(1-g_s^m)+\varepsilon\lambda_1)^3}\right)$$

$$\sigma_{avg}=\frac{-\mu\dot{\varepsilon}\lambda_1^3}{6}\left(\frac{1}{\lambda_1^3\left(1-g_s^m-\frac{\varepsilon}{2}\right)^3}+\frac{2}{\lambda_1^3(1-g_s^m+\varepsilon)^3}\right)$$

$$\sigma_{avg}=\frac{-\mu\dot{\varepsilon}}{6}\left(\frac{1}{\left(1-g_s^m-\frac{\varepsilon}{2}\right)^3}+\frac{2}{(1-g_s^m+\varepsilon)^3}\right)$$

$$\sigma_{avg}=\frac{-\mu\dot{\varepsilon}}{6}\left(\left(1-g_s^m-\frac{\varepsilon}{2}\right)^{-3}+2(1-g_s^m+\varepsilon)^{-3}\right)$$

Finally, the average stress is determined according to the following figure to normalize on a periodic section:

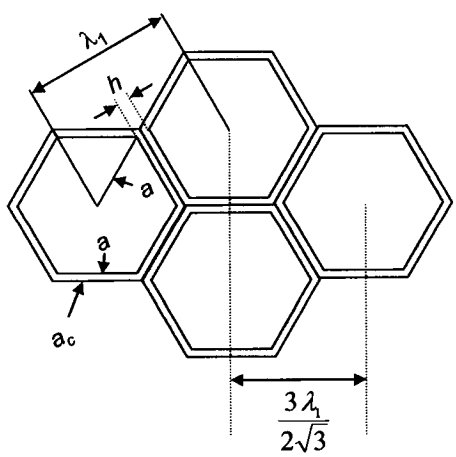

$$\sigma \cdot \frac{3\lambda_1}{2\sqrt{3}} = \sigma_{avg} \cdot \frac{\lambda_1}{\sqrt{3}}$$

thus:

$$\sigma_{avg} = \frac{3}{2}\sigma_{viscous}$$

or,

$$\sigma_{viscous} = \frac{2}{3}\sigma_{avg}$$

Consequently the viscous flow is determined by the following equation (sign is inversed for tension):

$$\sigma_{viscous} = \frac{\mu\,\dot{\varepsilon}}{9}\left(\left(1-g_s{}^m-\frac{\varepsilon}{2}\right)^{-3}+2\,(1-g_s{}^m+\varepsilon)^{-3}\right)$$

$$for \quad 0 \le \varepsilon \le 2(1-g_s{}^m)$$

Note: Equation not valid if no liquid in inclined channel, i.e., $\varepsilon_{max} = 2(1-g_s{}^m)$

Appendix II. DCSS test configuration and set-up

The experimental conditions are defined in a dedicated computer control program using data obtained from thermal and microstructure analyses. Figure II.1 shows the main experimental parameters set-up window used to enter the alloy characteristics used to trigger various conditions such as the container rotation and the strain gauge positioning.

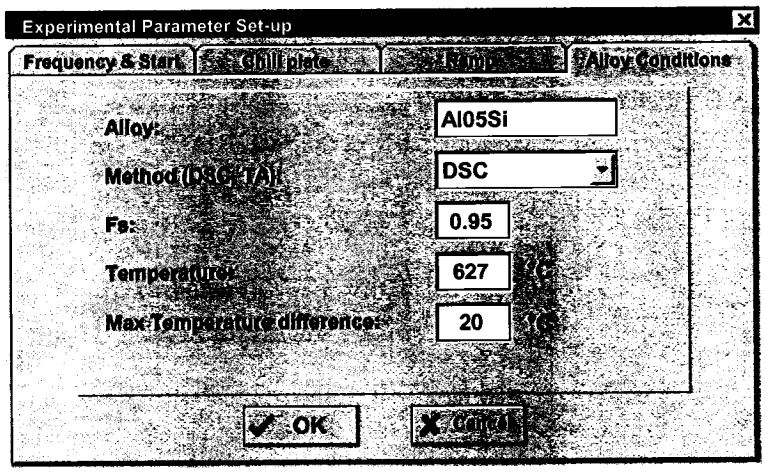

Figure II.1: Example of the computer control program

Figure II.2 shows the data acquisition window that appears on the computer screen during the experiments. This shows the main measurements taken during the test as well as the main activation button to start or stop the experiment or activate other specific functions.

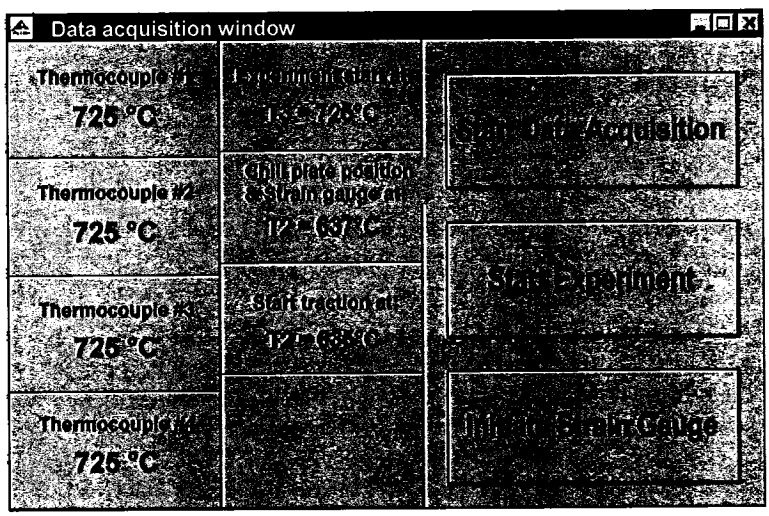

Figure II.2: Example of the data acquisition window

Appendix III. Container preparation and thermocouple installation

Installation of the ceramic blanket inside the container to absorb solid metal displacement during traction (Figure III.1 a) and V-shaped cutting to receive the anchor stem (Figure III.1 b).

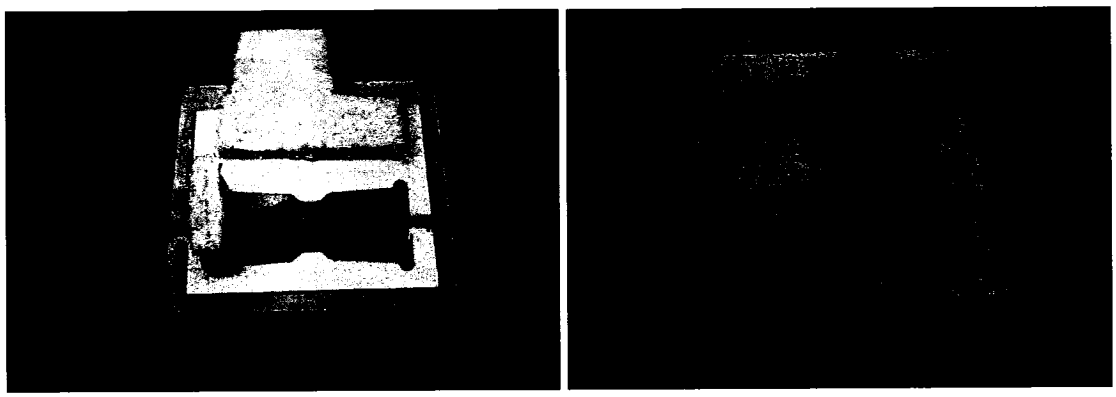

Figure III.1: Ceramic blanket (a) and V-shaped cut (b)

Installation and positioning of the thermocouples inside the container (Figure III.2a and Figure III.2b).

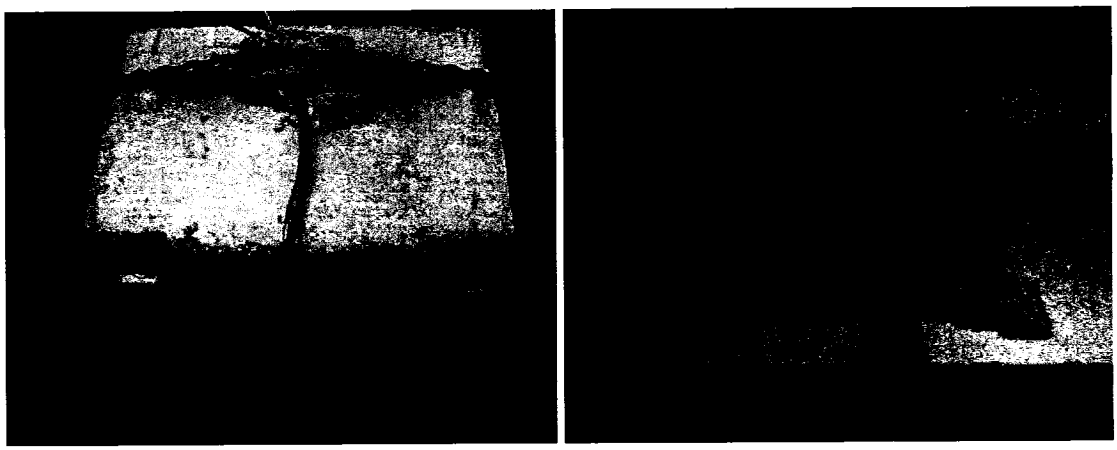

Figure III.2: Thermocouple installation (a) and positioning (b)

Appendix IV. Typical DCSS experimental procedure

Check list:

- Ensure water is circulating inside the chill plate and adjust water temperature (20 °C) and flow rate to 14 l/min.
- Check overall plate condition and refurbish the surface with 600 grit sand paper using parallel movement from top to bottom.
- Liquid metal temperature to 750 °C before pouring in container.
- Install safety pin to prevent rotation during manipulation
- Reset all parameters in the computer control program "Stress.exe"
- Check load cell calibration and reset

Main experimental steps:

- Step 1: Skim the surface of the aluminum melt before filling the container.
- Step 2: Start data acquisition.
- Step 3: Fill the pre-heated container with liquid metal at 750 °C (±5 °C)

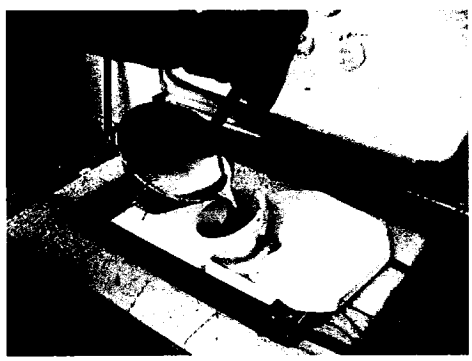

- Step 4: Transport and position the container and its content on the DCSS

- Step 5 : Remove oxydes present at the surface

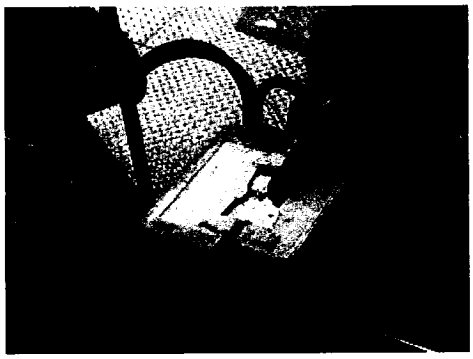

- Step 6: Position the anchor stems and seals

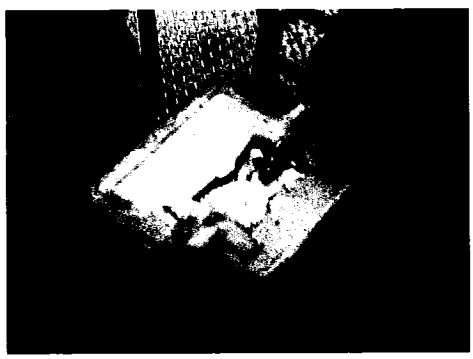

- Step 7: Put a ceramic fiber seal on top of the container and anchor stems

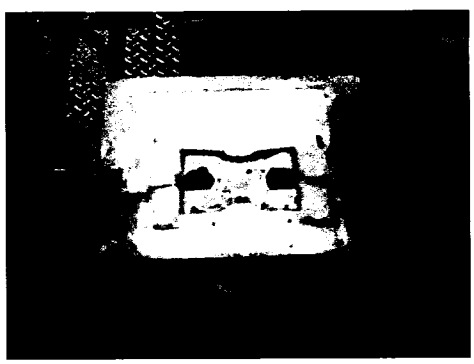

- Step 8: Install the large ceramic fiber seal on top of the container

- Step 9: Install the chill plate and lock in place (clamp)
- Step 10: Connect thermocouples
- Step 11: Start experiment and wait until the container rotates 90 degree (temperature criteria)

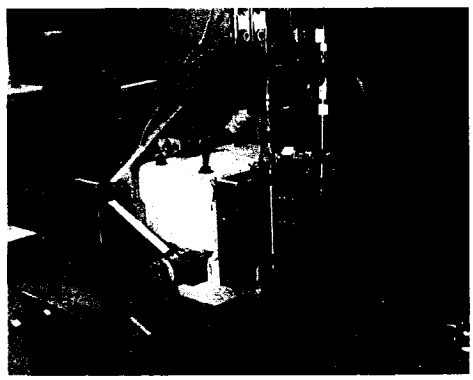

- Step 12: Wait until windows slides up. Install and align strain gauge probes (automatic start when load is applied)

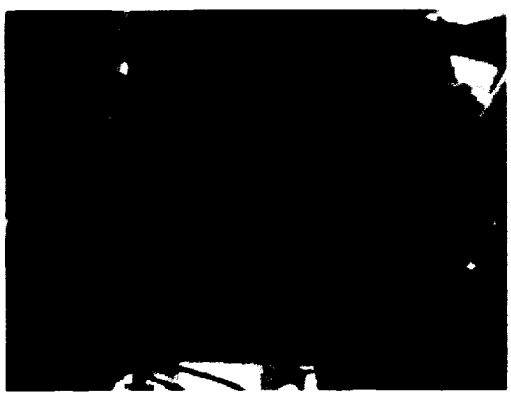

- Step 13: Stop experiment and let water running during 1 hour

Appendix V. Solid fraction from thermal analysis results

Table VI.1: Solid fraction results (Al-Si binary alloys)

f_s	Al-0.5Si
0.000	657.21
0.126	657.12
0.242	657.12
0.354	657.09
0.461	657.07
0.563	657.03
0.663	656.88
0.752	655.52
0.818	649.02
0.884	642.99
0.934	634.12
0.954	627.08
0.964	621.14
0.974	611.90
0.978	604.70
0.983	596.01
0.988	591.22
0.989	587.97
0.990	571.65
0.992	569.76
1.000	563.18

f_s	Al-1.5Si

f_s	Al-2.5Si

Table VI.2: Summary of coherency temperature

Alloy system	Temperature (°C)
Al-0.5wt%Si	647.5
Al-1.5wt%Si	640.2
Al-2.5wt%Si	637.2

Alloy system	Temperature (°C)	dT at Coherency
Al-0.5wt%Si	647.5	9
Al-1.5wt%Si	640.2	10.5
Al-2.5wt%Si	637.2	8

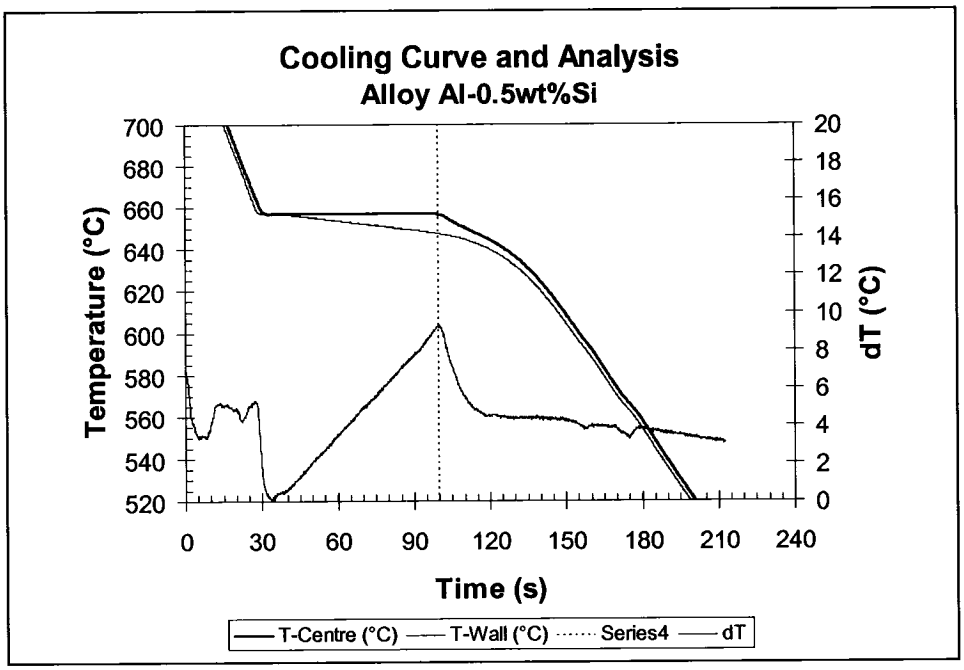

Figure V.1: Cooling curves and coherency point for Al-0.5Si (ΔT peak)

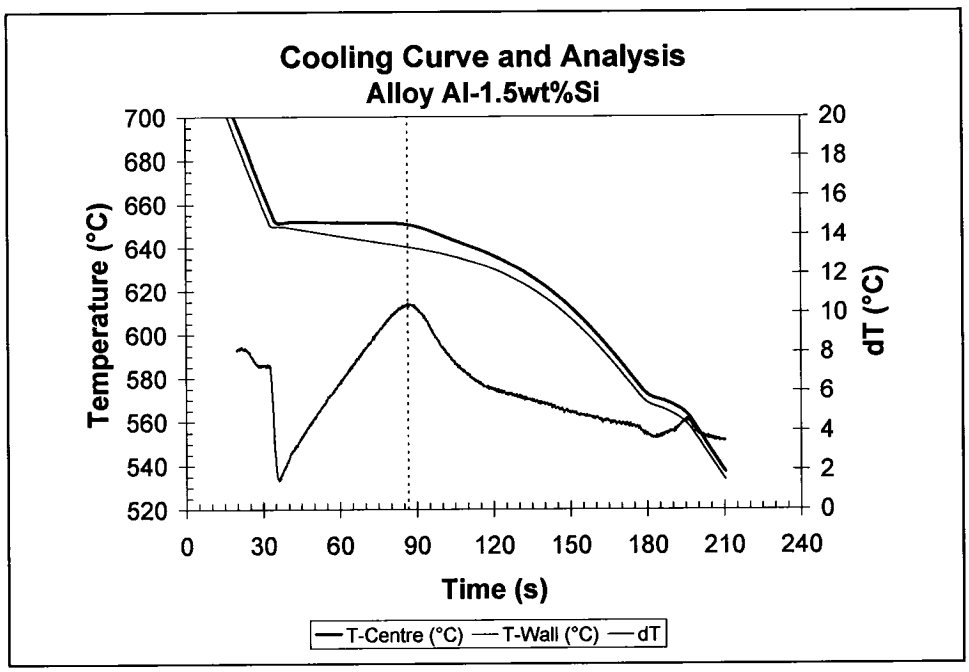

Figure V.2: Cooling curves and coherency point for Al-1.5Si (ΔT peak)

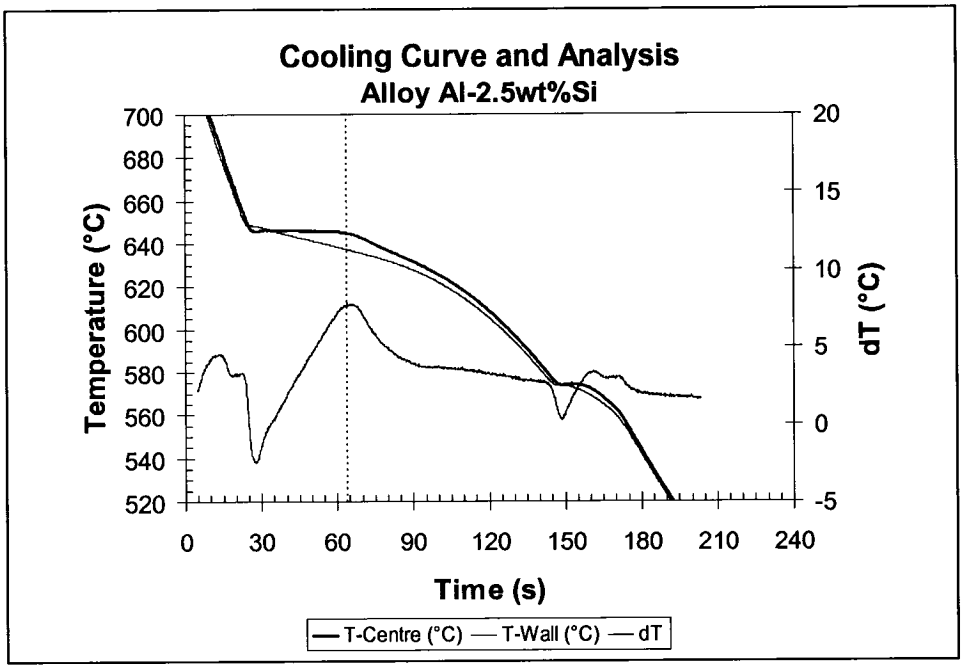

Figure V.3: Cooling curves and coherency point for Al-2.5Si (ΔT peak)

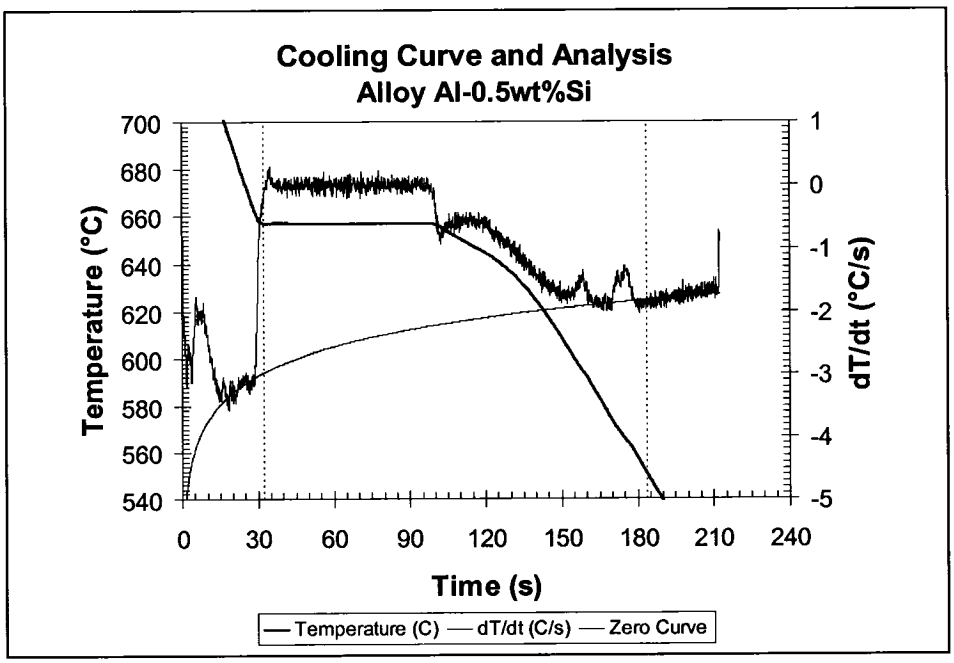

Figure V.4: Cooling curves with first derivative and zero curve (Al-0.5Si)

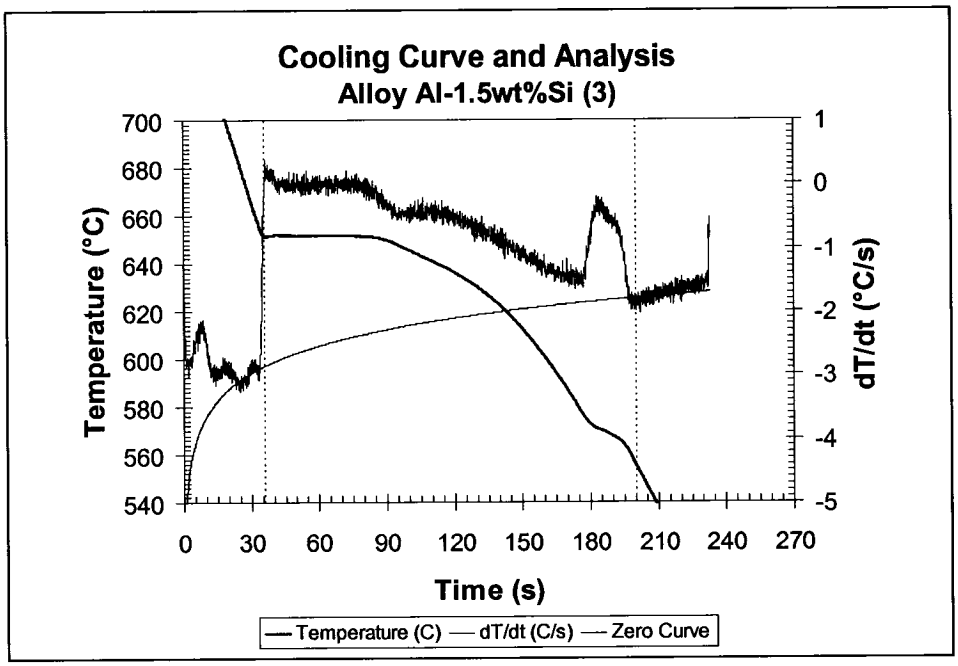

Figure V.5: Cooling curves with first derivative and zero curve (Al-1.5Si)

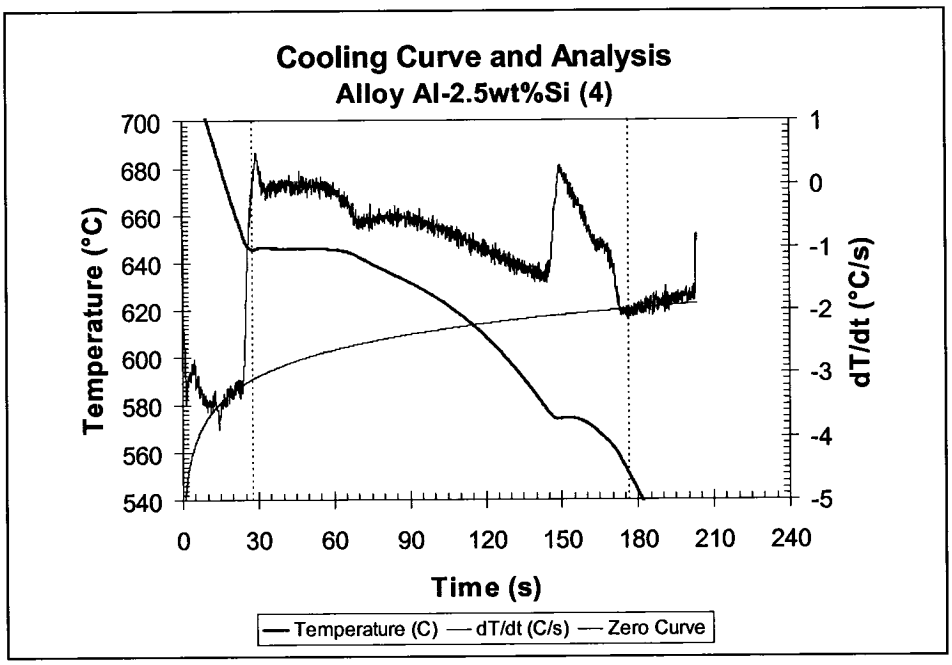

Figure V.6: Cooling curves with first derivative and zero curve (Al-2.5Si)

Appendix VI. Thermo-physical properties of Al-Si alloys

The main thermo-physical properties of the Al-Si alloys, such as the density, the heat capacity, and the thermal conductivity, were calculated, or determined using numerical approaches from ThermoCalc. The values obtained were used in the ProCAST™ model and other theoretical models developed during this work, i.e., mechanical and the microstructure (cellular automata) models.

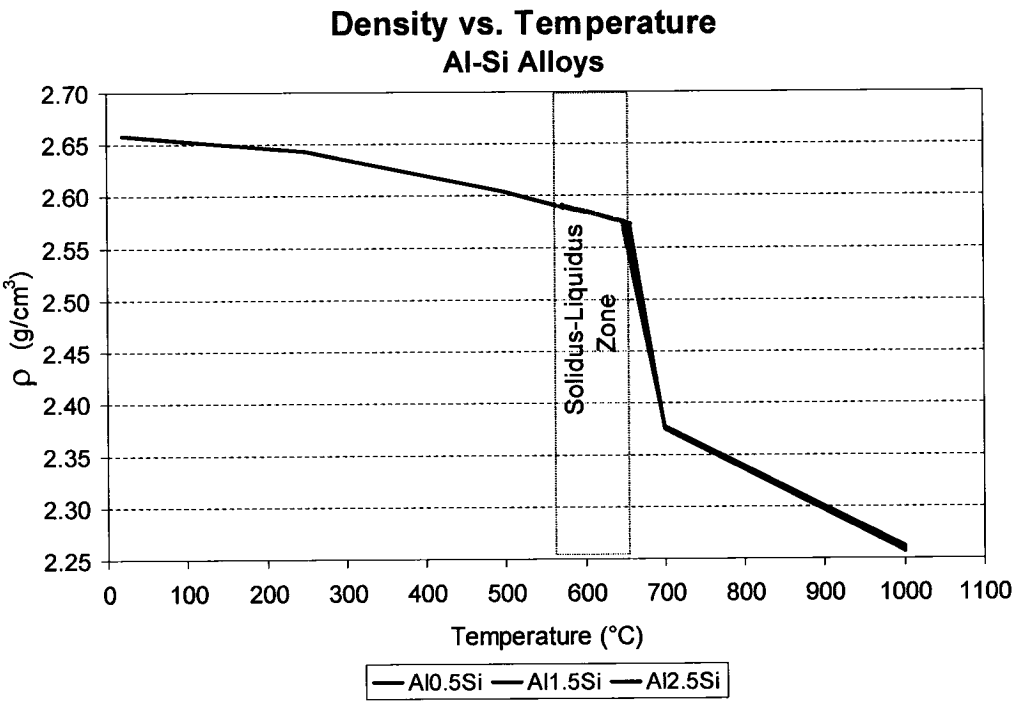

Figure VI.1: Calculated density variation with temperature

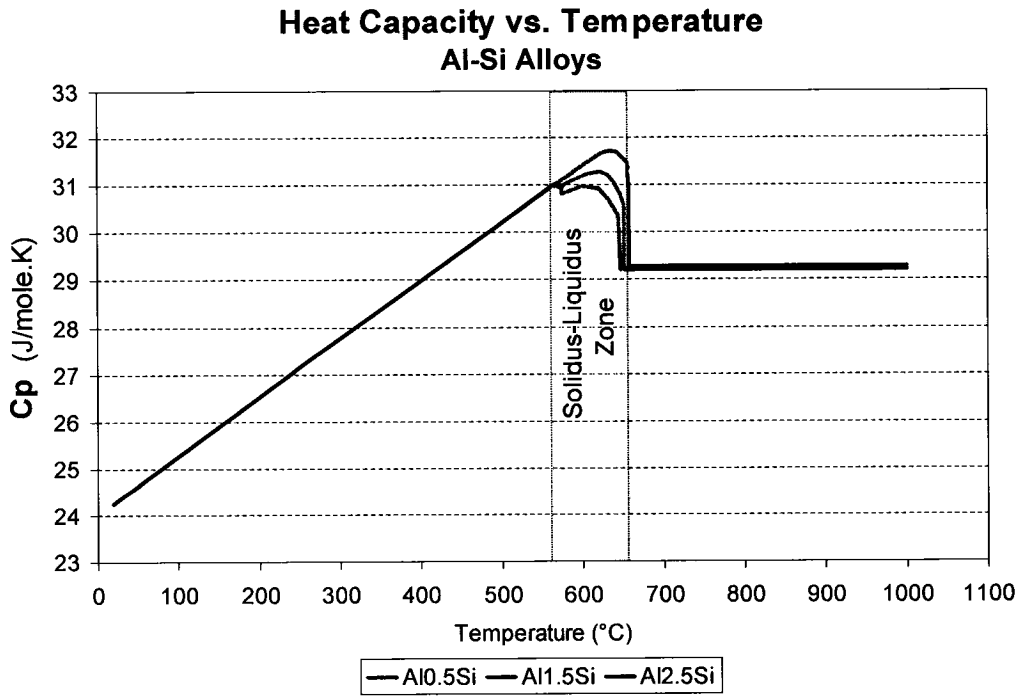

Figure VI.2: Calculated heat capacity versus temperature

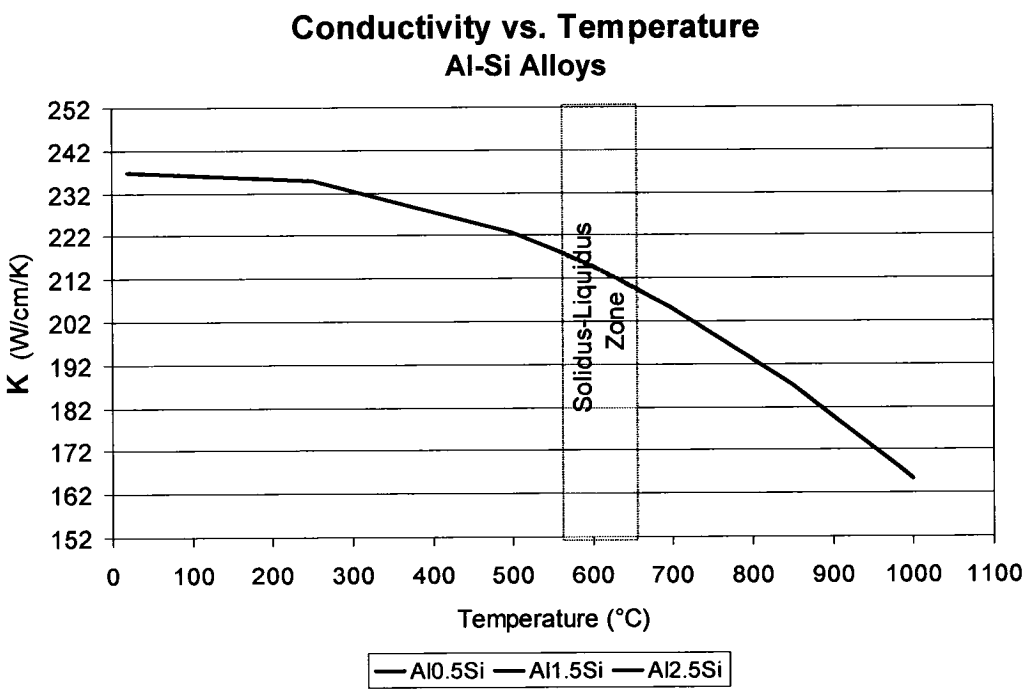

Figure VI.3: Calculated conductivity versus temperature

Table VII.1: Main data and equation used to determine the physical properties

Density

$\rho_{Al} = 2.7568-3.935 \times 10^{-4} * T$ g/cm^3 ($T>T_m$) $\rho = M/V$ $M=\Sigma xi*Mi$

$\rho_{Si} = 2.53$ g/cm^3 $V=\Sigma xi*Vi$

$\rho_{Al\_solid} = 2.7$ g/cm^3 $Vi=Mi/\rho i$

M_{Si}	28.086	g/mole	$\rho = (\Sigma xi*Mi)/(\Sigma xi*(Mi/\rho i))$
M_{Al}	26.98	g/mole	

Molar Fraction

$X_{Si} = [M_{Al} * C_o]/[M_{Al} * C_o + M_{Si}*(1-C_o)]$		0.004804051
$X_{Al} = 1 - X_{Si}$		0.995195949

Heat Capacity (liquid)

$Cp_{liquide} = a + b*T - c*T^{-2}$

$a=X_{Al}*(a_{Al})_{liq} + X_{Si}*(a_{Si})_{liq}$	Al	a=29.3 J/mole/K	b=0	c=0
$b=X_{Al}*(b_{Al})_{liq} + X_{Si}*(b_{Si})_{liq}$	Si	a=25.61 J/mole/K	b=0	c=0
$c=X_{Al}*(c_{Al})_{liq} + X_{Si}*(c_{Si})_{liq}$				

cp=Cp/M J/g/K cp as a function of mass imply dividing Cp molar by the molecular mass M

Note: A rough approximation can be obtained by the following method: Al-0.5wt%Si

$cp = \Sigma f_i*cp_i$ $f_{Al} = 0.995$ $f_{Si} = 0.005$

$cp_{Al} = 0.902$ J/g/K at 20°C

$cp_{Si} = 0.71$ J/g/K

$cp = 0.95*cpAl + 0.05*cpSi = 0.8924$ J/g/K at 20°C

Heat Capacity (solid)

$Cp_{solide} = a + b*T - d*T^{-2}$ J/m.K

$(a_{Al})_S = 20,7$	$(b_{Al})_S = 1,238$ E-2	$(c_{Al})_S = 0$	$(d_{Al})_S = 0$
$(a_{Si})_S = 23,85$	$(b_{Si})_S = 4,3$E-3	$(c_{Si})_S = 0$	$(d_{Si})_S = 4,44$E5

$a=X_{Al}*(a_{Al})_{sol} + X_{Si}*(a_{Si})_{sol}$

$b=X_{Al}*(b_{Al})_{sol} + X_{Si}*(b_{Si})_{sol}$

$c=X_{Al}*(c_{Al})_{sol} + X_{Si}*(c_{Si})_{sol}$

$d=X_{Al}*(d_{Al})_{sol} + X_{Si}*(d_{Si})_{sol}$

Thermal Conductivity

$k=\lambda_o T\sigma_i = \lambda_o T(x_{Al}.(\sigma_{Al}) + X_{Si}*(\sigma_{Si})_{liq})$

$(\sigma_{Al})_{liq} = (10.7 +0.0145*T)^{-1}$ $\mu Ohm^{-1}cm^{-1}$

$(\sigma_{Si})_{liq} = 0.0123$ μOhm-1cm-1

$(\sigma_{Al})_{solid} = (10.7 +0.0145*T)^{-1}$ $\mu Ohm^{-1}cm^{-1}$

$(\sigma_{Si})_{solid} = 0.0123$ μOhm-1cm-1

$k=V_{Al}*k_{Al} + V_{Si}*k_{Si}$

k_{Al} =	2.34	W/cm/K
k_{Si} =	1.48	W/cm/K

Al-Si phase diagram data

Liquidus slope:	(577-660.5)/12.6 =	-6.626984127 °C/wt%
Solute partition coeff.:	1.6/12.6 =	0.126984127
Diffusivity:		3.00E-09 m^2/s
C_E (12.6 % Si @ 577 °C)	0.126	
C_o (initial concentration)	0.005	

Temperature data

T_m pure Al =	933.65 K	660.5 °C	
T_m pure Si =	1687.15 K	1414 °C	
$T_{liquidus}$ Al-0.5wt%Si =	930.24 K	657.09 °C	(from Thermal Analysis - Backerud method)
$T_{solidus}$ Al-0.5wt%Si =	836.33 K	563.18 °C	(from Thermal Analysis - Backerud method)

Appendix VII. Cellular Automaton Program algorithm

Program Algorithm for modeling microstructure by

"CELLULAR AUTOMATA"

by

Joseph Langlais

Simulation of surface and sub-surface microstructure

Language: FORTRAN
USE DFLIB

```
Integer:  maxwidth,maxheigth,maxconditions
Integer:  i,j,k,p,asperities,surface,rnd48
Real:  a,solrange,diffusion,Gibbs,cs,cl,pi
Real:  L, ΔT,t,Lt,undercooling
Real:  nmax,S ΔTs,S ΔTn,B ΔTs,B ΔTn,nucleaterate,nuclei,nucleateprob,kdistr
Real:  pdistr,omega,vel,rnd
Real:  endgrowth, solidification_complete
Real:  germe,divis,rand
Real:  allocatable :: matrix(:,:,:)
```

Constant definition

a=1	a: growth constant formula
solrange=94	solrange: solidification range for Al-Si alloys (Al0.5Si: 657-563= 94°C; Al1.5Si: 652-562.6= 89.4°C; and Al2.5Si: 646.6-559.7= 86.9°C)
diffusion=0.000000003	diffusion coefficient (m2/s)
Gibbs=0.00000009	Gibbs Thompson coefficient
cs=0.5	solid concentration (Al-Si Alloys: 0.5 wt%Si, 1.5 wt% Si, and 2.5 wt% Si)
cl=0.065	cl: liquid concentration (Al-Si Alloys: 0.065 wt%Si, 0.195 wt%Si, and 0.325 wt%Si)
pi=3.14159	
maxwidth=501	maxwidth: number of X-cell in mesh
maxheigth=501	maxheigth: number of Y-cell in mesh
maxconditions=5	maxconditions: number of information per cell

```
allocate (matrix(maxheigth+1,maxwidth+1,5))
```

```
call SEED(RND$TIMESEED)
call RANDOM(rand)
germe=rand
```

Variables definition

L: cell width/step of the matrix in meter, m
ΔT: temperature extracted every dt
matrix: matrix defining the meshing
t: time interval for one loop
Lt: growth length for interval t
undercooling: total undercooling at time t
i,j,k,p: loop counters
asperities: spacing between surface asperities
S ΔTs: standard deviation related to ΔT for surface nucleation (solutal undercooling)
S ΔTn: undercooling corresponding to the highest surface nucleating rate
B ΔTs: standard deviation related to ΔT for bulk nucleation (solutal undercooling)
B ΔTn: undercooling corresponding to the highest bulk nucleating rate
nucleaterate: surface nucleation rate
nuclei: number of nuclei generated at a given undercooling
nucleateprob: nucleation probability at each cell
surface: number of surface cell
kdistr: liquid concentration/solid concentration (Cl/Cs)
pdistr: 1-kdistr
omega: growth law parameter
vel: growth rate (m/sec)
rnd= random
rnd48= random(48)
endgrowth: growth step finish
solidification_complete: solidification is completed
input: file containing nucleation and growth law values
output: file containing the matrix results

Initialisation_Procedure_(Initial state reseting)

```
t=0.
kdistr=0.
pdistr=0.
omega=0.
vel=0.
i=0
j=0
k=0
p=0
nmax=0.
surface=0
undercooling=0.
Lt=0.
nucleaterate=0.
nuclei=0.
nucleateprob=0.
```

```
solidification_complete=0.
do i=1,maxheigth
do j=1,maxwidth
do k=1,maxconditions
matrix(i,j,k)=0.
enddo
enddo
enddo
```

End of Initialisation_Procedure

File_Reading Procedure

```
open (1,file='input.txt',status='old')
Read (1,*)t
Read (1,*)L
Read (1,*) ΔT
Read (1,*)S ΔTn
Read (1,*)S ΔTs
Read (1,*)B ΔTn
Read (1,*)B ΔTs
Read (1,*)asperities
```

End of file_reading procedure

```
solidification_complete=0.
Beginning of Do While loop
do while(solidification_complete.eq.0.)
```

Surface_Nucleation Procedure

```
nmax=(float(maxwidth)*L)/(asperities/1.0e6).....Total number of asperities = number
                                                 of nuclei
nucleaterate=((nmax/(sqrt(2.*pi)*S ΔTs))*exp(((undercooling-S ΔTn)**2.)/(-
2.*(S ΔTs)**2.)))
nuclei=nucleaterate* ΔT
nucleateprob=nuclei/maxwidth.....Number of nuclei generated during
                                 the iteration
write(*,*) 'S',nucleateprob,surface
do j=1,maxwidth
if (matrix(1,j,1).eq.0.)then
call gen(germe,divis)
if (divis.LE.nucleateprob)then.....Random nucleation probability
call gen(germe,divis)
rnd48=int(divis*48.)
matrix(1,j,1)=((float(rnd48)*90./48.)-45.)
surface=surface+1.....Nucleation assign a crystallographic
                      orientation of -45° to +45° in 48
                      different/possible orientations
matrix(1,j,4)=1.....No growth during the first interval
```

```
matrix(1,j,5)=L*(cos(matrix(1,j,1)*pi/180.)+abs(sin(matrix(1,j,1)*pi/180.)))
endif
endif
enddo
```

End of Surface_Nucleation Procedure

Bulk_Nucleation Procedure

```
nmax=(float(maxwidth)*float(maxheigth))-float(surface)
nucleaterate=((nmax/(sqrt(2.*pi)*B ΔTs))*exp(((undercooling-B ΔTn)**2.)/(-
2.*(B ΔTs)**2.)))
nuclei=nucleaterate* ΔT.....Number of nuclei generated during this time
                                                    interval
nucleateprob=nuclei/nmax
write(*,*) 'B',nucleateprob,surface
do i=1,maxheigth
do j=1,maxwidth
if ((matrix(i,j,2).EQ.0.).and.(matrix(i,j,1).EQ.0.)) then
call gen(germe,divis)
if (divis.LE.nucleateprob) then.....rnd
call sleepqq(10)
call SEED(RND$TIMESEED)
call RANDOM(rand)
divis=rand
rnd48=int(divis*48.)
matrix(i,j,1)=(float(rnd48)*90./48.)-45.
surface=surface+1.....Nucleation assign a crystallographic
                                                    orientation of -45° to +45° in 48
                                                    different/possible orientations
matrix(i,j,4)=1.....No growth during the first interval
matrix(i,j,5)=L*(cos(matrix(i,j,1)*pi/180.)+abs(sin(matrix(i,j,1)*pi/180.)))
```

Compute the length to surround the next cell

```
endif
endif
enddo
enddo
```

End of Bulk_Nucleation Procedure

Growth Procedure

```
kdistr=cs/cl
pdistr=1.-kdistr
omega=undercooling/((undercooling*pdistr)+(solrange*kdistr))
vel=(diffusion*(omega)**2.)/(Gibbs*(pi**2.))*((solrange*kdistr)/(1-(omega*pdistr)))!!!
Growth rate in m/s
Lt=vel*t.....Growth in m
```

```
do i=1,maxheigth.....Incremental loop for growth
do j=1,maxwidth
if((matrix(i,j,1).NE.0.).and.(matrix(i,j,4).EQ.0.)) then

Check if cell is solid and growth not computed

matrix(i,j,3)=matrix(i,j,3)+Lt.....Increment growth of grain size by L(t)
endif
enddo
enddo
endgrowth=0.
Beginning Do while loop
do While (endgrowth.EQ.0.)
endgrowth=1.
do i=1,maxheigth.....Growth loop
do j=1,maxwidth
if((matrix(i,j,1).NE.0.).and.(matrix(i,j,4).EQ.0.)) then
endgrowth=0.....Check if cell is solid and growth not computed
matrix(i,j,4)=1.....Indicate that growth is done
if (matrix(i,j,3).GE.matrix(i,j,5)) then

Loop to capture neibourg cell at assign orientation

if((j+1.LE.maxwidth).and.(matrix(i,j+1,1).EQ.0.)) then
matrix(i,j+1,1)=matrix(i,j,1)
matrix(i,j+1,5)=matrix(i,j,5)
matrix(i,j+1,3)=matrix(i,j,3)-matrix(i,j,5)
surface=surface+1
endif

Assign remaining growth length to the new cells

if((j-1.GE.1.).and. (matrix(i,j-1,1).EQ.0.)) then
matrix(i,j-1,1)=matrix(i,j,1)
matrix(i,j-1,5)=matrix(i,j,5)
matrix(i,j-1,3)=matrix(i,j,3)-matrix(i,j,5)
surface=surface+1
endif

Assign remaining growth length to the new cells

if((i+1.LE.maxheigth).and.(matrix(i+1,j,1).EQ.0.)) then
matrix(i+1,j,1)=matrix(i,j,1)
matrix(i+1,j,5)=matrix(i,j,5)
matrix(i+1,j,3)=matrix(i,j,3)-matrix(i,j,5)
surface=surface+1
endif

Assign remaining growth length to the new cells

if((i-1.GE.1).and.(matrix(i-1,j,1).EQ.0.)) then
```

```
matrix(i-1,j,1)=matrix(i,j,1)
matrix(i-1,j,5)=matrix(i,j,5)
matrix(i-1,j,3)=matrix(i,j,3)-matrix(i,j,5)
surface=surface+1
endif
```

Assign remaining growth length to the new cells

```
endif
endif
enddo
enddo
```

End of Do while loop

```
enddo
```

End of Growth_Procedure

```
Write (*,*) 'Growth rate =', vel
Write(*,*) 'Growth (m)',Lt
```

Validation_Initialisation Procedure

```
solidification_complete=1.
do i=1,maxheigth
do j=1,maxwidth
matrix(i,j,4)=0.
```

Re-initialise growth indicator for the next step

```
if(matrix(i,j,1).EQ.0.)then
solidification_complete=0.
```

Cell liquid indicate that solidification is not completed

```
endif
enddo
enddo
```

End of Validation_Initialisation Procedure

```
undercooling=undercooling+ ΔT
Write (*,*) 'Undercooling =', undercooling

End of Do While loop
enddo
```

File_Writing Procedure

```
open(2,file='output.txt',status='unknown')
```

```
do j=1,maxwidth
write(2,100) (/ (matrix(i,j,1),i=1,maxheigth) /).....Output microstructure matrix
100 format (501(F7.2,','))
write(2,*)'          '
enddo

End of File_Writing procedure

Write (*,*) '                    '
Write (*,*) 'End of solidification'
end

SUBROUTINE gen(germe,divis).....Subroutine for random number
real germe,divis
germe=dmod(16807.d0*germe,2147483647.d0)
divis=germe/2147483647.d0
end
```

References

1. Singer, A.R.R., Jennings, P.H., Hot-Shortness of the Aluminium-Silicon Alloys of Commercial Purity, J. Inst. Met., 73, (1947), pp. 197-212

2. Pellini, W.S., Strain Theory of Hot Tearing, The Foundry, 80, (1952), pp. 124-199

3. Bishop, H.F., Ackerlind, C.G., Pellini, W.S., Metallurgy and Mechanics of Hot Tearing, Trans. AFS, 68, (1960), p. 818-833

4. Rosenberg, R.A., Flemmings, C., Taylor, H.F., Modern Casting, 38, (1960), pp. 112-122

5. Rogerson, J.H., Borland, J.C., Trans. Met. Society of AIME, Vol. 227, 1963, pp. 1-7

6. Metz, S.A., Flemming, C., Hot Tearing in Cast Metals, Trans. AFS, 77, (1969) pp. 329-34

7. Verö, J., The Hot-Shortness of Aluminium Alloys, Met. Ind. (London), 48, (1936), p. 431-34, p. 442

8. Bochvar, A.A., "Optimum Content of the Eutectic in Cast Alloys", Izvest. Akad. Nauk. S.S.S.R., Tekhn., 6, (1944), p. 358-361

9. Lees, D.C.G., The Hot Tearing Tendencies of Aluminium Casting Alloys, J. Inst. Metals, 72, (1946), p. 343-364

10. Apblett, W.R., Pellini, W.S., Weld. Res. Suppl. 33, (1954), pp. 83-90

11. Bishop, H.F., Ackerlind, C.G., Pellini, W.S., Trans. Am. Foundrymen's Soc. 65, (1957), pp. 247-258

12. Ohm, L., Engler, S., Festigkeiteigenschaften erstarrender Randschalen aus Aluminium-legierungen - Teil 1, GieBereiforschung, 42, (1990), 3

13. Dodd, R.A., Hot-tearing of Castings: A Review of Literature, Foundry Trade Journal, 101, (1956), pp. 321-31

14. Singer, A.R.E., Cottrell, S.A., Properties of the Aluminium-Silicon Alloys at Temperatures in the Region of the Solidus, Journal Inst. of Metals, 73, (1947), p. 33-54

15. Campbell, J., Castings, © Butterworth-Heinemann Ltd. 1991

16. Borland, J.C., Generalized Theory of Super-Solidus Cracking in Welds (and Castings), British Welding Journal, Vol. 7, No. 8, (1960), pp. 508-512

17. Borland, J.C., Hot Cracking in Welds, British Welding Journal, Vol. 7, No. 9, (1960), pp. 558-559

18. Arnberg, L., Dahle, A.K., Investigation of the dendrite coherency point in solidifying Al-Si foundry alloys, The Norwegian Institute of Technology, Dept. of Metallurgy, The 4th International Conference on Aluminium Alloys, 1994, pp. 91-98

19. Arnberg, L., Chai, G., Backerud, L., Determination of dendritic coherency in solidifying melts by rheological measurements, Materials Science and Engineering, A173, 1993, pp. 101-103

20. Chai, G., Backerud, L., Rolland, T., Arnberg, L., Dendrite Coherency during Equiaxed Solidification in Binary Aluminum Alloys, Met. And Mat. Trans. A, Vol. 26A, (1995), pp. 965-970

21. Smith, C.S., Grains, Phases, and Interfaces: An Interpretation of Microstructure, AIME Trans., Vol. 175, (1948), pp. 15-51

22. Van Vlack, L.H., Riegger, O.K., Warrick, R.J., Dahl, J.M., Trans. Met. Soc. AIME, Vol. 221, (1961), p. 220

23. Campbell, J., Metallography, 4, (1971), pp. 269-278

24. Tucker, S.P., Hochgraph, F.G., Metallography, 6, (1973), 457-464

25. Wray, P.J., Acta Metallurgica, 76, (1976), pp. 125-135

26. Pepe, J.J., Savage, W.F., Effects of Constitutional Liquation in 18-Ni Maraging Steel Weldments, Weld. Research Suppl., (1967), pp. 411-422

27. Couture, A., Edwards, J.O., The Hot-Tearing of Copper-Base Casting Alloys, AFS Transactions, 74, (1966), pp. 709-721

28. Marshall, W.K.B., A Note on the Relationship between Chemical Composition and Hot-Cracking in Mild and Alloy Steels, Brit. Welding Journal, Vol. 7, (1960), pp. 451-453

29. Pumphrey, W.I., Lyons, J.V., Cracking During the Casting and Welding of the More Common Binary Aluminium Alloys, Journ. Inst. Met., Vol. 74, (1948), pp. 439-455

30. Borland, J.C., Fundamentals of solidification cracking in welds: Part 1 & Part 2, Weld. Met. Fabrication, (1979), pp. 19-29, pp. 99-107

31. Pumphrey, W.I., Jennings, P.H., Journ. Inst. Metals, Vol. 75, (1948), pp. 235-256

32. Campbell, J., Clyne, T.W., Hot Tearing in Al-Cu Alloys, Cast Metals, Vol. 3, No. 4, (1991), pp. 224-226

33. Archbutt, S.L., Grogan, J.D., Jenkin, J.W., Journ. Inst. Metals, 40, (1928), p. 219

34. Norton, A.B., A Hot Shortness Testing Machine for Aluminium Alloys, Trans Am. Inst. Met., 8, (1914), pp. 124-127

35. Lange, E.A., Heine, R.W., A Test for Hot Tearing Tendency, Trans. Am. Foundrymen's Soc., 60, (1952), pp. 182-196

36. Hall, H.F., Strength and Ductility of Cast Steel During Cooling from the Liquid State in Sand Moulds, 2nd Special Report, Iron and Steel Institute, No. 15, Part IV, (1936), pp. 65-93

37. Tatur, A, Study of Cracks in Light Alloys, Fonderie, 59, (1950), pp. 2245-2256

38. Payne, R.J.M., Michael, A.D., Eade, R.W., New Magnesium-Zirconium Casting Alloy, Metal Ind., 80, (1952), pp. 103-104

39. Johnson, G.W., Investigation of Hot Tears in Steel Castings: Part I - Test Specimen for Evaluating Hot Tearing in Steel Castings, Trans., A.F.S., 60, (1952), pp. 137-140

40. Lillieeqvist, G.A., Fuqua, J.H., ibid., Part II - Evaluation of Hot Tear Test Casting, Trans., A.F.S., 60, (1952), pp. 141-Wyman, C.H., Faist, C.A., DiSylvestro, G.D., ibid., Part III - Hot Tear Investigation, Trans., A.F.S., 60, (1952), pp. 145-162

41. Chadwick, H., High strength, hot tear resistant A210 (K01) alloy, Aluminium Industry, Vol. 12, No. 3, (1993), pp.24-26

42. Chadwick, H., Hot Shortness of Al 4.5%Cu Alloy, Casting Metal, Vol. 4, No. 1, (1991), pp. 43-49

43. Williams, J.A., Singer, A.R.E., Deformation, Strength, and Fracture above the Solidus Temperature, Journ. Inst., Vol. 96, (1969), pp. 5-12

44. Matsuda, F., Nakata, K., Shimokusu, Tsukamoto, K., Arai, K., Effect of Additional Element on Weld Solidification Crack Susceptibility of Al-Zn-Mg Alloy (Report I), Japanese Weld. Research Inst., Vol. 12, No. 1, (1983), p. 81

45. Hall, H.F., Strength and Ductility of Cast Steel During Cooling from the Liquid State in Sand Moulds, 3rd Special Report, Iron and Steel Institute, No. 23, (1938), pp. 73-85

46. Gamber, E.J., Hot Cracking Test for Light Metal Casting Alloys, Trans., A.F.S., 67, (1959), pp. 237-241

47. Liu, Q., Smith, R.W., Sahoo, M., Trans., A.F.S., 101, (1993), p. 759

48. Heine, W.H., Rosenthal, P.C., Principles of Metal Casting, © 1955, McGraw-Hill Book Inc., Chapter 8, pp. 173-198

49. Warrington, D., McCartney, D.G., Development of a New Hot-Cracking Test for Aluminium Alloys, Cast Metals, Vol. 2, No. 3, (1989), pp.134-143

50. Warrington, D., McCartney, D.G., Hot-cracking in Aluminium Alloys 7050 and 7010 - a Comparative Study, Cast Metals.

51. Dowd, J.D., Weld Cracking of Aluminium Alloys, Welding Research Supplement, (1952), pp. 448-456

52. Savage, W.F., Lundin, C.D., Application of the Varistraint Technique to the Study of Weldability, Welding Research Supplement, November 1966, pp. 497-503

53. Tamura, H., Kato, N., Ochiai, S., Katagiri, Y., Cracking Study of Aluminium Alloys by the Variable Tensile Strain Hot Cracking Test, Transactions of the Japan Welding Society, Vol. 8, No. 2, (1977), pp. 63-69

54. Goodwin, G.M., Development of a New Hot Cracking Test - The Sigmajig, Welding Research Supplement, February 1987, pp.33-38

55. Cross, C.E., Olson, D.L., Hot Tearing Model to Assess Aluminium Weldability, Aluminum Alloys Their Physical and Mechanical Properties, Vol. III, Ed. Starke, E.A., (1986), pp.1869-1875

56. Cieslak, M.J., The Welding and Solidification Metallurgy of Alloy 625, Welding Research Supplement, February 1991, pp.49-56

57. Clyne, T.W., Davies, G.J., Comparison between experimental data and theoretical predictions relating to dependence of solidification cracking on composition, Solidification and Casting of Metals, Metals Soc. Conference, Sheffield, 1977, pp. 275-278

58. Clyne, T.W., Davies, G.J., The influence of composition on solidification cracking susceptibility in binary alloy systems, Journ. Brit. Foundryman, 74, No. 4, (1981), pp. 65-73

59. Fredikson, P.H, Lethinen, B., Continuous observation of hot crack-formation during deformation and heating in SEM, Solidification and Casting of Metals, 1979, pp.260-267

60. Grasso, D., Drezet, J.M., Farup, I., Rappaz, M., Direct formation of hot tear formation in organic alloys, Proceedings of the 7th conference on advanced materials and processes, EuroMat 01, June 2001, CD-ROM.

61. Ackermann, P., Kurz, W., Heinemann, W., In Situ Tensile Testing of Solidifying Aluminium and Al-Mg Shells, Materials Science and Engineering, vol.75, 1985, pp.79-86

62. Dickhaus, C.H.,Ohm, L., and Engler, S., *AFS Trans.*, 1994, vol. 101, pp. 677-684

63. Magnin, B., Maenner, L., Katgerman, L., and Engler, S., *Mat. Sci. Forum*, 1996, vols. 217-222, pp. 1209-1214

64. Ohm, L., and Engler, S., *Giessereiforschung*, 1990, vol. 42, No. 3

65. Ohm, L., and Engler, S., *Giessereiforschung*, 1990, vol. 42, No. 4

66. Fortina, G., A.F.S. Cast. Met. Journal, No. 2, (1980), pp. 25-29

67. Colley, L.J., Wells, M.A., and Maijer, D.M., *Mat. Sci. Engng A*, vol. 386, 2004, pp. 140-148

68. Arnberg, L., Bakerud, L., and Chai, G., Solidification Characteristics of Aluminum Alloys, Dendrite Coherency, Vol. 3, AFS Des Plaines, IL, 1990

69. C.L. Martin, M. Braccini and M. Suéry, Mat. Sci. Eng. A325, 2002, pp. 292-301

70. Fortina, G., Anselmi, A., Parameters for Analyzing DC Casting Behaviour of Al-Alloys, Light Metals, 2, (1977), pp.207-221

71. Flender,E., Hansen, P.N., Sahm, P.R., Giesserei-Forschung 39, 1987, pp. 137-149

72. Spencer, D.B., Mehrabian, R., Flemings, M.C., Met. Trans. 3, (1972), p. 1925

73. Katgerman, L., J. Metals, Vol. 2, No. 34, (1982), pp.46-49

74. Metz, S.A., Flemming, C., A Fundamental Study of Hot Tearing, Trans. A.F.S., 78, (1971) pp. 453-460

75. Feurer, U., Matematisched Modell der Warmrissneigung von binären Aluminiumlegierungen, Giesserei Forsch, 2, (1976), p. 75

76. Campbell, J., Trans. AIME, Vol. 245, pp. 2325-2334

77. Upaddhya, S., Cheng, S., Chandra, U., A Mathematical Model for Prediction of Hot Tears in Castings, Light Metals 1995, pp. 1101-1106

78. Chandra, U., Computer Prediction of Hot Tears, Hot Cracks, Residual Stresses and Distortions in Precision Castings: Basic Concepts and Approach, Light Metals 1995, pp. 1107-1117

79. Das, S, Upadhya, G., Chandra, U., Prediction of Macro and Micro-Residual Stress in Quenching using Phase Transformation Kinetics, First International Conference on Quenching & Control of Distortion, ed., G. Trotten, Metals Park, OH: ASM International, 1992, pp. 229-234

80. Asbjorn, M., Holm, E.J., On the Use of Constitutive Internal Variable Equations for Thermal Stress Predictions in Aluminum Casting, Journ. Of Thermal Stresses, 14, (1991), pp. 571-587

81. Purvis, A.L., Kannatey-Asibu, E., Pehlke, R., Modeling Thermal Stresses During Solidification, Modeling of Casting, Welding and Advanced Solidification Processes VI, ed., Piwonka, T.S., The Minerals, Metals & Materials Society, 1993, pp. 601-608

82. Katgerman, L., Journal of Metals, 47, (1982)

83. Wisniewski, Brody, H.D., Tensile Behavior of Solidifying Aluminum Ingot, Modeling of Casting, Welding and Advanced Solidification Processes V, ed., Rappaz M., The Minerals, Metals & Materials Society, 1991, pp. 273-278

84. Hannard, B., Cialti, R.V., Schalwijk, V., Light Metals, 1994, p. 879

85. Drezet, J.M., Rappaz, M., Carrupt, B., Plata, M., Experimental Investigation of Thermo-Mechanical Effects during Direct Chill and Electromagnetic Casting of Aluminium Alloys, Met. Trans., 26B, (1995), pp. 821-829

86. Drezet, J.M., Rappaz, M., Modeling of Ingot Distortions During Direct Chill Casting of Aluminum Alloys, Met. Trans., Vol. 27A, (1996), pp.3214-3225

87. Purvis, A.L., Elijah, K.A. Jr., Pehlke, R., A.F.S. Trans., Vol. 98, (1990), p.1

88. Purvis, A.L., Elijah, K.A. Jr., Pehlke, R., A.F.S. Trans., Vol. 99, (1991), p.525

89. Feurer, U., Wunderlin, R., Observation of Porosity Formation During Solidification of Aluminium Alloys by Accoustic Emission Measurements, Solid. Cast. Metals, The Metals Society, (1979), pp. 340-344

90. Larikov, L.N., Prokopenko, G.I., Franchuk, V.I., Yakubtsov, I.A., Acoustic Emission Examination of Embrittlement of Aluminum and Amg6 Alloy in Interaction with Liquid Gallium, Inst. Metals Physics, Academy of Sciences Ukrainian SSR, Kiev, No.3, (1990), pp. 5-9

91. Dahle, A.K., Arnberg, L., The rheological Properties of Solidifying Aluminum Foundry Alloys, Journ. Of Metals, The Minerals, Metals & Materials Society, Vol. 48, No. 3, (1996), pp. 34-37

92. Bellet, M., Decultieux, F., Ménai, M., Bay, F., Levaillant, J.L., Chenot, P.S., Svensson, Thermomechanics of the cooling stage in casting processes: three-dimensional finite element analysis and experimental validation, Met. Trans. 27B, (1996), p. 81

93. Guven, Y.F., Hunt, J.D., Cast Metals, Vol. 1, No. 2, (1988), pp. 104-111

94. Feurer, U., Giesserei., Vol. 28, No.2, (1980), pp. 75-80

95. Rappaz, Drezet, J.M., and Gremaud, M., A New Hot Tearing Criterion, Met. Trans., Vol. 30A, February 1999, 449-455

96. Drucker,D.C., High-Strength Materials, Proceedings of the Second Berkeley International Materials Conference, John Wiley & Sons, New York, 1964

97. Rappaz, M., Gandin, Ch.-A., Probalistic modelling of microstructure formation in solidification processes, Acta metal. mater., Vol. 41, No. 2, pp. 345-360, 1993

98. Rappaz, M., Gandin, Ch.-A., Prediction of grain structures in various solidification processes, Metallurgical and Materials Transactions A, Volume 27A, March 1996, pp. 695-705

99. Lahaie, D., and Bouchard, M., Metall. Mater. Trans. B, 2001, Vol. 32B, pp. 697-705

100. Brown, S.G.R., Spittle, J.A., Modeling of casting, welding and advanced solidification processes, *Editors:* M. Rappaz, M. Ozgu and K. Mahin, TMS, Warrendale, Pa (1991), p. 395

101. Srolovitz, D.J., et al., Acta. Metall. vol. 32, 783, (1984)

102. Langlais, J., Gruzleski, J., A Novel Approach to Assessing the Hot Tearing Susceptibility of Aluminum Alloys, Proceeding of the 7th International Conference ICAA7, Charlottesville, Virginia, April 9-14, 2000, Part 1, Materials Science Forum, Volumes 331-337 (2000), pp. 167-172

103. J. Langlais and J.E.Gruzleski: *Light Metals 1999*, M. Bouchard and A. Faucher, ed., pp. 247-263.

104. Fortier, M., Lahaie, D., Bouchard, M., et Langlais, J., Mould Surface Roughness Effects on the Microstructure and the Hot Tearing Strength for an Al-4. 5wt% Cu Alloy, Ligth Metals 2000, Ed. J.Kazadi and J.Masounave, August 2000

105. Sellars, C.M., Tegart, W.J.McG., Mem. Sci. Rev. Metall., 63, (1966), p.731

106. Almasan, C., Danu, D., Rosu, I., Rev. Roum. Sci. Tech. Mechanical Appl., 26, No. 2, Bucarest, (1981), p. 249

107. Raybould, D., Sheppard, T., J. Inst. Met., 101, (1973), p.65

108. Wong, W.A., Jonas, J.J., Trans. AIME, 242, (1968), p. 2271

109. Rogberg, B, Scandinavian Journal Metallurgy, vol. 12, 1983, p.51

110. Dickauss, C.H., Ohm, L., and Engler, S., Transactions AFS, vol. 118, 1993, p.677

111. Adamson, A.W., Physical Chemistry of Surfaces, 2nd ed., John Wiley & Sons, Inc., New York, 1967

112. Backerud, L., Krol, E.I, Tamminen, J., Solidification Characteristics of Aluminium Alloys, Volume 1: Wrought Alloys, Skanaluminium, P.O. 2456 – Solli, N-0202 Oslo 2, Norway, Copyright 1986, ISBN 82-00-36380-5

113. Mechanics and Materials II, Spring 2004, Creep and Creep Fracture: Part III , ©L.Anand, Department of Mechanical Engineering, MIT Cambridge(source internet)

114. Larouche, D., Langlais, J., Wu, W., Bouchard, M., A Constitutive Model for the Tensile Deformation of a Binary Aluminum Alloy at High Fractions of Solid, Metallurgical & Materials Transactions B: June 2006, pp. 431-443